Development of a Soil Compaction Management System: Using Hyperspectral-Based Soil Properties Sensing

(土壌踏圧管理システムの開発：ハイパースペクトルベース土壌センシング)

2025

Hokkaido University, Graduate School of Agriculture,

Frontiers in Production Sciences Doctor Course

Amanor, Ishmael Nartey

Development of a Soil Compaction Management System: Using Hyperspectral-Based Soil Properties Sensing

By

Amanor, Ishmael Nartey

Dissertation

Submitted to the Department of Environmental Resources in the Graduate School of Agriculture

Hokkaido University, Sapporo, Japan, 060-8589 in partial fulfillment of the requirements for the degree of

Doctor of Philosophy

2025

Table of Contents

Acknowledgments

I would like to express my sincere gratitude to my supervisor, Dr. Noboru Noguchi, and my co-supervisor, Dr. Ricardo Ospina, for their continuous guidance and support throughout my research journey and knowledge acquisition. I extend my profound appreciation to Dr. Kazunobu Ishii and Dr. Yoshitomo Yamasaki for their invaluable contributions to this research. I am also grateful to all staff and students of the Laboratory of Vehicle Robotics, with special thanks to Awakawa-kun and Mawari-kun for their assistance with the experimental work.

I am deeply indebted to the Embassy of Japan in Ghana and the Ministry of Education, Culture, Sports, Science, and Technology (MEXT) for the scholarship that enabled my doctoral studies. I would also like to express my appreciation to the Student Affairs Section of the Graduate School of Agriculture at Hokkaido University for their ongoing support throughout my academic journey.

On a personal note, I wish to express my heartfelt gratitude to my family. To my wife, Narkie, thank you for being my pillar of strength and my greatest motivator; your unwavering support has kept me focused and determined. To my son Jormy, thank you for giving me purpose and inspiration; your happiness is my constant motivation. I am grateful to my brother Isaac and my mother for their prayers and regular communication, which have provided emotional support despite the distance. I also acknowledge Cape Coast Technical University and my colleagues, especially Nana Yaa, for their significant assistance during my studies. Finally, I would like to thank all my friends in Ghana and Japan, whose encouragement has contributed significantly to this achievement.

List of Figures

List of Tables

Acronyms and Abbreviations

FAO – Food and Agriculture Organization

USDA – United States Department of Agriculture

USEPA - United States Environmental Protection Agency

GTD – Ground truth data

HSC – Hyperspectral camera

PD – Packing density

BD – Bulk density

MCW – Moisture content wet basis

MCD - Moisture content dry basis

VMC – Volumetric moisture content

CC – Clay content

SC – Soil content

STC – Silt content

OMC – Organic matter content

ANOVA - Analysis of variance

PLSR - Partial least squares regression

MLR – Multiple linear regression

LR – Linear regression

SD - Standard deviation

CR - Cambridge roller

$\mathbf{N_{veg}}$ - Vegetated pixels

$\mathbf{N_{total}}$ - Total pixels

FVC - Fractional vegetation cover

VIF - Variable Inflation Factor

ROI - Regions of interest

RPD - Ratio of performance to deviation

NDVI – Normalized difference vegetation index

VNIR – Visible, Near infrared

SWIR – Shortwave infrared

LMC - linear model of co-regionalization

$\mathbf{R^2}$ – Coefficient of determination

r – Correlation

RMSE - Root mean square error

$\mathbf{m_s}$ - Weight of solids

$\mathbf{m_w}$ – Mass of water

$\mathbf{v_s}$ - Volume of solids

$\mathbf{v_w}$ - Volume of water

$\mathbf{v_T}$ - Sediment volume

PA – Precision agriculture

SC – Soil compaction

PT – Precision tillage

RS – Remote sensing

CHAPTER 1. INTRODUCTION

1.1. Research background

1.1.1. Global agriculture and mechanization drive

The average global agricultural productivity growth has declined since 2020, with organizations such as the Food and Agriculture Organization (FAO) and Global Agricultural Productivity (GAP) reporting an annual growth rate of 1.1 to 1.3%. This is well below the 1.73 to 2.4% yearly growth target required to meet global food demand by 2050 (FAO, 2023b; Steensland, 2022). The downward trend in average annual productivity growth was already evident between 2011 and 2020, at 1.93%, marking a decline from the 2.72% observed between 2001 and 2010. As a result, current global productivity growth has fallen by approximately 57% compared to the previous two decades. This decline is attributed to a reduction in total factor productivity (TFP) growth, which measures output relative to input use (Fuglie et al., 2024).

In places like North America, Europe, and East Asia, farmers have managed to boost their crop yields by around 15% to 20% with better farming techniques. But in parts of Sub-Saharan Africa and South Asia, things are tougher because they do not have the same access to technology (Parras-Burgos et al., 2018). This gap is slowing down global progress in farming, and right now, we are not growing enough food fast enough to keep up with the world's population, which needs at least a 1.73% increase every year to be sustainable by 2050 (FAO, 2022; FAO, 2023a).

To tackle this, the agricultural sector worldwide is quickly picking up new technology to solve many of the issues, like dealing with a shortage of workers and the aging farmer population in richer countries. At the same time, there is a big need to boost productivity in developing nations, where farming often makes up more than 25% of their economies. These different but related problems call for solutions that fit local contexts, considering the environment, economic situations, and available infrastructure (Ruane, 2019; World Bank, 2024).

1.1.1.1. Evolution of mechanization and challenges

The initial stages of agricultural mechanization involved simple handheld tools such as hand plows, sickles, and hoes made from wood, stone, or bone. These tools marked the transition from manual labor to mechanized assistance in farming (Biering, 2025; Fadat, 2024). The inception of the use of animal muscle power to draw implements, such as plows and other cultivators, transformed farming. Animals such as bulls, oxen, horses, donkeys, and buffalo provided the power needed for tasks like tilling, planting, harvesting, and transporting cops to barns and markets. This increased efficiency and crop yields, while also lowering human labor requirements (Greene, 2023; Turay et al., 2022).

The transition from animal-drawn implements to steam-powered machinery, exemplified by Fowler's Steam Plow in the 1850s, marked the initial phase of agricultural mechanization. This evolution was further advanced by the introduction of the gasoline-powered Fordson Model F in 1917, the first mass-produced tractor, which significantly transformed the labor demands of farming (Campbell and Bartley, 2007; McWilliams, 2019). This era witnessed the development of essential tools such as mechanical plows, harrows, and seed drills, designed to be operated by early tractors. As noted by Thompson (2009) in his extensive history of agriculture, this initial wave of mechanization boosted labor productivity. However, it was constrained by the technological limitations of the period.

The early tractor attachments, like moldboard plows, sickle bars, and many more, were supported manually during operation. The three-point hitch by Ferguson in the late 1930s standardized implement attachment and enabled hydraulic control (Becker, 2024). The introduction of diesel engines, with models like the John Deere Model R in 1949, increased power and efficiency. Further developments in tractor design up to the 1950s produced systems such as the power takeoff (PTO), which allowed implements to draw power directly from the tractor engine (Chowdhury, 2025; Machine Finder, 2025). Rubber tires replaced steel wheels, improving field performance and becoming the first effort to reduce soil compaction (SC) (Lal, 2015). This period also saw the introduction of more specialized implements like combine harvesters, dramatically reducing grain harvesting labor requirements (Kaur et al., 2023). Four-wheel-drive tractors like the Massey Ferguson Model 1500, released in the 1970s, improved traction and tackled heavier tasks (Big Tractor Power, 2001).

The addition of electronics into agricultural machinery during the late 20th century revolutionized farming practices. According to (Marçal de Queiroz et al., 2022), the adoption of sensors, controllers, and early computer systems in tractors and implements laid the foundation for precision agriculture (PA). GPS technology in the 1990s further advanced this field by allowing precise positioning and facilitating the development of auto-steering systems (Kumar and Moore, 2002). Pierce and Nowak (1999) highlighted the transformative impact of technologies that enabled variable rate application of agricultural inputs, effectively minimizing waste and environmental impact while enhancing productivity. The development of the ISOBUS standard in the early 2000s significantly improved interoperability between tractors and implements from various manufacturers (Fountas et al., 2015).

The 21st century has witnessed a digital revolution in agricultural mechanization. Shamshiri et al. (2018) noted that modern tractors now incorporate advanced telematics, integrated data management systems, and connectivity to farm management software. Implements have advanced to feature precision sensors, cameras, and microprocessors capable of real-time adjustments (Wolfert et al., 2017). Walter et al. (2017) described the emergence of autonomous guidance systems and the advent of fully autonomous tractors, which operate without human intervention. Leading companies such as Kubota, Yanmar, and John Deere have launched commercially available autonomous tractors (Lowenberg-DeBoer et al., 2020).

1.1.1.2. Environmental impacts of conventional tillage systems

The quest to increase food production and minimize its negative effect on the environment marginally, or using natural resources related to food production efficiently, has become necessary to achieve sustainable food security (United Nations, 2013; WHH, 2023). Mechanization has significantly boosted agricultural productivity, enhancing cost efficiency, output value, income, and return rates across all crop types (Khater et al., 2023; Peng et al., 2022). Although the use of farm machinery has enormous benefits that have been reported by researchers (Diao et al., 2016; Hasan et al., 2020), one cannot overlook the implications of the use of farm machinery on the environment, such as SC among others (FAO, 2020). The use of heavy machinery during the cropping season often leads to SC, which restricts crop development (Askari et al., 2021; Twum and Nii-Annang, 2015). Tillage is a common improvement strategy, with conventional and conservation tillage being the primary methods. However, intensive tillage leaves soil exposed and susceptible to wind and water erosion, accelerating topsoil loss at rates 10-100 times faster than natural soil formation (Montgomery and Matson, 2007). Tilling soil releases stored carbon dioxide into the atmosphere by exposing organic matter to rapid decomposition. Research shows that switching from conventional tillage to no-till practices can help in the sequestration of approximately 0.3-0.5 tons of carbon per hectare annually (Lal, 2004). However, regular tillage disrupts soil ecosystems, damages soil aggregates, and worsens compaction issues. A comprehensive review found that conventional tillage significantly reduces soil aggregate stability compared to conservation tillage systems (Six et al., 2000). Furthermore, intensive tillage operations have been shown to reduce earthworm populations by 50-80% (Chan, 2001; Crittenden et al., 2014). Tillage also increases erosion, leading to sedimentation in waterways. According to the USDA, agricultural runoff contributes to the impairment of approximately 48% of stream miles in the United States (Scott and Haggard, 2021; Singh et al., 2023).

Modern agricultural mechanization faces increasing scrutiny regarding its environmental impact. Fuel consumption and emissions from farm machinery contribute significantly to agriculture's carbon footprint (Notarnicola et al., 2017). Alternative power sources, including biofuels, hydrogen, and electric drives, are being explored but face significant implementation challenges (Mousazadeh et al., 2011). Basso et al. (2019) noted that PA technologies are an inexpensive alternative to reducing environmental impacts through optimized input applications and site-specific intervention activities. They further stated that the effectiveness of PA requires proper planning, implementation, and management. Legislative measures across the globe, such as the US Farm Bill, the EU's greening measures, and initiatives in Brazil and Australia, emphasize the need to shift towards conservation practices such as PA to alleviate agriculture's environmental footprint (Claassen et al., 2018; Derpsch et al., 2010; Luo et al., 2010; Mceldowney, 2020).

1.1.1.3. Emergence of precision agriculture approaches

PA, also called precision farming, emerged in the late 20th century as a response to the growing need for sustainable agricultural practices. It leverages advanced technologies such as geographic information systems (GIS), global positioning systems (GPS), remote sensing (RS), and data analytics to optimize crop management on a site-specific basis (Masud Cheema et al., 2023; Petrović et al., 2024). Initially, the PA approach focused on variable-rate application of inputs like fertilizers and pesticides based on spatial variability within fields (Kushwaha et al., 2024). However, recent developments in PA aim to transform traditional farming using advanced technologies to improve productivity, reduce resource waste, and minimize environmental impact. This is achieved by tailoring agricultural inputs and practices to meet the specific needs of different field zones (Getahun et al., 2024).

The early 2000s marked a significant expansion of PA technologies. McBratney et al. (2005) introduced the concept of ‘digital agriculture’, emphasizing the integration of advanced sensing technologies, data analytics, and decision support systems. This development led to the development of more advanced tools, including satellite and aerial RS for crop monitoring, ground-based sensor networks, UAVs for high-resolution field imaging, and advanced soil sampling and mapping techniques. The backbone technological drivers have been GPS and positioning technologies, advanced sensor technologies, big data analytics, machine learning, artificial intelligence (AI), and Internet of Things (IoT) in agriculture (Getahun et al., 2024).

Zhang et al. (2002) emphasized the environmental and economic benefits of PA and demonstrated PA's potential in reducing farm input use and eco-friendly significance. Similar research by Pivoto et al. (2018) identified four fundamental routes for the establishment of PA. These include predictive analytics for crop management, real-time monitoring and decision support systems, automated and autonomous farming technologies, and finally, the integration of big data and artificial intelligence (AI). Current PA approaches are more focused on hyper-site specific crop management, sustainability with resource optimization, climate change adaptation, and integrated ecosystem management.

The development of PA was enhanced by advancements in computing power, sensor technologies, and satellite imagery during the 1980s and 1990s. This progress made yield mapping and variable-rate technology (VRT) possible, allowing farmers to apply inputs precisely where needed (Getahun et al., 2024; Masud Cheema et al., 2023). The introduction of GPS to farm machinery further accelerated the adoption of PA practices, facilitating real-time data collection and site-specific management. PA gained momentum as researchers showcased its potential to tackle challenges such as soil variability, nutrient inefficiencies, and water scarcity (Mgendi, 2024). Research by Bongiovanni and Lowenberg-Deboer (2004) indicated that variable-rate fertilizer applications can significantly reduce input costs while maintaining or improving yields. Similarly, Mulla (2013) found that RS technologies were effective for monitoring crop health and detecting stress factors such as pests and nutrient deficiencies.

The modern era of precision agriculture (PA) increasingly relies on predictive modeling, with machine learning algorithms emerging as a key focus area. These algorithms assist farmers in anticipating crop performance under varying conditions (Kamilaris et al., 2017). Similarly, automation is revolutionizing PA through autonomous tractors, drones, and robotic systems designed for planting, weeding, harvesting, and monitoring. These technologies significantly reduce labor needs while enhancing precision in field operations (Hoque and Padhiary, 2024). For example, drones equipped with multispectral cameras can quickly and accurately assess crop health across large areas. Conventional farming practices often involve excessive machinery traffic across fields, resulting in detrimental soil compaction. To address this, precision tillage (PT) and optimized path planning have become essential components of PA, helping to minimize soil disturbance while maintaining productivity. Building on these developments, future research aims to make PA more accessible through affordable technologies such as open-source software platforms and low-cost sensors (Wolfert et al., 2017).

1.1.2. Soil compaction: Processes, impacts, and solutions

SC in the agricultural field is where heavy machinery, livestock traffic, natural occurrences, and other human activities compress the soil. This process forces air out of the pore spaces between soil particles (British Columbia Ministry of Agriculture, 2015; Cambi et al., 2015). This makes it difficult for the crop roots to access water, air, and nutrients in the soil, inhibiting crop development. (Bengough et al., 2011; Peralta et al., 2024). When the soil is compacted, the individual soil particles are pressed closer together. This leads to a greater mass per unit volume, which is reflected by a higher bulk density (BD) value. Thus, the more compacted a soil is, the higher its BD (Peralta et al., 2024). Tilling at inappropriate moisture levels, insufficient crop diversification, and inadequate organic matter incorporation can degrade soil structure and increase compaction risk (Mehra et al., 2018).

Despite technological advances, SC remains a significant challenge. Hamza and Anderson (2005) identified how increasing machinery weight has led to deeper subsoil compaction that can persist for decades. Advances in tire technology, including low-pressure radial tires and tracked systems, have helped mitigate surface compaction, but often cannot prevent subsoil compaction (Batey, 2009). Controlled traffic farming systems, where machinery is restricted to permanent lanes, have shown promise in reducing compaction across fields (Chamen et al., 2015; Tamirat et al., 2022). However, Tullberg et al. (2018) noted that adoption remains limited due to implementation challenges and equipment compatibility difficulties. These adoption barriers need more flexible and adaptable compaction management solutions. PT practices address these challenges by allowing farmers to target only compacted areas with appropriate tillage depth, reducing the need for investment in specialized equipment, and working within existing field traffic patterns, providing variable treatment based on soil conditions. Unlike whole-field approaches, PT can be implemented incrementally with conventional machinery, potentially increasing adoption rates while effectively managing surface and subsoil compaction (Šarauskis et al., 2024).

1.1.2.1. Effects on soil physical and chemical properties

SC significantly alters soil fundamental structure that supports plant growth, causing disruption to physical properties and affecting soil ecosystem functions. When soil particles are compacted, BD increases while porosity decreases, creating a cascade of damaging effects (Horn et al., 2003). These changes affect water mobility by up to 90% in severely compacted soils, which causes an increased surface runoff and erosion risk. This diminishes both water retention capacity and the drainage ability of soils (Batey, 2009). Traditional assessment of these physical changes has relied heavily on BD sampling and penetrometer readings, which provide accurate point measurements but are labor-intensive and sometimes disruptive to the soil profile (Grossman and Reinsch, 2002). The small sampling area achievable with these methods often fails to capture the spatial heterogeneity of compaction across larger fields. RS technologies offer alternative data collection methods by detecting variations in surface moisture dynamics and identifying areas prone to waterlogging or vegetation with water stress that indicate underlying compaction issues. However, these require calibration with ground-truth data acquired through conventional measurements (Mohanty et al., 2017).

Compaction stress subjects the chemical properties of a soil to substantial modifications, often with a negative impact on nutrient cycling and availability. Reduced aeration caused by SC affects the oxidation-reduction ability, altering nutrient solubility, mobility, and chemical transformations (Nawaz et al., 2013). Traditional soil testing procedures for nutrient availability and pH can reveal SC effects; however, they require laboratory analysis with considerable time delays between sampling and results (Najdenko et al., 2024). This temporal gap limits the ability to make timely management decisions, particularly when SC varies seasonally with moisture conditions. Hyperspectral sensing is a powerful tool that can provide rapid assessment of soil properties across large areas. Studies have demonstrated the capability of hyperspectral sensing in detecting variations in organic matter content, soil pH, and nutrient status that often correlate with SC patterns (Ben-Dor et al., 2009; Ge et al., 2011). However, these spectral methods require extensive calibration with standard soil tests to establish reliable models to show relationships between spectral signatures and actual soil properties under local field conditions (Stenberg et al., 2010)

The final effect of compaction on soil physical, chemical, and other properties manifests as reduced agricultural productivity and negative environmental impact. Traditional yield monitoring systems can identify productivity losses, but often cannot distinguish SC from other stress factors without additional soil information (Adamchuk et al., 2004). The grid soil sampling method has been used throughout history to map compaction variability; however, practical constraints typically limit the grid sizes (Raper, 2005). RS platforms provide the spatial resolution and rapid assessment capability needed to map this variability more efficiently. Multitemporal satellite imagery can track crop vigor throughout the growing season, identifying areas where compaction stress limits productivity (Mulla, 2013). When these observations are combined with targeted soil sampling at representative locations, farmers can develop more accurate SC management zones while reducing the total number of physical samples required (Quraishi and Mouazen, 2013).

Implementing site-specific compaction management effectively requires acquiring timely information on soil conditions across entire fields. However, traditional point-sampling methods are tedious, costly, and time-consuming, making them less practical for large-scale applications. A promising approach combines strategic soil sampling to establish site-specific relationships between soil properties and SC with broader-scale proximal and RS to extend these relationships across fields (Castaldi et al., 2019). For example, penetrometer measurements along transects can be correlated with electrical conductivity surveys to generate continuous maps of soil strength (Fulton et al., 2010). Similarly, BD samples at reference points can be calibrated to reflectance spectra from aerial imagery to estimate compaction status across broader areas. This integration of conventional and advanced sensing approaches enables farmers to combine the accuracy of direct measurements with the extensive spatial coverage provided by RS technologies. As a result, PT operations can be optimized to apply targeted remediation only where necessary (Quraishi and Mouazen, 2013). The evolution toward integrated sensing systems represents a significant advance beyond the limitations of isolated sampling techniques, providing a more complete basis for sustainable soil management decisions.

1.1.3. Plant responses to soil compaction

SC triggers complex stress responses in plants, disrupting both root development and aboveground growth processes. Compacted soils with increased BD and mechanical impedance significantly restrict root penetration and propagation, leading to shallower root systems with reduced exploration capacity (Colombi and Keller, 2019). This restriction significantly limits water and nutrient access for crop roots, particularly in cereals with fibrous root systems that typically explore large soil volumes. Wheat (*Triticum aestivum* L.), a globally important cereal crop, exhibits notable sensitivity to SC, causing a reduction in root length density under compaction (Yu et al., 2024). The physiological response includes transformed hormone signaling, with increased ethylene production triggering radial root thickening and reduced elongation (Wang et al., 2013). These root adaptations come at a cost, diverting energy from productive growth to overcoming compaction restrictions (Nosalewicz and Lipiec, 2014).

The aboveground impact of SC manifests through reduced growth rates, altered plant structure, and reduced yield rates. Tracy et al. (2013) observed delays in wheat phenological development under SC conditions, with flowering occurring 3-7 days later compared to non-compacted controls. Yield reductions in wheat commonly range from 15-30% in moderately compacted soils, with greater losses under severe compaction or when combined with other stresses (Arvidsson and Håkansson, 2014). The yield decline is a result of multiple factors, including fewer tillers per plant, reduced grain number per pod, and lower grain weight (Whalley et al., 2008). Andersen et al. (2013) demonstrated that modern wheat varieties with semi-dwarf characteristics often experience greater yield reductions under SC stress compared to taller, traditional varieties. This suggests that breeding for high yield potential under optimal conditions may have accidentally reduced tolerance to physical soil constraints. Despite these challenges, genetic variability in SC tolerance exists among wheat germplasm, with some varieties exhibiting an enhanced ability to penetrate compacted layers through increased root tip force or altered root structure (Colombi et al., 2017).

1.1.3.1. Nutrient uptake limitations in compacted soils

SC significantly impairs nutrient acquisition by plants through multiple interrelated mechanisms affecting both nutrient availability and root uptake capacity. As soil BD increases, reduced pore space restricts water movement and gas exchange, creating localized anaerobic conditions that alter nutrient solubility and transformation processes (Nawaz et al., 2013). Phosphorus availability is particularly limited in compacted soils due to reduced diffusion rates, with studies indicating a decrease of up to 75% in phosphorus diffusion coefficients at high bulk densities (Lipiec and Stcpniewski, 1995). Nitrogen dynamics are also affected, as compaction promotes denitrification and increases nitrogen losses through gaseous emissions while reducing mineralization rates that supply plant-available forms (Bouwman et al., 2013). The combined effect creates a nutrient-limited environment even when total nutrient content appears adequate in standard soil tests.

Root system constraints in compacted soils exacerbate nutrient availability issues by reducing the efficiency of nutrient interception and uptake. The decreased root length density and restricted exploration volume directly limit the soil area from which nutrients can be acquired (Colombi and Keller, 2019). Nosalewicz and Lipiec (2014) demonstrated that wheat grown in compacted soil explored only 40-60% of the soil volume compared to plants in uncompacted conditions, significantly reducing contact with nutrient pools. Physiological adaptations to compaction stress also impair nutrient uptake processes. Chen et al. (2014) reported reduced expression of key nutrient transporter genes in wheat roots experiencing mechanical impedance. Additionally, the high energy costs of root growth through dense soil divert resources away from active transport mechanisms required for efficient nutrient acquisition, further diminishing uptake efficiency (Lynch, 2019). These factors collectively create a nutrient acquisition bottleneck that persists even when fertilizers are applied, explaining why standard fertility management often fails to overcome yield limitations in compacted fields.

1.1.3.2. Wheat-specific responses and yield impacts

Wheat exhibits distinct physiological and developmental responses to SC, which result in characteristic yield decline patterns. Among cereals, wheat shows moderate to severe sensitivity to compaction, being more tolerant than maize but less so than barley (Arvidsson and Håkansson, 2014). Early seedling establishment is particularly vulnerable, with Mooney et al. (2012) documenting delayed emergence and reduced seedling health in compacted soils. This early growth suppression initiates a cascade of developmental adjustments throughout the life cycle, including delayed tillering, reduced stem elongation and size, and compressed reproductive development phases (Whalley et al., 2008). Water stress symptoms often appear earlier and more severely in wheat grown on compacted soils, even under moderate moisture deficit conditions, due to limited root access to subsoil water reserves (Lipiec and Hatano, 2003).

Yield analysis reveals that SC affects wheat productivity through multiple pathways. The number of grains per pod typically shows the maximum sensitivity, with Grzesiak et al. (2013) reporting reductions of 15-30% in the number of grains per pod under 1.34 Mgm^{-3} compaction stress. This happens because restricted root systems intensify carbohydrate limitations during early reproductive development, leading to increased floret abortion (Ihsan et al., 2016). Grain weight also decreases in compacted conditions, though to a lesser extent than the number of grains per pod, reflecting limitations in photosynthate supply during Milk formation (Whalley et al., 2008). Modern short-statured wheat varieties often exhibit higher yield consequences under SC compared to taller, older varieties, suggesting that breeding for responsiveness to optimal conditions may have inadvertently selected for reduced tolerance to physical soil constraints. Despite these general trends, significant genotypic variation exists in SC responses, with some cultivars maintaining up to 90% of potential yield under 1.49-1.55 Mgm^{-3} compaction while others suffer losses exceeding 50% under identical conditions (Colombi et al., 2017).

Management strategies to mitigate the impact of SC on wheat production must address both genetic factors, such as root system traits, and environmental factors, including soil moisture and tillage practices. Cultivar selection represents a critical first step, with Lukaszewski et al. (2014) identifying varieties with enhanced root penetration ability and greater allocation to deeper roots as promising candidates for compacted fields. The timing of field operations should be scheduled to avoid wet soil conditions, as this minimizes the risk of SC, particularly during planting when seedbed conditions play a crucial role in root establishment patterns (Chamen et al., 2015). Nutritional management in compacted soils requires adjustments, with banded fertilizer placement near developing roots proving more effective than broadcast applications for overcoming diffusion limitations (Nkebiwe et al., 2016). However, implementing this method is challenging on large-scale farms due to logistical constraints. Biological approaches, including cover cropping with deep-rooted species and promoting beneficial soil microorganisms, show increasing promise for alleviating compaction effects on wheat through physical and biochemical mechanisms (Acuña et al., 2019). However, their efficiency is constrained by practical challenges such as delayed benefits (3-5 years for measurable improvements), labor-intensive management of cover crops, and site-specific dependencies on soil type, climate, and microbial community viability (Maldonado, 2025). For instance, fibrous-rooted cover crops such as grasses may fail to penetrate hardpans in heavy clay soils, while microbial activity is suppressed in severely compacted anaerobic zones (Duiker, 2005).

A site-specific SC management approach, integrating rapid sampling and PT, offers a more immediate and adaptable solution. By mapping compaction zones using RS data or on-line in-situ sensors, farmers can target interventions like subsoiling only in high-risk areas, reducing fuel use by 27% compared to uniform deep tillage (Sudduth, 2025). This strategy aligns with PA frameworks that optimize soil health practices to address spatial variability in SC severity, root-limiting layers, and nutrient availability (NCSU, 2025). Such tailored management ensures sustainable wheat productivity while avoiding overinvestment in ineffective general remedies.

1.1.4. Site-specific soil compaction management approach

Site-specific SC management represents a targeted approach within PA that addresses the spatial variability of soil physical conditions across agricultural fields. Unlike conventional tillage methods that apply uniform treatments regardless of the varying soil conditions across field, PT tailors' mechanical interventions to address only areas where the local SC could limit the productivity of specific crops (Kaufmann et al., 2010; Raper, 2005). This method considers the variability in SC within fields due to differences in soil texture, organic matter content, moisture regimes, and traffic patterns (Usowicz and Lipiec, 2017). By identifying compaction-affected areas and applying appropriate mechanical interventions only where needed, farmers can optimize both agronomic and environmental outcomes (Reetz, 2016). The inclusion of advanced sensing technologies like geospatial analysis and variable-rate implements has transformed what was historically an experience-based practice into a data-driven management technique (Adamchuk et al., 2004). This evolution aligns with broader natural resources and farm input sustainability goals by maximizing productivity while minimizing energy consumption, soil disturbance, and associated environmental impacts (Shamal et al., 2016).

1.2. Problem Statement and Research Gaps

1.2.1. Current limitations in soil compaction management

Tillage is widely employed as a conventional solution to address SC, encompassing both traditional and conservation tillage methods. However, these interventions are energy-intensive, costly, and, in the case of conventional tillage, intensify soil erosion risks (Holland, 2004; Singh et al., 2023). Despite technological developments in soil management practices, SC remains a pervasive challenge across diverse agricultural regions, contributing to substantial yield deficits in high-input farming systems. Previous studies (Batey, 2009; British Columbia Ministry of Agriculture, 2015; Zhang et al., 2024) estimate that SC accounts for approximately 6% to as much as 50% of global crop yield losses, depending on regional conditions and farming practices (Shaheb et al., 2021).

Current SC management approaches face practical implementation challenges and high resource demands. Conventional deep tillage effectively alleviates compaction, but it requires significant energy inputs, resulting in high fuel costs and increased carbon emissions (Šarauskis et al., 2018). The intensive soil disturbance also accelerates organic matter decomposition and increases the risk of erosion, resulting in a counterproductive cycle of soil degradation (Holland, 2004). Conservation tillage approaches reduce these impacts but often fail to adequately address subsoil compaction issues, particularly in heavy clay soils where mechanical intervention remains necessary (Derpsch et al., 2010). Controlled traffic farming offers promising SC prevention but requires significant infrastructure investment and equipment modifications that present adoption barriers (Tullberg et al., 2018). These limitations underscore the need for innovative strategies that not only mitigate SC but also enhance soil resource resilience and sustainability.

PT is an innovative practice designed to target mechanical soil interventions only in specific areas of a field where they are needed, such as zones with compacted layers (Kaufmann et al., 2010; Shamal et al., 2016). This approach has been confirmed to reduce energy consumption during tillage activities while enhancing crop growth and yield (Shamal et al., 2016). Implementing PT requires detailed soil condition information, traditionally obtained through laboratory experiments. However, these methods are invasive, labor-intensive, and time-consuming (Orangi et al., 2019; Poppiel et al., 2022). Due to the challenges associated with traditional techniques, such as extended data collection and processing times, they are impractical for large-scale fields, as they could delay critical operations during the cropping season.

Despite significant advances in sensing technologies and variable-rate tillage implements, substantial integration challenges persist in creating an easy workflow from detection to implementation. The sequential disconnect between rapid and non-destructive sensing of relevant soil properties related to SC and PT planning for execution represents a primary barrier. This is important because soil conditions can change between the time of assessment and intervention. Additionally, using heavy machinery for data collection can alter the soil's condition, affecting the accuracy of the data (Adamchuk et al., 2004). This challenge is particularly acute for moisture-dependent properties, where rainfall events can significantly alter the optimal tillage depth and intensity compared to what was prescribed based on earlier measurements (Mouazen and Kuang, 2016). Data format compatibility between diverse sensing platforms and farm equipment control systems adds complexity to PA. Proprietary systems often limit interoperability, even with ongoing ISOBUS standardization efforts aimed at enabling seamless communication between equipment from different manufacturers (Auernhammer, 2001). The resolution mismatch between high-density sensor data and the practical implementation capabilities of variable-rate implements further complicates integration, requiring appropriate aggregation methods that maintain critical information while creating manageable management zones (Fulton et al., 2010).

There are few research works that investigated the development of an on-line soil properties measurement device, which can be applied in SC management (Kodaira and Shibusawa, 2020; Shamal et al., 2016). However, most of these devices are robust and tend to disturb the soil ecosystem significantly during data collection. These characteristics limit their applicability in evaluating SC conditions in fields sensitive to marginal disturbances, such as those with high clay content (Gürsoy, 2021).

1.2.2. Knowledge gaps in site-specific interventions

The traditional tillage system currently utilized poses significant limitations for sustainable agriculture. Conventional tillage increases soil susceptibility to erosion (Holland, 2004), while conservation tillage, although an improvement, remains energy-intensive and costly (Singh et al., 2023). More importantly, both methods overlook site-specific differences in SC patterns within fields. Treating non-uniform fields uniformly leads to resource wastefulness and missed opportunities for targeted interventions.

PT shows promise as an alternative approach, with research highlighting its energy efficiency advantages. However, significant knowledge gaps remain regarding site-specific tillage interventions and their agronomic and environmental impacts. Inadequate studies have explored how spatial variations in SC impact soil-crop interactions, which could support the case for the benefits of site-specific tillage (Beylich et al., 2010). Addressing this gap through further research could enhance the effectiveness and sustainability of PT practices, contributing to more productive agricultural systems.

Traditional soil properties testing methods have significant limitations due to their invasive nature, labor-intensive processes, and time-consuming procedures (Orangi et al., 2019; Poppiel et al., 2022). These limitations render them impractical for large-scale field applications, particularly during time-constrained growing seasons. Previous attempts to address this issue, such as on-the-go soil property measurement systems (Kodaira and Shibusawa, 2020; Shamal et al., 2016), have produced robust tools, but their high soil disturbance disrupts the soil ecosystem. This makes them unsuitable for fields sensitive to minimal disturbances, such as clay-rich soils (Gürsoy, 2021). Therefore, there is a need to assess non-invasive RS technologies to rapidly acquire soil condition data, which will enable PT planning.

To improve PT systems, a deeper understanding of crop responses to SC is essential. Wheat serves as an ideal model crop for this purpose, as SC impacts its productivity. As the second most consumed crop globally, improving wheat yield directly supports food security (Reynolds and Braun, 2022). While studies have documented SC effects on wheat productivity (Liu et al., 2022; Yu et al., 2024), nutrient deficiencies (Sun et al., 2024), and root growth (Yu et al., 2024), research gaps persist regarding SC's influence on nutrient accessibility (Ishaq et al., 2001; Islam et al., 2014). Bridging these gaps is vital for refining PT strategies to address site-specific SC challenges.

The complex soil-plant interactions under varying SC levels present several challenges for nutrient dynamics evaluation in wheat cultivation. Compacted soils restrict and hinder root penetration, creating barriers to soil moisture and nutrient mobility and uptake (Wu et al., 2024). Current methods fail to account for the spatial variability of SC and its relationship with residual nutrient patterns (Feng et al., 2024). This research gap leads to the inability to develop predictive models that can accurately forecast wheat yield variations under different SC levels. Therefore, reducing the effectiveness of PT implementation, as ideal tillage planning relies on a detailed understanding of crop responses to varying SC conditions across a field. Addressing this gap requires research into how SC affects wheat productivity and developing models that can predict yield outcomes based on different SC conditions. This would enable more precise PT strategies, enhancing both crop yields and resource efficiency in PA practices.

1.3. Research questions and objectives

1.3.1. Research questions

1. How accurately can hyperspectral imaging detect and quantify SC parameters like bulk density for PT applications?
2. How do varying levels of SC (low, medium, high) affect wheat crop nutrient access (magnesium, phosphorus, etc.), growth rates, and final yield in a field environment?
3. What decision-support frameworks can convert hyperspectral-derived SC insights into PT recommendations?

1.3.2. Research aim

This research aims to develop a soil compaction management system by integrating hyperspectral RS technology with agronomic data from wheat production. The goal is to provide farmers with a practical decision-support tool for optimizing PT operations, enhancing resource efficiency, and improving crop productivity through targeted soil management.

1.3.3. Research Objectives

Objective 1: Development of a remote sensing approach for soil compaction assessment

- Evaluate the ability of hyperspectral camera (HSC) imaging to capture soil conditions relevant to soil compaction.
- Establish correlations between hyperspectral signatures and key soil properties influencing soil compaction.
- Develop a standardized workflow for processing hyperspectral data into spatial SC maps suitable for PT planning.

Objective 2: Quantification of soil compaction effects on wheat productivity

- Collect and analyze ground truth data (GTD) to determine the relationship between initial soil bulk density (BD) levels and soil physicochemical properties.

- Assess the impact of varying SC levels on wheat growth parameters across different developmental stages.
- Quantify the yield response to different SC levels to establish threshold values for intervention.

Objective 3: Integration of findings into the precision agriculture framework

- Develop an integrated practical framework and data flow procedure that translates remote sensing data into site-specific tillage recommendations for implementing PT practices in agricultural systems.
- Develop farm input management maps based on the understanding of soil-plant interactions at various growth stages.

1.4. Thesis Organization

This thesis presents the development of a SC management system using a combination of traditional ground truth data collection and hyperspectral-based soil property sensing. The thesis is organized into seven chapters:

- Chapter 1 introduces the research, including the background, problem statement, research gaps, research questions, and objectives.
- Chapter 2 presents the theoretical framework supporting the research principles.
- Chapter 3 details the key methodologies and experimental designs adopted in the study.
- Chapter 4 describes the experimental procedures and outcomes related to the development of a remote sensing methodology for soil compaction assessment.
- Chapter 5 presents the procedures and results for quantifying the effects of soil compaction on wheat productivity.
- Chapter 6 integrates the findings into a precision agriculture framework.
- Chapter 7 provides the conclusions and recommendations arising from the research.

CHAPTER 2: THEORETICAL FRAMEWORK

The theoretical foundation for understanding and managing soil compaction (SC) in wheat production systems is reviewed in this chapter. The main context of the chapter is the dynamic interaction at the soil-root interface, where the physical and chemical properties of the soil directly influence root development, nutrient acquisition, and crop yield. Theories and models from soil mechanics and root physiology explain how varying levels of SC influence root exploration and function. These concepts emphasize that both excessive and insufficient compaction can negatively affect root growth, nutrient uptake, and crop yield. The literature highlights the importance of balancing soil-root contact for efficient nutrient uptake with adequate pore space for root growth and aeration. However, while the existence of an optimum compaction level is hypothesized, where these competing factors are best balanced, its precise value is not universally defined and often varies with soil type, moisture, and crop variety. Recent studies have shown that SC effects on wheat depend strongly on weather conditions and soil texture, and that yield responses to compaction are highly context-dependent, sometimes even beneficial in certain environments when water is limiting (E-Ashid and Sheikh, 1977; Liu et al., 2022; Yu et al., 2024). Thus, identifying an actual optimum compaction level for a given production system typically requires empirical determination through field experiments and yield analysis, rather than relying solely on theoretical predictions.

To comprehensively assess the effects of SC across entire fields, recent research has increasingly turned to advances in remote sensing (RS) technology. Hyperspectral imaging and vegetation indices such as NDVI have enabled the non-invasive monitoring of soil properties, including BD and moisture, as well as crop health indicators, providing real-time data that reflect the impacts of SC on different wheat growth stages (Karimli and Selbesoğlu, 2023; Tan et al., 2024). These RS tools are widely recognized for their ability to bridge the gap between traditional point measurements and field-scale assessments, offering a more complete picture of spatial variability and crop response (De Sousa Mendes et al., 2020; Tekin et al., 2008).

The inherent spatial variability in agricultural landscapes has led to the adoption of geostatistical concepts for mapping and quantifying differences in SC and nutrient availability (De Sousa Mendes et al., 2020; Karimli and Selbesoğlu, 2023). Geostatistical methods, such as kriging, and machine learning approaches have been successfully applied to generate detailed soil maps and support targeted management strategies that address site-specific field conditions (De Sousa Mendes et al., 2020; Karimli and Selbesoğlu, 2023). This shift from uniform to site-specific management is crucial for optimizing both yield and resource efficiency.

Recent literature also highlights the integration of soil-root dynamics, RS data, and spatial variability models within PA decision frameworks (De Sousa Mendes et al., 2020; Karimli and Selbesoğlu, 2023; Tan et al., 2024). Advanced machine learning algorithms are increasingly used to translate complex, multi-sourced data into actionable, site-specific tillage recommendations, thereby optimizing crop yield and promoting sustainable soil management (De Sousa Mendes et al., 2020; Karimli and Selbesoğlu, 2023). However, the precise determination of an ideal SC range for optimal root health and productivity remains context-dependent and requires empirical validation, as highlighted in studies showing that compaction effects on crops are strongly influenced by the crop physiology, soil texture, moisture, and weather conditions (Liu et al., 2022; Yu et al., 2024).

2.1. Soil-Root Interface Dynamics

The soil-root interface represents the critical zone where plant roots interact with the soil matrix to access water and nutrients essential for growth and development. This interface is highly dynamic, responding to changes in soil physical properties, particularly SC levels. Recent advances have highlighted the importance of root hairs and rhizodeposition in modifying soil structure and enhancing resource acquisition (Hallett et al., 2022). Understanding the theoretical principles governing these interactions provides the foundation for optimizing soil management practices in wheat production systems. It is important to note, however, that while theoretical models can explain the mechanisms underlying root responses to compaction, the precise ideal compaction level for maximum yield is not a fixed value but must be determined empirically for each soil and environmental context (Yu et al., 2024).

2.1.1. Mechanical impedance theories and root response models

Mechanical impedance, defined as the resistance soil offers to root penetration, is fundamentally altered by compaction processes. Several theoretical frameworks explain the relationship between soil strength and root elongation:

Greacen and Oh's (1972) pressure balance theory posits that root elongation occurs only when the root growth pressure exceeds the mechanical resistance of the soil plus the osmotic pressure within the root cells. This theory establishes that root growth is directly inhibited when soil strength exceeds the maximum pressure roots can exert, typically 800-1500 kPa for most crops, with wheat demonstrating a threshold around 1200 kPa (Eavis et al., 1969).

The critical penetration resistance model developed by Dexter (1987) suggests a non-linear relationship between root elongation rate and penetration resistance. According to this model, root elongation remains relatively unaffected until a critical resistance threshold is reached, beyond which elongation rates decline exponentially. For wheat, this critical threshold typically occurs at penetrometer resistance values between 2-3 MPa (Bengough et al., 1991).

Bengough et al.'s (1997) integrated approach combines mechanical impedance with considerations of root cellular responses. This model accounts for how root cells modify their metabolism, wall properties, and division rates in response to mechanical stress, explaining the observed changes in root diameter and architecture under compaction. The model predicts the characteristic root thickening observed in compacted soils as roots allocate more resources to radial expansion to overcome axial resistance.

Jin et al. (2017) developed the root-soil contact model, which theorizes that moderate compaction can improve root nutrient uptake by increasing the contact area between roots and soil particles. This model helps explain the observed optimum compaction level for wheat yield, as it accounts for the trade-off between improved nutrient transfer at the root-soil interface and the increased resistance to root penetration.

2.1.2. Nutrient uptake kinetics under varying compaction scenarios

Nutrient uptake at the soil-root interface is governed by various interrelated processes, which are significantly influenced by SC levels:

The Barber-Cushman nutrient uptake model (Barber, 1995) describes nutrient acquisition as a function of three transport mechanisms: root interception, mass flow, and diffusion. This model, when modified to include SC effects (Dunbabin et al., 2002), provides a theoretical basis for understanding how compaction alters nutrient availability by changing soil hydraulic conductivity and tortuosity factors that affect diffusion pathways.

Drew (1975) localized supply effect theory explains how roots proliferate in nutrient-rich zones when overall soil volume exploration is constrained by SC. This compensatory growth mechanism is particularly relevant for understanding wheat's adaptation to heterogeneous SC patterns in field conditions.

The buffer power concept introduced by Nye (1966) and elaborated by Tinker and Nye (2000) describes how soil's ability to replenish nutrients in the soil solution (buffer power) is altered by SC. Higher BD typically increases buffer power for phosphorus but may decrease it for potassium and nitrogen, helping explain the differential impact of SC on various nutrient uptake efficiencies observed in wheat.

Seeling and Zasoski (1993) integrated an uptake model that considers how root-induced pH changes in the rhizosphere interact with soil physical conditions to affect nutrient solubility and availability. This model is particularly relevant for understanding phosphorus dynamics in compacted soils, where wheat roots often utilize acidification strategies to enhance P solubilization under restricted growth conditions.

2.1.3. Root architecture adaptation to physical constraints

Plant roots demonstrate remarkable plasticity in response to physical constraints imposed by SC. The following theoretical frameworks explain these adaptive mechanisms:

Lynch's (2007) architectural trade-off theory proposes that root systems balance exploration efficiency against exploitation capacity when adapting to soil constraints. This theory explains why wheat develops shallower but more laterally extensive root systems in compacted soils, a strategy that optimizes resource acquisition under limiting conditions.

The functional equilibrium model (Brouwer, 1983) predicts that plants allocate resources between roots and shoots based on the most limiting factor for growth. Under SC stress, this model explains the observed increases in root ratios as plants allocate more resources to overcome soil resistance.

Fitter’s (1987) topological approach to root architecture characterizes root systems based on their branching patterns and connectivity. This framework helps explain the shift from herringbone patterns toward more dichotomous branching observed in wheat roots under compacted conditions, which represents an optimization strategy for soil exploration under physical constraints.

The compensatory growth model proposed by Crossett and Campbell (1975) describes how roots preferentially proliferate in uncompacted soil volumes when heterogeneous compaction exists. This model is particularly relevant for understanding wheat root distribution patterns in field conditions with variable compaction levels, and supports the practice of PT targeting only overly-compacted zones.

Hodge's (2004) root plasticity framework integrates local and systemic signaling mechanisms that regulate root development in response to soil physical conditions. This model explains how wheat roots sense and respond to mechanical impedance through hormone-mediated pathways, particularly through altered auxin transport and ethylene production that trigger the characteristic morphological responses to SC.

Together, these theoretical models and frameworks provide a comprehensive foundation for understanding the complex relationships between SC, root development, nutrient acquisition, and wheat yield. The integration of these theories supports the empirical finding of an optimum compaction level for wheat, where the benefits of soil-root contact for nutrient transfer are balanced against the limitations imposed by mechanical impedance to root exploration. This theoretical framework guides the development of precision tillage approaches that aim to maintain SC within the optimal range across heterogeneous field conditions, thereby maximizing wheat productivity while minimizing the negative impacts of either excessive or insufficient SC.

2.2.Remote sensing of soil and crop parameters

RS has appeared as a transformative technology in PA, offering non-invasive methods to assess soil properties and crop conditions across spatial and temporal scales. The theoretical foundations, methodological approaches, and effectiveness of RS applications for monitoring soil and crop parameters are rereviewed here, with particular importance on applications related to SC assessment.

2.2.1. Level of sensing effectiveness

The effectiveness of RS for soil and crop parameter assessment varies depending on the sensor type, platform, target property, and environmental conditions. Understanding these varying levels of effectiveness is fundamental for implementing suitable sensing strategies in PA.

2.2.1.1. Direct versus indirect sensing

RS of soil properties functions through two fundamental mechanisms: direct and indirect sensing (Viscarra Rossel et al., 2009). Direct sensing measures soil properties through their inherent spectral signatures, while indirect sensing relies on proxy indicators or vegetation responses that reflect underlying soil conditions. Understanding these mechanisms is vital for developing RS strategies to assess SC, a key factor influencing wheat productivity.

Ben-Dor et al. (2009) systematically evaluated the effectiveness of direct soil sensing across the electromagnetic spectrum, finding that visible-near infrared (VNIR, 400-1000 nm) and shortwave infrared (SWIR, 1000-2500 nm) regions demonstrate high effectiveness for organic matter (R^2 = 0.65-0.89) and clay content (R^2 = 0.61-0.87), but only moderate effectiveness for soil moisture (R^2 = 0.54-0.75). These findings align with Stenberg et al.'s (2010) comprehensive review, which established that the effective hierarchy for direct soil sensing follows: organic constituents > mineralogical properties > physical structure > dynamic properties like compaction.

In recent experimental work using the HSC described in Chapter 3, under controlled laboratory conditions to assess its effectiveness in direct soil moisture sensing. The setup involved scanning soil samples within an enclosed environment illuminated by four 50-watt halogen lamps, ensuring consistent lighting conditions. Soil samples were prepared with moisture contents ranging from 0% to 50% on a wet basis, in 5% increments. The resulting spectral signatures, depicted in Figure 2.1, display distinct variations corresponding to the different moisture levels, highlighting the sensitivity of hyperspectral imaging to soil moisture content. A predictive model developed from this spectral data achieved a cross-validation coefficient of determination (R^2) of 0.867, as shown in Figure 2.2, indicating a strong correlation between the spectral signatures and soil moisture levels. These results are consistent with findings from the literature when similar bare soil conditions and measurement protocols are used. However, the effectiveness of direct sensing may be reduced under unpredictable field conditions due to factors such as surface roughness, vegetation cover, and variable soil moisture distribution.

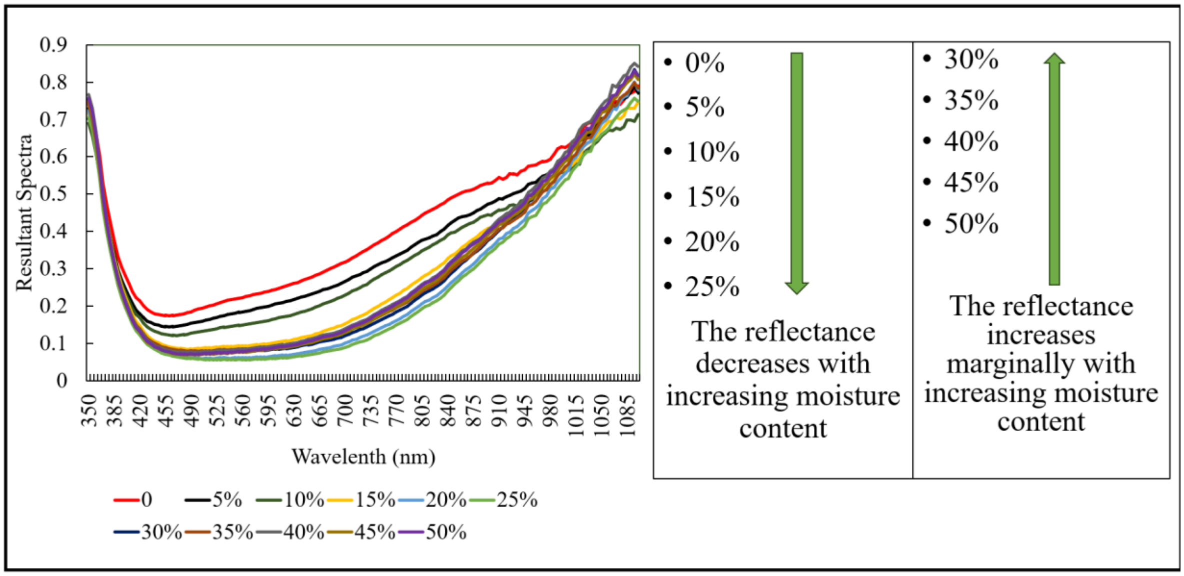

Figure 2.1: Spectral results of room scanning of soil moisture with HSC

The non-linear relationship between soil moisture content and hyperspectral reflectance shown in Figure 2.1 follows a well-documented pattern in literature. The initial decrease in reflectance with increasing moisture (0-25%) occurs because water molecules absorb light and darken the soil's appearance, following established water absorption principles in the VNIR/SWIR regions. The unexpected reflectance increase, at higher moisture levels (30-50%) is explained by Lobell and Asner (2002) as the result of water film formation on soil particles creating specular reflection that increases albedo. This physical transition occurs because at approximately 25% moisture content, the soil approaches saturation with most pores filled with water, while at 50%, water mass equals soil particle mass. This fundamentally changes the optical properties of the surface, reducing the shadowing and roughness effects that decrease reflectance in moderately moist soils. The resulting water-filled surface creates more specular (mirror-like) reflection than the diffuse reflection characteristic of drier soils. This phenomenon varies with soil texture, with clay soils showing the most pronounced inflection point, typically around 25-30% moisture content, due to differences in pore size distribution and water retention properties (Tan, 2014).

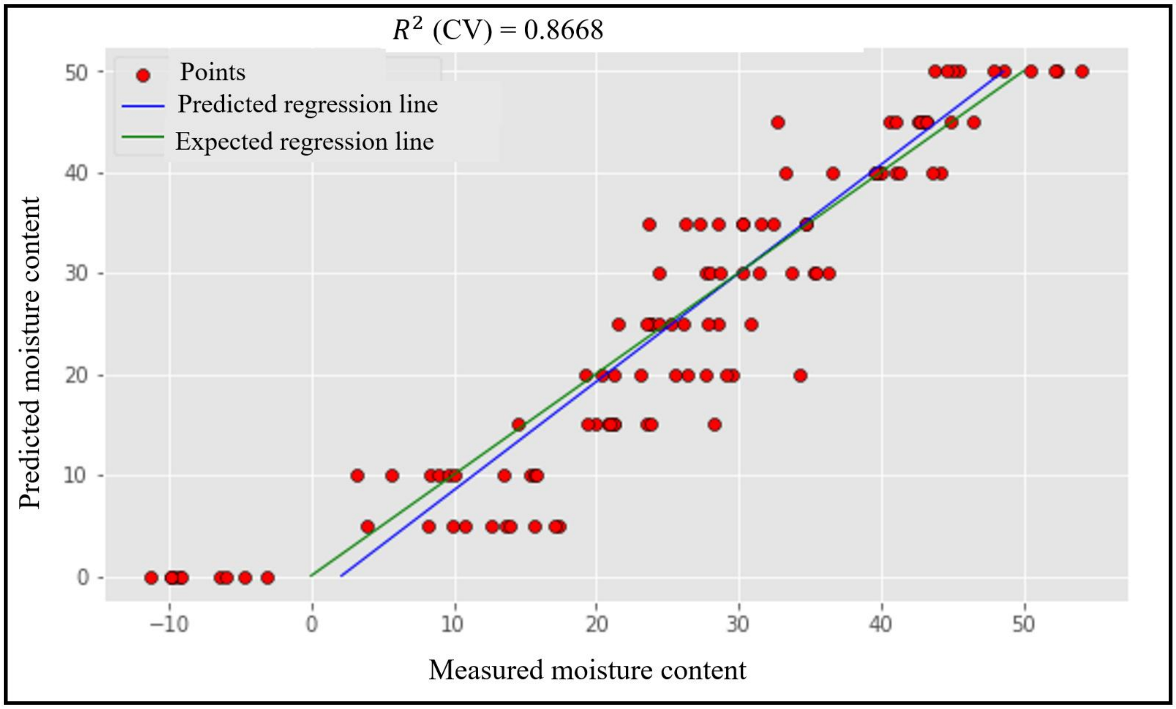

Figure 2.2: Plot of predicted moisture content against actual moisture content

For SC specifically, Naderi-Boldaji et al. (2013) demonstrated that direct spectral assessment of BD achieved limited success (R^2 = 0.31-0.58), primarily because compaction affects spectral signatures indirectly by altering soil surface characteristics rather than through distinct absorption features. Given these limitations, researchers have increasingly turned to indirect sensing approaches for compaction assessment.

Indirect sensing effectiveness for SC has been evaluated through two primary pathways: (1) correlating spectral properties with field measurements of penetration resistance and BD, and (2) assessing vegetation responses to compaction stress. Vegetation indices, such as NDVI, are widely used as proxies for plant health and can indirectly reflect underlying soil conditions, including compaction stress. (Barnes et al., 2000) established moderate correlations (R^2 = 0.45-0.67) between vegetation indices and penetrometer readings in cotton fields, while Tracy et al. (2013) achieved improved correlations (R^2 = 0.58-0.74) by incorporating temporal dynamics of vegetation stress responses.

Adamchuk et al. (2018), conducted a meta-analysis and quantified the effectiveness of RS across different soil properties, suggesting that the effectiveness hierarchy for indirect sensing follows: nutrient deficiencies (R^2 = 0.65-0.85) > water stress (R^2 = 0.60-0.80) > structural limitations including compaction (R^2 = 0.40-0.65). This hierarchy reflects the more complex causal pathways between soil physical properties and observable spectral responses.

Collectively, these findings highlight the potential of RS, both direct and indirect-for assessing soil properties relevant to wheat production, with important implications for site-specific management and PA.

2.2.1.2. Spatial and temporal resolution considerations

The effectiveness of RS is linked to spatial and temporal resolution capabilities. Mulder et al. (2011) established that soil property mapping requires spatial resolutions of 5-20 m for field-scale applications, while crop stress monitoring may require finer resolutions of 0.5-5 m to capture early indicators of SC stress. This creates an important resolution threshold that influences platform selection.

Temporal effectiveness follows definite patterns across the growing season. Fitzgerald et al. (2006) documented that early-season imagery (Emergence to Tillering in wheat) provides superior information about soil background properties (including SC) with effectiveness metrics 30-45% higher than mid-season imagery when vegetation coverage exceeds 40%. Conversely, mid-season imagery (stem Pinnacle to Heading) better captures the cumulative effects of SC on crop performance, with Jin et al. (2017) reporting peak correlation coefficients ($r = 0.78$-0.84) between vegetation indices and known compaction zones during this period.

2.2.1.3. Penetration depth limitations

A major drawback in RS effectiveness is penetration depth. While SC often extends 15–30 cm into the profile, soil surface optical sensing is limited to the top few millimeters. Hartemink and Minasny (2014) established that this surface limitation creates an effectiveness gap, with direct correlations between surface reflectance and subsurface compaction typically achieving R^2 values below 0.40 without additional covariates. This limitation underscores the challenge of relying solely on surface reflectance to infer deeper soil conditions, which are critical for accurate compaction assessment.

This gap has prompted the exploration of alternative approaches, including indirect sensing from vegetation and residual land covers, which can integrate information from deeper soil layers through plant responses and surface residue patterns (Knorr et al., 2025; Van Der Leeuw et al., 2024; Yang et al., 2021). Additionally, multi-sensor fusion approaches have been developed to enhance subsurface property estimation. Mohanty et al. (2017) demonstrated that integrating optical data with microwave sensing (such as SAR) significantly improves BD predictions, achieving R^2 values of 0.68-0.73 across varied soil conditions-a 27-35% improvement over optical-only models. Such developments highlight the potential of combining multiple sensing modalities to bridge the effectiveness gap and provide more comprehensive assessments of SC.

2.2.1.4. Prediction accuracy across properties

Reviews by Ge et al. (2011) and Kuang et al. (2012) compared prediction accuracies across soil properties using hyperspectral sensing, establishing a consistent accuracy hierarchy in terms of Ratio of Performance to Deviation (RPD): texture (RPD = 1.8-2.4) > organic matter (RPD = 1.7-2.3) > moisture content (RPD = 1.5-2.1) > bulk density (RPD = 1.4-1.8). This hierarchy reflects the directness of spectral relationships, with BD and SC showing consistently lower prediction accuracies due to their indirect spectral expressions. Consequently, there is a need to adopt indirect sensing approaches-such as monitoring vegetation or residual land covers-to predict properties linked to BD and improve estimation accuracy.

For wheat specifically, Gomez et al. (2016) quantified prediction effectiveness for key soil properties affecting root growth, achieving RPD values of 2.1 for clay content, 1.9 for organic carbon, 1.6 for soil moisture, and 1.5 for BD, confirming the consistent effectiveness gradient across properties relevant to SC assessment.

RPD: values >2.0 indicate excellent predictions, 1.4-2.0 indicate good predictions suitable for quantitative applications, and <1.4 indicate predictions useful only for qualitative screening.

2.2.2. Sensing methods

RS techniques for soil and crop parameter estimation incorporate diverse platforms, sensors, and analytical approaches. The reviews of the primary methodological strategies utilized for assessing soil properties related to compaction and the resulting crop responses are considered under this section.

2.2.2.1. Platform-Based Classification

RS platforms comprise satellites, aircraft, UAVs, and proximal sensors, each offering unique spatial and temporal advantages. Satellite-based sensing (e.g., Sentinel-2, WorldView-3) provides broad coverage and moderate resolution, useful for regional mapping but with limited sensitivity to subtle SC gradients ($R^2 = 0.5$-0.64) and higher costs for finer resolutions (Castaldi et al., 2019; Mohite et al., 2023; Rogge et al., 2018). Aerial platforms (e.g., hyperspectral aircraft, UAVs) balance coverage and detail, with UAV-based multispectral systems showing strong correlation (85-92%) with ground truth of developmental parameters in wheat fields (Ishimwe et al., 2014). Proximal sensors (e.g., spectroradiometers, active sensors) offer the highest resolution and signal quality, detecting early stress ($R^2 = 0.72$-0.78 for BD) but are limited to small areas (Kodaira and Shibusawa, 2020).

2.2.2.2. Sensor Technology Classification

Multispectral sensors (4-10 bands) remain widely used, with indices like NDVI moderately correlated with SC ($r = -0.57$ to -0.68) (Bronson et al., 2005; Stafford, 2000). Hyperspectral sensors (hundreds of bands) enable more precise identification of soil structural features, outperforming multispectral approaches ($R^2 = 0.69–0.82$ for BD) (Gomez et al., 2008; Viscarra Rossel et al., 2006). Thermal infrared sensors detect water stress linked to compaction, with canopy temperature differences providing useful indirect indicators (78% accuracy) (Jones et al., 2009). Microwave sensors (SAR) penetrate deeper, improving BD estimation ($R^2 = 0.58–0.66$), especially when combined with optical data (23-31% accuracy gain) (Baghdadi et al., 2012; Castaldi et al., 2016). LiDAR measures surface and canopy structure, indirectly identifying SC-prone areas ($R^2 = 0.61–0.72$) (Keller et al., 2007).

2.2.2.3. Analytical Methods

Vegetation indices (e.g., NDVI) and their temporal analysis improve compaction zone delineation (Xue et al., 2025). Spectral unmixing isolates soil signals in partially vegetated fields (83% accuracy) (Somers et al., 2011). Machine learning (SVR, RF, CNNs, PLSR) outperforms traditional regression for BD prediction (Nawar et al., 2016). Radiative transfer models and data fusion (optical, thermal, radar) further enhance accuracy (34% improvement over single-sensor approaches) (Castaldi et al., 2019; Verrelst et al., 2012). Spatiotemporal frameworks (e.g., EOF analysis) and explainable AI improve interpretability and robustness (Montero et al., 2009; Tsakiridis et al., 2019).

2.2.2.4. Current Trends and Future Directions

Multi-scale integration (satellite, UAV, proximal) and high-frequency temporal sampling are improving the detection of subtle SC effects (Ge et al., 2007). Transfer learning and explainable AI address model transferability and interpretability (Padarian et al., 2019; Tsakiridis et al., 2019), while autonomous multi-sensor platforms increase spatial variability detection by 36% (Shamshiri et al., 2018). The indirect HSC soil BD sensing method aligns with these advances by integrating vegetation or residual land cover spectral response with GTD-based SC models. By leveraging the plant and residual land cover as a bio-indicator of subsurface conditions, the limitations of direct sensing could be overcome and provide robust, actionable insights for PT.

2.3. Spatial variability concepts

Understanding spatial variability is fundamental to SC management in PA. This theoretical framework characterizes, analyzes, and interpret spatial patterns of soil properties, with emphasis on quantifying SC across agricultural fields and its impact on wheat productivity.

2.3.1. Scale-dependent relationships in soil physical properties

Soil properties exhibit distinct patterns of variability across spatial scales, from microscopic pore networks to landscape-level gradients. These scale-dependent relationships significantly affect SC dynamics and measurement approaches.

At the microscale (1-100 µm), SC modifies pore connectivity and size distribution, which directly impacts root penetration and water transport. Dexter's (2003) soil quality framework establishes that compaction-induced changes to micropore distribution follow predictable patterns based on soil texture, with clay soils showing greater sensitivity to structural degradation than sandy soils. The scale-dependent relationship between BD and pore size distribution follows a power law function, where a slight increase in BD disproportionately reduces macro-porosity, while preserving micropores (Horn et al., 1995).

At the mesoscale (0.1-10 m), compaction heterogeneity creates distinct zones with varying physical and hydraulic properties. The spatial organization of these compaction patterns follows boundary-line theory, where property relationships exhibit stronger correlations within homogeneous zones than across zone boundaries (Shahin et al., 2020).

At the field scale (10-1000 m), topography and soil type create hierarchical patterns of variability in compaction vulnerability. According to Webster's (2000) nested hierarchy concept, SC variance can be partitioned into distinct spatial components corresponding to broad topographic features (accounting for 40 to 60% of total variance) and localized management effects (accounting for 20 to 40% of variance). Specifically for wheat fields, Mouazen and Ramon (2006) found that topography-driven patterns of soil moisture create predictable spatial organization of compaction severity, with accumulation zones showing 25 to 40% higher susceptibility to compaction than well-drained positions.

These scale-dependent relationships create a theoretical basis for multi-scale monitoring approaches. Lark's (2011) wavelet analysis framework provides a mathematical formalization for decomposing soil property variation into scale-specific components, allowing identification of the dominant scales at which compaction patterns emerge. For wheat production systems, Atwell (1990), Mondal and Chakraborty (2023), and Richard et al. (2001) established that the critical scales for monitoring compaction effects on root development occur at 5-15 cm vertically and 10-25 m horizontally, corresponding to key rooting zone constraints and machinery-induced patterns, respectively.

The integrative theory of scale-dependent hierarchy (O'Neill et al., 2021) provides a unifying framework, suggesting that processes at one scale constrain and condition those at finer scales. For SC, this means that landscape-scale patterns create the template within which management-induced compaction operates, which in turn constrains microscale root-soil interactions. This hierarchical constraint concept is essential for designing efficient sampling strategies that capture the relevant scales of variation for wheat productivity assessments.

2.3.2. Geostatistical principles for soil compaction mapping

Geostatistical methods provide the theoretical foundation for quantifying and mapping spatial patterns of SC. These methods rely on the concept of spatial autocorrelation, where measured values at neighboring locations tend to be more similar than those farther apart.

The semi-variogram function operates as the basis of geostatistical analysis, quantifying the degree of spatial dependence in soil properties. For SC parameters, semi-variograms typically show distinct structural properties that reflect fundamental processes. Cambardella et al.'s (1994) spatial dependence ratio (nugget-to-sill ratio) provides a standardized measure for classifying spatial dependence strength. In agricultural fields, penetration resistance typically shows moderate to strong spatial dependence (ratio <0.50), while BD often demonstrates weaker spatial structure (ratio 0.50-0.75) due to greater measurement variability (Veronesi et al., 2012).

The theoretical range parameter from variogram models represents the distance beyond which samples become spatially independent. For SC metrics in wheat fields, typical ranges span 20-60 m, corresponding to the scale of machinery operations and soil management zones (Kerry and Oliver, 2007). Kerry and Oliver's (2007) sampling optimization framework indicates that effective characterization of compaction patterns needs sample spacing at approximately half the range distance, translating to 10-30 m grid sampling for most agricultural fields.

Kriging interpolation, based on variogram parameters, presents theoretically optimal predictions at unsampled locations. For SC mapping, ordinary kriging typically gives better results than inverse distance weighting because of the incorporation of spatial structure information (Mueller et al., 2001). However, compaction parameters often demonstrate non-stationarity (trending surfaces) that violate kriging assumptions. In such cases, universal kriging or regression kriging incorporating topographic covariates provides more robust predictions, reducing estimation errors by 15-30% compared to ordinary kriging (Odeh et al., 1995).

The nugget effect in compaction variograms represents measurement error and sub-grid variability. For penetrometer resistance, this unresolved variance typically accounts for 20 to 40% of total spatial variation (Corwin and Lesch, 2005). This theoretical limit on mapping accuracy sets the minimum achievable uncertainty in compaction assessment when using point measurements, emphasizing the value of continuous sensing approaches that can resolve fine-scale spatial patterns.

Co-regionalization theory (Goovaerts, 1997) provides a framework for analyzing multiple interrelated soil properties simultaneously. The linear model of co-regionalization (LMC) partitions spatial covariance into scale-specific components, revealing how relationships among compaction metrics and crop performance change across spatial scales. Webster et al. (2006) demonstrated that soil-root interactions show scale-dependent correlations, with stronger relationships emerging at the scale of management zones (20 to 50 m) than at either finer or coarser scales.

For wheat-specific compaction mapping, the incorporation of ancillary data through hybrid geostatistical approaches has theoretical advantages. McBratney et al. (2003) scorpan framework formalizes this integration, showing how compaction predictions can be improved by incorporating soil type, topography, and management history covariates. In practice, regression kriging incorporating these factors typically reduces prediction error variance by 25-45% compared to traditional kriging approaches (Knotters et al., 1995).

2.3.3. Temporal stability of spatial patterns in field conditions

Spatial patterns of SC show varying degrees of temporal stability, depending on pedological, climatic, and management factors. Understanding this temporal dimension is essential for developing sustainable SC management strategies.

The concept of time-stability analysis, introduced by Vachaud et al. (1985), provides a theoretical framework for quantifying the persistence of spatial patterns across time. For SC parameters, Starr (2005) demonstrated that relative difference analysis can identify field locations that consistently maintain their rank order of compaction severity across seasons. In wheat production systems, locations with extreme SC values (either extremely high or extremely low) typically show greater temporal stability (Spearman rank correlations >0.8 across seasons) than locations with intermediate values ($r = 0.4$ to 0.6).

The temporal persistence of SC patterns follows the dynamic equilibrium theory proposed by Huisman et al. (2003), which suggests that soil physical properties tend toward characteristic steady states determined by the balance between compaction and natural recovery processes. For agricultural soils, SC patterns induced by heavy machinery can persist for 3-7 years without remedy, with decay rates following negative exponential functions modulated by soil texture and climate (Håkansson and Reeder, 1994).

Freeze-thaw and wetting-drying cycles are the primary natural mechanisms for SC alleviation, but their effectiveness varies significantly across climatic zones. SC recovery rates depend on soil texture, climate, and management practices. Coarse-textured soils in warmer climates often recover from compaction within five years, whereas fine-textured (clayey) soils in cooler climates may take decades to return to pre-disturbance conditions (Page-Dumroese et al., 2021; Saco et al., 2021).

Management-induced modifications interact with natural temporal dynamics, creating complex temporal patterns. Cassel (1983) cumulative effects model implies that repeated traffic over the same areas leads to non-linear increases in compaction severity, with each subsequent pass causing diminishing additional SC after 3 to 4 passes. This theoretical saturation effect establishes an upper bound on compaction severity in intensively trafficked areas.

For wheat production systems specifically, root-induced structural changes create crop-specific temporal patterns. The bio-drilling effect measured by Cresswell and Kirkegaard (1995) suggests that wheat roots can partially improve SC through physical and biochemical processes, reducing BD by 3 to 7% over a growing season in the active rooting zone. This biological recovery is most significant in the 5 to 15 cm depth range where root density is highest.

Wavelet-based time-series analysis provides a mathematical framework for separating cyclical and trend components in temporal SC dynamics. Milne and Lark (2009) demonstrated that most agricultural fields demonstrate both seasonal oscillations in SC severity (driven by moisture cycles and cropping patterns) and longer-term trends related to cumulative management effects. For wheat-based rotations, the dominant temporal cycle typically spans 1 to 2 years, reflecting the interaction between seasonal dynamics and rotational patterns.

The temporal stability of spatial patterns has significant implications for sampling efficiency. According to Douaik et al.'s (2006) temporal sampling optimization theory, understanding the temporal stability characteristics of SC patterns can reduce monitoring requirements by 60 to 75% through strategic sampling of representative locations. For wheat systems, this typically translates to monitoring a subset of 15 to 25% of field locations that capture the extremes and mean conditions of SC severity.

This theoretical understanding of spatial variability concepts across scales, geostatistical principles, and temporal stability forms the foundation for developing effective monitoring and management strategies for SC in wheat production systems. It confirms the conceptual framework for designing spatially and temporally optimized sampling schemes, interpreting observed patterns, and implementing targeted interventions to maintain SC within the optimal range for wheat productivity.

2.4. Precision agriculture decision framework for soil compaction management

This framework provides a suited theoretical foundation for research on PT decisions based on important soil physical properties that directly impact SC. It delves into relevant mathematical relationships and specific threshold necessary for PT planning within the PA framework.

2.4.1. Threshold determination for intervention

The foundation of successful PT depends on establishing scientifically appropriate thresholds for soil physical properties that prompt site-specific intervention. For SC management, BD and PD serve as primary quantitative indicators that inform tillage decisions.

2.4.1.1. Theoretical basis

The theoretical basis for threshold determination based on soil physical properties related to SC comes in three categories as follows:

- **Soil-specific critical value theory**: This establishes that intervention thresholds for BD must be texture-dependent, as the impact of a given BD varies significantly across soil types (Horn et al., 1995). The critical BD value (BD_{crit}) can be expressed as a function of clay content (CC):

  $$BD_{crit} = f(CC) \qquad (2.1)$$

  where intervention becomes necessary when measured BD > BD_{crit}

- **Packing density frameworks**: Building upon BD limitations, packing density ($PD = BD + 0.009 \times CC$) provides a texture-corrected parameter that enables consistent thresholds across varying soil types (Naderi-Boldaji et al., 2016). This offers a unified metric where: $PD < 1.40$ g/cm³: No intervention needed $1.40 < PD < 1.75$ g/cm³: Moderate intervention recommended $PD > 1.75$ g/cm³: Intensive intervention required. These set thresholds are general and do not tailor the recommendations to the specific crop requirements of crop being cultivated.

- **Depth-stratified threshold models**: Recognizing that SC severity and its impact on root growth vary with depth, creating a theoretical framework where intervention thresholds form a depth-dependent function rather than static values (Schjønning et al., 2015).

These theoretical basics converge to form a tillage decision threshold framework that is:

1. **Texture-specific**: Accounting for how soil composition modifies the agronomic significance of density measurements

2. **Depth-differentiated**: Recognizing the varying implications of compaction at different soil horizons

3. **Crop-responsive**: Incorporating a general crop-specific tolerance thresholds for root-restricting BD

2.4.2. Multi-criteria decision models for variable-rate operations

PT needs balancing multiple objectives including alleviating SC, minimizing energy consumption, preserving soil structure, and optimizing economic returns through formal multi-criteria frameworks that integrate bulk and PD data.

2.4.2.1. Theoretical components

The theoretical component to consider in instituting multi-criteria decision for variable-rate tillage operation includes:

- **Soil resistance-density functions**: Mathematical relationships measuring how tillage energy requirements increase exponentially with BD and PD, enabling energy-optimized variable-rate tillage(Destain et al., 2016).
- **Compaction-yield response models**: Functional relationships between measured soil physical properties (BD/PD) and crop yield potential, enabling economic evaluation of tillage interventions across field zones (Batey, 2009):

  Relative Yield = f(BD, soil texture, crop type, moisture regime) (2.2)

- **Environmental impact functions**: Theoretical frameworks linking tillage intensity to soil carbon dynamics, erosion risk, and greenhouse gas emissions as functions of pre-tillage soil physical properties (Abdalla et al., 2013).

The integration of these theoretical elements enables:

1. **Site-specific tillage optimization**: Variable-depth and variable-intensity tillage prescriptions based on spatially explicit BD/PD measurements.

2. **Economic threshold determination**: Cost-benefit frameworks for tillage that incorporate fuel consumption, equipment wear, yield benefits, and soil health implications.

3. **Sustainable tillage planning**: Balancing immediate SC alleviation with long-term soil structural stability.

2.4.3. Uncertainty management in precision tillage decisions

PT based on BD and PD measurements faces multiple sources of uncertainty that must be formally addressed within the decision framework.

2.4.3.1. Theoretical Framework

The key factors to consider in managing uncertainty in PT decision are as follows:

- **Measurement error propagation theory**: Mathematical formulations of how sampling and measurement errors in BD and PD assessment propagate through the decision models, enabling confidence-adjusted tillage recommendations (Marchant and Lark, 2007) represented in Eq. 2.3.

  $$BD\_measured = BD\_true \pm \text{error in measurement} \tag{2.3}$$

- **Temporal dynamics models**: Theoretical constructs capturing the temporal instability of BD and PD because of wetting-drying cycles, biological activity, and natural consolidation, informing optimal timing of both measurements and tillage operations (Obour et al., 2017).
- **Soil moisture-compaction state relationships**: Frameworks for understanding how moisture conditions affect both the measurement accuracy of soil physical properties and the effectiveness of tillage interventions, incorporating soil moisture as a critical uncertainty factor (Keller et al., 2019).

These theoretical constructions support:

1. **Probabilistic tillage prescription**: Moving beyond deterministic thresholds to express tillage recommendations as probability distributions based on confidence in BD/PD assessments.
2. **Seasonal intervention windows**: Theoretical models identifying optimal timing for both SC assessment and remediation based on moisture conditions.
3. **Adaptive tillage strategies**: Frameworks incorporating real-time soil physical property sensing to adjust tillage depth and intensity during operation.

The integrated PT decision framework synthesizes these three theoretical domains into a cohesive approach that enables evidence-based tillage management using BD and PD as primary decision parameters. This framework provides the theoretical foundation for translating soil physical property data into spatially explicit tillage prescriptions that optimize soil structure while minimizing energy consumption and soil disturbance.

2.5. Conclusion

This theoretical framework illustrates the complex interaction between soil physical properties and agricultural decision-making for PT operations. At its foundation lies the critical soil-root interface, where BD and PD directly impact root development, nutrient acquisition, and crop yield in wheat production systems. The framework identifies that both excessive and insufficient SC can negatively impact root growth and function, highlighting the importance of finding an optimal balance between soil-root contact for efficient nutrient uptake and suitable pore space for root exploration and aeration.

While the theoretical components presented in this chapter establish the mechanisms through which SC affects wheat productivity, they also emphasize that the optimal SC level is not universally defined but varies with soil texture, moisture conditions, and crop variety. This context-dependency is evident in recent research demonstrating that compaction effects on wheat are strongly modulated by environmental factors, with some studies also reporting beneficial effects under water-limiting conditions (E-Ashid and Sheikh, 1977; Liu et al., 2022; Yu et al., 2024).

The PA decision frameworks presented, from threshold determination to uncertainty management, acknowledge this variability and provide the theoretical structure for site-specific tillage management. However, the literature clearly indicates that identifying the actual optimum SC level for a given production system requires empirical determination through field experimentation rather than relying solely on theoretical predictions. This recognition of the limitations of pure theory proves the importance of integrating the conceptual frameworks in literature with field-based measurements and adaptive management approaches to create a practical wheat-specific PT action plan.

CHAPTER 3. METHODOLOGY AND EXPERIMENTAL DESIGN

3.1. Experimental site characteristics and treatments

The study site was located at the experimental farm of Hokkaido University, located in the central-western (Kita-Ku, Nishi-Jo) part of the Sapporo campus. Sapporo is in the southwestern region of the Ishikari Plain, on the alluvial fan of the Toyohira River, a tributary of the Ishikari River, in the Hokkaido Prefecture, Japan (Government of City of Sapporo, 2025). Sapporo is located between latitudes 42°46' N and 43°11' N, and longitudes 140°59' E and 141°21' E (Government of City of Sapporo, 2025). The city has a humid continental climate, characterized by a wide temperature range between summer and winter. Summers are warm and humid, while winters are cold and snowy, with an average snowfall of 4.79 m per year (Japan Meteorological Agency, 2024). Sapporo is one of the few cities in the world with such heavy snowfall (Government of City of Sapporo, 2025). The city's annual average precipitation is 1,100 mm, and the mean annual temperature range is -7.0 to 26.4 degrees Celsius (Japan Meteorological Agency, 2024). Hokkaido Prefecture alone has 25% of Japan’s cultivated land, and it is the leading producer of seventeen agricultural products, including wheat and rice. The soil in the area consists of volcanic ash soils, brown forest soils, peat soils, and heavy clay soils, which are highly fertile and have good water holding capacity (NARO, 2017).

The Hokkaido University Experimental Farm, shown in Figure 3.1, has been a research facility for agricultural studies since its establishment in 1876. The farm spans approximately 35 hectares of arable land. The fields are characterized by brown lowland soil (*Fluvisol*) with a silty clay loam texture in the topsoil layer (0-0.3 m), which is representative of agricultural lands in the Ishikari Plain region. The organic matter content of the soil in the experimental plots typically ranges from 4.5% to 6.2%, with a pH(H_2O) of 5.8-6.2. A standardized crop rotation system is applied at the farm, including wheat, potato, soybean, and sugar beet, reflecting common agricultural practices in the Hokkaido region. The experimental fields maintain detailed records of management history, including tillage operations, fertilization regimes, and crop performance data, making it an ideal site for controlled agricultural research. The annual mean precipitation at the farm site is approximately 1,150 mm, marginally higher than the city average. Approximately 60% of the yearly precipitation falls during the growing season, from May to September, creating good conditions for conducting the experiments (Field Science Center for Northern Biosphere, 2025).

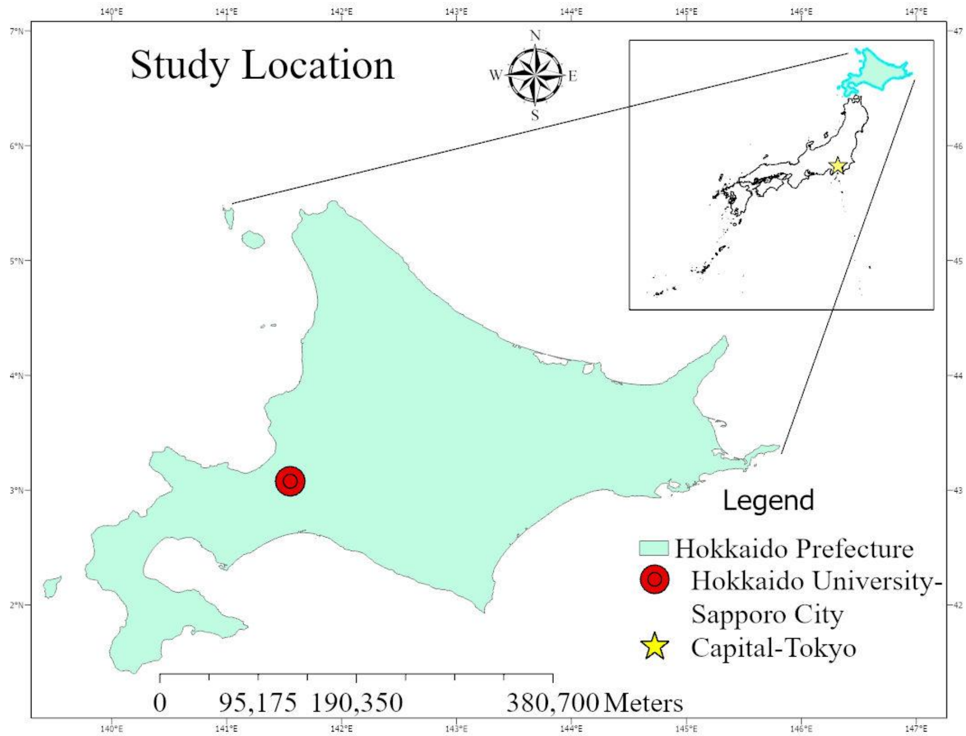

Figure 3.1: Experimental field location

3.1.1. Experimental treatments

Two experimental field setups were utilized for the distinct phases of the research.

3.1.1.1. Field 1: Remote sensing assessment for soil compaction measurement

The first field was a 30 × 160 m freshly harvested wheat field assessed at the end of July, which corresponds to the typical harvesting period in Hokkaido. The residual vegetation consisted of approximately 90% stubble and straw of the '*Harukirari*' wheat variety, 4% freshly emerging weeds (mainly *Phleum pratense* L. and *Festuca pratensis* Huds.), and 6% bare soil. These soil coverage percentages were estimated through visual field inspection.

For comprehensive spatial analysis, the experimental field was divided into 48 grids, each measuring 10 × 10 m, as illustrated in Figure 3.2. Soil samples were collected from three depth ranges (0-0.1 m, 0.1-0.2 m, and 0.2-0.3 m), corresponding to typical plowing depths for four tillage treatments: no tillage, shallow tillage, medium tillage, and deep tillage. This sampling strategy enabled the vertical profiling of soil properties, which is critical for assessing the effects of compaction. The violet circles in Figure 3.2 indicate the center of each grid, where soil samples were collected. Measured properties were georeferenced to these grid centers to facilitate spatial interpolations and generate a comprehensive characterization of soil conditions across the entire field.

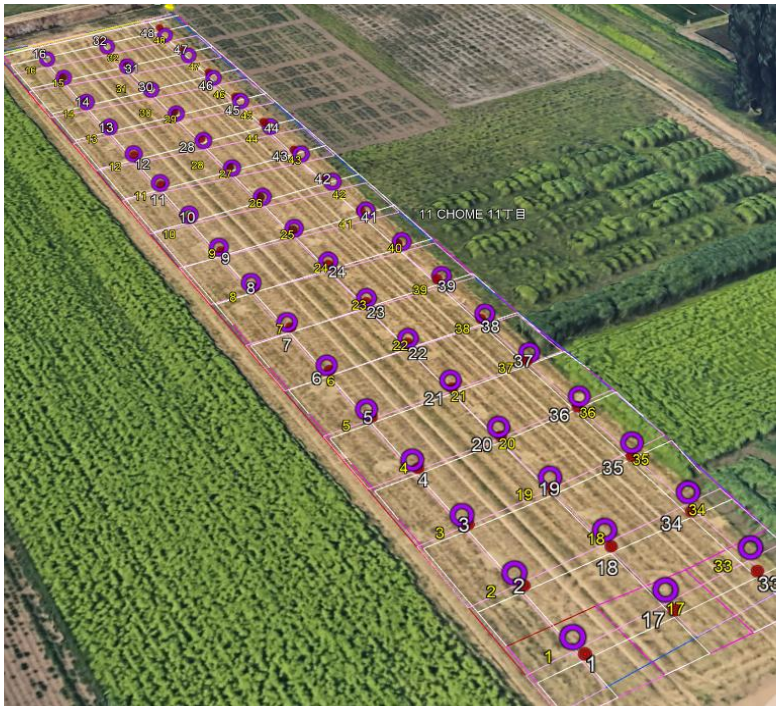

Figure 3.2: First experimental field

3.1.1.2. Field 2: Controlled Soil Compaction Experiment

The SC experiment was conducted on a 17 × 18.9 m field selected for its uniform topography to minimize variability. Before applying the five SC treatments, initial measurements of particle size distribution, organic matter content, soil BD, and soil moisture content were taken to confirm the spatial homogeneity of the field.

The experimental design, as shown in Figure 3.3, was a randomized complete block layout with three replications for each compaction treatment. Each subplot measured 2.5 × 3.0 m. This design was chosen to account for potential residual micro-environmental gradients across the field and ensure robust statistical analysis.

Each subplot in Figure 3.3 received precisely controlled compaction treatments using a 400 kg vibratory plate compactor with 6.8 kW of power (Bomag Fayat Group, Germany). Target BD levels were achieved for four compaction treatments (BD1 to BD4) and a Control subplot, with BD1 representing the highest compaction level and BD decreasing incrementally to BD4. This systematic approach ensured that differences observed in wheat development and yield components could be directly attributed to the applied SC treatments rather than environmental variability or pre-existing field conditions.

Figure 3.3: Second experimental field treatment

3.2. Platforms and instrumentation

3.2.1. Hardware

This research employed three primary instruments: (1) an NH-7 hyperspectral camera (EVA Japan Co., Ltd.) operating in the 350-1100 nm range for non-invasive spectral analysis of soil properties, (2) a JXBS-300-NPK-RS version 2.0 sensor (Weihai JXCT Electronic Technology Co., Ltd., China) for in-situ measurement of soil physical parameters, and (3) a SPAD-502 chlorophyll meter (Konica Minolta Sensing Singapore Pte Ltd., Singapore). for rapid, non-destructive assessment of leaf chlorophyll content.

3.2.1.1. Hyperspectral imaging system

Hyperspectral imagery was acquired using the NH-7 hyperspectral camera shown in Figure 3.4. This is a push-broom imaging system that captures spectral data across the 350-1100 nm range (near-ultraviolet to near-infrared), with a spectral resolution of 5 nm and 150 distinct spectral bands. The camera features a 1.31-million-pixel CMOS sensor with a spatial resolution of 1280 × 1024 pixels.

The NH-7 spectroscopic imaging system features an internal scanning mechanism, eliminating the need for external movement of either the camera or the subject during image shooting. This design enhances data stability and makes the system well-suited for field applications. The NH-7 provides a 60-degree field of view and achieves a complete hypercube acquisition in just 7.7 seconds, ensuring efficient and reliable spectral data collection. These attributes make the camera suitable for rapid data collection and prompt data analysis, which enhances PT planning in this research.

For field data collection, the camera was mounted on an adjustable tripod and positioned at a consistent height of 0.75 m above the surface of the residual vegetation or crop, with the lens angled 38 degrees from the vertical. This configuration maintained uniform spatial resolution across all sampled plots while minimizing shadow effects. The tripod used ensured stable positioning for consistent image quality across the variable field terrain.

Calibration was performed before each imaging session using a Spectralon® reference panel (Labsphere Optical Equipment Co., Ltd., China) to account for ambient light conditions. All images were collected between 10:00 and 14:00 under bright sky conditions to minimize the effects of diurnal illumination variations and to standardize solar zenith angles across the dataset.

Figure 3.4: NH-7 hyperspectral camera

3.2.1.2. JXBS-300-NPK-RS sensor

Soil moisture sensor system

The JXBS-300-NPK-RS (Figure 3.5) was specifically utilized for in-situ measurement of soil moisture content in this study. While this integrated sensor system is designed with ion-selective electrode (ISE) technology to measure both soil macronutrients and moisture, only the moisture measurement functionality was utilized due to reliability considerations.

Technical specifications

Moisture measurement principle: Electrical conductivity/resistivity

Moisture measurement range: 0-100% volumetric water content

Operating voltage: 12 - 24V DC

Response time: ≤2 seconds

Communication protocol: Modbus-RTU via RS-485 interface

Environmental tolerance: Operating temperature range of -20°C to +60°C

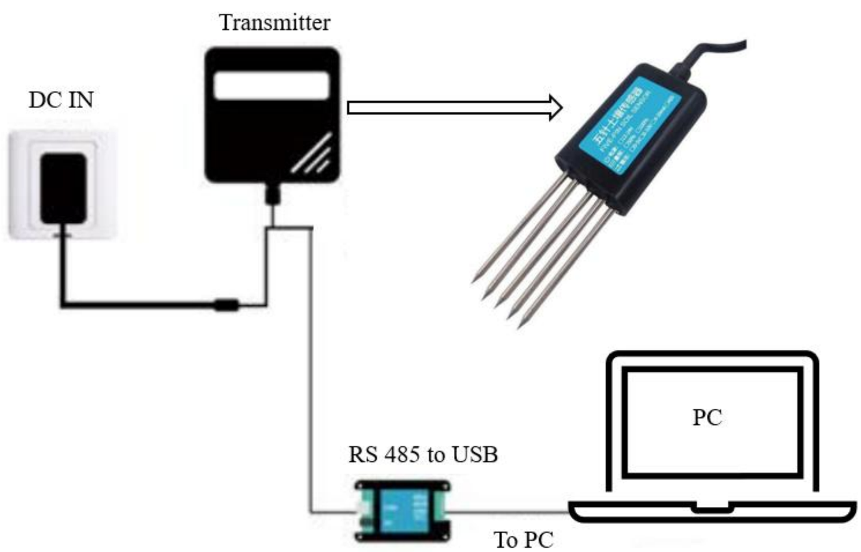

Figure 3.5: JXBS-300-NPK-RS sensor

Measurement methodology

The JXBS-300-NPK-RS sensor utilizes the electrical conductivity principle to measure volumetric water content. For this research, the probe was directly inserted between 0-0.3 m at each sampling location to capture soil moisture conditions of the root zone. After insertion, readings were recorded following a 30-second waiting period as protocol to ensure signal stabilization.

The sensor's rapid data acquisition capability (≤2 seconds per reading) facilitated efficient mapping of spatial moisture variability across the experimental subplots, which was influenced by varying soil SC levels. This fast assessment was particularly advantageous for monitoring changes in soil moisture conditions throughout different crop growth stages.

Sensor calibration and usage

Before the seven-in-one soil sensor (JXBS-500-NPK-RS version 2.0, Weihai JXCT Electronic Technology Co., Ltd., China) was used for rapid soil properties measurements to reduce the time-consuming process of repeated sampling and laboratory analyses, the sensor was calibrated. The parameters and error margins of the sensor are available in the sensor's manual (JXCT, 2020). After evaluation, we identified the need for calibration for certain properties. The pH and soil temperature sensing had acceptable margins of error, while P, K, N, and moisture content measurements were not precise. For this study, the sensor was calibrated to measure soil volumetric moisture content, moisture content dry basis, and moisture content wet basis.

The calibration process started by drying 1.5 kg of agricultural soil using the oven drying method (Motsara et al., 2008). To standardize the soil volume measurement, three clean graduated cylinders were filled with oven-dried soil. The cylinders were tapped three times from a height of 0.1 m to facilitate natural particle settling. Soil was incrementally added until reaching the 32 mL mark, representing the combined volume of voids and solids. The weight of solids (m_s) is calculated by subtracting the weight of the cylinder from the combined weight of the cylinder plus the soil, before adding an amount of deionized water (m_w) corresponding to about 1.5 times the volume of material in the cylinder. The content was then covered in aluminum foil to limit evaporation or moisture gain and was allowed to rest for 24 hours at room temperature. This method determined the volume of solids (v_s) by subtracting the volume of water (v_w) added and the excess clear water (v_{ex}) above the sediments from the final sediment volume (v_T), as shown in Eq. 3.1. When the v_s is set, the v_w is adjusted from 5% of the soil/solids mass to 100%. VMC is calculated using Eq. 3.2, MCW is calculated using Eq. 3.3, and MCD is calculated using Eq. 3.4. The relation between the calculated values using Eqs. 3.2 to 3.4, and the sensor readings are plotted in Figure 3.6. When a known moisture level is set, the setup is covered with aluminum foil for 24 hours to achieve a homogeneous mixture before measuring using the sensor. This step is valuable in setting up a low moisture content soil. The water must blend with the soil uniformly before the sensor can read the true value of the soil moisture content.

$$volume\ of\ solids\ (v_s) = v_T - (v_w - v_{ex}) \tag{3.1}$$

$$volumetric\ moisture\ content\ (VMC) = (v_w/v_T) \tag{3.2}$$

$$moisture\ content\ wet\ basis(MCW) = (m_w/m_T) \tag{3.3}$$

$$moisture\ content\ dry\ basis\ (MCD) = (m_m/m_s) \tag{3.4}$$

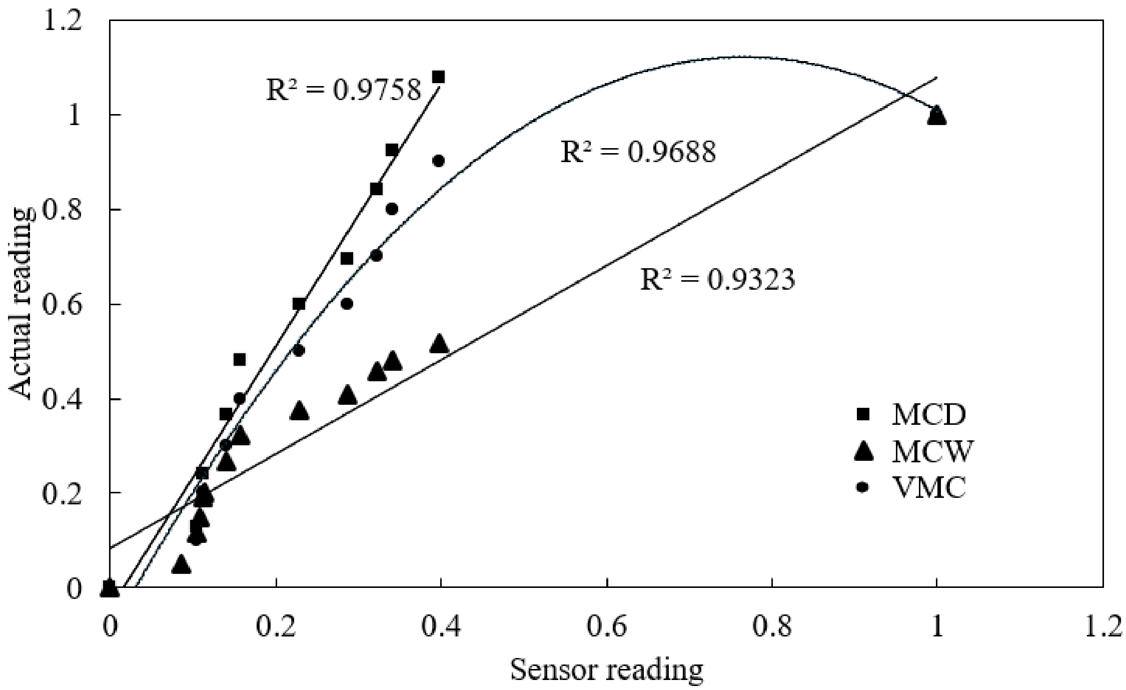

Figure 3.6: Sensor calibration plot

The functions generated for correcting the sensor readings into VMC, MCW, and MCD are given by Eqs. 3.5 to 3.7. The respective R^2 of the functions are 0.9688, 0.9323, and 0.9758 as indicated in Figure 3.6. The difference in the calibration plot in Figure 3.6 is linked with the empirical formulas for calculating the different moisture contents presented in Eqs. 3.2 to 3.4. The zero-moisture content measure is the same for MCD and VMC, while it is practically impossible to achieve zero MCW. Furthermore, MCD reaches 100% when the soil weight and the weight of water are equal, but 100% MCW or VMC means only water without soil. The VMC plot’s appearance results from added water progressively filling soil pores. Initially, this creates a proportional increase in water volume relative to the total soil-water system. This trend continues until the soil reaches its field capacity at around 80%. Beyond this point, the soil enters a 'free water dominance' regime. Here, excess water accumulates beyond the soil’s pore space, leading to the parabolic effect observed in the plot.

$$VMC = -2.0741x^2 + 3.1768x - 0.0944 \quad (3.5)$$

$$MCW = 0.9951x + 0.0828 \quad (3.6)$$

$$MCD = 2.7812x - 0.046 \quad (3.7)$$

3.2.1.3. SPAD-502 chlorophyll meter

Chlorophyll content assessment system

The SPAD-502 Plus in Figure 3.7 was used for non-destructive assessment of leaf chlorophyll level in the wheat crop. This portable chlorophyll meter provides rapid quantification of relative chlorophyll concentration through optical density measurements at two specific wavelengths.

Technical specifications

Measurement principle: Dual-wavelength optical absorbance (650 nm and 940 nm)

Measurement area: 2 mm × 3 mm sampling window

Measurement range: -9.9 to 199.9 SPAD units

Resolution: 0.1 SPAD units

Accuracy: ±1.0 SPAD units for SPAD values between 0.0-50.0

Response time: Approximately 2 seconds

Storage capacity: 30 measurements with averaging function

Power source: Two AA alkaline batteries (approximately 20,000 measurements per set)

Figure 3.7: SPAD-502 Plus chlorophyll meter

Measurement methodology

The SPAD-502 Plus was used to quantify leaf chlorophyll content by measuring the difference in light attenuation at 650 nm (red light, absorbed by chlorophyll) and 940 nm (near-infrared, used as an internal reference). Measurements were consistently taken from the most recently fully expanded leaf, at the midpoint between the leaf margin and midrib, while avoiding major leaf veins to ensure accuracy.

For each experimental subplot, SPAD readings were collected from ten randomly selected plants and averaged to produce a single representative SPAD value per subplot. To minimize diurnal variation, all measurements were conducted between 10:00 and 14:00. Chlorophyll content was tracked at critical growth stages: Tillering, Pinnacle, Heading/Beginning of flowering, Milk formation, and Milk ripening.

The SPAD values provided a non-destructive proxy for leaf health status and nutrient availability. These measurements offered insights into potential nutrient accessibility limitations caused by varying SC treatments. Using this SPAD meter ensured that the crop integrity is preserved for the subsequent developmental stage assessments.

3.2.2. Software

The data analysis was conducted using an image analyzer for the NH-7 hyperspectral camera, a combination of programming tools for image analysis, machine learning implementation, and spatial mapping.

3.2.2.1. HSAnalyzer version 12

The hyperspectral images captured with the NH-7 camera were processed using HSAnalyzer v12, which supported key preprocessing and analysis steps, including:

1. ***Image Correction***: Raw hyperspectral images were corrected using a white reference image (Spectralon® reference panel) captured under equal lighting conditions. This step accounted for sensor response, non-uniformity, and lighting variability across the spectral range, ensuring an accurate reflectance value for each pixel.
2. ***White and black Reference Calibration***: The black and whiteboard image served as a calibration baseline to convert raw intensity data into reflectance values. The two images were captured before the subplot's images were taken and applied during correction to normalize reflectance across all wavelengths.
3. ***Region of Interest (ROI) Extraction***: Specific regions of interest (ROIs) corresponding to the target areas were manually selected within the HSAnalyzer interface. This step minimized background noise and ensured that spectral information was extracted exclusively from target areas, enhancing analytical precision.

HSAnalyzer version 12 provided an efficient workflow for converting raw hyperspectral data into reliable reflectance spectra, making the data suitable for further statistical and spectral analyses.

3.2.2.2. Python packages

In this study, several Python libraries were utilized to support data processing, spectral analysis, and visualization of results. The Python language was chosen for its versatility and extensive library support, which facilitated efficient data handling and analysis. NumPy (version 1.26.4) provided efficient array operations and numerical computations, serving as the foundation for data handling. Its ability to manage large datasets efficiently was particularly beneficial for processing the hyperspectral data (Harris et al., 2020).

Pandas (version 2.2.2) was used for data manipulation, organization, and exporting results to formats such as comma-separated values (CSV) (McKinney, 2010). This enabled easy integration with other tools and facilitated data sharing. SciPy (version 1.13.1) aided computation and statistical analysis, particularly in processing spectral data (Virtanen et al., 2020). Its good statistical functions were essential for analyzing the complex spectral signatures obtained from the hyperspectral image data.

For machine learning tasks, including predicting properties from hyperspectral data, Scikit-learn (version 1.4.2) was employed. This library offers a wide range of algorithms suitable for building predictive models (Pedregosa et al., 2011). Matplotlib (version 3.8.4) and Seaborn (version 0.13.2) were used for result visualization, creating high-quality statistical charts suitable for publication (Hunter, 2007; Waskom, 2021). These libraries enabled the visualization of spectral waveforms and predicted-versus-actual property plots, which were essential for interpreting the research findings.

All plots and analysis outputs were saved in standard formats such as JPEG and CSV to facilitate further interpretation and reporting of research findings. Figures 3.8 and 3.9 show a schematic diagram of the data processing workflow.

3.2.2.3. ArcGIS ArcMap

For spatial analysis and visualization, ArcGIS ArcMap (ESRI ArcGIS™ version 10.7.1; ESRI, 2019, CA, USA) was employed to process geolocation data and generate distribution maps of soil properties. The software facilitated the conversion of Keyhole Markup Language (KML) files to layer and projected shape files. Two interpolation techniques were applied within ArcGIS to process spatial data and generate soil property distribution maps. Ordinary spherical kriging was used for soil properties mapping based on grid sampling points. This geostatistical method accounted for spatial correlation, ensuring accurate predictions at unsampled locations by modeling the variability of soil properties across the experimental field.

For data from the controlled compaction experiment, the Inverse Distance Weighting (IDW) was utilized with the default power parameter set to 2 and a search radius of 3 m to match the subplots' dimensions. IDW uses a deterministic approach where the influence of sampled points diminishes with distance, giving greater weight to closer points within the specified radius. This method provided a smooth interpolation surface suitable for analyzing compaction effects across subplots.

Raster analysis tools within ArcGIS were used to transform the interpolated data into final property distribution maps, enabling comprehensive visualization and interpretation of spatial patterns.

3.3. Data collection protocols and sampling methods

The data collection protocol designed for the two experiments was used to characterize the soil physical and chemical properties, as well as to quantify the effects of SC on wheat performance.

3.3.1. Phase 1: Non-invasive soil properties assessment

In the first experiment, hyperspectral imaging was conducted using the camera described in Section 3.2.1. The imaging was coupled with traditional soil core sampling to a depth of 0.3 m, with samples collected using a triangular sampling pattern (n=3 per grid) within forty-eight 10×10 m grid subplots. Core samples were extracted using a 0.3 m T-shaped soil auger to preserve soil structure. The dual-method approach established correlations between surface spectral signatures and laboratory-measured SC indicators, including BD (g/cm^3), gravimetric moisture content (%), and organic matter content determined by loss-on-ignition. Multiple regression and partial least squares regression techniques were employed to develop predictive models that could estimate SC parameters non-invasively from the hyperspectral image data.

3.3.2. Phase 2: Controlled compaction-crop response study

The second experimental field was divided into thirty subplots with five different SC levels (1.17, 1.19, 1.24, 1.25, and 1.3 Mg/m^3). Each compaction level had six replicates. Wheat growth parameters were measured at five growth stages. These parameters included relative crop growth rate, crop height, emergence count, crop population, and grain yield. Soil moisture and nutrient access were also monitored to see how SC affected the crops' development.

3.4. Analytical approaches and statistical methods

3.4.1. Statistical methods

3.4.1.1. Image pre-processing

The raw hyperspectral images underwent a series of pre-processing steps from steps 1 to 3, as outlined in Figure 3.8 under the 'Phase-One' notation, to minimize noise and prepare the data for analysis. First, dark current correction was applied to reduce sensor-specific noise. Next, reflectance calibration was performed using the white reference panels to convert raw digital numbers into absolute reflectance values. Finally, geometric correction was applied to account for camera positioning and ensure spatial accuracy across the study area using Eq. 3.8.

$$\text{Corrected reflectance} = \frac{\text{Observed reflectance}}{\sin\theta} \tag{3.8}$$

where θ is the camera angle in degrees relative to the nadir (vertical) position. By dividing by $sin\,\theta$, the formula normalizes reflectance to a nadir-equivalent value, assuming a Lambertian (perfectly diffuse) surface. This is a simplified version of corrections used in satellite and UAV RS (Schaepman-Strub et al., 2006; Shunlin, 2003).

3.4.1.2. Reflectance extraction

Reflectance data extraction, represented in Figure 3.8 as ‘Phase-two’ was done using two distinct methodologies tailored to the experimental contexts:

Experiment 1: ROI-based extraction

Regions of Interest (ROIs) were manually set out using field observations and ground-truth markers. Mean spectral signatures for each ROI were calculated by averaging pixel values within the defined boundaries, ensuring alignment with soil properties measured at corresponding sampling locations (Thenkabail et al., 2000). This approach minimized variability and ensured the spectral representativeness of ground-truth data.

Experiment 2: NDVI-based binarization

For the controlled compaction experiment, the Normalized Difference Vegetation Index (NDVI) was computed as:

$$NDVI = \left(\frac{NIR-Red}{NIR+Red}\right) \tag{3.9}$$

Where NIR and Red represent near-infrared (780 nm) and red (650 nm) reflectance, respectively. A threshold of 0.05 was applied to separate vegetation (NDVI > 0.05) from non-vegetation pixels (soil/debris) (Yang et al., 2021). Only vegetation-classified pixels were retained for analysis at the step denoted as 3 in Figure 3.8, eliminating soil reflectance interference. This allowed isolation of compaction-induced differences in vegetation reflectance (indirect sensing) across growth stages and their linkage to soil properties affecting crop development (Zhang et al., 2024).

3.4.1.3. Spectral pre-processing

The extracted reflectance spectra from ‘Phase-One’ analysis (Figure 3.8) underwent additional pre-processing during ‘Phase-Two’ to enhance signal quality and emphasize spectral features associated with soil properties. To reduce noise at the edges of the spectrum, wavelengths between 350 to 395 nm, and 1010 to 1100 nm were removed.

Savitzky-Golay filtering

A Savitzky-Golay filter was applied, following the method described by Demetriades-Shah et al. (1990), to smooth spectral signatures while preserving key features. This technique uses local polynomial regression to calculate smoothed values for each point in the spectrum. The filter parameters were optimized with a window size of eleven points and a polynomial order of 2, based on cross-validation performance.

First Derivative transformation

After smoothing, the first derivative of the reflectance spectra was calculated to enhance subtle absorption features and minimize illumination variation (Curran, 1989). The first derivative was computed as:

$$\frac{dR}{d\lambda} = \frac{R(\lambda_{i+1}) - R(\lambda_i)}{\lambda_{i+1} - \lambda_i} \tag{3.10}$$

Where $R(\lambda i)$ represents reflectance at wavelength λi. This transformation highlights changes in spectral slopes, which are often more strongly correlated with soil properties than absolute reflectance values Gao et al., 2000).

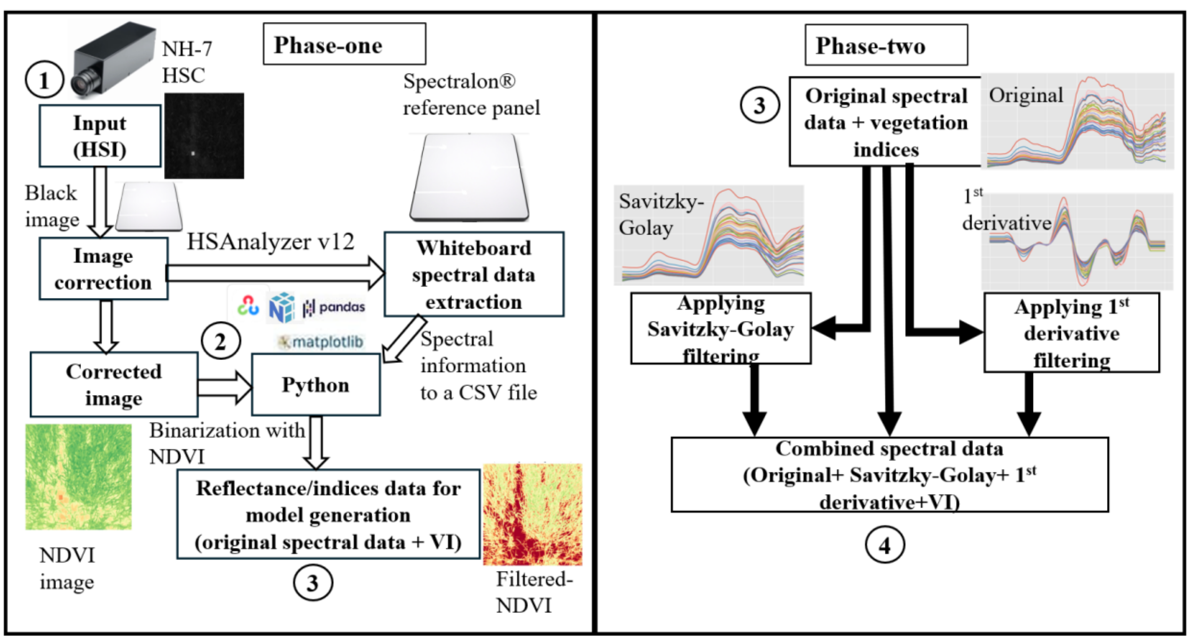

Figure 3.8: Schematic diagram of image pre-processing (phase-one) and spectral data preprocessing (phase-two)

3.4.1.4. Machine Learning Models

The pre-processed spectral data were combined at Step 4 (Figure 3.8) to enhance scale sensitivity by integrating broad-scale patterns and fine-scale spectral features. This multi-representation approach improves the detection of subtle soil property variations by expanding the range of potential predictors, allowing feature selection algorithms to identify the most relevant variables (Chlouveraki et al., 2025; Tissier et al., 2019). The combined data served as input for the analysis at 'Phase-three' shown in Figure 3.9, where machine learning models were trained to predict target soil and crop growth properties.

Model development

At the 'Phase-three' analysis stage, several regression models were evaluated to predict soil properties using spectral data from Step 4 of the 'Phase-two' analysis stage. The models included Partial Least Squares Regression (PLSR) (Wold et al., 2001), Random Forest (RF) (Breiman, 2001), Support Vector Regression (SVR) (Cortes and Vapnik, 1995), Gradient Boosting (GB) (Friedman, 2001), Lasso Regression (Tibshirani, 1996), Ridge Regression (Hoerl and Kennard, 1970), and Elastic Net (ENET) (Zou and Hastie, 2005). These models were trained using the spectral data as predictor variables and laboratory-measured soil properties, such as BD and moisture content, as response variables.

To optimize model performance and address multicollinearity among explanatory variables, a feature selection process was implemented before the model training. Partial Least Squares Regression (PLSR) was initially utilized to identify key spectral wavelengths and measured variables most relevant for predicting the target soil properties. PLSR reduces dimensionality by identifying variables with high loading weights that contribute significantly to the prediction of target variables (Mevik and Wehrens, 2007; Wold et al., 2001). This approach helped minimize redundancy in the dataset while highlighting features strongly correlated with target soil properties.

In cases where PLSR did not sufficiently resolve multicollinearity, typically due to its limited capacity to detect redundancy among highly correlated variables, Variable Inflation Factor (VIF) analysis was employed to improve the selection of explanatory variables and ensure model stability. VIF quantifies the degree of multicollinearity by assessing how much the variance of a regression coefficient is exaggerated due to correlations with other predictors. Variables with VIF values exceeding a threshold of five were iteratively removed to stabilize the final models and improve prediction accuracy (Kock and Lynn, 2012; O'brien, 2007) .

This method of feature selection strategy ensured that only the most effective predictors were retained for model development.

Training and validation

The dataset was divided using different approaches based on sample size. For the first experiment (n=144), the data were randomly split into training (70%) and testing (30%) subsets. For the second experiment (n=90), leave-one-out and 5-fold cross-validation techniques were applied (Hastie et al., 2009; Kuhn and Johnson, 2013). The adoption of different strategies in the analysis is to address sample size constraints and mitigate risks of overfitting and model instability. Models were trained on the training subset with hyperparameter optimization performed using k-fold cross-validation (k=5) (James et al., 2021). Model performance was assessed using standard statistical metrics, including coefficient of determination (R^2), root mean square error (RMSE), mean square error (MSE), and mean absolute error (MAE) (Chai and Draxler, 2014). The combination of spectral data preprocessing and robust feature selection enhanced the models' ability to detect subtle differences in soil properties.

Feature importance analysis

For models supporting feature importance analysis, the contribution of individual wavelengths to prediction accuracy was evaluated at Step 5 in Figure 3.9 . This analysis identified the spectral regions most strongly associated with specific soil properties, providing insights into the underlying physical and chemical mechanisms.

Model selection

Final model selection at Step 6 in Figure 3.9 was based on a combination of prediction accuracy (RMSE, R^2), model complexity, and computational efficiency (Kuhn and Johnson, 2013). The selected models were then applied to the entire hyperspectral dataset to predict properties for the creation of spatial maps using ArcGIS (ESRI, 2019).

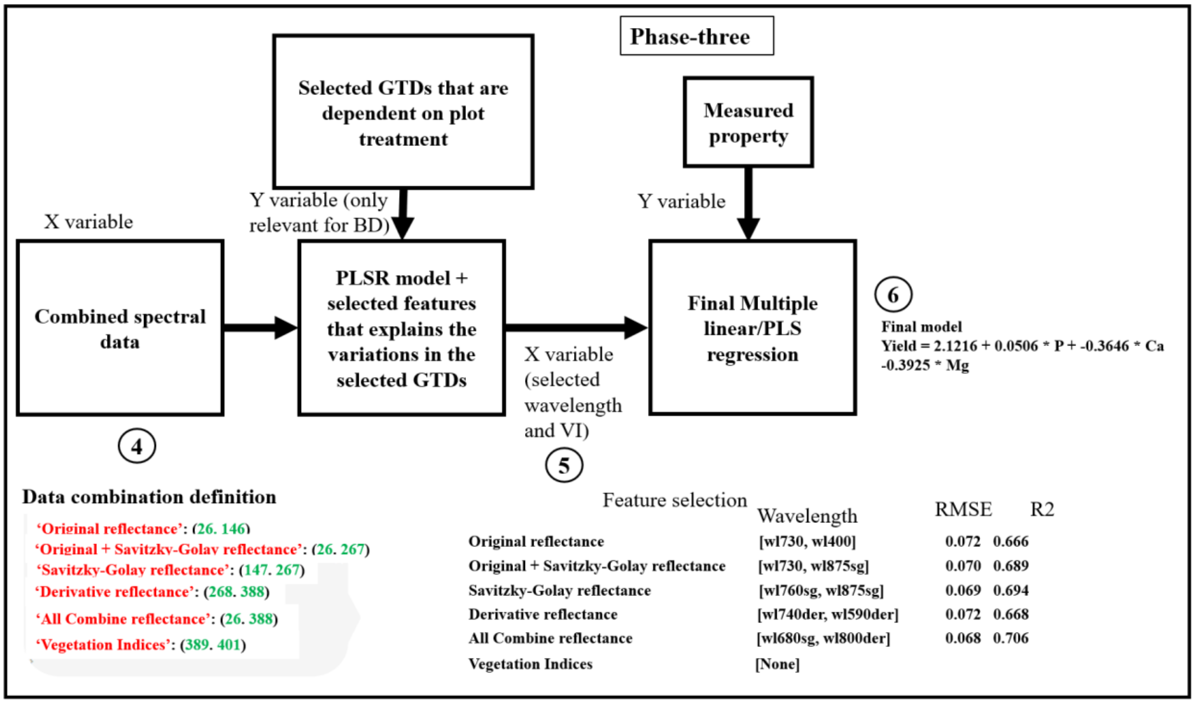

Figure 3.9: Schematic diagram of model generation workflow (phase-three)

3.4.2. Spatial analysis

3.4.2.1. Geolocation and data preparation

The experimental fields' coordinates were plotted in Google Earth Pro to capture site conditions during the data collection period accurately. Base markers were placed to define field boundaries and establish measurement grids within the study areas, which measured 30 × 160 m and 17 × 18.9 m. The geolocation data was exported as a KML file to preserve spatial references for subsequent analysis.

3.4.2.2. GIS processing and map generation

Spatial analysis was conducted using ArcGIS ArcMap (ESRI ArcGIS™ version 10.7.1, 2019, CA, USA). The KML file containing the site coordinates was imported and converted into a layer file. It was then projected using the UTM zone 54N, which is the UTM reference for the experimental area, to generate a shapefile. These spatial references were integrated with both ground truth data (GTD) and model-predicted soil and crop properties to generate spatial distribution maps.

3.4.2.3. Interpolation methods

Two interpolation techniques were utilized depending on the specific analysis requirements:

1. Ordinary spherical kriging described in Raid et al. (2013) was used to generate soil property maps in the first experiment. This geostatistical method was chosen for its ability to account for both the distance and spatial arrangement of known data points when predicting values at unmeasured locations. A semi-variogram was used to model the spatial variability of soil properties, ensuring that the resulting maps produced smoothly varying surfaces that accurately reflect the underlying spatial structure. The semi-variogram method was used due to its ability to capture complex spatial patterns.

2. Inverse Distance Weighting (IDW) interpolation described by Benmoshe (2025) was utilized for the controlled compaction experiment. The coverage parameter was set to 3 m, while the number of points was maintained at the default settings. IDW was chosen because it effectively preserved the distinct boundaries between treatment areas, which were rectangular subplots with specific compaction levels. This function of IDW was essential in ensuring the accurate representation of treatment effects.

Raster analysis was subsequently performed on the interpolated data to create finalized property maps that visualized the spatial distribution of soil characteristics across the study area.

3.5. Conclusions

This chapter provides an overview of the methodology and experimental design employed in this study conducted between 2022 and 2025. The experimental site characteristics were described, including soil properties, climatic conditions, and the treatments applied across test fields. The research utilized innovative platforms and instrumentation, such as hyperspectral imaging technology and laboratory analytical equipment, to ensure high-quality results. Systematic data collection protocols and efficient sampling methods were applied to maintain consistency and reduce experimental error during both fieldwork and laboratory analysis.

The data analysis process incorporated innovative image processing techniques, spectral analysis methods, and machine learning approaches to extract meaningful information from the hyperspectral data. The statistical methods were carefully selected and applied to ensure strong model development, validation, and interpretation of results. This methodology proves the scientific basis of the findings presented in later chapters and offers a reproducible framework for future research in a similar area.

CHAPTER 4. DEVELOPMENT OF REMOTE SENSING METHODOLOGY FOR SOIL COMPACTION ASSESSMENT

4.1.Introduction

Expanding agricultural productivity through mechanization has contributed positively to cost reduction, output value, income, and return rate of all types of crops (Khater et al., 2023; Peng et al., 2022). This has encouraged the introduction of more advanced technologies in agriculture to improve productivity and solve pertinent problems in the sector.

While the use of farm machinery offers many advantages, as reported by researchers such as Diao et al. (2016), Hasan et al. (2020), and Ma et al. (2018), its environmental implications, particularly soil compaction (SC), cannot be overlooked (FAO, 2020). The operation of heavy machinery during the cropping season often leads to SC, which restricts root growth, reduces water infiltration, and restricts crop development (Askari et al., 2021; Twum and Nii-Annang, 2015). Tillage is commonly utilized to manage SC, with conventional and conservation tillage being the most frequently used methods. However, these traditional approaches are energy-intensive and costly, with conventional tillage increasing soil susceptibility to erosion (Holland, 2004; D. Singh et al., 2023).

Modern innovative tillage practices, such as PT, aim to address SC by targeting areas in a field that require mechanical action only, such as compacted layers (Kaufmann et al., 2010; Shamal et al., 2016). PT has been shown to reduce energy consumption during tillage while improving crop growth and yield (Shamal et al., 2016). However, executing PT requires detailed information about soil conditions, which is traditionally obtained through invasive, labor-intensive, and time-consuming field and laboratory experiments (Orangi et al., 2019; Poppiel et al., 2022). These traditional methods are less practical for large fields because data collection and processing can take months, cutting into valuable cropping seasons.

Some research efforts have focused on developing devices and methods for assessing SC (Kodaira and Shibusawa, 2020; Shamal et al., 2016). While these tools are robust, they often disturb the soil ecosystem during data collection. This makes them unsuitable for fields sensitive to marginal disturbances, such as fields with high clay content (Gürsoy, 2021).

This chapter explores the potential of hyperspectral camera (HSC) imaging for assessing soil conditions related to SC. It aims to establish correlations between hyperspectral signatures and key soil properties influencing SC. Additionally, it seeks to develop a standardized workflow for processing hyperspectral data into spatial SC maps suitable for PT planning.

4.2. Experimental methods

This research utilizes a dual-approach methodology that combines traditional laboratory techniques with advanced remote sensing (RS) to evaluate SC conditions in a harvested wheat field. The experimental design integrated ground truth data collection through established soil density and other soil physical measurement protocols with HSC imaging to develop a novel RS workflow for PT applications.

The methodology is built upon established research that has defined critical BD and PD thresholds for tillage decision-making (Kaufmann et al., 2010; Shamal et al., 2016). While previous studies have validated these thresholds for PT planning, they often relied on labor-intensive or mechanically invasive soil sampling methods, limiting practical implementation in most cases. This research methodology addresses this limitation by developing and validating a hyperspectral imaging approach that can rapidly assess the SC status of fields.

The experimental framework was organized to evaluate the relationship between spectral signatures captured by HSC and soil physical properties measured through traditional laboratory analysis. The significant contribution of this study lies in establishing a comprehensive RS workflow that translates hyperspectral data into site-specific tillage recommendations, thereby enhancing the feasibility of PT adoption in commercial agriculture.

4.2.1. Field data collection method

A grid sampling method was utilized for this study; samples and data were collected from three points in each grid. A 0.3 m T-shaped soil auger was used to extract representative soil samples from three depths of interest (0-0.1 m, 0.1-0.2 m, and 0.2-0.3 m). In total, 432 samples were collected in two days, placed in hermetic bags, and labeled for further processing at the laboratory.

The NH-7 hyperspectral camera was used to capture the field surface image data. A shooting distance of 0.75 m above the field surface was set for the data collection in this study. Each grid was scanned with the HSC three times, with a 90-degree horizontal adjustment each time. The resolution and sharpness of the images were constantly checked and adjusted accordingly, using a Spectralon® reference panel (Yamasaki et al., 2022). A total of 144 images were collected from the field using the HSC.

4.2.2. Data processing

The experimental process for this study is represented in Figure 4.1 below, which shows how the two types of data collected were processed.

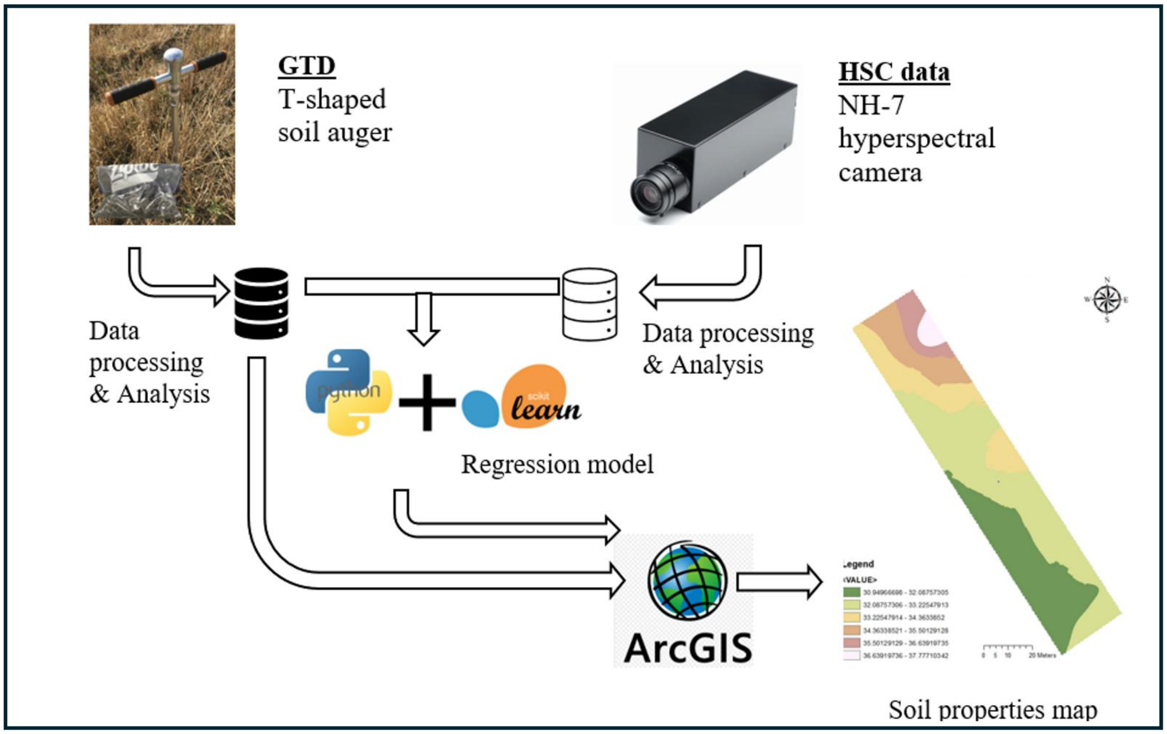

Figure 4.1: Soil Compaction Assessment Research Flow Chart

The soil samples were processed at the laboratory, and the results were used as the ground truth data (GTD). In Figure 4.1, it can be observed that the GTD is key for comparison purposes and to achieve the final model of the soil properties. Each collected sample was divided into two parts, the first part was used to measure soil dry bulk density (BD), packing density (PD), soil moisture content wet basis (MCW), soil moisture content dry basis (MCD), volumetric soil moisture content (VCM) and organic matter content (OMC). The second part was used to determine sand (SC), clay (CC), and silt (STC) content of the soil. The data from the GTD, shown in the left side of Figure 4.1, were processed using the statistical tool pack from Microsoft Excel 2016 and the mean value of each grid was placed in the ArcGIS ArcMap (ESRI ArcGISTM version 10.7.1, 2019, CA, USA) to develop the soil property maps as seen on the right side in Figure 4.1. The HSC data was processed in Python 3.9.12 using Scikit-learn (v1.0.2), NumPy (v1.21.5), and Pandas (v1.4.2) to develop a regression model based on GTD input. The model's predictions were then imported into ArcGIS ArcMap to generate maps for soil properties.

4.2.2.1. Ground truth data

Bulk density/Packing density

Samples for BD were extracted using the ring excavation method described in Soil Survey Staff (2014). Sampling was done cautiously to avoid large particles like rocks, wood, etc. The samples were taken from three different depths as described in Section 4.2.1 and replicated three times on each grid. The samples were oven-dried at 105 degrees Celsius for 24 hours. Eqs. 4.1 and 4.2 were used to compute the BD and PD, respectively (Shamal et al., 2016). For PT planning across the entire recommended depth of 0.3 m (Kaufmann et al., 2010; Selolo et al., 2023), the average values of 0-0.3 m depth were used, and the soil properties were computed per grid. It must be acknowledged that researchers like Shamal et al. (2016) used 0-0.15 m, while others adopted different soil depths for similar purposes.

$$\text{Bulk density (BD)} = \frac{\text{Oven dried weight of soil (g)}}{\text{Volume of soil (cm}^3\text{)}} \tag{4.1}$$

$$PD = BD + 0.009CC \tag{4.2}$$

Soil moisture content

The method used for measuring soil moisture content in this experiment is the oven-drying method. The MCW, MCD, and VMC were determined by using Eqs. 4.3 to 4.5, respectively. Soil samples were sieved through a 2 mm mesh to remove coarse fragments, ensuring uniform particle size distribution and minimizing potential biases in subsequent analyses.

$$MCW = \frac{\text{Wet soil weight (g)} - \text{Oven dried weight of soil (g)}}{\text{Wet soil weight (g)}} \times 100\% \tag{4.3}$$

$$MCD = \frac{\text{Wet soil weight (g)} - \text{Oven dried weight of soil (g)}}{\text{Oven dried weight of soil (g)}} \times 100\% \tag{4.4}$$

$$VMC = MC_D \times \frac{BD}{Density\ of\ water} \tag{4.5}$$

$$MCW = 0.6048 \times (MC_D) + 4.8092 \tag{4.6}$$

$$VMC = 2.379 \times (MC_D) - 0.8276 \tag{4.7}$$

The MCW and the VCM relation to the MCD can be expressed as functions generated from this research's data in Eqs. 4.6 and 4.7, respectively. These equations enable the conversion of one form of measured moisture content into another to fast-track data collection and save the cost of acquiring multiple moisture measuring instruments.

Organic matter content

To determine the OMC of the experimental field soil, the 'Loss on Ignition' method was adopted. The procedure outlined by Motsara et al. (2008) was carefully followed, using the samples obtained from the moisture content experiment. The OMC for all grid points was calculated using the formulas provided in Eqs. 4.8 and 4.9.

$$\text{Burnt content (BC)} = \frac{\text{dried weight of soil @ 105 }^{0}\text{C} - \text{dried soil @ 400 }^{0}\text{C}}{\text{dried weight of soil @ 105 }^{0}\text{C}} \times 100\% \quad (4.8)$$

$$OMC = BC \times 0.58 \quad (4.9)$$

Soil texture

The soil texture of the samples was determined following the procedure outlined by Motsara et al. (2008). The samples were sieved through a 2 mm mesh, and the sieved portion was dried. From this dried portion, 50 g of soil was weighed and placed into a one-liter graduated container. The container was then half-filled with distilled water, and 10 ml of sodium hexametaphosphate solution was added to disperse aggregated particles.

The sample was stirred for 4 minutes in a clockwise direction, followed by another 4 minutes in an anticlockwise direction. After stirring, the container was filled with distilled water up to the 1-liter mark and placed on a stable platform for further stirring. This time, the stirring was done gently to avoid creating a circular motion in the solution.

At time zero, the solution was stirred and left to settle briefly before being stirred again after 20 seconds without taking any reading. The solution was then left to settle completely, and the first sediment reading was taken at 40 seconds. A second reading was recorded after 2 hours. The sand, clay, and silt content of the soil was calculated using Eqs. 4.10 to 4.15.

$$SP = SV_{40s} \times 0.65 \quad (4.10)$$

$$CP = (1 - SV_{2h}) \times 0.015 \quad (4.11)$$

$$STP = (SV_{2h} - SV_{40s}) \times 0.5 \quad (4.12)$$

$$SC = \frac{SP}{TP} \times 100 \quad (4.13)$$

$$CC = \frac{CP}{TP} \times 100 \quad (4.14)$$

$$STC = \frac{STP}{TP} \times 100 \quad (4.15)$$

SP, CP, and STP refer to the volumes of sand, clay, and silt particles, respectively, within a 1-liter soil suspension. SV_{40s} and SV_{2h} represent sediment volume readings taken after 40 seconds and 2 hours. SC, CC, and STC denote the calculated percentages of sand, clay, and silt, while TP represents the total particle volume.

The constants 0.65, 0.5, and 0.015 in the equations correspond to the estimated volume proportions of sand, silt, and clay in the suspension. These values account for particle packing, with sand assumed to have 35% pore space and silt 50% (Gartell, 1992; Walters, 2021).

Results were plotted on a textural triangle (Figure 4.2), revealing that the majority of grid points in the study area fall into the loam (79%), silt loam (17%), and sandy clay loam (4%) textural classes.

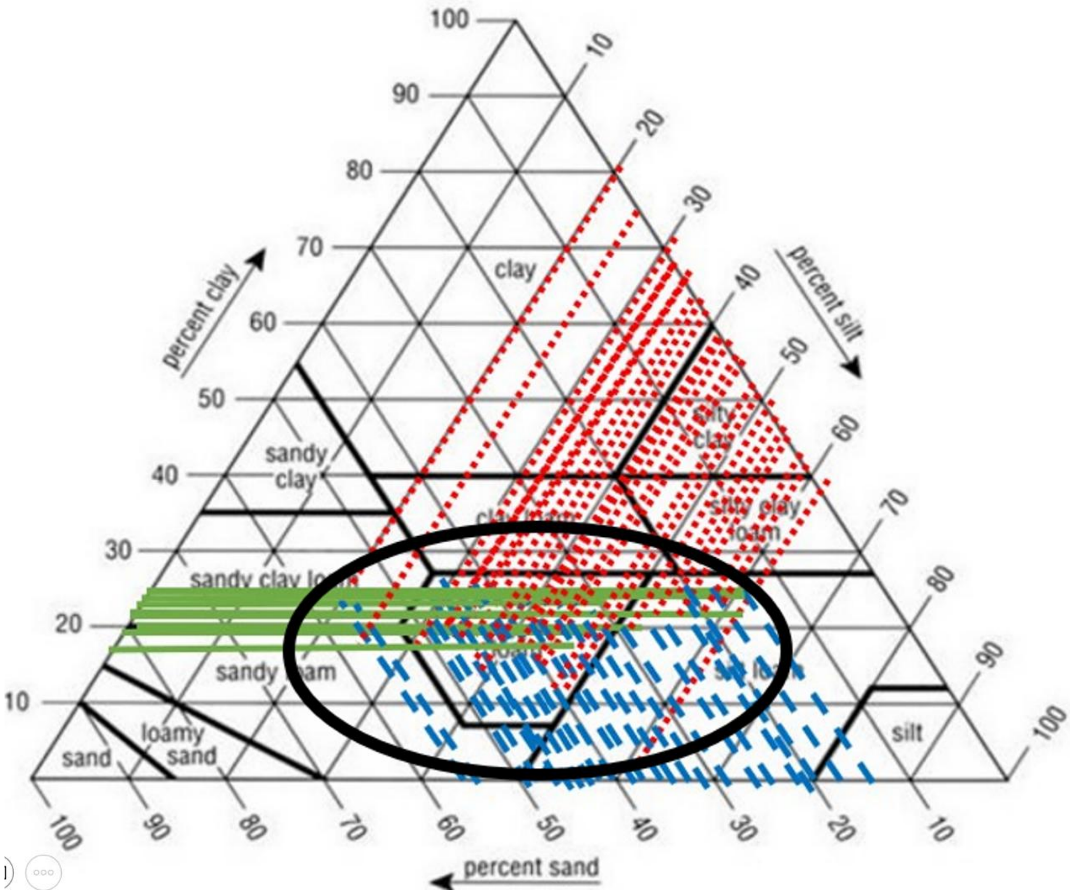

Figure 4.2: Compaction assessment study site soil textural classification

The color plots in Figure 4.2 represent the percentage of sand content (blue), clay content (green), and silt content (red), which were computed from Eqs. 4.13 to 4.15. The soil texture type is determined by the section of the diagram where the three lines converge, marked with a black oval line.

4.2.2.2. HSC data processing

Figure 4.3 shows an example of an image captured using the HSC mounted on a tripod 0.75 m above the residual vegetation surface. The HSC data collected was first pre-examined to detect defects in images. Then, the images were processed using HSAnalyzer version 12. Each image contained three carefully selected regions of interest (ROIs) to represent the residual vegetation components outlined in Section 3.1.1.1, namely, stubble and straw, emerging weeds, and bare soil. Care was taken to avoid including foreign objects such as stones or unnatural bright spots, as their presence has been shown to distort spectral signatures (Yamasaki et al., 2022). This selection process ensured the reliability of spectral data used for analysis. Each ROI was about 185×187 pixels (4.89×4.95 cm) and demarcated as shown in Figure 4.3. The spectra data was utilized in Eq. 4.16 to calculate the corrected image spectra (Feng et al., 2023; Yamasaki et al., 2022).

$$I_{(corrected)} = \frac{I_1 - I_2}{I_3 - I_2} \tag{4.16}$$

Where I_1, I_2, and I_3 represent the raw image, dark image, and whiteboard image, respectively.

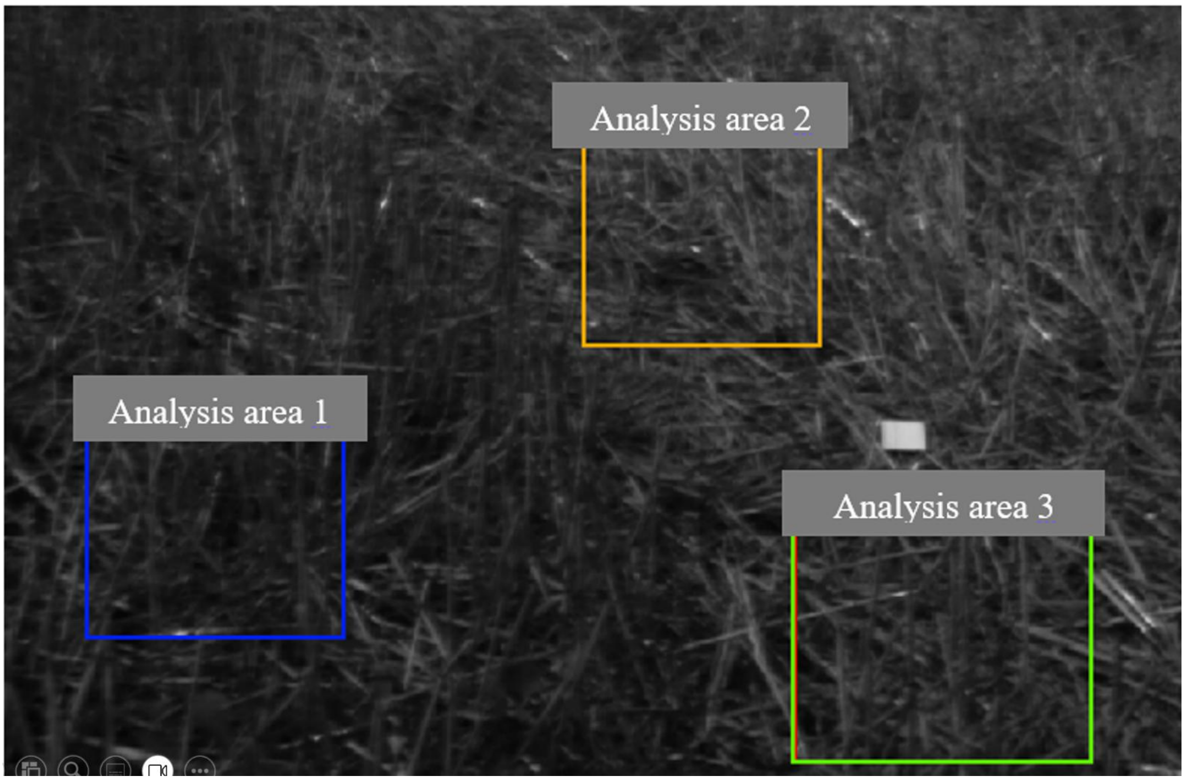

Figure 4.3: HSC image of the study field with the selected regions of interest

The spectra data and ground truth data results were compiled into a single file and processed using Scikit-learn, NumPy, and Pandas libraries in Python. The relevant wavelengths were identified using the PLSR coefficients with 1st and 2nd derivatives; further description of this method can be found in Mehmood et al. (2012).

4.2.3. Model development and evaluation

First, feature selection was conducted as described in Section 3.4.1.4 of Chapter 3. This step identified the most relevant wavelengths from the soil spectra data collected across all 48 grids in the study field for the ground truth data sets (GTDs). Next, various machine learning and statistical tools, also detailed in Section 3.4.1.4, were evaluated to find the best-performing model. For model training and evaluation, 70% of the samples were randomly selected as the training set, while the remaining 30% were used as the test set. The model's predictive accuracy was assessed using the coefficient of determination (R^2), mean square error (MSE), and mean absolute error (MAE).

The subsequent part of the prediction model development consisted of the selection of simple correlations between key GTD's, such as MCW versus BD, MCD versus BD, and OMC versus BD, as illustrated in Figure 4.4. These key GTD's were used to generate similar correlations with the spectra data from the HSC and selected indices, then used to predict BD and PD for the different grids. The performance of the correlation models was evaluated by the determination coefficients (R^2).

The models developed from both methods were finally evaluated based on Eq. 4.17, which is the percent error of deviation of the predicted soil property, i.e., the PD, from the actual GTD.

$$E_d = \frac{|D_G - D_P|}{D_G} \times 100 \tag{4.17}$$

Where E_d, D_G, and D_P mean the percent error of deviation, the ground true value, and the predicted value, respectively.

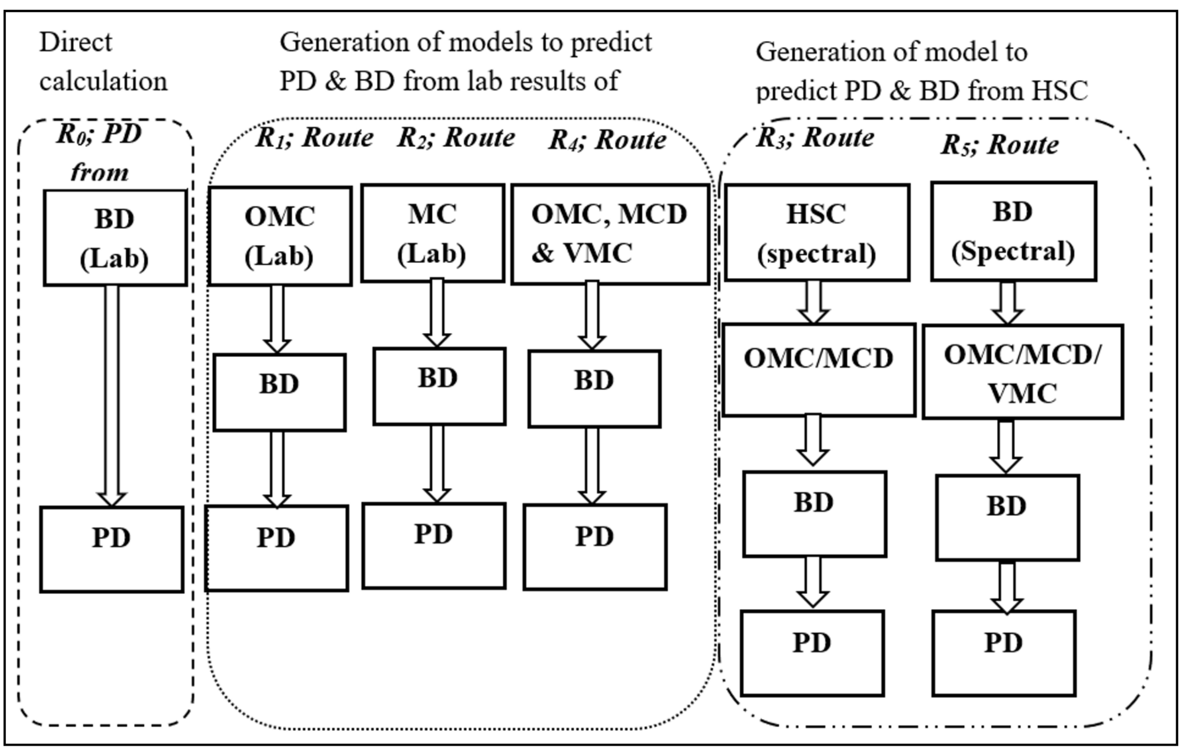

Figure 4.4: Model development methods

The six methods used in this research are represented in Figure 4.4, which also shows the various paths of data processing leading to the PD data calculation or prediction. The direct calculation of PD; R_0 from Eq. 4.2 is the simplest and most direct of all the methods, but since the process of manually extracting BD and CC data is tedious and time-consuming, it is difficult to practice on a large scale. The study field used in this research was only 30x160 m, but for fields with a very wide area, such as the fields found in North America and Africa, the method R_0 is not practical. Hence, the need to explore the other methods, R_1, R_2, R_3, R_4, and R_5. These methods are classified into two sets: the first set of methods groups R_1, R_2, and R_4, and the second set of methods includes R_3 and R_5. The first set of methods uses the measured GTD to develop prediction models or functions. The second set of methods applies data obtained from the HSC and uses the functions developed in the first set to predict PD. As will be described later, the second set of methods can be used to estimate PD in larger fields, making it suitable for commercial PT applications.

4.2.4. PT planning

The borders of the 30×160 m study site were marked, and files were prepared and processed as described in Section 3.4.2 of Chapter 3. The prepared KML file, along with both GTD and predicted soil properties, was used in ArcGIS ArcMap (ESRI ArcGISTM version 10.7.1, 2019, CA, USA) to develop maps, following the method described in Section 3.4.2.3. These maps display different color-coded layers representing varying levels of SC (for PD maps) or variations in specific soil properties, as illustrated in Figure 4.1. Based on the level of compaction of an area on the PD maps, Kaufmann et al. (2010) made the guide in Table 4.1 for the type of tillage needed in every PD level.

Table 4.1: The packing density classes as related to tillage type and crop growth

PD value (kg/m^3)	Crop growth condition	Level of tillage
<1400	Below optimum range	No tillage
1400-1550	Lower optimum range	No tillage
1550-1700	Upper optimum range	Shallow cultivation or tillage (7cm)
1700-1820	Lower limiting range	Medium cultivation or tillage (20 cm)
>1820	Upper limiting range	Deep cultivation or tillage (30 cm)

Research indicates the optimum PD for crop growth is approximately 1550 kg/m^3 (Kaufmann et al., 2010). At PD levels below this threshold, crop growth remains unaffected, corresponding to a 'no tillage' recommendation (Shamal et al., 2016) as outlined in Table 4.1. Conversely, when PD exceeds this optimum range, the tillage interventions recommended in Table 4.1 become necessary to ensure proper crop development. This established relationship between PD thresholds and tillage requirements serves as the foundational framework for evaluating the hyperspectral camera's (HSC) capability to measure soil properties related to compaction.

4.3. Results and discussion

4.3.1. PT relevant soil properties

Selected soil properties that were mentioned in the methods were measured on the field, processed, and analyzed to determine the properties that have an appreciable level of impact on SC, which is highly linked to BD by researchers like Beylich et al. (2010), Dörner et al. (2022) and Reintam et al. (2009). The results of the correlation analysis of GTD, presented in Table 4.2, reveal significant negative correlations between BD and key soil properties at the 0-0.30 m depth. Specifically, MCW exhibits a correlation coefficient of -0.413, moisture MCD shows a value of -0.269, and OMC demonstrates a strong negative correlation of -0.571. These findings highlight the inverse relationship between BD and soil parameters critical to SC. This trend is constant across the data for the various depth sections as well. A negative correlation indicates two variables that tend to move in opposite directions. A correlation around –0.50 means that there is a moderate negative relationship between a soil property and the BD. A correlation close to 0 would mean that there is no linear relationship between a given soil property and the BD. A correlation of +1.0 means a perfect positive linear relationship, such as the PD and the BD. Their R^2 values are also quite significant, and their relationship with the BD is evident. In the other hand, soil texture properties such as clay content CC, sand content SC and silt content STC have a correlation close to 0 and a quite small R^2, which means that although they are important parameters to understand the composition of the soil they are not related directly to the BD, at least not individually.

Table 4.2: R^2 and correlation of all soil properties with the bulk density

	0-0.10 m		**0.10-0.20 m**		**0.20-0.30 m**		**0-0.30 m**	
Soil properties	**R^2**	**Corr**	**R^2**	**Corr**	**R^2**	**Corr**	**R^2**	**Corr**
MCW	0.156	-0.396	0.014	-0.119	0.105	-0.325	0.16	-0.413
MCD	0.155	-0.394	0.025	-0.159	0.113	-0.335	0.19	-0.269
OMC	0.063	-0.250	0.203	-0.412	0.046	-0.177	0.35	-0.571

	0-0.10 m		0.10-0.20 m		0.20-0.30 m		0-0.30 m	
Soil properties	**R^2**	**Corr**	**R^2**	**Corr**	**R^2**	**Corr**	**R^2**	**Corr**
VMC	0.141	0.375	0.291	0.540	0.361	0.601	0.3	0.389
CC	0.003	0.045	0.001	-0.030	0.042	-0.198	0.00012	0.014
SC	0.014	-0.120	0.0003	-0.016	0.003	0.047	0.0023	0.075
STC	0.016	0.125	0.002	0.023	0.001	-0.033	0.011	-0.082
PD	1.000	1.000	1.000	1.000	1.000	1.000	0.9993	1.0

Table 4.3 provides a summary of the mean and standard deviation (SD) values of the soil properties. The data was obtained from the GTD. Note that the mean values of the BD and the PD are similar and have the same units (kg/m^3) with the same SD across the same depth sections, which was expressed as a high correlation in Table 4.2. Although the other parameters are percentage values, they can be correlated to the BD. Also note that MCW, MCD, CC and OMC have SD values that are less than 2% for the entire depth and had the least SD values across the depth sections, which means that they were somewhat uniform all along the study field. On the other hand, SD values of the SC and STC were about 10%, which indicates that the soil texture can vary significantly even for a small-sized field. The compaction level of the field, which is evident from the BD and PD values in Table 4.3, increases by approximately 200 kg/m^3 for every 0.10 m along the soil depth from 0-0.30 m. This pattern is also seen in the MCW, MCD, OMC, and VMC data, but most of the changes in these parameters were marginal. Thus, for the field used in this study, the difference in moisture content and organic matter across the depth sections is marginal, and using the average of the values for the entire depth is appropriate.

Table 4.3: Essential statistical summary of soil properties (mean ± SD)

Soil properties	**Depth**			
	0-10 cm	**10-20 cm**	**20-30 cm**	**0-30 cm**
BD (kg/m^3)	2165.02±179.52	2366.41±133.24	2526.19±194.91	2352.54±126.29
MCW (%)	23.23±1.94	24.86±1.52	25.44±1.40	24.51±0.99
MCD (%)	30.40±3.27	33.15±2.34	34.18±2.41	32.58±1.68

Soil properties	Depth			
	0-10 cm	**10-20 cm**	**20-30 cm**	**0-30 cm**
OMC (%)	1.26±0.73	1.38±0.47	3.03±0.93	1.89±0.53
VM (%)	65.52±6.95	78.35±6.43	86.16±7.28	76.68±4.23
CC (%)	20.81±1.65	20.36±1.54	20.31±0.87	20.55±1.14
SC (%)	38.68±11.09	40.54±10.65	38.29±11.03	39.75±9.91
STC (%)	40.51±10.03	39.10±9.58	41.40±10.62	39.71±9.173
PD (kg/m^3)	2165.03±179.52	2366.41±133.24	2526.19±194.91	2352.54±126.29

The 0-0.3 m depth section data listed in Tables 4.2 and 4.3 can be depicted on a map, as shown in Figure 4.5. The map of MCD in Figure 4.5 (d) and OMC in Figure 4.5 (b) have their low values at the south-western portion, with most of the western portion having fairly low values. The BD map in Figure 4.5 (c), on the other hand, has its higher values on the south-western portion of the map, which is opposite to that of MCD and OMC, which provides backing for the negative correlation between those properties listed in Table 4.2. This result confirms the negative correlation between the BD and the moisture content (Özdemir et al., 2022), in addition to results that also reported a negative correlation between the BD and the OMC (Zheng et al., 2021).

Properties showing positive correlations with BD generally exhibit minimal influence, as indicated in Table 4.2. However, exceptions include VMC and PD: VMC displays an R^2 value of 0.3 and a correlation coefficient of 0.389, while PD demonstrates an R^2 of 0.9993 and a near-perfect correlation coefficient of 1.0, highlighting their stronger relationship with BD. From the PD map in Figure 4.5 (a), it can be observed that it has a similar appearance to the BD map in Figure 4.5 (c), which explains the correlation value of 1.0 in Table 4.2. The relationship between PD and BD can be found in Eq. 4.2. In this experiment, where CC ranged narrowly between 18.99% and 24.15%, both PD and BD provided similarly effective measurements of SC. This differs from findings by Shamal et al. (2016), where clay content had a significant impact on SC measured as PD, with their study featuring a wider clay content range (30.1% to 45.8%). These contrasting results suggest that higher clay content levels have a more appreciable effect on SC measurements than lower clay content levels, which explains why minimal differences between PD and BD as compaction indicators were observed in this study.

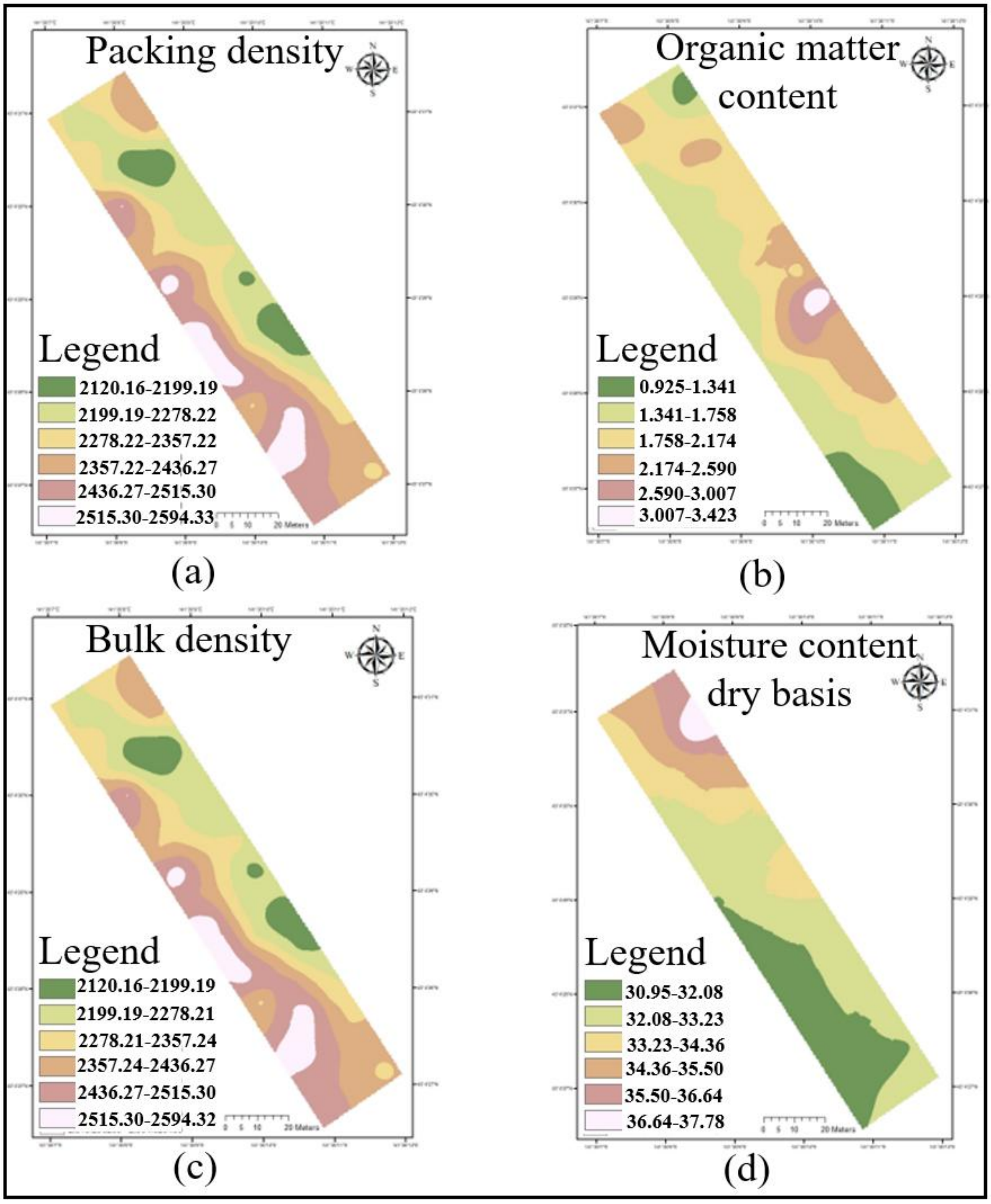

Figure 5: Maps of soil properties (0-0.30 m)- GTD (a) PD map, (b) Organic matter content map, (c) Bulk density map, and (d) Moisture content dry basis

4.3.2. Assessment of remote sensing PT data flow

Most research on RS applications for measuring soil properties relies on combinations of contact IoT devices and spectrophotometers that collect data either from underground trenches or through direct soil contact (Kodaira and Shibusawa, 2020; Shamal et al., 2016) The present study explores a different approach: remotely measuring SC using hyperspectral imagery captured above the soil surface. This indirect measurement method leverages soil properties discussed in Section 4.3.1. These properties exhibit variability that can be effectively detected through non-contact spectral measurements and are significant indicators of SC parameters such as BD (Reintam et al., 2009). This research identified the different moisture contents (MC) and OMC as key properties that explain variations in soil composition. These properties are readily detectable using HSC, enabling estimation of their variability across field conditions. Similar observations regarding the detectability of MC and OMC through hyperspectral imaging have been reported in previous studies (Bartholomeus et al., 2008; Mu et al., 2023; Xie et al., 2022; Z. Yin et al., 2013).

The selected soil properties' ability to explain the variations in BD and PD were developed into functions, listed in Table 4.4. The various functions listed in Table 4.4 are denoted by methods R_0, R_1, R_2, R_{3a}, R_{3b}, R_4, and R_5. The methods are divided into two groups, the first set (R_1, R_2, and R_4) are novel functions that were generated from the GTD; and the second set (R_{3a}, R_{3b}, and R_5) are the respective corresponding methods of the first set applied to the remotely sensed data using the HSC. The meaning and relevance of the methods and their functions are explained in detail below:

I. R_0: This is the benchmark function that is used for this work. The source can be seen in Table 4.4 and Eq. 4.2. The BD and CC in the function were derived from field sampling and laboratory analysis. The data calculated from R_0 were used to serve as the basis for checking the error margin of the other methods. In addition, it was used to generate a log function, listed as F2 in Table 4.4. F2 utilizes BD as the input variable to enable direct PD computation from the BD data without the need for CC. F2 is critical for predicting PD using remotely sensed data, as variations in CC could not be reliably detected from HSC data during this study.

II. R_1: This is the method derived from a log function between the BD and the OMC; consisting of F1 and F2. This function enables the prediction of BD directly from OMC and will be especially useful in predicting BD/PD from both directly measured and remotely sensed OMC data.

III. R_2: Since MCD is one of the simplest ways to estimate the level of moisture in soil, it was utilized in method R_2 to generate a log function listed as F3 for predicting BD from MCD data. Combining F3 and F2 enables the prediction of BD and PD using MCD. This method is key for estimating BD or PD from remotely sensed data.

IV. R_{3a}: This method combines function F1 from Method R_1 with function F4, which estimates OMC using HSC data. F4 employs a log function at 410 nm in the violet spectrum region to derive OMC from HSC spectral data. The OMC estimates from F4 are then substituted into F1 to calculate BD based on HSC data. Finally, these BD values are input into function F2 to predict PD, completing the process of estimating SC parameters entirely from RS.

V. R_{3b}: Method R_{3b} adopts a similar approach to method R_{3a}, but this time, F3 is used instead. F3 is the function that estimates BD from MCD listed in Table 4.4. The function F5 utilizes the Green Residual Cover Index (GRCI) as described by Kavoosi et al. (2020) to estimate MCD from HSC data. GRCI is calculated using a combination of Band 2 (blue) and Band 3 (green) from the visible spectrum.

VI. R_4: Using derived relevant soil properties to predict the BD and the PD independently yielded satisfactory results. Hence method R_4 combines these properties using the multiple linear regression model to generate a function that could predict BD and PD. Method R_4 combines MCD, OMC, and VMC data to predict BD, listed as F6 in Table 4.4. Then, the results are used in F2 to predict the PD. This method will be useful in instances where OMC and soil moisture levels (MCD and VMC) are measured or estimated from a RS device.

VII. R5: This method utilizes function F6 (from method R_4) to estimate BD using HSC data, as shown in Table 4.4. Functions F4, F5, and F7 are used to estimate OMC, MCD, and VMC, respectively, from the HSC data. Notably, F7 uses a wavelength of 455 nm, which corresponds to Band 2 (blue) in the visible region of the electromagnetic spectrum. The outputs from F4, F5, and F7 are substituted into F6 to estimate BD, which is then used in function F2 to estimate PD from the HSC data.

Table 4.4: List of methods and their respective functions

Method	Route	Model/Functions	Error (%)
$\boldsymbol{R_0}$	PD_{GTD}	$PD = BD_{GTD} + 0.009CC$ $----$(Shamal *et al*., 2016; Renger, 1970)	-
$\boldsymbol{R_1}$	$OMC_{GTD} \rightarrow BD_{R1} \rightarrow PD_{R1}$	$BD_{R1} = -610.619 \times \log_{10}(OMC_{GTD}) + 2511.14 \quad --- F1$ $PD_{R1} = 5420.39 \times \log_{10}(BD_{R1}) + (-15919.2) ---- F2$	0.06-7.9

Method	Route	Model/Functions	Error (%)
$\boldsymbol{R_2}$	$MCD_{GTD} \rightarrow BD_{R2} \rightarrow PD_{R2}$	$BD_{R2} = -2856.38 \times \log_{10}(MCD_{GTD}) + 6320.11 ---- F3$ $PD_{R2} = 5420.39 \times \log_{10}(BD_{R2}) + (-15919.2) ---- F2$	4.12-23.08
$\boldsymbol{R_{3a}}$	$OMC_{HSC} \rightarrow BD_{3a} \rightarrow PD_{3a}$	$OMC_{HSC} = -0.3935 \times \log_{10}(wl410) + 1.46789 --- F4$ $BD_{R3a} = -610.619 \times \log_{10}(OMC_{HSC}) + 2511.14 ---- F1$ $PD_{R3a} = 5420.39 \times \log_{10}(BD_{R3a}) + (-15919.2) ---- F2$	0.11-12.09
$\boldsymbol{R_{3b}}$	$MCD_{HSC} \rightarrow BD_{R3b} \rightarrow PD_{R3b}$	$MCD_{HSC} = -5.01384 \times \log_{10}(GRCI) + 28.959 --- F5$ $BD_{R3b} = -2856.38 \times \log_{10}(MCD_{HSC}) + 6320.11 ---- F3$ $PD_{R3b} = 5420.39 \times \log_{10}(BD_{R3b}) + (-15919.2) ---- F2$	7.40-23.34
$\boldsymbol{R_4}$	$OMC_{GTD}+MCD_{GTD}+VMC_{GTD} \rightarrow BD_{R4} \rightarrow PD_{R4}$	$BD_{R4} = 2374.65 - 5.28855934(OMC_{GTD}) - 70.29(MCD_{GTD}) + 29.74(VMC_{GTD}) --- F6$ $PD_{R4} = 5420.39 \times \log_{10}(BD_{R4}) + (-15919.2) ---- F2$	0.045-2.51
$\boldsymbol{R_5}$	$OMC_{HSC}+MCD_{HSC}+VMC_{HSC} \rightarrow BD_{R5} \rightarrow PD_{R5}$	$OMC_{HSC} = -0.3935 \times \log_{10}(wl410) + 1.46789 --- F4$ $MCD_{HSC} = -5.01384 \times \log_{10}(GRCI) + 28.959 --- F5$ $VMC_{HSC} = 1.52371 \times \log_{10}(wl455) + 78.1602 --- F7$ $BD_{R5} = 2374.65 - 5.28855934(OMC_{HSC}) - 70.29(MCD_{HSC}) + 29.74(VMC_{HSC}) --- F6$ $PD_{R5} = 5420.39 \times \log_{10}(BD_{R5}) + (-15919.2) ---- F2$	0.19-10.22

In Table 4.4 the PD_{GTD} is the PD from ground true data, PD_{R1} to PD_{R5} are the corresponding packing densities of methods R_1 to R_5, OMC_{GTD} is the organic matter from the ground true data, OMC_{HSC} is the organic matter content from the hyperspectral camera data, MCD_{GTD} is the moisture content dry basis from the ground true data, MCD_{HSC} is the moisture content dry basis from the HSC data, BD_{R1} to BD_{R5} are the bulk densities from methods R_1 to R_5, and VMC_{HSC} is the volumetric moisture content from the HSC data.

4.3.2.1. Accuracy of the proposed method

The accuracy of the methods can be assessed using the percentage of error between the estimated PD data and the data from R_0 in Table 4.4. It can be observed from Table 4.4 that the magnitude of the error in the second set of methods (remote sensing: R_{3a}, R_{3b}, and R_5) is highly dependent on the functions in the first set of methods (R_1, R_2, and R_4). For example, R_4 shows the smallest error range (0.045–2.51%) among the first set of methods. Therefore, incorporating function F6 from R_4 into method R_5 results in the lowest error margin (0.19–10.22%) within the second set of methods. The estimated PD data from methods R_1 and R_2 had error margins of 0.06-7.9% and 4.12-23.08%, respectively. These margins were reflected in the estimated PD data of their corresponding remote sensing methods R_{3a} and R_{3b}, which had error margins of 0.11-12.09% and 7.40-23.34%, respectively. Hence, the accuracy of the estimated PD data from a scanned HSC image above the soil surface is highly dependent on the accuracy of the GTD functions. The methods that predict PD from HSC image data offer the added advantage of significantly reducing the time needed to extract and process soil properties for PD determination.

4.3.3. Selecting the best remote sensing data stream

Maps displaying the spatial distribution of PD in a field can inform PT decisions. These PD maps enable SC management decisions based on the specific crop intended for cultivation or the current field usage requirements. Figure 4.6 presents a comparison of the measured and modeled PD distributions along with their corresponding recommended PT strategies. The displayed maps were generated using method R_0 and the two most accurate methods: R_4 and R_5. Maps generated from the less accurate methods are included in Appendix A. Note that R_4 belongs to the first set of methods, while R_5 belongs to the second set of methods as discussed in Section 4.3.2. R_0 is the map generated from the GTD from the study field and serves as the reference map for the first and second sets of methods.

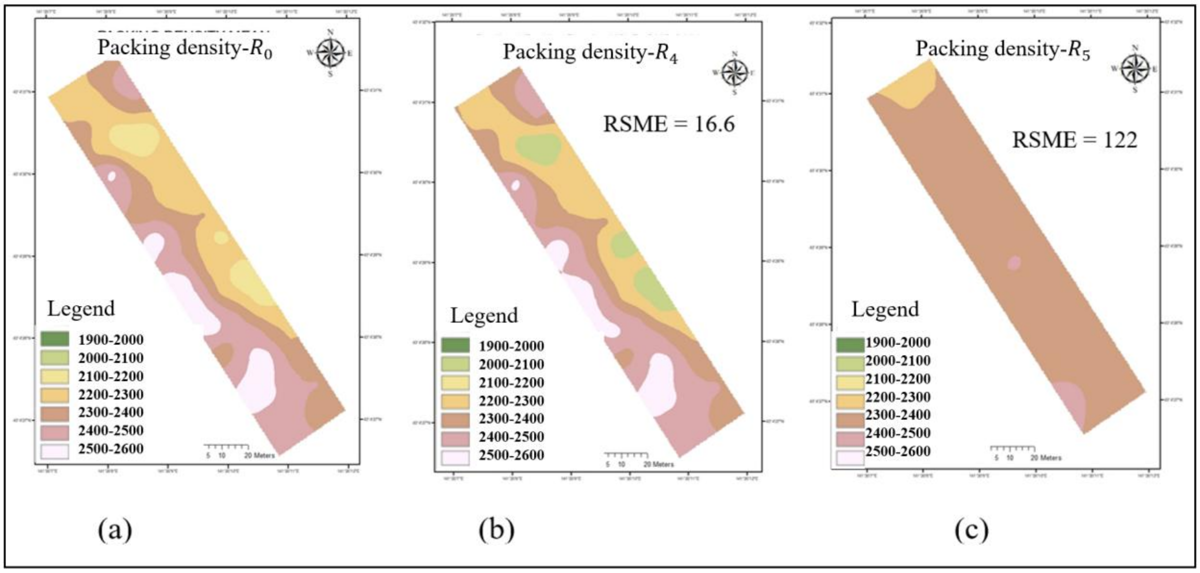

Figure 4.6: PD maps for PT recommendation (0-0.30 m). (a) ground true data PD map from R_0, (b) PD map from R_4, (c) PD map from R_5

The maps in Figure 4.6 (a), (b), and (c) are the PD maps, which show the various levels of SC across the experimental field used. Figure 4.6 (a) corresponds to the R_0 PD map, which is the GTD map, and it shows that the south-western side of the field is more compacted, whilst the compaction level of the mid-eastern portion is relatively low. These maps can be used to implement PT when combined with information on PD level tillage action recommendations in Table 4.1. The Figure 4.6 (b) map shares similar features with Figure 4.6 (a), whilst Figure 4.6 (c) shows the highly compacted zones but has less representation for the less compacted zones.

The entire field's PD in this experiment (Table 4.3) were greater than 1820 kg/m^3 (1.82 mg/cm^3) upper limiting range for crop development captured in Table 4.1, hence the recommended tillage strategy for optimum crop development is a deep tillage/cultivation which corresponds to a plowing depth of about 0.3 m. It is also worth noting that the average difference in PD between the tillage action recommendations in Table 4.1 is about 140 kg/m^3, whilst the RMSE values of method R_4 and R_5 are 16.6 kg/m^3 and 122 kg/m^3, respectively.

The methods R_4 and R_5 explored in this study gave comparable results to that of R_0 regarding the tillage action to be taken on the study field before the next crop is cultivated. Looking at the PD range of 140 kg/m^3 in Table 4.1 and the RMSE values of R_4 and R_5, it means that the variation that is expected when the two methods are used for predicting PD for PT application is less than the range between the tillage action recommendation values. Hence, the developed methods can be an effective alternative to the traditional method of PD data collection for map generation, which is labor-intensive and time-consuming. Moreover, the method R_5, being a RS method, can provide farmers with PD data faster and more easily for prompt PT decisions.

Method R_4 will be suitable for small fields or experimental purposes because of the time factor in extracting the GTD, and it will not be feasible for large commercial fields in the West or Africa. Therefore, the RS option implemented in method R_5 has the potential to be applied on a larger scale and can aid in assessing SC conditions of a wider area in PT applications. PT estimation plays a vital role in reducing carbon footprint, as related research by Shamal et al. (2016) demonstrated that PT applications can reduce fuel consumption by 22-44%.

The results obtained from this study suggest that it is feasible to take a PT decision or plan a PT strategy based on remotely sensed data using an HSC. To select the best method for applying non-contact RS to predict the soil properties relevant to SC management and execute PT, Table 4.5 further expands the prediction errors into various categories. Error categories are divided into 5% steps, ranging from 0-4.9%, 5-9.9%, 10-14.9%, 15-19.9%, and 20-24.9%. The percentage of predicted data sets that fall under each error category is listed in Table 4.5.

Table 4.5: Error percentages of predicted PD from GTD

Method	**Route** **Error**	**0-4.9%**	**5.0-9.9%**	**10.0-14.9%**	**15.0-19.9%**	**20.0-24.9%**	**Ranks**
R_0	PD_{GTD}	-	-	-	-	-	-
R_1	$OMC_{GTD} \rightarrow BD_{R1} \rightarrow PD_{R1}$	70.8%	29.2%	0%	0%	0%	2
R_2	$MCD_{GTD} \rightarrow BD_{R2} \rightarrow PD_{R2}$	2.1%	8.3%	18.8%	58.3%	12.5%	5
R_{3a}	$OMC_{HSC} \rightarrow BD_{3a} \rightarrow PD_{3a}$	52.08%	43.75%	4.17%	0%	0%	4
R_{3b}	$MCD_{HSC} \rightarrow BD_{R3b} \rightarrow PD_{R3b}$	0%	10.42%	33.33%	33.33%	22.92%	6
R_4	$OMC_{GTD}+MCD_{GTD}+VMC_{GTD} \rightarrow BD_{R4} \rightarrow PD_{R4}$	100%	0%	0%	0%	0%	1
R_5	$OMC_{HSC}+MCD_{HSC}+VMC_{HSC} \rightarrow BD_{R5} \rightarrow PD_{R5}$	60.42%	35.42%	4.16%	0%	0%	3

In Table 4.5, the first set (R_1, R_2, and R_4) and the second set (R_{3a}, R_{3b}, and R_5) of methods are ranked based on the amount of data that falls under minimum error categories. It is evident that all the data obtained from method R_4 has an error of 0-4.9%, hence it is ranked as number 1. R_1 is the next method on the rank because 70.8% of its data has an error of less than 4.9%, and the remaining 29.2% has an error of 5-9.9%. R_5 is the 3rd-ranked method overall and the best method corresponding to the RS set, with 60.42%, 35.42%, and 4.16% of its data sets under 0-4.9%, 5-9.9%, and 10-14.9% of error, respectively. Note that method R_5 has an overall error of less than 15%. R_5, although being a RS method, had a higher rank (lower error) than R_2, which is a method that utilizes GTD. Method R_5 demonstrates strong predictive capability for RS applications. Figure 4.8 below illustrates the complete workflow of method R_5, including all terms used and offering flexibility in measurement approaches. Specifically, function F6 in Figure 4.8 incorporates the organic matter content term ($-5.2886\times(OMC_{HSC})$), which traditionally requires time-consuming laboratory methods to obtain ground truth data (GTD). Function F6 also includes moisture content terms ($70.29(MCD_{HSC}) + 29.74(VMC_{HSC})$). Unlike organic matter content, moisture content can be measured quickly, typically within a day, depending on field size, using methods such as oven-drying or portable moisture sensors. This creates an opportunity to enhance R_5's accuracy by combining remotely sensed organic matter content with in-situ measured moisture content, using Eq. 4.6 or 4.7 to estimate BD PD for PT decisions.

$$OMC_{HSC} = -0.3935 \times \log_{10}(wl410) + 1.46789 \ ---F4$$
$$MC_{D\text{-}HSC} = -5.01384 \times \log_{10}(GRCI) + 28.959 \ ---F5$$
$$VMC_{HSC} = 1.52371 \times \log_{10}(wl455) + 78.1602 \ ---F7$$

$$BD_{R5} = 2374.65 - 5.28855934(OMC_{HSC}) - 70.29(MCD_{\text{-}HSC}) + 29.74(VMC_{HSC}) \ ---F6$$

Substituting F4, F5, & F7 into F6

$$BD_{R5} = 2655.8431 + 2.0811 \times \log_{10}(x) + 352.42 \times \log_{10}(y) + 45.3148\log_{10}(z) \ ---F6i$$

$$PD_{R5} = 5420.39 \times \log_{10}(BD_{R5}) + (-15919.2) \ ----F2$$

Substituting F6i into F2

$$PD_{R5} = \log_{10}[(2655.8431 + \log_{10}(x^{2.0811} \times y^{352.42} \times z^{45.3148}))^{5420.39}] - 15919.2 \ ----F2i$$

Where x is Wl410, y is GRCI, and z is wl455.

Figure 4.8: Flow of method R_5

Based on the results presented, method R_5 can be concluded as the recommended methodology for transforming HSC-based RS data into practical PT information.

4.4. Conclusions

This chapter explored the potential of a RS approach for measuring soil parameters relevant to PT implementation. The research combined grid sampling methodology with HSC data to assess soil properties for effective SC management. Among the nine measured properties, two were found to have a strong influence on SC: organic matter content and two types of moisture content.

Maps of the PD generated using the ESRI ArcMap software have a good potential to be used for PT decisions, since all the variations in PD of the field were represented and captured in zones. However, the results from samples taken for this study had a minimum average PD that is above 1.82 Mg/cm^3; hence, for the field used in this research, the tillage decision is deep tillage (30 cm deep).

Six possible data flow methods (R_1, R_2, R_{3a}, R_{3b}, R_4 and R_5) were compared based on the percentage of error of the PD prediction using the ground truth data of the PD obtained from the laboratory analysis. All the errors were less than 25%, and the best method from the first set derived from the GTD was R_4, whilst the best RS method was R_5.

These results suggest that it is possible to use hyperspectral imaging to measure soil properties related to SC. The merit of using this method lies in the ability to cover large areas effortlessly. The HSC can be installed in a small tractor or utility vehicle to perform the field survey. If weather conditions are favorable, it is possible to obtain hyperspectral images from satellites. In addition, the PD results can be obtained faster in comparison with traditional sampling methods.

The main limitation of applying this method is that for fields with uniform soil conditions, the intention of adopting site-specific compaction management or PT cannot be achieved. In addition, the camera's image shooting speed is 7.7 seconds, limiting the rate at which images can be taken when a vehicle is adopted for data collection. Also, it is necessary to account for lighting conditions because the sunlight changes during the day. A calibration panel was adopted to account for light conditions, and the calibration procedure cannot be omitted. The effective depth of soil properties determination might be an issue since this study considered depths up to 0.30 m, and the prediction accuracy might change when deeper depths are considered. Given that there are different field vegetation conditions at the beginning of crop seasons, further research is needed for other field conditions to develop a RS device that can operate with hyperspectral imaging for real-time SC management.

CHAPTER 5. QUANTIFICATION OF SOIL COMPACTION EFFECTS ON WHEAT PRODUCTIVITY

5.1. Introduction

Soil compaction (SC) impedes crop root access to water, air, and nutrients, thus inhibiting plant development (Cambi et al., 2015; Hamza and Anderson, 2005). The compression of soil particles increases mass per unit volume, measurable through higher bulk density (BD) values (FAO, 2023a; Frene et al., 2024; Peralta et al., 2024). Previous studies (British Columbia Ministry of Agriculture, 2015; Kopittke et al., 2019; Zhang et al., 2024) indicate that SC is a significant issue across various agricultural regions, with substantial yield shortfalls in high-input farming systems. Furthermore, SC is considered to contribute approximately 6% to as much as 50% of worldwide crop yield drops, depending on the region and farming practices involved (Jamali et al., 2021; Shaheb et al., 2021).

Most research focuses on specific effects of SC on crop productivity (Liu et al., 2022; Yu et al., 2024), resulting in uncertainties about comprehensive nutrient dynamics. Some research works have examined nutrient deficiencies (Sun et al., 2024) and root growth responses (Yu et al., 2024). However, there is limited research about how SC influences overall nutrient accessibility (Ishaq et al., 2001; Islam et al., 2014). Understanding nutrient accessibility under varying SC levels is necessary for boosting crop yields and improving sustainable agricultural practices.

Site-specific SC management, a subfield of PA, involves precisely identifying and mapping areas within a field that exhibit various levels of SC. This approach allows farmers to address compaction issues by targeting specific zones with tailored tillage practices known as precision tillage (PT). While various methods have been used to study soil-plant interactions, such as root growth imaging, nutrient uptake assessment through tissue analysis, yield-nutrient relationship studies, and weather impact correlations, these methods often overlook spatial variability in SC and its impact on nutrient dynamics. There is inadequate evidence for a unified model that effectively predicts yield variations across different SC levels.

This chapter investigates site-specific SC by varying the BD of subplots to evaluate PT within the framework of PA. The study established four distinct compaction treatments alongside a control subplot to assess how varying levels of SC influence wheat growth and resource use. This setup enabled the evaluation of how initial soil BD affects *Triticum aestivum* L. yield and nutrient use efficiency.

To achieve these goals, this research investigated the effects of initial SC variations on wheat crop soil nutrient access and yield. This was achieved by taking ground truth data (GTD) to examine the degree of impact of SC levels in terms of BD on soil properties, crop growth properties, and yield. Spatial analysis revealed that SC impacts multiple nutrient pathways simultaneously, demonstrating a non-linear relationship between compaction level and yield. Notably, a moderate SC level was identified as optimal for wheat productivity, providing compelling evidence for the relevance of PT strategies tailored to site-specific soil conditions.

5.2.Field preparation methods

The field preparation process started by marking out the perimeter of the 17x18.9 m experimental field. Then, the field was plowed with a rotary plow before completing the tillage process with two passes of a rotary harrower. A Nordsten row planter with a 2.5 m width (Kongskilde Industries, Denmark) was calibrated to ensure accurate seed and fertilizer application. This calibration was completed before initiating the planting process. A Cambridge roller (Sugano Ltd, Japan) was run once on the field as per the standard practice of wheat sowing in the Hokkaido region. This step enables a firm root system development of wheat crops. Furthermore, it is a measure to limit the evaporation of soil moisture, hence, it is very necessary for the growth of wheat (Dierauer, 2017). Table 5.1 contains the technical data of the machinery involved in the sowing and the initial soil conditions measured through standard laboratory processes.

Table 5.1: Initial soil conditions and machinery details

Parameter	Data	Remarks
Tractor for Plowing	Weight: 1880 kg Speed: 6 km/h	Massey Ferguson MF5608
Depth of plow/harrow	0.3 m	Uniform tillage level
Cambridge roller	Weight: 25 kg per piece	25 rings in a row
Planter	11-row planters	Mechanical system
Initial moisture content-dry basis	22%	-
Initial moisture content-wet basis	18.1%	-
Initial organic matter	3.4%	-
Initial bulk density	1.18 g/cm^3	-
Initial cone reading	2.9 g/cm	-
Initial clay content	20.6%	-
Initial sand content	39.8%	-
Initial silt content	39.7%	-
Seed	120 kg per ha	Spring wheat
Fertilizer	70 kg per 4 ha (10-18-12-5)	Bulk blended (N-P-K-Mg)

The field compaction treatment for this experiment has been clearly described in Section 3.1.1.2 of Chapter 3. Figure 5.1 illustrates the 5 different levels of BD associated with the various SC treatments. The vibratory plate compactor was used four times over the more compacted subplots, whereas it passed only once over the less compacted subplots. It was not applied in the Control subplots, establishing distinct BD treatments. The compactor was operated on a wooden board placed on the soil surface to prevent the compactor from sticking to the soil and to make the compaction as uniform as possible along each subplot of land. This field-based approach captured the soil's actual response to mechanical loading, which cannot be effectively reproduced in computer simulations.

The SC methodology used in this study was designed to realistically simulate soil conditions resulting from short to long-term farm machinery traffic on a piece of field. Using 1 to 4 passes of the vibratory plate compactor, a gradient of compaction types was established (shown in Fig. 5.1), producing incremental BD rises of 1%, 5%, 1%, and 4% for 0-1, 1-2, 2-3, and 3-4 passes, respectively. These incremental changes closely reflect field observations under typical machinery traffic. This non-linear response aligns with literature, which shows the highest compaction changes occur in the first few passes, with reducing effects thereafter (Hamza and Anderson, 2005; Nawaz et al., 2013). The single-season design depicted a broad range of compaction levels, reflecting the range typically seen over multiple seasons, thus providing vigorous and field-relevant data on soil-plant interactions across compaction gradients.

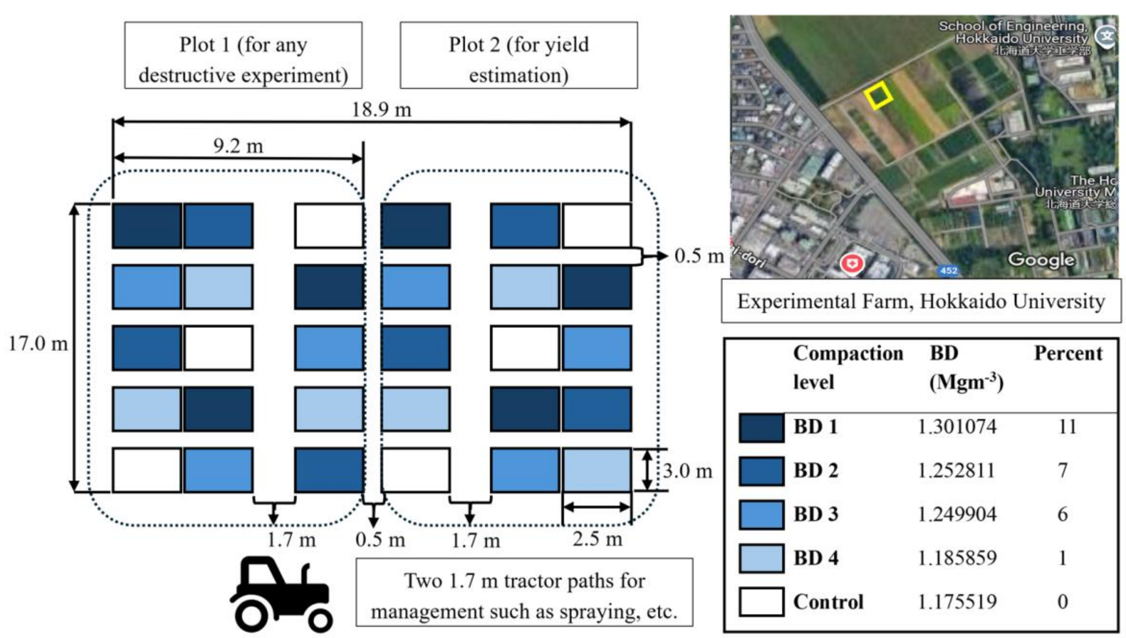

Figure 5.1: Study field location and layout for spring wheat

The study field included two 1.7 m-wide tractor traffic paths and 0.5 m-wide walking paths to facilitate easy management and the application of pesticides and herbicides without disturbing the SC treatments. Figure 5.1 shows the tractor traffic paths as vertical gaps. The walking paths appear as horizontal gaps and as the central vertical gap between the colored rectangles. In Figure 5.1, the subplots of land with a dark blue color indicate the hardest SC level. The hardness level decreases as the blue color fades to white, representing the Control subplot. The hardest subplot is denoted BD1, with BD2, BD3, and BD4, respectively, having their compaction level decrease accordingly as indicated in the legend on Figure 5.1. On the top right side of Figure 5.1, the satellite image (Google Maps, 2025) shows the study field location. It can be observed that the study field is not too close to the road on the north side. There are a total of 30 subplots, each subplot measuring 2.5 x 3.0 m. Therefore, there are 6 subplots for each compaction treatment.

5.2.1. Data collection and processing methods

The data collection started 10 days after planting with the initial seedling emergence count. This is because wheat crops in the Hokkaido region take 6 to 10 days to fully emerge (Kazuto, 2009; NARO, 2017). The number of seedling rows that emerged on each subplot was counted. Rows with at least three visible seedlings above the soil were counted as an emerged row. This measurement exercise was conducted until no more rows were emerging. This data is summarized in Figure 5.2 (a). The legend BD1 represents the average data from all six BD1 subplots. The same applies to all the other BD treatments. To differentiate between the early development levels among the various subplots, the crop population count per square meter was performed at the end of the emergence count exercise (Bradley et al., 2008). This was 17 days after planting, and the results are plotted in Figure 5.2 (b). The total rows per subplot are approximately 20 rows, and by the 12th day after planting, the Control subplots and the BD4 subplots had at least 3 seedlings emerging in every row, whilst BD3 and BD2 subplots took one extra day to show comparable results. All BD1 subplots, which were the hardest, took about 15 days after planting to have all rows emerge. The data plot in Figure 5.2 (b) clarifies the developmental status of crops on each subplot by showing the average number of crops per square meter for each subplot of land. Although the rows had emerged, the average crop population results show that BD1 and BD2 had less crop population compared to the Control and BD4, which is the softest, with BD3 having the highest average crop population.

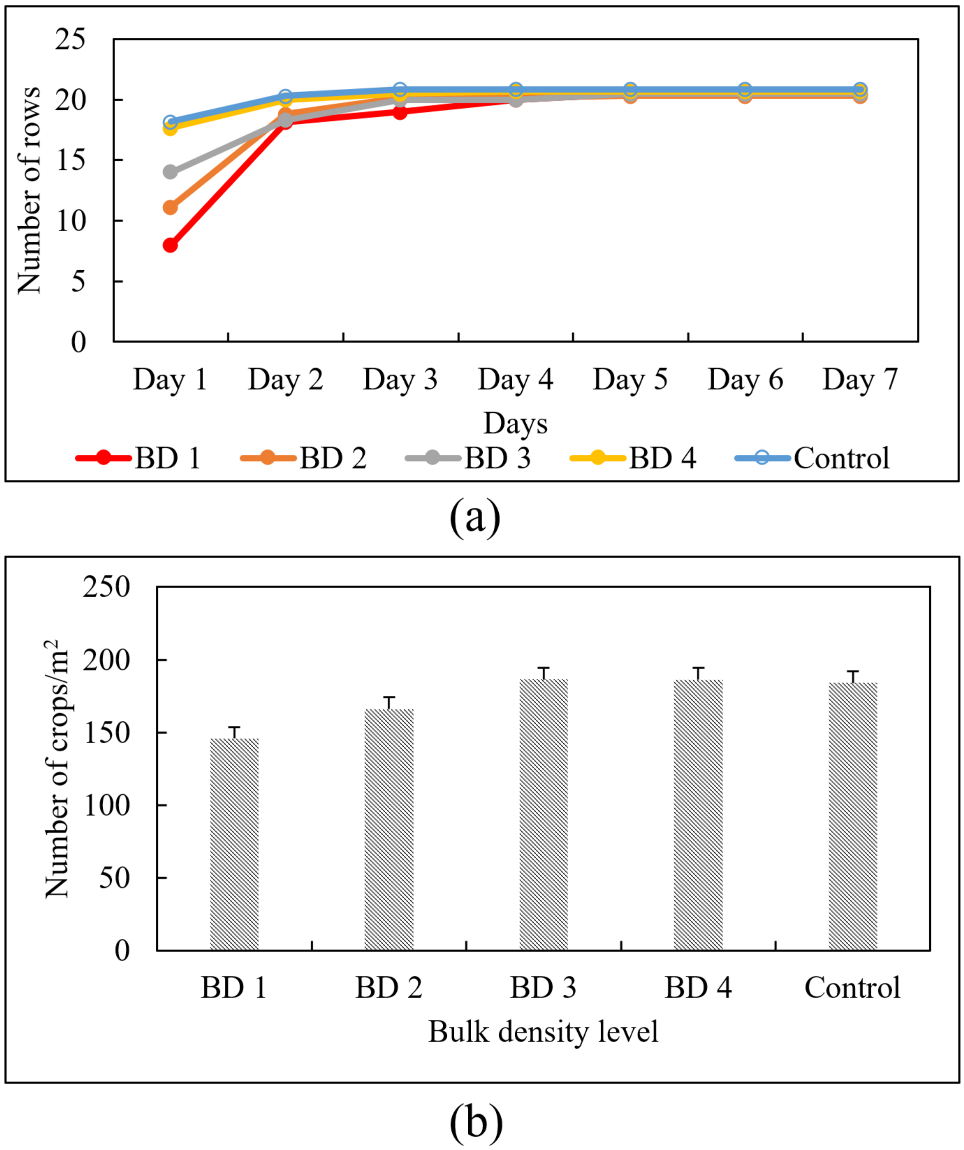

Figure 5.2: (a) Seedling emergence count per day, (b) Initial crop population per m^2

The data collected throughout the experimental process have been grouped into four categories: soil physical properties, crop growth data, soil chemical properties, and absorbed macronutrient content in crop biomass. The data collection was done at five different growth stages, illustrated in Figure 5.3, spanning from 5 to 10 weeks after planting. The wheat development per stage diagram in Figure 5.3 was adopted from previous research (White and Edwards, 2007).

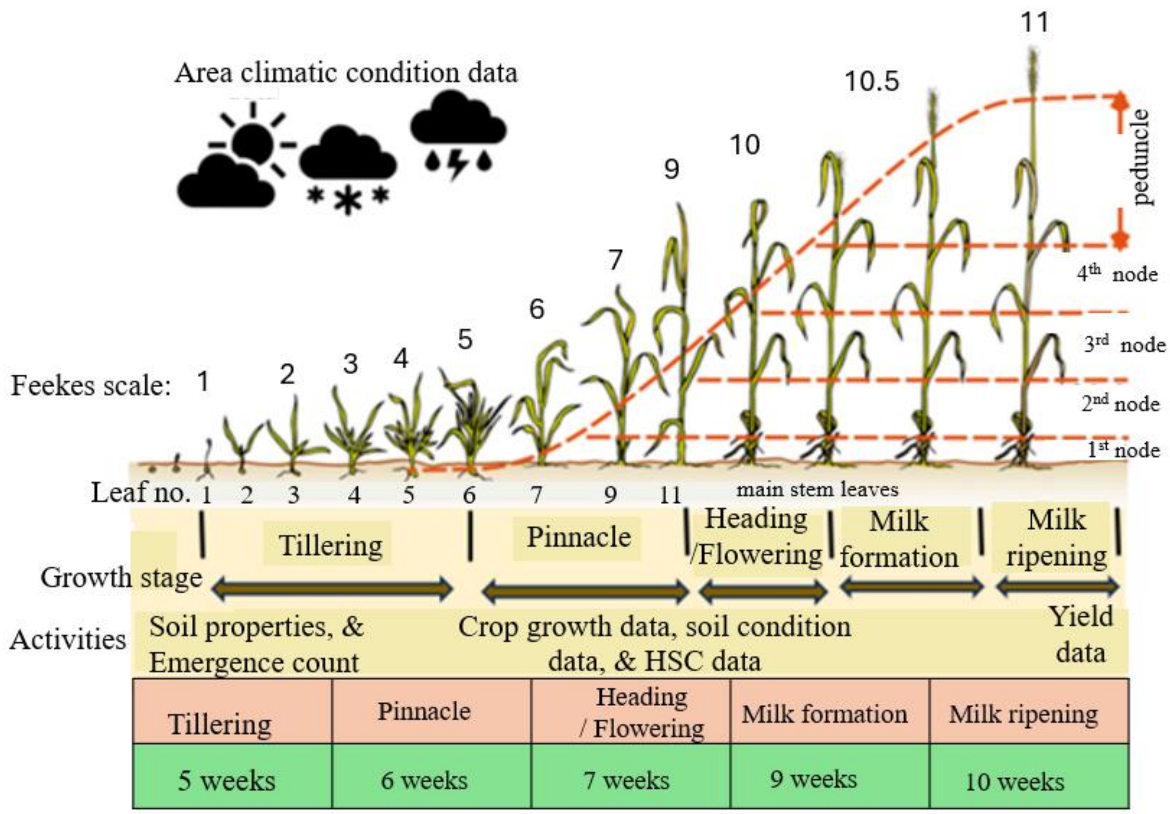

Figure 5.3: Wheat growth stage and activity chart

From Figure 5.3, the first stage was the Tillering stage, followed by the Pinnacle stage, Heading/Beginning of flowering stage, Milk formation stage, and Milk ripening stage (Bradley et al., 2008; Wise et al., 2024). Soil physical properties data, and crop growth data were taken at all the growth stages, while soil chemical properties data and absorbed macronutrient content in crop biomass were taken at the Heading/Beginning of flowering stage. The Feekes growth scale in Figure 5.3 is used in different countries to describe specific morphological changes in wheat development. The weeks refer to the time elapsed since planting. Figure 5.3 also illustrates the leaf count that is used in conjunction with the time in weeks to estimate the growth stage for wheat. The number of nodes is also illustrated, which is used to verify the approximate height of the plants. Note that the fourth node should be evident after 9 weeks. Although intuitive, it is important to note these parameters to assess the different development rates in different subplots of land (BD1 to Control).

The observed developmental stages consistently aligned with the Feekes growth scale throughout the experiment. The Tillering process was at its optimum stage in week 5, corresponding to Feekes scale 2 to 5. This began with the emergence of the first tiller from the axil of the first leaf, Feekes scale 2, and continued until tillers were fully formed. By the end of week 5, leaf sheaths were strongly erected, and tillers were fully developed, though stem elongation had not yet begun. The Pinnacle stage at week 6 corresponds to Feekes scale 6 to 10, starting when the first node becomes visible at the base of the shoot around the beginning of week 6, corresponding to Feekes scale 6. The stem rapidly elongates as additional nodes appear above the soil surface at Feekes 7 to 8. This stage concluded when the head was fully developed at the Feekes scale 10, but remained enclosed within the flag leaf sheath. Heading/ Beginning of flowering occurred at week 7, corresponding to the Feekes scales 10.1 to 10.52. This stage began as the head emerged from the flag leaf sheath at the start of week 7. Flowers first appeared at mid-head, Feekes scale 10.51, and continued to develop until flowering concluded by the end of week 8. Milk formation was observed in week 9, corresponding to the Feekes scale 11.1 to 11.5, while Milk ripening occurred in week 10, corresponding to the Feekes scale 11.4 in this experiment. The timing of these developmental stages can vary based on environmental conditions, particularly daily temperature accumulation and total sunshine per month. Figure 5.4 shows the environmental conditions during this experiment. While these stages represent typical progression for spring wheat under these specific conditions, actual development varied slightly between treatments due to SC impact.

5.2.1.1. *Soil physical properties*

The initial soil BD, MC, OMC, soil texture, and cone index readings were conducted between the field preparation and planting period. These results are included in Table 5.1. In addition, further soil sampling was conducted on the 30th day after the SC treatment. The sampling depth was 0 to 0.3 m, and soil was collected at three depth ranges (0 to 0.1 m, 0.1 to 0.2 m, and 0.2 to 0.3 m) using soil ring samplers. This specific depth was chosen because about 70 percent of crop root biomass is within this range (Jackson et al., 1996). The extracted samples were used to determine the BD variation in the various subplots. These measured BD values for each subplot served as the baseline indicators for SC conditions. The reason is to imitate the concept of farming, where once crops are planted in the field, the SC is not manipulated through tillage again but only through other activities like rain droplets, evapotranspiration, etc. (Jeschke and Lutt, 2019; Shaheb et al., 2021). In that regard, the development and yield variations in the field are linked with the initial BD level/tillage practice.

Soil physical properties that rapidly change with time, such as MCD, MCW, VMC, and soil temperature, were measured at every growth stage to understand the effect of BD variation on these properties and the crop. Firstly, the standard laboratory procedures for the determination of these properties were followed according to a laboratory procedure guide (Motsara et al., 2008). A calibrated JXBS-500 soil sensor was utilized for a rapid soil moisture measurement. As a rule, data on soil physical properties were collected only when the soil was well-drained (approximately 2000 kPa penetration resistance). Specifically, measurements were taken using the guide of a cone penetrometer about 72 hours after a heavy downpour and about 48 hours after a light downpour of rain. This is in line with the standard practice regarding the use of farm machinery in fields after rain (US Department of forest service, 2022). The prevailing weather and climatic conditions during the period of the experiment, obtained from the Japan Meteorological Agency (2024), are illustrated in Figure 5.4 below.

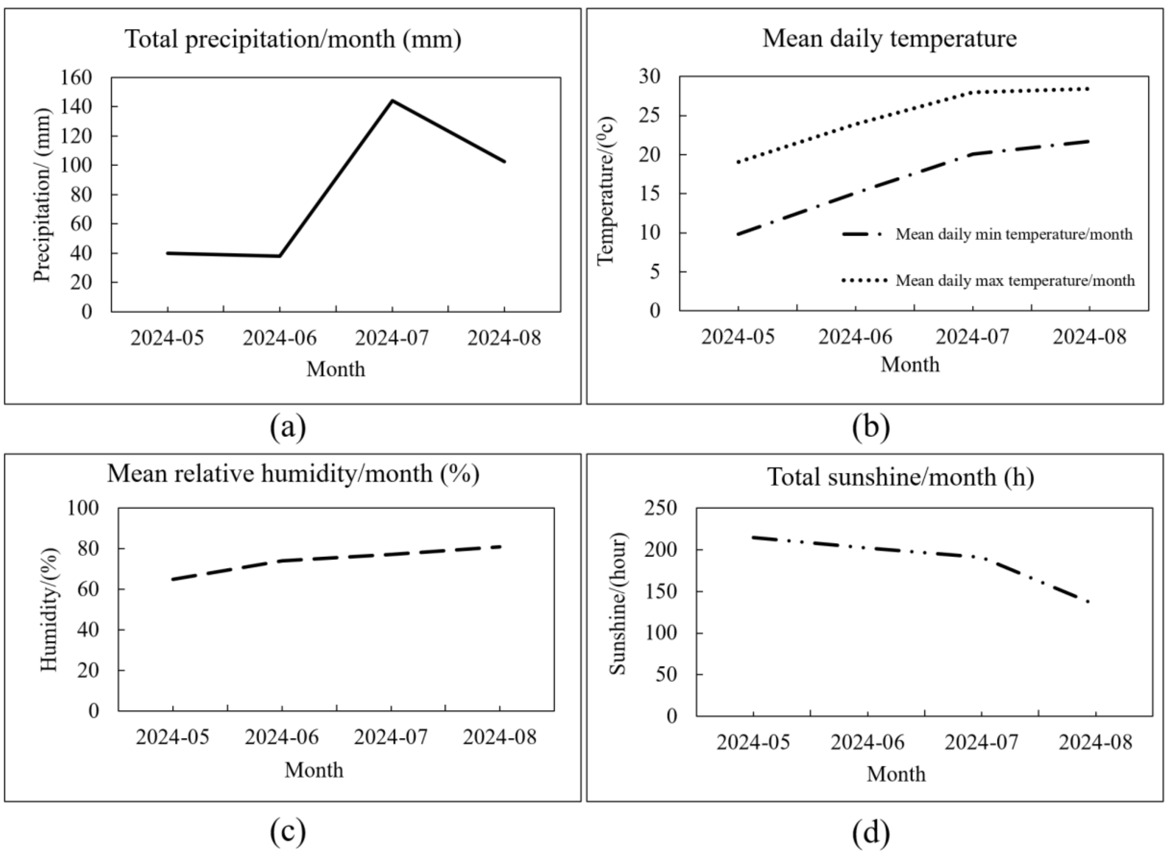

Figure 5.4: Climatic conditions data at Sapporo city (Sapporo WMO station ID-47412)

Figure 5.4 (a) indicates the total precipitation record in mm per month; it is evident that the total rainfall for May and June 2024 was about 50 mm, with the highest rainfall recorded in July 2024. The precipitation during the early growth stages in May and June 2024 was relatively low. Typically, spring wheat requires at least 70 mm of rain in a month under rainfed conditions at the Tillering stage for optimal development (Abayomi and Wright, 1999). Figure 5.4 (b) illustrates the average daily temperature records in degrees Celsius per month. The minimum and the maximum average daily temperature increased as the summer sun radiation increased, with a temperature range of 9.8 to 28.4 degrees Celsius. Figure 5.4 (c) presents the mean relative humidity in percentage per month, evidencing a mean humidity of 65 to 81%. Figure 5.4 (d) displays the total sunshine in hours per month, indicating that the total sunshine per day in a month was 214.6 h in May 2024 and reduced moderately every month to 155.7 h at the end of the experiment.

5.2.1.2. *Crop growth data*

Crop growth and development monitoring started as soon as the seedlings emerged. The first data collected were the average crop emergence count per subplot and the crop population per m², as described in Section 5.2.1 and Figure 5.2. The rate of crop and root growth per subplot was recorded as the relative growth rate of crops (RGR-Crop) and relative growth rate of root (RGR-Root) using Eq. 5.1. RGR was measured by gently uprooting a 0.5 x 0.5 m area of wheat crops at each growth stage and cleaning the soil from the roots, then separating the roots from the vegetative parts. The fresh mass of roots and vegetative parts was weighed and recorded before drying the plants at 60 degrees Celsius to a constant weight (Bhayal et al., 2022; Liu et al., 2022; Sun et al., 2021). The RGR-Crop and RGR-Root were calculated using Eq. 5.1. Additionally, Eq. 5.2 was applied to determine crop biomass moisture content (Crop-MC).

$$RGR = \frac{\ln m_2 - \ln m_1}{d_2 - d_1} \tag{5.1}$$

$$Crop - MC = [(m_w - m_d)/m_w] \times 100 \tag{5.2}$$

In Eq. 5.1, m_2 is the mass of the dried crops' vegetative parts or roots at the current growth stage. Also in Eq. 5.1, d_2 is the number of days from planting to the current growth stage. Similarly, m_1 and d_1 are the parameters from previous growth stages. In Eq. 5.2, m_w is the fresh mass of crops' vegetative parts, while m_d is the dried mass of crops' vegetative parts.

Crop development, in terms of health and greenness, is a key parameter for evaluating the status of field crops. Chlorophyll content was assessed using a SPAD chlorophyll meter (SPAD-502Plus, Konica Minolta Sensing Singapore Pte Ltd., Singapore). Ten random top leaves were measured from each subplot at every growth stage. The crop height in each subplot, influenced by different BD treatment levels, was measured and recorded at each growth stage using a measuring tape.

5.2.1.3. *Soil chemical properties and crop tissue nutrient content*

For this experiment, soil phosphorus (P), potassium (K), calcium (Ca), and magnesium (Mg) content, in addition to pH and cation exchange capacity (CEC), were considered as the soil chemical properties of interest. This decision is in line with advice from wheat growth guidelines (Gelderman and Lee, 2019; Jones, 2015; Paulsen et al., 1997; Wise et al., 2024). The total nitrogen (Total-N), P, K, Ca, and Mg content were also considered when measuring the absorbed macronutrient levels in crop biomass.

Soil samples from 0 to 0.3 m depth and crop biomass samples were collected at the Heading/Beginning of the flowering stage; which is a critical growth stage for wheat based on both the measured SPAD result trend depicted in Figure 5.5, and the cumulative nutrient uptake data reported by previous research (Jones, 2015; Paulsen et al., 1997). For each subplot treatment, 200 g of soil and 150 g of crop biomass samples were prepared and sent to the Tokachi Agricultural Cooperative Association Chemical Research Institute in Obihiro, Hokkaido, Japan, for analysis. The measure of P, K, Mg, and Ca was in their oxide form, which is P_2O_5, K_2O, MgO, and CaO, respectively, and is the form that crops access these nutrients (Pandey et al., 2020; Paulsen et al., 1997). The reporting of P, K, Mg, and Ca as their oxide forms in soil testing is rooted in historical chemistry practices and fertilizer industry conventions. Thus, most wet chemistry laboratory methods often convert nutrients into oxides during testing. This is to conform with fertilizer grades like NPK ratios, which are usually labeled as %N-%P_2O_5-%K_2O, and to help standardize nutrient content globally. Soil test results using nutrient oxide forms allow for direct and easy comparison with fertilizer recommendations for farmers (Sandhya et al., 2023).

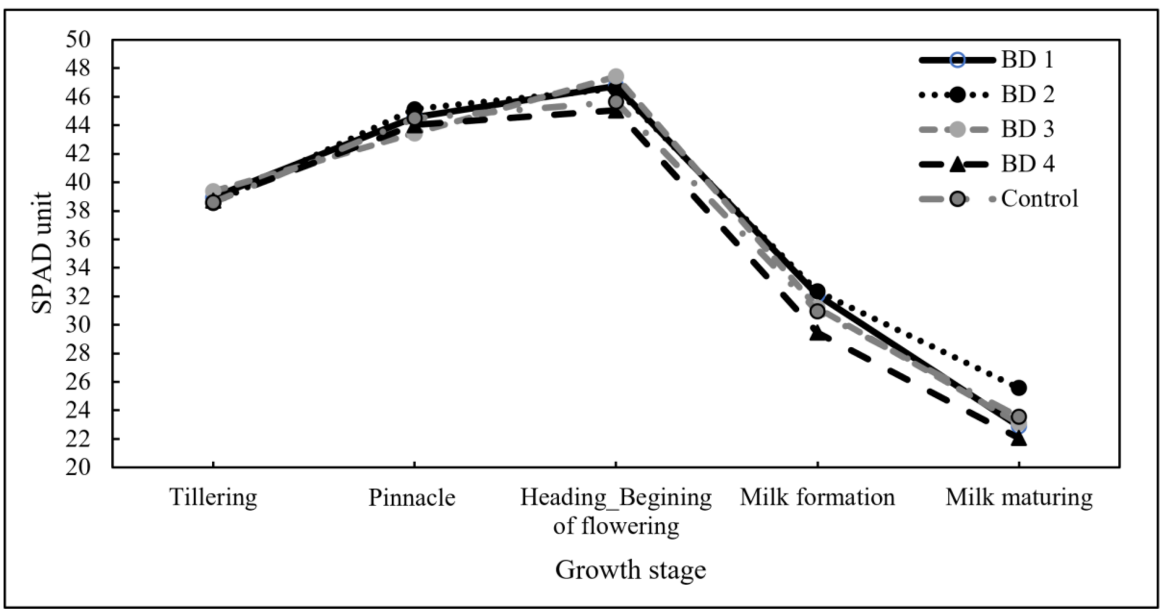

Figure 5.5: Measured crops leave SPAD trend

A critical review of extensive documentation on wheat growing by (Gelderman and Lee, 2019; Jones, 2015; Wise et al., 2024) suggests that mid-season soil sampling during the

Heading to Flowering stages, which corresponds to the Feekes scale 9 to 10.5, is effective for detecting nutrient deficiencies in wheat. Wheat plants undergo rapid development during this critical growth stage and have increased nutrient demands. By the end of the heading and flowering stages, over 70% of the total above-ground nitrogen (N) and phosphorus (P) have accumulated. Additionally, approximately 55% of the nitrogen and phosphorus found in the grain is derived from the redistribution of these accumulated nutrients. Lower leaves may die during Milk ripening because nutrients stored in the lower leaves move to the grain. This phenomenon of critical growth stage described above was evident in Figure 5.5, the highest SPAD readings recorded were at the Heading/Beginning of flowering growth stage, after which the level dropped below the levels recorded in the first two growth stages.

The increasing SPAD values from Tillering through the Heading/Beginning of flowering in Figure 5.5 indicate robust chlorophyll accumulation as the crop enhances its photosynthetic capacity. The maximum SPAD value at the Heading/Beginning of flowering represents optimal chlorophyll content, coinciding with the crop's transition from vegetative to reproductive growth.

The substantial decrease in SPAD readings in Figure 5.5 during Milk formation and Milk ripening reflects the natural senescence process. During the Milk formation stage, wheat plants remobilize nutrients from vegetative tissues to developing grains, resulting in chlorophyll degradation and lower SPAD values. Trends in Figure 5.5 demonstrate efficient chlorophyll dynamics and nutrient remobilization from vegetative to reproductive structures, which is a key trait for grain yield. The steep decline of approximately 50% from the Heading/Beginning of flowering to Milk ripening highlights significant nutrient translocation to the developing grains. Table 5.5 summarizes the trends and impact of SPAD values across subplots, with detailed analysis provided in Section 5.3.1.

5.2.2. Data analysis

GTD collection is schematized as step 1 on the top left side of Figure 5.6. The collected data were organized into individual subplots and then processed to understand the trends and patterns, as shown in the second step on the left side of Figure 5.6. A total of twenty-six distinct properties were recorded, each with a minimum of three replicates, across five growth stages for the thirty subplots shown in Figure 5.1.

The data was organized and processed using the libraries Matplotlib version 5.8.4, SciPy version 1.15.1, Seaborn version 0.15.2, Scikit-learn version 1.4.2, NumPy version 1.26.4, and Pandas version 2.2.2 in Python version 5.12.5. The ANOVA p-value and Kruskal-Wallis's H-statistic analysis methods were employed to understand the dependency of the different data collected on the BD treatment across the five growth stages, as shown in the third step on the left side of Figure 5.6To better understand the changes observed during wheat growth, the correlation between each subplot's initial BD and the measured properties across all growth stages was also examined at this step. Properties across the growth stages that were strongly affected or influenced by the initial subplot's BD treatment were identified, and a further assessment of these properties on wheat crop yield was conducted. The partial least squares regression (PLSR) method with leave-one-out and 5-fold cross-validation techniques was utilized in selecting the best features from the measured properties (Wold et al., 2001). In addition, PLSR, multilinear regression (MLR), and linear regression (LR) suitability for a simple final yield prediction were assessed, using the influential properties by following the third step through to the fifth step illustrated in Figure.5.6. The influential properties, original yield data, and the predicted yield data were used in the ArcGIS ArcMap (ESRI ArcGISTM version 10.7.1, 2019, CA, USA) application to develop their respective data maps as seen on the fifth step of Figure 5.6. The HSC data collection and processing methods described in Sections 3.4.1.3 and 3.4.1.4 were used to establish the RS dataset. Additionally, the map generation methodology outlined in Section 3.4.2 (all in Chapter 3) was applied to facilitate a comprehensive interpretation of the study results.

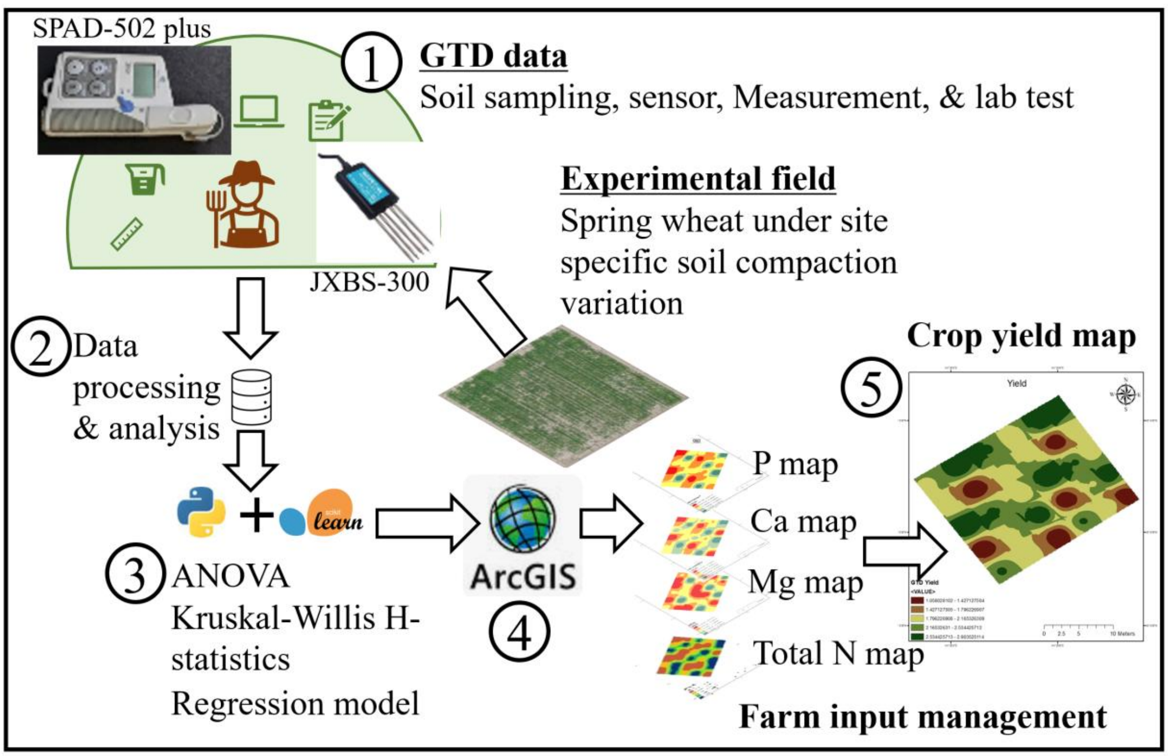

Figure 5.6: Research flow diagram

5.2.3. Yield assessment

Crop yield in tons per hectare was calculated by harvesting a one-meter square area of wheat on each subplot and applying Eq. 5.3 (Martin et al., 2011). This study examined yield variations across different subplots by assessing the effect of initial BD treatment on soil-plant interactions. The analysis included variations in all property groups to identify which had the greatest impact on yield in tons per hectare.

$$Crop\ yield(\frac{ton}{ha}) = (A \times B \times C)/10000 \tag{5.3}$$

Where A is the average number of pods/ m^2, B is the average number of grains per pod, and C is the average weight of 100 grains of wheat.

5.3.Results and discussion

5.3.1. Soil and crop growth data profile

The initial BD treatment, established as outlined in Section 5.2, and the resulting SC levels measured at three depths are summarized in Table 5.2. SC, which is associated with BD and cone penetration resistance (Beylich et al., 2010; Dörner et al., 2022; Reintam et al., 2009), was the variable adjusted in this study. Its effect on crop yield may help justify the need for a specific level of tillage. The field-level SC methodology using controlled vibratory plate compactor passes (1-4) provided realistic soil-load response data in Table 5.2. This approach revealed actual soil behavior under compaction forces, offering insights that computer simulations typically cannot capture due to the complex interactions between soil particles, moisture, and organic matter.

Table 5.2: Average initial bulk density treatment for the study (bulk density $\pm$SD)

Compaction level	0-0.1 m	0.1-0.2 m	0.2-0.3 m	Mean 0-0.30 m	Percent
BD 1	1.274±0.03	1.254±0.07	1.374±0.03	1.301	11
BD 2	1.276±0.04	1.236±0.03	1.246±0.04	1.253	7
BD 3	1.290±0.06	1.225±0.06	1.235±0.07	1.2499	6
BD 4	1.191±0.07	1.180±0.05	1.187±0.06	1.1859	1
Control (C)	1.208±0.05	1.147±0.06	1.172±0.08	1.1755	0

From Table 5.2, the Control, BD4, and BD3 plots had their highest BD at the top 0.1 m section, with 3%, 0.34%, and 4.45%, respectively, being the difference in BD between the top section and the bottom section of the soil. BD1 exhibited its highest BD in the bottom section, whereas BD2's peak density occurred in the top section, displaying a pattern similar to the lower three BD levels (BD3, BD4, and Control). "All plots exhibited relatively lower BD in the mid-section of the soil profile compared to both the top and bottom sections. This pattern can be attributed to the compaction mechanism of the vibratory plate compactor, which typically exerts uneven pressure distribution through the soil profile. Since about 70 % of crop roots are within the top 0.3 m of soil depth (Jackson et al., 1996). The mean BD in the fifth column of Table 5.2 was used as the compaction level indicator for this research, hence, all the other properties measured were evaluated against the average BD.

To understand the influence of the initial BD levels on the spring wheat growth, the data groups described in Section 5.2.1.2 were monitored, measured, or assessed and the results are displayed in Table 5.3 and Table 5.4. Table 5.3 covers data that was captured across the five growth stages, while Table 5.4 lists the data that was taken at the Heading/Beginning of flowering stage, which was the peak nutrient demand growth stage, explained with the record of the SPAD levels in Figure 5.5.

Table 5.3: Average soil and crop growth data across growth stages

Growth stage	BD	MCD (%)	MCW (%)	VMC (%)	pH	TEMP (^{0}C)	SPAD	RGR-Crop (g/d)	RGR-Root (g/d)	Crop-M (%)	Height (m)
Tillering	BD1	19.21	16.03	24.99	6.4	29.7	38.9	0.10	0.09	77.27	0.180
	BD2	24.03	19.33	30.11	6.6	28.9	38.5	0.10	0.09	77.60	0.193
	BD3	21.61	17.54	27.02	6.7	32.3	39.4	0.09	0.08	76.42	0.197
	BD4	23.24	18.82	27.56	6.6	29.3	38.7	0.10	0.09	78.70	0.195
	C	21.70	17.75	25.51	6.8	29.9	38.6	0.11	0.09	77.58	0.192
Pinnacle	BD1	15.03	5.48	5.81	6.4	30.6	44.6	0.13	0.13	70.66	0.330
	BD2	17.82	6.47	6.84	6.7	30.6	45.1	0.11	0.13	66.43	0.338
	BD3	14.42	5.26	5.58	6.6	30.6	43.4	0.14	0.17	70.95	0.342
	BD4	25.08	9.07	9.53	6.4	30.3	44.0	0.13	0.14	68.14	0.335
	C	20.47	7.42	7.83	6.6	30.6	44.5	0.10	0.17	70.75	0.361
Heading/ Before flowering	BD1	27.97	10.11	10.61	6.6	31.8	46.8	0.07	0.01	56.52	0.515
	BD2	28.95	10.46	10.97	6.4	32.2	46.6	0.06	0.02	52.43	0.517
	BD3	26.58	9.61	10.09	6.4	32.2	47.4	0.10	0.04	56.03	0.498
	BD4	27.42	9.91	10.40	6.5	32.2	45.1	0.06	-0.02	54.80	0.516
	C	30.15	10.89	11.42	6.3	32.5	45.6	0.07	-0.04	51.07	0.500
Milk formation	BD1	25.51	9.23	9.69	6.9	36.0	32.1	0.02	-0.05	59.29	0.770
	BD2	28.04	10.13	10.64	6.7	35.0	32.3	0.03	-0.03	61.54	0.764
	BD3	25.66	9.28	9.75	6.7	34.5	31.2	0.00	-0.07	57.52	0.767
	BD4	23.38	8.46	8.90	6.8	34.7	29.5	0.03	0.00	57.89	0.753

Growth stage	BD	MCD (%)	MCW (%)	VMC (%)	pH	TEMP (^{0}C)	SPAD	RGR-Crop (g/d)	RGR-Root (g/d)	Crop-M (%)	Height (m)
	C	27.83	10.06	10.55	6.8	35.3	30.9	0.03	-0.01	59.74	0.720
Milk ripening	BD1	15.03	5.48	5.81	6.7	28.1	22.9	-0.02	0.05	60.19	0.732
	BD2	17.82	6.47	6.84	6.6	28.4	25.6	-0.01	0.01	58.18	0.746
	BD3	14.42	5.26	5.58	6.6	27.3	23.1	0.01	0.06	52.83	0.749
	BD4	25.08	9.07	9.53	6.6	29.0	22.1	-0.02	-0.01	56.89	0.741
	C	20.47	7.42	7.83	6.8	28.9	23.5	-0.03	-0.01	54.37	0.737

The result for the properties under each BD treatment is the average value for the six replicated subplots that represent each BD. The averages of the results observed from the experiment indicate the moisture content of the subplots at different growth stages. Generally, soil moisture of 50 to 70% of field capacity, which corresponds to about 25 to 35% moisture content dry basis, should be maintained for optimal wheat growth, with a variation of about ±10% across different growth stages (Panda et al., 2003; Sela, 2024). The results in Table 5.3 show that all the subplots had an adequate supply of moisture compared to previous research (Panda et al., 2003), even though the hardest subplot had lower moisture levels for most of the growth stages. Hence, the key influencing factor is root access to moisture. The most critical stage when it comes to root development is the Pinnacle stage, about 6 weeks after planting (Kirby, 1985). At this stage, BD3 and Control subplots had the highest RGR-Root of 0.17 g/day, followed by BD4 with 0.14 g/day. The BD1 and BD2 subplots, which are the top two hardest subplots, had 0.13 g/day. When the level of crop development at a particular stage is not achieved, crops usually try to make up for the shortfall, therefore resulting in allocating valuable resources meant for the growth of other parts, yield penalties, timing mismatch, altered root architecture, and reduced nutrient-use efficiency (Hadir et al., 2024; White and Kirkegaard, 2010; Zhou et al., 2022). The soil pH recorded in this experiment, as shown in Table 5.3, ranges from 6.3-6.9. This checks with the ideal soil pH for wheat cultivation, which typically ranges from 6.0 to 7.0, with some studies suggesting an optimum target of around 6.5 for the best growth and nutrient availability in wheat crops. Soil pH significantly affects nutrients such as N, P, and K, which are more readily available to plants at ideal soil pH levels (Warner et al., 2023). Lower pH levels, which are acidic soils, can lead to nutrient deficiencies, significantly affecting wheat growth and yield (Daba et al., 2021). Soil temperatures (Temp) that were measured were all above 30 degrees Celsius for all subplots during the peak of summer, which coincides with the Pinnacle to the Milk formation growth stages. The variance in soil temperature values in Table 5.3 is much more dependent on ambient weather conditions in Figure 5.4 than subplot BD variations. The critical stage for SPAD is from Tillering to Heading/Beginning of flowering, with BD1 rising from 38.9 to 46.8, BD2 rising from 38.5 to 46.6, BD3 from 39.4 to 47.4, BD4 from 38.7 to 45.1, and

Control rising from 38.6 to 45.6. These were all within the safe range of SPAD values (40 to 50), which indicates healthy growth (Yin et al., 2023), with BD3 having a relatively higher value. In terms of crop height, the maximum average mature height was observed at the Milk formation stage with BD1 having 0.77 m, BD2 with 0.764 m, BD3 with 0.767 m, BD4 with 0.753 m, and Control having 0.72 m. Note that the general height range for mature wheat is 0.60 to 1.20 m (Rankel, 2024). It is worth noticing that the height of the wheat on some of the subplots was reduced at the Milk ripening stage due to the weight of the grain, which caused the weaker and slender stems to bend. The reduction in crop height on BD1 is 5%, BD2 is 2%, BD3 is 2%, and BD4 is 1%, while the crop height on the Control subplot increased by 2%.

Table 5.4: Soil and crop nutrient data

Properties	**BD1**	**BD2**	**BD3**	**BD4**	**C**
CEC (me/100g)	29.9	30.2	30.8	29.8	29
Mg (mg/100g)	125.7	107.2	105.7	115.7	114.3
P (mg/100g)	22.8	21.6	21	21.4	20.5
K (mg/100g)	38.4	39	38.6	40.1	39.4
Ca (mg/100g)	565.1	559.9	548.1	552.5	539.2
Total N_d (%)	2.455	2.377	2.247	2.194	2.197
P_d (%)	0.317	0.313	0.298	0.263	0.282
Ca_d (%)	0.169	0.165	0.174	0.167	0.163
Mg_d (%)	0.128	0.117	0.121	0.11	0.11
K_d (%)	2.718	2.535	2.571	2.348	2.43
Total N_w (%)	2.018	1.988	1.87	1.816	1.818
P_w (%)	0.261	0.262	0.248	0.217	0.234
Ca_w (%)	0.139	0.138	0.144	0.139	0.135
Mg_w (%)	0.106	0.098	0.101	0.091	0.091
K_w (%)	2.234	2.12	2.139	1.943	2.01

From Table 5.4, the properties of keen interest are the Mg, P, Ca, and Total N_d. The reason for selecting these properties is justified in Section 5.3.3.1. The results in Table 5.4 are the levels of the various properties measured at the critical growth stage. The BD3 treatment subplot exhibited the lowest Mg concentration while maintaining the second-lowest concentrations of P and Ca, with values ranking just after the Control subplot. BD4 followed a similar pattern, ranking after BD3. This nutrient distribution pattern indicates that crops grown in the BD3, Control, and BD4 treatments had relatively higher access to available soil nutrients than those in the BD1 and BD2 treatments. The Total N_d, which is the total nitrogen content dry basis in the plant biomass at the Heading/Beginning of flowering stage, had somewhat higher concentrations in BD1 than the rest of the subplots, with the results trend being an increasing Total N_d content with an increasing BD level.

5.3.2. Soil compaction effect on soil and crop growth properties

The treatment dependency across growth stages is illustrated in Figure 5.7. The degree of dependency or effect assessment is captured in Figure 5.7 (a). The possible impact of initial BD treatment levels on the various properties across the five growth stages can be visualized in Figure 5.7 (b).

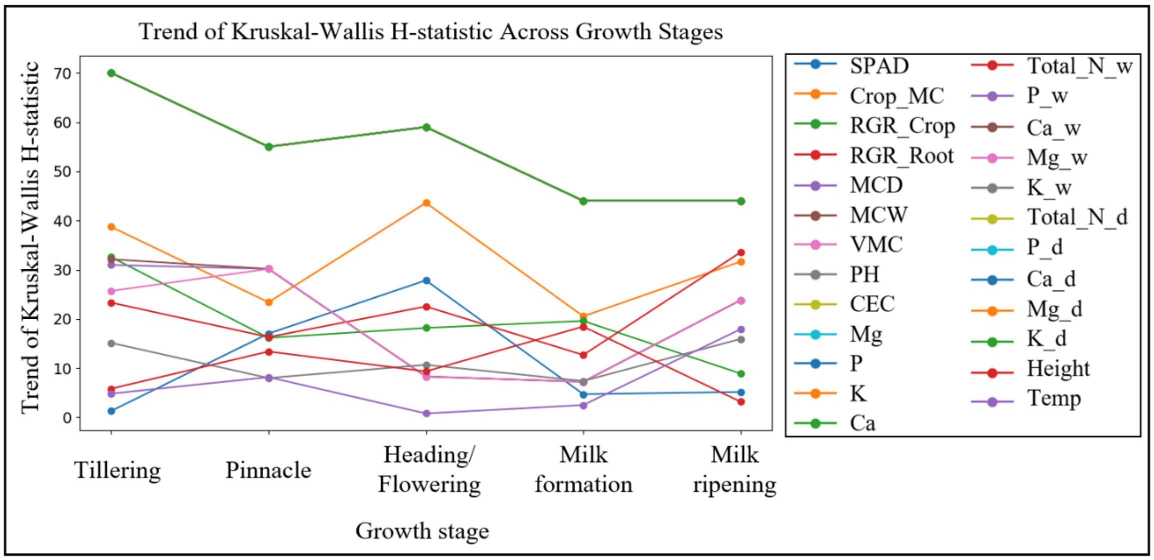

(a)

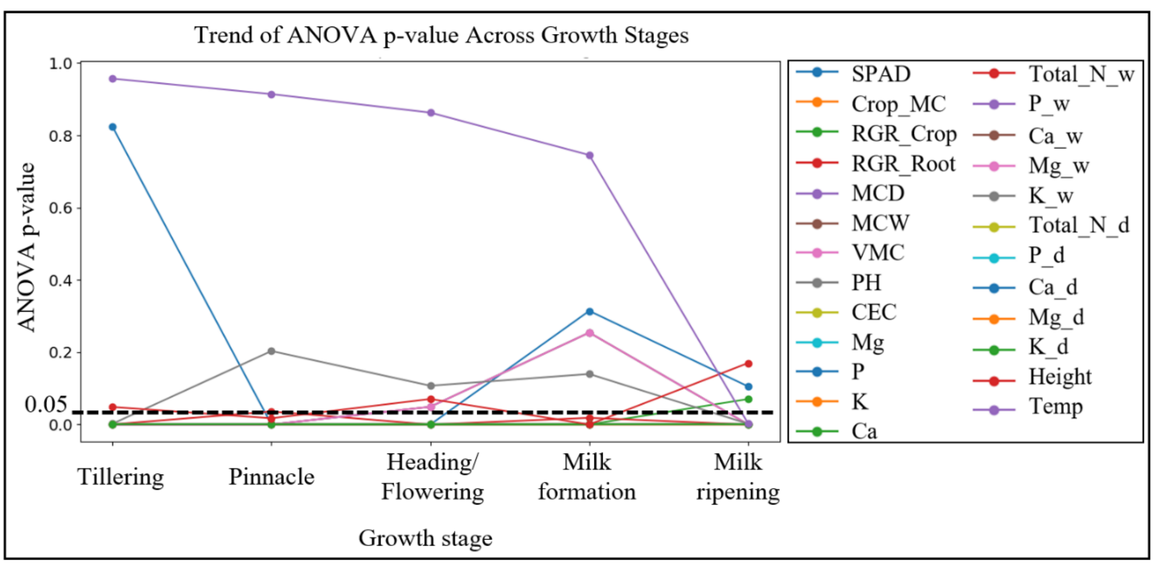

(b)

Figure 5.7: Plot treatment dependency across growth stages (a) Plot of Kruskal-Wallis H-statistic, and (b) ANOVA p-value

The measured level and content of most properties and crop data were influenced by subplot BD treatment at the Pinnacle stage (about 6 weeks after planting) to the Milk formation stage (9 weeks after planting), with most properties' p-values falling below the 0.05 mark, which is the threshold mark for destemming dependency, represented with a black dashed line as can be seen in Figure 5.7 (b). Some properties, like Temp, can be seen from Figure 5.7 as not dependent on BD treatment, whereas SPAD, height, and pH were also not reliant on BD at several growth stages.

Figure 5.7(a) shows that BD level strongly influences several properties: RGR-Crop, Ca, K_d, Crop-MC, K, Mg_d, P, Mg, Total-N_d, MCD, MCW, VMC, and RGR-Root. The variance in BD treatments explains the measured differences in these properties.

5.3.2.1. *Soil compaction effect*

To further evaluate how initial BD treatments affected the measured properties/variables, correlation analysis was performed between BD and all measured variables, with results displayed in Figure 5.8. The visualization organizes correlations into four distinct data groups (soil physical properties, crop growth data, soil chemical properties, and absorbed macronutrient content in crop biomass) to illustrate effects across different growth stages. Points that fall above the zero line mean that the concentration or the level was higher on highly compacted subplots and lower on the less compacted regions; that is, a positive correlation. Those below the zero line have lower concentrations or levels on highly compacted subplots and higher on less compacted ones, which means a negative correlation.

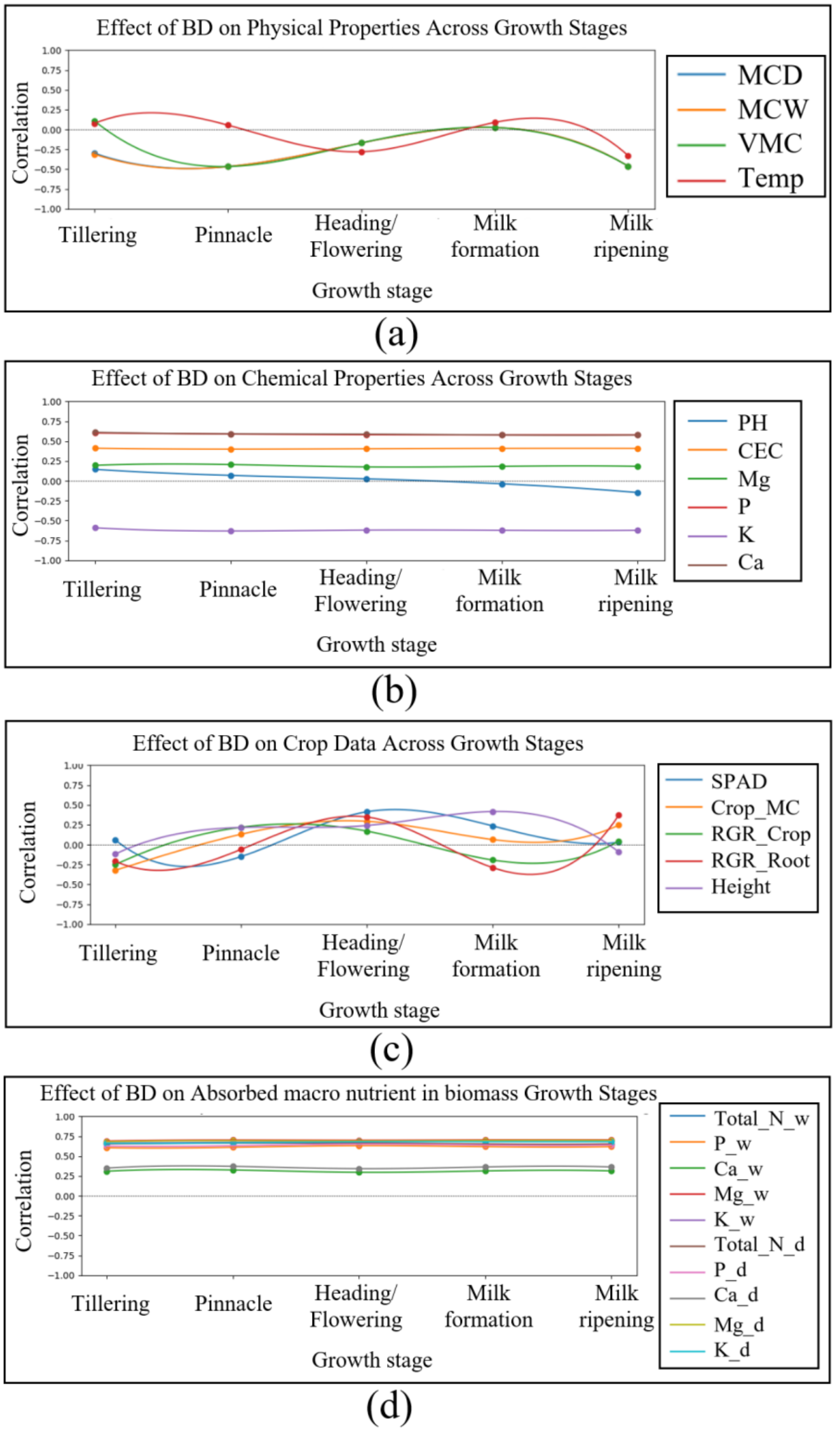

Figure 5.8: Effect of BD on measured properties (a) soil physical properties, (b) soil chemical properties, (c) crop growth data, and (d) absorbed macronutrient in biomass

The results in Figure 5.8 (a) show the soil's physical properties, such as the moisture content levels and the soil temperature across the growth stages. The expected effect of BD on moisture content is a higher level of moisture on soft subplots and a lower level of moisture on harder subplots (negative correlations). This effect was stronger at the Pinnacle and Milk ripening stages, and minimal at the Tillering stage. The limited precipitation period from May to June, shown in Figure 5.4, coincided with the critical Tillering and Pinnacle growth stages. This drought timing likely intensified the effects of SC treatments, as evidenced by the negative correlations observed during these stages and their impact on key growth parameters. By the Heading and Milk formation stages, although still negatively correlated, the compaction effect became nearly neutral, due to the fully developed crop canopy, which helped conserve soil moisture below the surface. The phenomenon of negative correlation of soil moisture content to BD was also reported previously (Liu et al., 2022; Romero-Ruiz et al., 2022). The Temp measured did not align with the BD treatment; it aligned more with the climatic conditions in Figure 5.4.

The overall trends in the results shown in Figure 5.8 (b) imply that the residual concentrations of P, Ca, CEC, and Mg were higher in highly compacted zones than in the less compacted ones (positive correlation). K was the opposite; it had a higher concentration on less compacted subplots of land than in the highly compacted ones. The effect of compaction variation on pH was almost neutral, with its variations aligning more closely with moisture levels rather than soil BD treatment. Previous research (Arvidsson, 1999; Frene et al., 2024) supports the fact that SC significantly decreases the rate at which crops access available soil nutrients, while another study (Long et al., 2024) reported a 12 to 35% reduction in various nutrient absorption rates, which subsequently affects crop development and yield.

The expected negative correlations between BD variation and crop data (SPAD, Crop-MC, RGR-Root, RGR-Crop, and height) were observed at different growth stages for each parameter, as shown in Figure 5.8 (c). Most crop data exhibited positive correlations during the Heading and Milk ripening stages, whereas the Tillering stage showed more properties with negative correlations. The RGR-Root was lower in compacted soils compared to less compacted soils during the Pinnacle and Milk formation stages, thus, critical periods for root development that influence yield (Kirby, 1985; Miller, 1996). RGR-Crop's negative correlation at the Milk formation stage, as shown in Figure 5.8 (c), indicates the influence of BD in the grain formation process; thus, subplots of land with less compaction had relatively heavier grain formed than the harder subplots.

All the absorbed macronutrients in the measured crop's biomass (Total N_d, K_d, P_d, Ca_d, Mg_d, Total N_w, K_w, P_w, Ca_w, Mg_w) showed higher concentrations in highly compacted subplots and lower concentrations in less compacted ones. This pattern demonstrates a positive correlation, as shown in Figure 5.8 (d). The level of the effect of BD on the absorbed macronutrients in crop biomass concentration was dependent on the transportation mode of that nutrient, whether it was through water uptake or diffusion. The nutrients taken into the tissues of crops are transported via the protoplasmic connection. Crop nutrient uptake occurs through mass flow (water-driven transport) and diffusion (Tsukagoshi and Shinohara, 2020). SC restricts water accessibility by crop roots, impairing mass flow and forcing reliance on diffusion alone. This limits nutrient distribution, causing localized accumulation of diffusion-dependent nutrients that remain inaccessible for crop use, ultimately reducing crop productivity. Nutrients like nitrogen, phosphorus, potassium, and magnesium are part of the mobile nutrients (a higher percentage is moved by diffusion), whilst calcium is an immobile nutrient; thus, a greater percentage is moved by water (Bayer Group, 2024).

5.3.3. Crop yield and impact of soil compaction on yield level

The yield parameters measured/monitored, and recorded in this research are listed in Table 5.5. The number of pods per m² area was highest on subplot BD3 with 261, followed by BD4 with 235 and Control with 229. BD3 again had the highest grains per pod at 32.77, followed by the Control at 31.77 and BD4 at 29.46. The two most compacted subplots showed significantly lower grain counts, with BD2 being 20% lower than BD3 and BD1 being 50% lower than BD3.

Table 5.5: Average yield data per BD treatment

Compaction level	Average number of pods/head per square meter	Average number of grains per pod	Average weight of 100 grains (g)	Yield, t/ha
BD 1	177	21.3	2.805	1.058
BD 2	217	27.23	3.28	1.938
BD 3	261	32.77	3.395	2.904
BD 4	235	29.46	3.285	2.274
Control	229	31.77	3.545	2.579

The average weights of 100 grains recorded for each BD treatment in Table 5.5 were within the range of 2.805 g for the hardest subplot to 3.545 g for the Control subplot. Since the average weight of 100 grains of wheat is 3.4 g, as previously reported (Agriculture Victoria Connect, 2024), Control, BD3, BD4, and BD 2 are the closest to 3.4 g. However, the Control plot produced the heaviest grains at 3.545 g.

The results in Table 5.5, with the aid of Eq. 5.3, produced the yield result plotted in Figure 5.9. The highest average yield per BD treatment was recorded on the BD3 subplots, which was 173.6% greater than that of the subplots with the minimum yield, BD1. The Control subplot also recorded an average yield that is 143.4% greater than that of BD1. Since the Control subplot had heavier grains and about 7.8% more grains per pod than the BD4 subplot, as shown in Table 5.5, its yield is slightly greater than BD4, as seen in Figure 5.5. Previous research (Longepierre et al., 2022) also discovered a 40% reduction in wheat yield and a 60% reduction in corn due to SC effects. The results of soil amendments are to improve yield and, to some extent, improve the environment (Davis et al., 2024; De Corato, 2023).

The increasing temperatures from June to July in Figure 5.4 coincided with the critical Heading/Beginning of flowering and Milk formation stages, potentially accelerating grain development in less compacted subplots while increasing moisture stress in highly compacted soils as seen in Figure 5.9. The reduction in sunshine hours from July to August coincided with the milk ripening stage of wheat and may have contributed to the observed differences in final yield components, particularly between control subplots and those subjected to high SC treatments.

Figure 5.10 shows that the average number of pods per m^2 area can be used to estimate final wheat grain yield. Farmers commonly use this approach to quickly estimate wheat yield during the Tillering stage by assuming each tiller is going to bear grains (Martin et al., 2011; Paulsen et al., 1997).

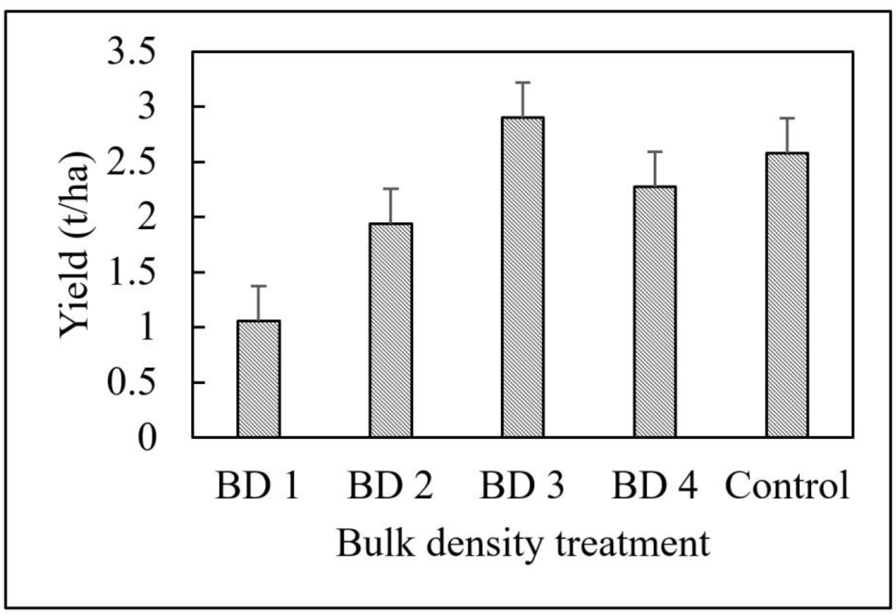

Figure 5.9: Wheat yields in tons per hectare

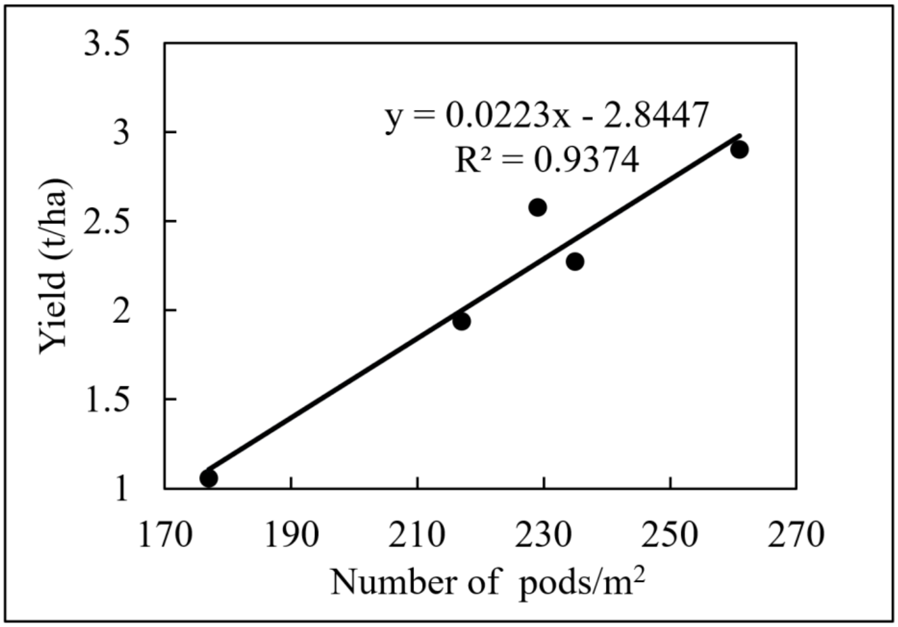

Figure 5.10: Plot of yield versus number of pods per m^2

However, in this research, the actual number of pods per m^2 is used, allowing a more accurate prediction ($R^2 = 0.9374$) between the Heading to the Milk ripening stage. This could permit the adoption of RS/machine vision techniques, such as unmanned aerial vehicles, to fast-track the estimation of yield. This strong relationship in Figure 5.10 explains the observed pattern of decreasing yield with increasing SC in Figure 5.9, with BD3 as the notable exception. In highly compacted soils (BD1 and BD2), restricted root development limited nutrient and water uptake, resulting in fewer pods per m^2, as seen in Table 5.5. Fewer pods per m^2 consequently result in lower grain yields. The significant reduction in the number of pods under these conditions highlights the sensitivity of reproductive development to excessive SC stress.

Interestingly, BD3 emerged as the optimal SC level for wheat production, outperforming even the Control treatment. With the highest pod count and grain yield, BD3 represents an optimal range of SC. The SC was firm enough to enhance soil-root contact and potentially improve water retention during the early-season low precipitation period in Figure 5.4, yet not so dense as to hinder root development or gas exchange.

The slightly lower performance of the Control and BD4 treatments, compared to BD3 suggests that moderate SC may be beneficial under the environmental conditions of this experiment, which can be found in Figure 5.4. This is particularly relevant given the low rainfall during critical early growth stages from May to June, where moderately compacted soil improved water retention and nutrient availability in the root zone. These findings have significant agronomic implications. Rather than eliminating SC, managing it to achieve an optimal level, such as BD3, could maximize wheat productivity under similar environmental conditions.

5.3.4. Soil Properties and crop data influence on crop yield

To interpret the implications of the effect of BD treatment on the measured properties in this experiment, the prediction/estimation of wheat grain yield using the recorded variations in the properties across the growth stages was plotted in Figure 5.11.

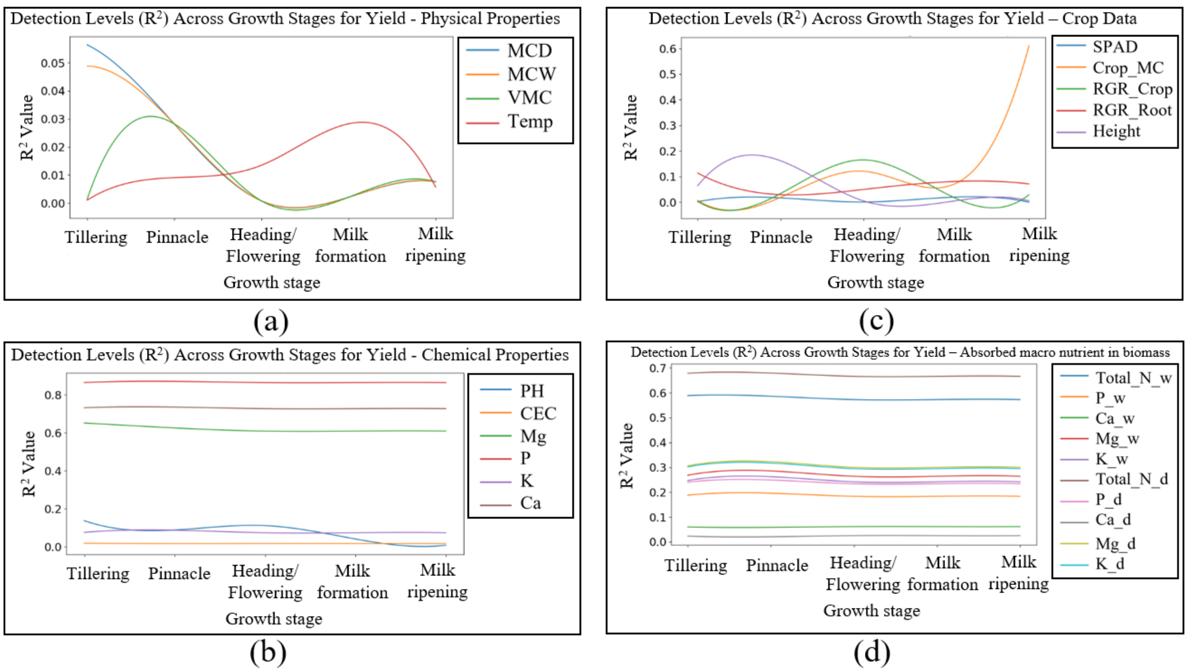

Figure 5.11: Wheat yield prediction (a) R^2 versus soil physical properties at different growth stages, (b) R^2 versus soil chemical properties at different growth stages, (c) R^2 versus crop growth data at different growth stages, and (d) R^2 versus absorbed macronutrient in biomass at different growth stages

The plots in Figure 5.11 represent the four different property groups, with each plot having a color-coded legend attached to indicate its specific properties.

Figure 5.11 (a) illustrates the R^2 plot of the soil physical properties' yield predictions, showing a low prediction tendency with R^2 of -0.005 to -0.075. The soil physical properties measured in this study appear to have a limited direct influence on final yield. However, as shown in Figure 5.11 (a), their impact, particularly from MCD and MCW, was more evident during early growth stages and decreased as the crop matured. This suggests that soil moisture-dependent properties and developmental parameters are most affected during the initial stages of crop development.

Concerning the data in Figure 5.11 (b), the level of soil P, Ca, and Mg were the properties that had higher yield prediction tendencies. The yield prediction R^2 for the soil residual K was 0.05, CEC was -0.05, and the pH was 0.1 to -0.05. These R^2 values are quite low, hence, K, CEC, and pH measured levels cannot be used to explain the variance in the final crop yield. It was observed in previous research (Ma et al., 2022) that P enhances the growth and yield of wheat by enhancing the leaf photosynthesis, and other studies (Bradley et al., 2008; Pandey et al., 2020; Paulsen et al., 1997) also emphasized the importance of soil P, Ca, Mg, K, N, and other nutrients regarding wheat growth and yield.

The crop growth data in Figure 5.11 (c) also has a low yield estimation tendency for almost all properties of the experimental setup, with R^2 of -0.005 to 0.15, except for the Crop-MC at the Milk ripening stage, which predicted yield with R^2 of 0.6. Table 5.3 and Figure 5.9 show an inverse relationship between Crop-MC and final average yield during the Milk ripening stage. Crops in highly compacted subplots (BD1 and BD2) exhibited 6 to 8% Crop-MC higher than the subplots with high yield. This suggests developmental delays caused by SC, where plants prioritize compensatory growth, which causes a reduction in grain production. Although the direct impact of RGR-Root and RGR-Crop on final yield was less, RGR-Root had a higher yield prediction at the Pinnacle stage, and RGR-Crop's was at Heading/Before flowering, while that of SPAD was almost constant across the growth stages.

Figure 5.11 (d) shows that the levels of Total N_d and Total N_w were the best in estimating the final crop yield. The yield prediction R^2 for Mg_d, Mg_w, K_d, K_w, P_d, and P_w were all between 0.15 to 0.3, while that of Ca_d and Ca_w is zero and below. This means that the measured levels of these properties are not able to explain the variation in the final yield with an appreciable accuracy of at least R^2 of 0.6.

5.3.4.1. Crop yield prediction by soil properties and crop data

Building on established research demonstrating the collaborative effects of multiple soil chemical nutrients on crop yields (Zörb et al., 2018). The combinations of key soil chemical properties (P, Ca, and Mg) were assessed to predict wheat yield. Figure 5.12 (a) shows how the best individual property performs, while Figure 5.12 (b) and Table 5.6 highlight the best results when P and Ca are combined. This combination gave strong models with an R^2 of 0.855 and RMSE of 0.24 t/ha for both PLSR and MLR. These findings match earlier work (Bonfil et al., 2004), which also found better predictions ($R^2 = 0.83$) when combining soil P and Ca.

Table 5.6: Yield estimating models' parameters: GTD-base

Properties	PLSR		MLR/LR	
	R^2	RMSE (ton/ha)	R^2	RMSE (ton/ha)
P only	0.8528	0.2418	0.8528	0.2418
P & Ca	0.8551	0.2399	0.8551	0.2399
P, Ca & Mg	0.9720	0.1054	0.9720	0.1054
P, Ca, Mg & SPAD	0.9734	0.1028	0.9734	0.1028
P, Ca, Mg & Crop-MC	0.9711	0.1070	0.9711	0.1070

When we added the three key soil chemical properties (P, Ca, and Mg) to the model, as shown in Figure 5.12 (c) and Table 5.6, prediction accuracy improved significantly. The R^2 value increased to 0.972, and RMSE dropped to 0.1054 t/ha for both PLSR and MLR models. This matches the findings by (Zhao et al., 2015), who also saw better maize yield predictions (R^2 from 0.76 to 0.89) when combining multiple soil nutrients, including P, Ca, and Mg. Another research (Meng et al., 2013) demonstrated that integrated soil fertility models incorporating multiple nutrients improved wheat yield prediction accuracy from R^2 values of 0.71-0.79 for single nutrients to 0.88-0.92 for combined nutrient models. The substantial increase in accuracy from using one to three nutrients shows how these elements interact to affect wheat productivity.

Further analysis examined whether incorporating crop growth data could improve prediction accuracy. Adding SPAD readings to the P-Ca-Mg model resulted in a marginal increase of 0.14%, whereas including Crop-MC slightly decreased accuracy by 0.09%, as shown in Figure 5.12 (d) and Table 5.6. The figures displaying the performance of other constructed models not selected due to their lower performance can be found in Appendix B. These results suggest that once primary soil chemical nutrients are accounted for, additional crop-based parameters contribute minimally to yield prediction under these experimental conditions. Thus, focusing on soil P, Ca, and Mg levels provides an efficient approach for predicting wheat yield potential, particularly in environments where SC may influence available nutrients' accessibility.

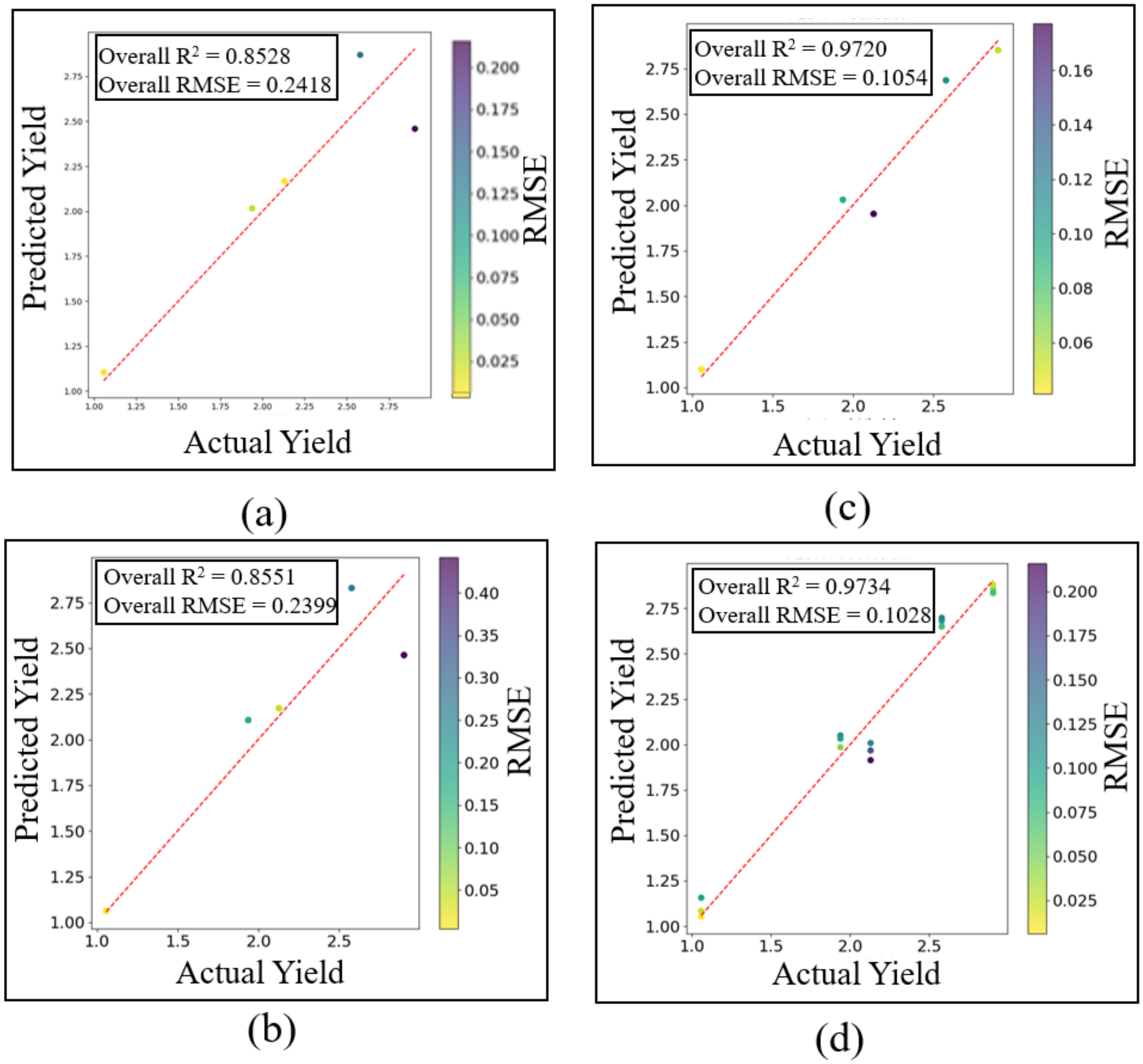

Figure 5.12: Estimated yield versus actual yield: GTD-base (a) P only, (b) P & Ca, (c) P, Ca, & Mg, (d) P, Ca, Mg, & SPAD

Figure 5.13 presents the HSC-based yield prediction (PLSR models) developed from the influential properties identified through GTD analysis. Although predictions were conducted across all growth stages, the Milk ripening stage demonstrated superior performance and is highlighted in Figure 5.13. The comprehensive model figures and performance metrics are available in Appendix C. The predictive capacity of these HSC-based models directly correlated with the statistical strength (R^2) of the constituent properties. Parameters for the HSC-based influential properties are documented in Table 1C, Appendix C, with the model development methodology detailed in Chapter 3, Section 3.4.1.

The HSC-based single-property yield prediction model utilizing P, identified as the most influential standalone property during GTD analysis, achieved an R^2 value of 0.6437 with an RMSE of 0.3762 in Figure 5.13 (a). The dual-property P-Ca model demonstrated modest improvement with an R^2 of 0.6595 and RMSE of 0.3678, shown in Figure 5.13 (b). More substantial predictive power was observed in the P-Ca-Mg model, which attained an R^2 of 0.7425 and RMSE of 0.3198, Figure 5.13 (c). Applying a 75% RMSE threshold to the P-Ca-Mg model enhanced model performance by 17.9%, as illustrated in Figure 5.13 (d). These findings demonstrate the possibility of HSC-based yield prediction, with the optimized P-Ca-Mg model achieving a performance (R^2 = 0.9215) comparable to the GTD-based model (R^2 = 0.972), suggesting potential for practical implementation of hyperspectral imaging in PA yield prediction.

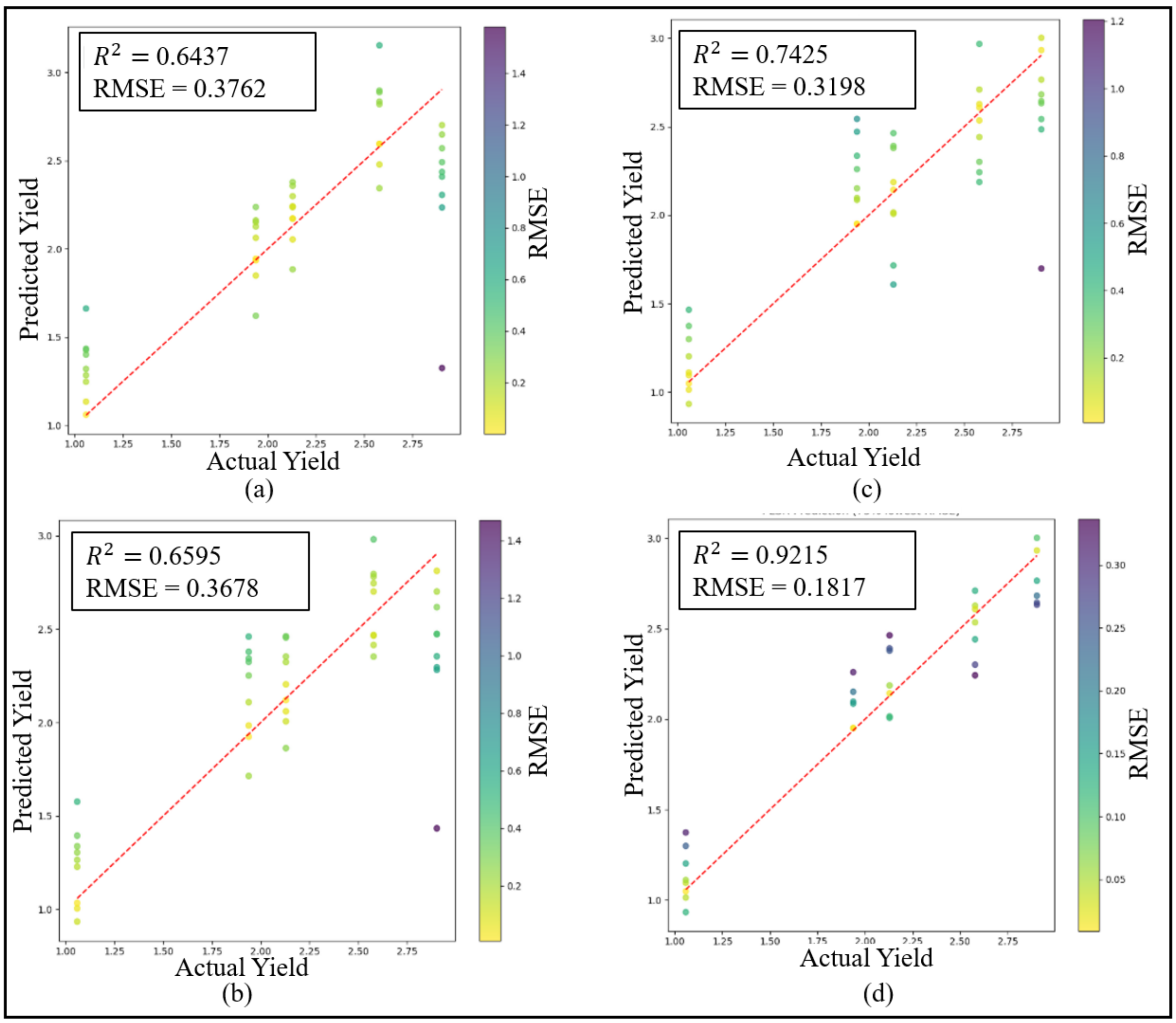

Figure 5.13: Estimated yield versus actual yield-HSC base (a) P only, (b) P & Ca, (c) P, Ca, & Mg, (d) P-Ca-Mg with 75% RMSE threshold

The strong predictive capacity of the P-Ca-Mg combination in both the GTD-based and the HSC-based models can be explained by their complementary roles under varying SC conditions. P mobility primarily occurs through diffusion and is particularly sensitive to SC, which restricts pore connectivity and root exploration (Bengough et al., 2011). In moderately compacted soils like BD3, improved soil-root contact may facilitate P diffusion over short distances while preserving enough macropores to support root growth.

Ca and Mg help both crop growth and soil structure. Ca promotes better soil aggregation that can partially mitigate SC effects (Bronick and Lal, 2005). Mg is essential for chlorophyll production and enzyme activation in energy processes. These functions become vital when crops are stressed in compacted soils (Cakmak and Yazici, 2010).

The strong predictive performance of the P-Ca-Mg combination (R^2 = 0.972 for the GTD model and 0.9215 for the HSC-based model) is due to their interactive effects on plant growth. Under moderate compaction (BD3), an optimal balance between soil-root contact and pore space can enhance nutrient availability and uptake efficiency. This accounts for the higher yields at this compaction level, even though there was a general negative relationship between SC and final crop yield across other treatments.

Regarding increasing or optimizing spring wheat yield, the result from this research indicates that spring wheat requires a certain level of SC to achieve an optimum yield. From the outcome of this research, it is evident that BD3 was the best SC condition that produced high yield; hence, running a Cambridge roller two times more on the field could facilitate the field to approach this optimum SC condition and improve the yield of spring wheat by about 12%.

5.4.Conclusions

This chapter examined the effects of SC on soil physical properties and soil chemical properties. It also assessed crop growth data and macronutrient uptake in crop biomass across five growth stages of spring wheat. The effect or influence of these property groups was used to explain the variance in the final wheat yield. There were three properties out of the twenty-six measured, which were all soil chemical properties, and their discrete response to BD treatment levels reflected/corresponded to the variation in the final yield. The combination of soil P, Ca, and Mg levels allowed the estimation of yield with about a 14 % improvement in the coefficient of determination (R2 = 0.9720) compared to the best sole property estimation (R2 = 0.8528). Additionally, the final yields recorded in the soft subplots, Control and BD4, were more than 100% higher than those in the hardest subplot, BD1. Results from this research suggest that, when it comes to spring wheat, the soil needs a certain level of SC, about 1.24 Mg/m3, to produce an optimum yield.

These results suggest that soil amendments such as tillage affect the final crop yield, and as such, the level of SC needs to be managed to suit the specific requirement of the crop being cultivated. This is why the top two hardest plots, BD1 and BD2, had low moisture at the root zones and less access to available soil nutrients, thus resulting in a low final yield. This supports the logic behind site-specific SC, termed PT, which is to apply the required depth of tillage to specific zones/ regions where it is essential, and the research results prove why the PT concept is important.

Furthermore, this study demonstrates the efficacy of HSC technology in developing robust yield prediction models for PA applications. Through systematic analysis of influential soil properties, particularly the P, Ca, and Mg combination during the Milk ripening stage, the HSC-based approach achieved prediction accuracy ($R^2 = 0.9215$) after applying the 75% RMSE threshold optimization, comparable to traditional ground truth data methods ($R^2 = 0.9720$). This remarkable performance confirms that remotely sensed spectral data can effectively capture the complex relationships between soil nutrient status and crop productivity. These findings represent a significant development toward non-invasive, efficient field monitoring systems that can inform PA decisions in wheat production, potentially reducing the need for extensive ground sampling while maintaining high prediction reliability.

The setup of this experiment limited the cause of SC to soil densification by heavy farm machinery, which reduces the pore spaces in the soil structure and does not affect the textural structure of the soil particle sizes by breaking them into smaller pieces. Hence, the outcome of this research is restricted to such a concept of compaction. Additionally, further research is needed with different crops to fully grasp their responses to BD treatment as well. Different crops have different nutrient requirements and physiology, which could affect their responses to SC variation throughout their growth stages.

CHAPTER 6. INTEGRATION OF FINDINGS INTO THE PRECISION AGRICULTURE FRAMEWORK

6.1.Introduction

Remote sensing (RS) technology is a powerful diagnostic and analytical tool in agriculture, enabling a comprehensive assessment of soil, crops, and environmental conditions. RS enables the establishment of an early warning method for agricultural stakeholders to intervene on time to curb developing problems before they largely impact crop productivity and threaten global food security (Khanal et al., 2020).

Agricultural RS incorporates various platforms, including ground-based instruments (hyperspectral and multispectral cameras), aerial systems (unmanned aerial vehicles), and satellite technologies (Read and Torrado, 2009). These technologies have become important for monitoring crop health and environmental factors, improving yields, enhancing resource utilization, and assisting early detection of plant diseases (Karmakar et al., 2024).

Among these technologies, hyperspectral imaging (HSI) represents a promising innovation for precision agriculture (PA). Different from the conventional RGB imaging or multispectral approaches (Jovanović and Govedarica, 2014; Ram et al., 2024), HSI provides substantially more detailed spectral information about crop and soil conditions, supporting improved targeted farm management decisions (Ram et al., 2024).

A useful application of HSI can be found in the PT planning process, where soil pulverization operations are applied only where necessary, particularly in areas with SC or compacted layers (Kaufmann et al., 2010; Shamal et al., 2016). Successful implementation of PA requires rapid acquisition and processing of SC data to avoid planting delays associated with traditional laboratory methods, which are labor-intensive and time-consuming.

This chapter uses insights from wheat developmental responses under varying SC levels to develop a wheat-specific PT framework. Building on the optimum SC level identified in Chapter 5, PT recommendations designed to maximize yield according to experimental results are presented. The soil nutrient management maps created from residual soil nutrients during critical wheat growth stages provide spatial nutrient information for subsequent fertilization planning. Additionally, the HSI and processing methodologies introduced in Chapters 3 and 4 support an efficient workflow for rapid assessment of SC effects on wheat development, facilitating timely and targeted interventions. This integration creates a comprehensive framework relating RS capabilities with agronomic understanding to produce practical, site-specific SC management solutions for wheat producers.

6.2.Integration methodology

A comprehensive framework that uses HSC technology to study soil properties without damaging crops or soil was developed. This looked at how wheat grows under different SC. The results enabled wheat-specific PA implementation through targeted PT actions and site-specific nutrient management plans. The main idea is to find the best SC for boosting wheat yield by looking at growth data and HSC readings.

As shown in Figure 6.1, data from growth monitoring and HSC images across five important growth stages of wheat, which you can find detailed in Chapter 5, were combined. This method included a comprehensive analysis of yield variance, trends in yields, and what influenced wheat growth, which is documented in Table 5.5, along with the changes in soil properties across different test subplots.

Fractional vegetation cover (FVC), a key HSC-derived parameter, was utilized to quantify RS-identified variance related to SC levels. This integrated approach, combining FVC-based differentiation, soil physicochemical property variance, and crop growth data, which supported the development of farm input management plans presented in Figures 6.4-6.7. Furthermore, an HSC-based SC assessment and management workflow, detailed in Figure 6.2, was also developed. The resulting framework provides a practical methodology for implementing PA strategies specifically optimized for wheat production systems under varying SC conditions.

6.2.1. PT framework development and validation

The wheat yield data and SC impacts stated in Section 5.3.3, along with yield predictions based on soil properties and crop data (both GTD-based and HSC-based) from Section 5.3.4.1 in Chapter 5, identified BD3 (BD = 1.24 Mg/m^3) as the optimum SC level for maximizing wheat yield. The derived models demonstrated that SC affects multiple nutrient pathways, with the P-Ca-Mg model providing the best explanation for yield variations across different compaction levels in both datasets. These findings informed the development of the framework illustrated in Figure 6.1.

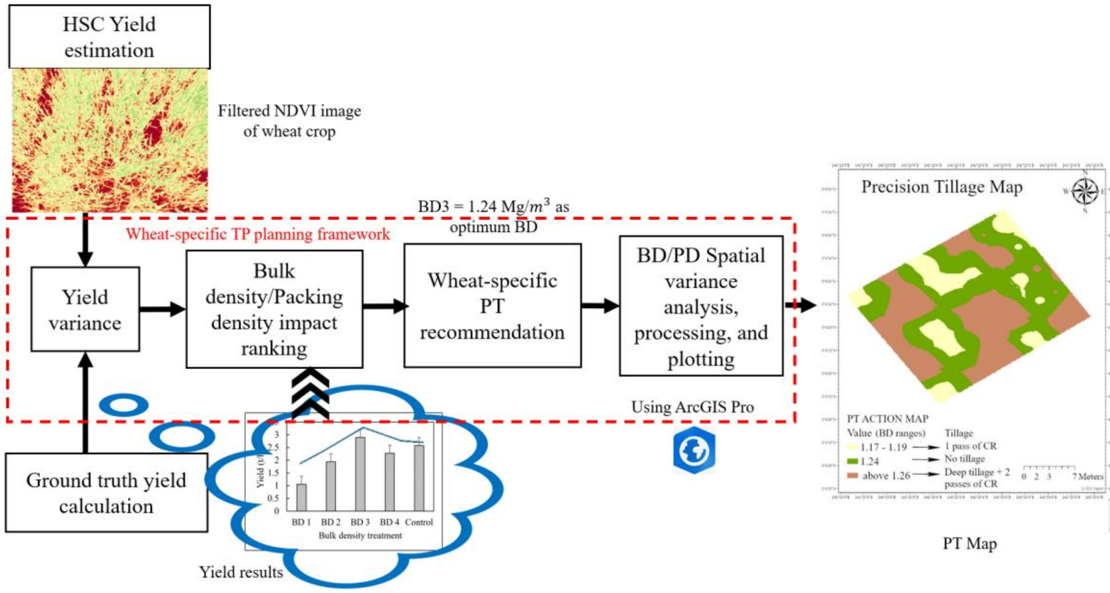

Figure 6.1: Wheat-specific PT planning flow diagram

The observed yield trends established the basis for defining BD/PD ranges for effective SC management. The set management goal is to apply targeted amendments to specific field sites to optimize SC levels toward the ideal range (BD3 = 1.24 Mg/m³), based on measured yield values at different compaction levels. Yield data from Table 5.5 showed that higher compaction levels (BD1 = 1.30 Mg/m³ and BD2 = 1.25 Mg/m³) produced lower yields, while lower compaction levels (BD4 = 1.19 Mg/m³ and Control = 1.17 Mg/m³) outperformed the most compacted experimental subplots. This pattern suggests a dual management approach: increasing compaction in looser soils while reducing compaction in harder soils.

To further validate the management approach required to achieve the ideal wheat production SC level derived, a field compaction test was conducted using the Cambridge roller (CR) after a section of the field had been plowed to mimic wheat sowing conditions. The CR was run twice on the plowed field, resulting in an average BD of 1.2486 Mg/m³ with a standard deviation of 0.129 Mg/m³. The detailed table containing the SC level for the validation test can be found in Table D12, Appendix D. This demonstrates that running the CR twice can yield an SC level close to the optimum derived for maximizing wheat yield.

The workflow presented in Figure 6.1 begins with yield trend identification through either GTD or HSC-based yield predictions (left side of Figure 6.1), proceeds to BD/PD range definition, advances to tillage recommendation assignment, and concludes with spatial variance analysis and mapping using ArcGIS Pro (ESRI ArcGIS™ version 2.4.0, 2019, CA, USA). This sequential process generates spatially explicit maps with site-specific tillage recommendations, defining PT decisions as shown on the right end of Figure 6.1.

6.2.2. Farm input management plan development

The farm input management plan is derived from the experimental workflow presented in Figure 5.6, Chapter 5. This workflow includes spatial residual soil nutrient mapping as its fifth step, which has been adapted for comprehensive farm input management. These nutrient distributions were visualized using distinct color schemes to clearly illustrate spatial variability in underutilized soil resources.

This approach captures residual soil nutrients after crops have utilized approximately 70-80% of their accumulated nutrient needs, enabling more precise fertilizer application rates plan for a subsequent season. The method offers two significant advantages: first, it provides site-specific residual nutrient data, allowing for precise determination of supplemental nutrient requirements; second, it reduces laboratory analysis time prior to the subsequent growing season. The validation tests indicate the best HSC-based predictions achieve R^2 values of 0.75 to 0.86 compared to standard laboratory analyses for key nutrients. The full HSC-based prediction R^2 per growth stages can be found in Table D6, Appendix D.

The HSC-based methodology detailed in Chapter 3 for acquiring residual nutrient data significantly reduces the labor associated with traditional soil sampling while delivering results more rapidly. Conventional laboratory analyses typically require 2-3 months for processing, whereas the HSC approach generates actionable data within 1-4 days, representing a significant reduction in processing time.

The nutrient maps generated through this process directly inform site-specific fertilizer application rates by deducting the residual nutrient from the crop-specific nutrient requirements, which convert residual nutrient levels to supplemental fertilizer. Validation procedures comparing HSC-derived nutrient maps against laboratory standards indicate lower RMSE values as seen in Figure 6.5 to 6.7 and Figure D1 to D4, Appendix D.

Certain limitations need to be considered when implementing this approach, including environmental factors captured in Figure 5.4, and ambient light conditions that may affect HSC readings. These variables are accounted for using the calibration panel described in Section 3.2.1.1 and shown in Figure 3.4 to account for light conditions, and the calibration procedure cannot be excluded.

6.2.3. Workflow for remote sensing of SC under wheat field

Observations and results from the controlled SC level experiments in Chapter 5 indicate that variance in soil physical properties is significantly affected during early growth stages. Wheat and many crops demonstrate adaptive capacity through substitutional development to compensate for developmental shortfalls under stress conditions (Islam et al., 2022).

Consequently, RS of SC via wheat vegetation was most effective during the initial two growth stages (Tillering and Pinnacle).

The methodology adopted, first assessed possible combinations of measured parameters that could explain the variation in initial SC levels, denoted as route *M1* in Figure 6.2. The second step estimated these SC-linked parameters using HSC data for SC level detection, represented as the *M2* flow route in Figure 6.2. Both routes (*M1* and *M2*) were evaluated against the reference method of direct BD measurement and PD calculation as proposed by Shamal et al. (2016).

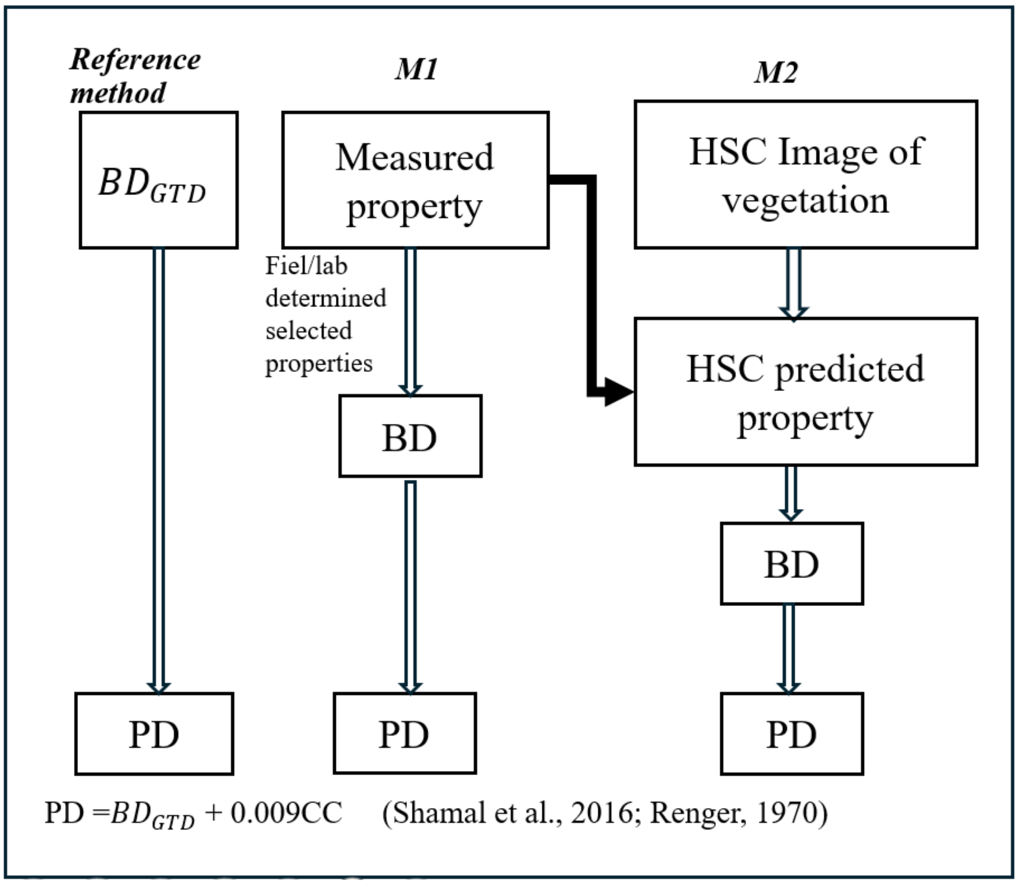

Figure 6.2: Workflow for Remote sensing-based SC

For real-time RS monitoring of SC levels under field conditions, Fractional Vegetation Cover (FVC) was calculated using hyperspectral imagery through a normalized difference vegetation index (NDVI)-based thresholding approach. This method classifies pixels as vegetated or non-vegetated based on spectral reflectance characteristics. NDVI was derived from hyperspectral bands in the red (650–680 nm) and near-infrared (780–1100 nm) regions using Eq. 3.8. A threshold of NDVI ≥ 0.05 was applied to distinguish vegetated pixels from bare soil, effectively separating vegetation while minimizing soil background influence (Carlson and Ripley, 1997).

This approach proved particularly valuable during the Heading, Milk formation, and Milk ripening stages when crops had fully developed with minimal exposed soil surface. Under these conditions, alternative methods based on soil reflectance rather than vegetation would have produced less accurate results.

Pixels exceeding the NDVI threshold were classified as vegetated, with FVC computed as the ratio of vegetated pixels (N_{veg}) to total pixels (N_{total}) within each spatial unit:

$$FVC = \frac{N_{veg}}{N_{total}} \tag{6.1}$$

This binary classification approach offers computational efficiency and direct interpretability, particularly advantageous for large-scale analyses where endmember extraction presents significant challenges.

6.3.Results and discussion

6.3.1. PT framework implementation

The introduction of targeted or site-specific SC management, termed PT, has demonstrated significant potential for enhancing environmentally sensitive agricultural practices (Godwin and Miller, 2003; Mouazen and Ramon, 2006). This emerging approach necessitates streamlined tillage innovations for improved crop-specific SC management. Table 6.1 presents PT decisions for wheat cultivation, formulated based on field-verified experimental results. These management guidelines integrate insights from Chapter 5, combining traditional GTD and unique HSC-based extraction of SC parameters as developed in Chapter 4.

The foundation of these recommendations lies in the identification of optimal SC levels for maximizing wheat yield. In the experimental fields utilized for this study, clay content (CC) remained below 25% within a range of 6%, resulting in PD calculations from Eq. 4.2 not differing significantly from BD measurements. Consequently, BD values were employed for accurate threshold establishment. In areas with higher clay content (CC ≥ 30%) with approximately 15% range variation (Shamal et al., 2016), PD values may substitute for BD values in Table 6.1.

Table 6.1 comprises four essential components: established BD ranges (first column), corresponding wheat yield level descriptions (second column), appropriate tillage recommendations (third column), and remarks on expected improvements and recommended practices (fourth column). This structured approach offers a comprehensive framework for implementing PT in wheat production systems under different SC conditions, as it incorporates the soil's natural response to compaction. The BD thresholds presented in Table 6.1 are based on results from actual field compaction experiments.

Table 6.1: Wheat-specific bulk density level-based tillage action recommendation

BD values (kg/m^3)	Wheat yield	Recommended tillage action	Remarks
< 1170	Below optimum	2 passes of standard Cambridge roller (CR)	Originally required 1 pass of CR
1170 – 1190	Lower optimum range	1 pass of standard Cambridge roller	Up to 12% yield improvement
1240 ± 20	Optimum performance	No tillage	-
> 1260	Limiting range	Deep tillage (0.30 m) + 2 passes of CR	143 - 173% yield improvement

In establishing the recommended tillage actions, results from Table 5.5 were utilized, revealing that the Control treatment yielded 12.4% less than the optimum SC level (BD3). The Control subplot required one pass of the Cambridge roller (CR) following standard plowing and harrowing operations (detailed in section 5.2 and Table 5.1). These findings informed the tillage actions outlined for the < 1170 kg/m^3 and 1170-1190 kg/m^3 BD ranges in Table 6.1. Since post-plowing-harrowing BD typically falls below the Control subplot's BD values, the recommended tillage action consists of two CR passes to achieve the optimal BD3 SC level. Similarly, the Control treatment requires one additional CR pass to reach the optimal BD3 level.

The identified optimum SC level corresponds to a BD of 1240 kg/m^3 with a standard deviation (SD) of 20 kg/m^3, based on the average SD of mean BD values across soil depth sections reported in Table 5.2. As this BD represents the optimum SC for spring wheat, no tillage is recommended for soils exhibiting this compaction level. The BD value of 1240 kg/m^3 (1.24 Mg/m^3) serves as the benchmark for wheat-specific PT planning and establishes a foundation for further research into optimizing additional parameters for comprehensive wheat-specific PA implementation.

BD ranges exceeding the identified optimum represent the highest SC levels in this experiment. The substantial yield differences between the optimum and BD2 (49.8%

reduction) and between the optimum and BD1 (173.6% reduction) are particularly noteworthy. Even though the incremental increase in SC from BD3 to BD2 was merely 1% (see Figure 5.1), resulting from an increase from two to three passes of the vibration plate compactor described in Section 5.2, the yield penalty was considerable. The incremental SC increase from BD3 to BD1 was 5%, achieved with two additional vibration plate compactor passes beyond BD3 treatment. These findings demonstrate that even marginal BD increases beyond the optimum SC level can cause significant yield reductions, justifying the recommendation for deep tillage to reset highly compacted soils to conventional tillage levels, followed by two CR passes to achieve the optimum SC level.

To illustrate the potential benefits of the PT framework presented in Table 6.1, the experimental plot used in the controlled compaction experiment and its corresponding BD levels were used to develop an example PT action map shown in Figure 6.3. This figure presents both BD-based (Figure 6.3a) and PD-based (Figure 6.3b) maps for the experimental field. The maps feature color-graded legends corresponding to different BD/PD ranges used in establishing thresholds, with tillage action instructions explicitly indicated for each zone. For example, green regions represent optimum SC zones requiring no tillage. Light yellow regions indicate SC levels below the optimum, requiring one CR passes as noted in the Figure 6.3 legend. Brown regions denote highly compacted zones requiring deep tillage (0.30 m) plus two CR passes.

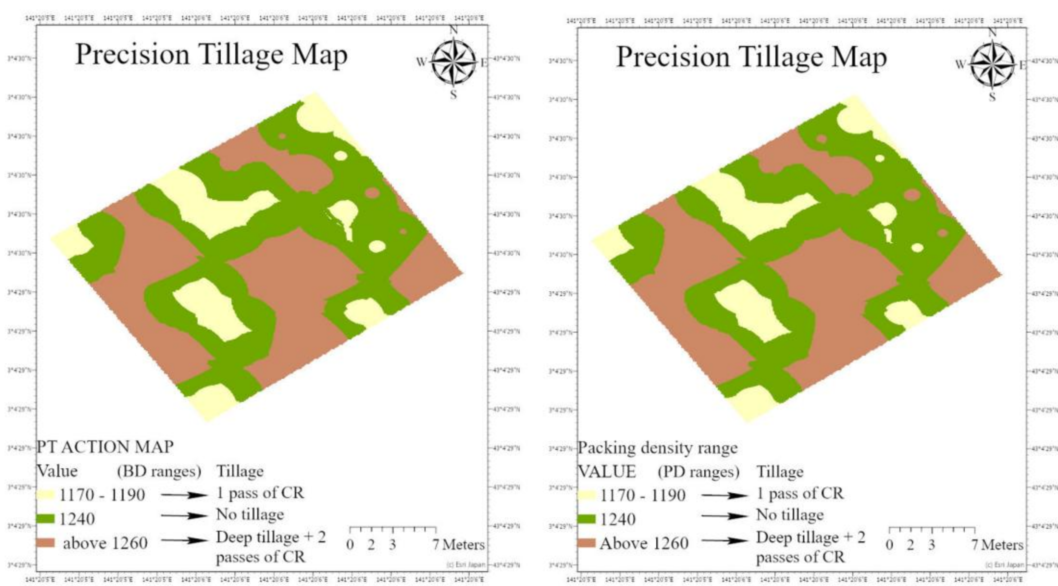

(a) (b)

Figure 6.3: PT action map demonstrating type and level of tillage the study field, (a) BD-based map, (b) PD-based map

This PT action map demonstrates that high-energy conventional tillage operations are limited to approximately 40% of the field, resulting in significant energy savings and reduced dust pollution. Based on standard energy requirements for conventional tillage operations (approximately 15-20 liters of diesel fuel per hectare for deep plowing) (Godwin, 2007; Moitzi et al., 2014), implementation of this PT approach could reduce fuel consumption by 9-12 liters per hectare in the example field. The alternative approach of implementing uniform no-till practices across the entire field could potentially result in a total yield deficit of approximately 49.52% when adjusting BD4 yield deficit to the level of the Control subplot. Conversely, implementing uniform conventional three-step tillage (deep plowing-harrowing-Cambridge roller) would incur the combined costs of unnecessary energy expenditure for deep plowing 60% of the field that does not require such intervention, plus applying CR on 20% of the field where it is not needed, ultimately resulting in a 12.4% yield deficit compared to implementing the proposed PT framework.

These exemplary maps, combined with the framework presented in Table 6.1, provide farmers with clear guidance regarding specific tillage actions appropriate for different zones or site-specific SC levels within wheat fields. Furthermore, the ArcGIS-based methodology used to create these maps, as explained in Chapter 3, enables integration with modern smart/robotic agricultural tractors for automated implementation of PT actions based on stored spatial information, advancing the practical application of PA for wheat production systems.

6.3.2. Yield insight and nutrient access evaluation

The maps developed from the experimental outcomes for comparative analysis of SC level-residual nutrient level-yield relationship are displayed in Figure 6.4. While Figure 6.5-6.7 shows the input management plan maps. In Figure 6.4 (a), the map of the BD treatment is shown with the dark-brown and light-brown colors representing harder subplots. The orange, yellow, and green colors indicate the medium compaction to the noncompacted subplots. The spatial variations in final crop yield are shown on the map in Figure 6.4 (b). The dark-brown and light-brown colors in Figure 6.4 (b) indicate regions with less yield, while the yellow, light-green, and green colors show medium to high-yield areas. Knowledge about the precise level of nutrients in the soil of a field, as shown in Figure 6.4-6.7, has become a key resource in planning soil input/amendment and understanding crop yield trends, especially for recent developments in PA practice (Hedley, 2015; Juhos et al., 2015). The colors shown in Figure 6.4 (c)-6.4 (e) and Figure 6.5-6.7 indicate spatial variations in the nutrient contents of the soil. The metallic-green and light-metallic-green correspond to areas with relatively high levels of nutrients, while yellow, orange, and red colors represent areas with medium to low soil nutrient levels.

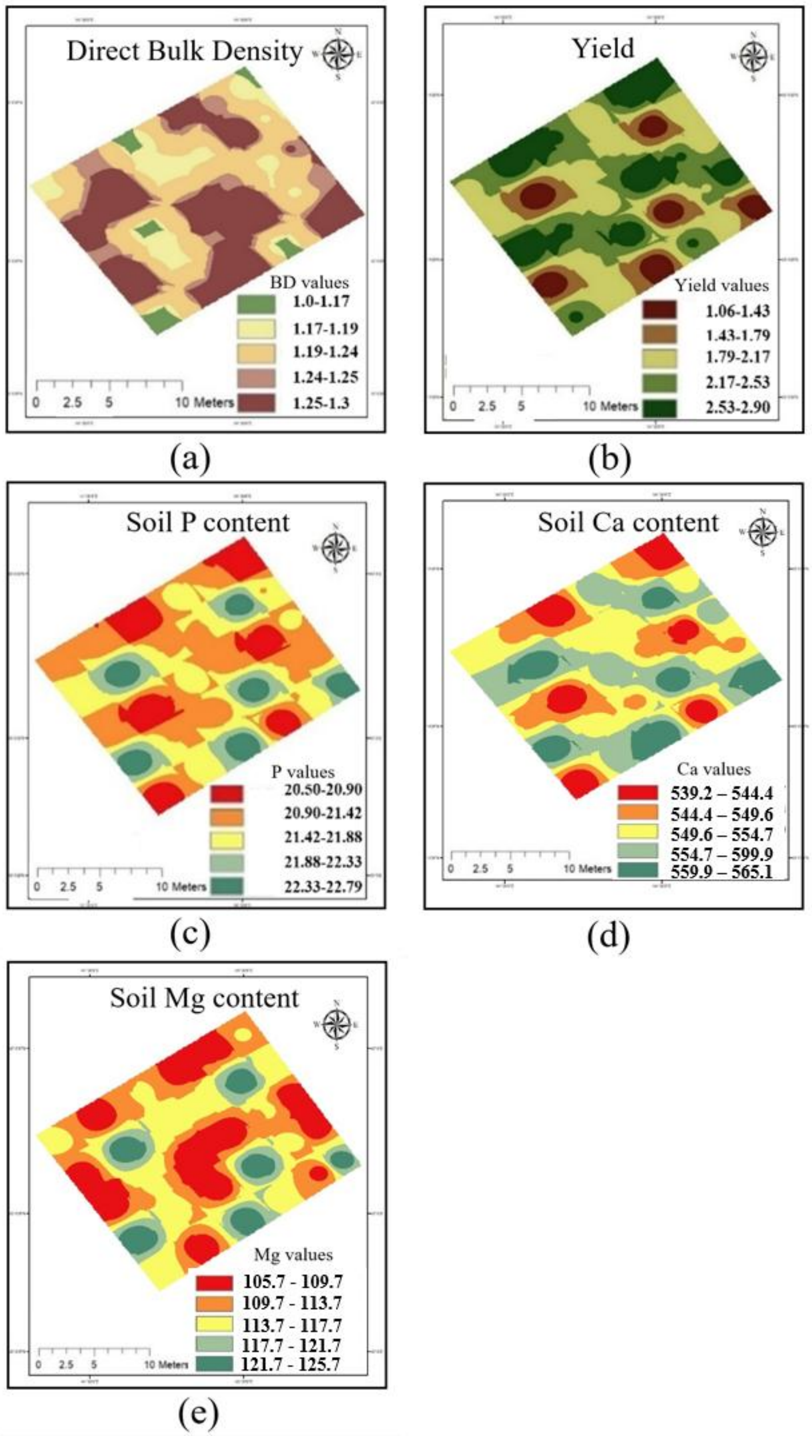

Figure 6.4: Farm input management maps (a) BD spatial map, (b) Final crop yield spatial map, (c) Soil P spatial map, (d) Soil Ca spatial map, and (e) Soil Mg spatial map

Figure 6.4 (b) shows that low-yield areas, which are the dark-brown and light-brown regions, align with high concentrations of remaining nutrients indicated with the metallic-green and light-metallic-green regions on the P, Ca, and Mg maps shown in Figure 6.4-14 (e) and Figure 6.5-6.7. These low-yield areas also correspond to the hardest subplots on the BD map shown in Figure 6.4 (a), denoted by dark-brown and light-brown regions. These compacted subplots fall within BD1 and BD2 subplots (1.25 to 1.3 Mg/m^3), suggesting a link between soil hardness, nutrient retention, and yield variations.

This spatial correlation in Figure 6.4 demonstrates a critical aspect of SC's impact on nutrient cycling efficiency. The most compacted areas (BD1 and BD2) had higher P, Ca, and Mg residuals. This suggests reduced nutrient uptake efficiency rather than soil nutrient deficiency. Despite adequate nutrient presence in these regions, the physical constraints imposed by severe SC limited the crop's ability to access and utilize these nutrients effectively. This finding supports the observation by (Lipiec and Stcpniewski, 1995) that SC primarily affects nutrient acquisition through restricted root growth and impeded diffusion paths rather than by changing the total amount of nutrients available.

The spatial patterns reveal a distinct non-linear relationship between SC and nutrient utilization. In Figure 6.4 (e) and Figure 6.7, the moderate compaction level (BD3) showed lower residual Mg than all subplots. BD3 also had the second-lowest residual P and Ca in Figure 6.4 (c) and 6.4 (d). Only the Control treatment had lower levels of P and Ca compared to BD3. However, as shown in Figure 6.4(b), BD3 produced higher yields than both the highly compacted subplots (BD1 and BD2) and the less compacted subplots (BD4 and Control). This finding supports the earlier result in Table 5.5, which informed the development of the PT framework, indicating that BD3 represents an optimal SC level. At this level, improved soil-root contact enhances nutrient uptake efficiency while sufficient pore space is maintained for root exploration.

The consistent pattern observed for P, Ca, and Mg in Figure 6.4 supports the yield regression model findings ($R^2 = 0.972$) in Chapter 5, indicating that these nutrients interact to influence wheat yield under different SC conditions. The spatial visualization highlights how SC creates a physical constraint. This constraint affects multiple nutrient pathways simultaneously. This multi-pathway limitation explains why multivariate models perform better than single-nutrient models for both GTD-based and HSC-based yield models in Chapter 5. Specifically, models incorporating all three nutrients provided substantially improved yield predictions compared to models using just one nutrient.

The analysis revealed a rare non-linear relationship between SC levels and nutrient retention patterns. Notably, the moderate SC level (BD3) showed optimal nutrient-use efficiency, deviating from the linear trends observed at other SC levels (BD1, BD2, BD4, and Control).

This demonstrates that effective site-specific management strategies focusing on maintaining an optimal SC range, rather than simply minimizing SC levels is the best. The data trends and spatial patterns in Figures 6.4–6.7 support adopting precision fertilizer strategies that account for non-linear nutrient uptake efficiency, moving beyond traditional soil nutrient content-based approaches. Furthermore, the spatial analysis of compaction-nutrient-yield dynamics provides critical validation for the PT framework developed in Section 6.3.1, which tailors' tillage strategies to achieve the identified optimal SC level. By integrating residual nutrient maps (for site-specific fertilization) with the PT framework, farmers could enhance nutrient accessibility while maintaining soil functionality.

The soil nutrient maps generated during the Heading/Beginning of flowering stage of wheat in the controlled compaction study (Figures 6.5–6.7) provide time-efficient and spatially precise guidance for fertilization planning. By analyzing residual P, Ca, and Mg when wheat had already utilized approximately 70-80% of its cumulative nutrient needs. This approach eliminates the typical two to three-month delay associated with laboratory soil test results. Such delays often disrupt optimal planting schedules for subsequent growing seasons. Critically, these maps reveal site-specific nutrient concentration patterns across different field zones, enabling precision variable-rate fertilizer applications tailored to the actual nutrient status of each specific field location. This spatially explicit approach aligns with advanced PA frameworks (Khosla et al., 2008) while addressing the practical timing constraints faced by farmers. Combining spatial nutrient distribution data with SC information for specific zones creates a suitable decision-support tool. This tool allows targeted fertilizer applications based on observed nutrient dynamics in specific field areas. Such an approach could improve nutrient use efficiency, reduce input costs, and lessen environmental impacts from over-fertilization in future growing seasons.

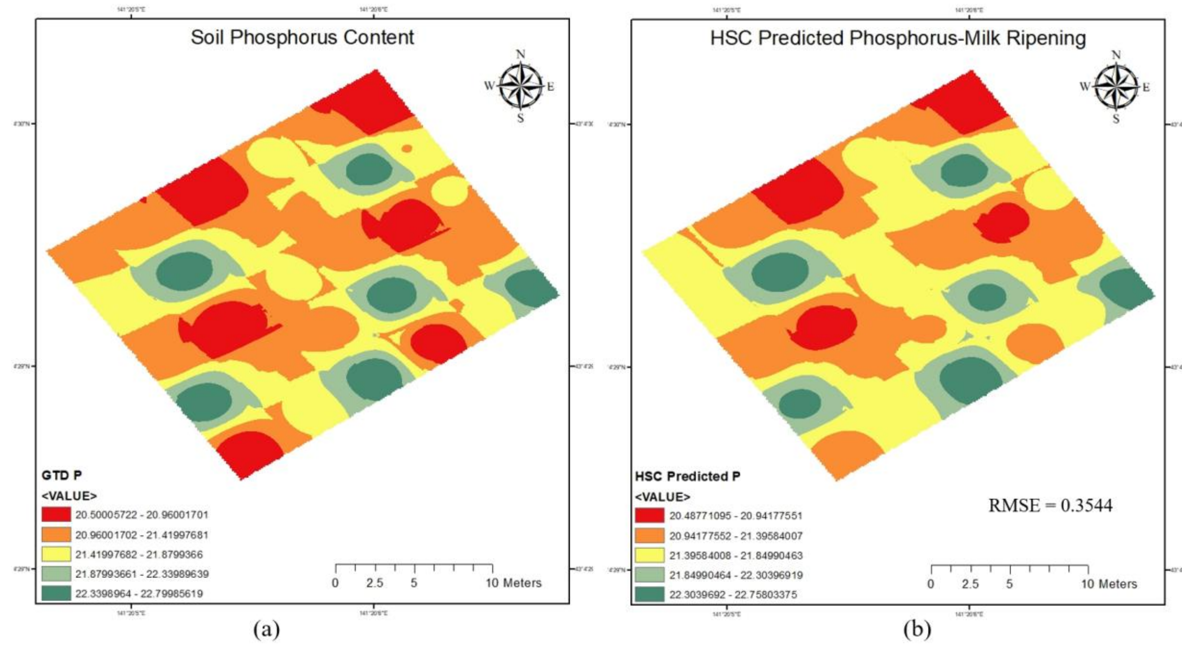

Figure 6.5: Soil phosphorus content management map (a) GTD map, (b) HSC-based map

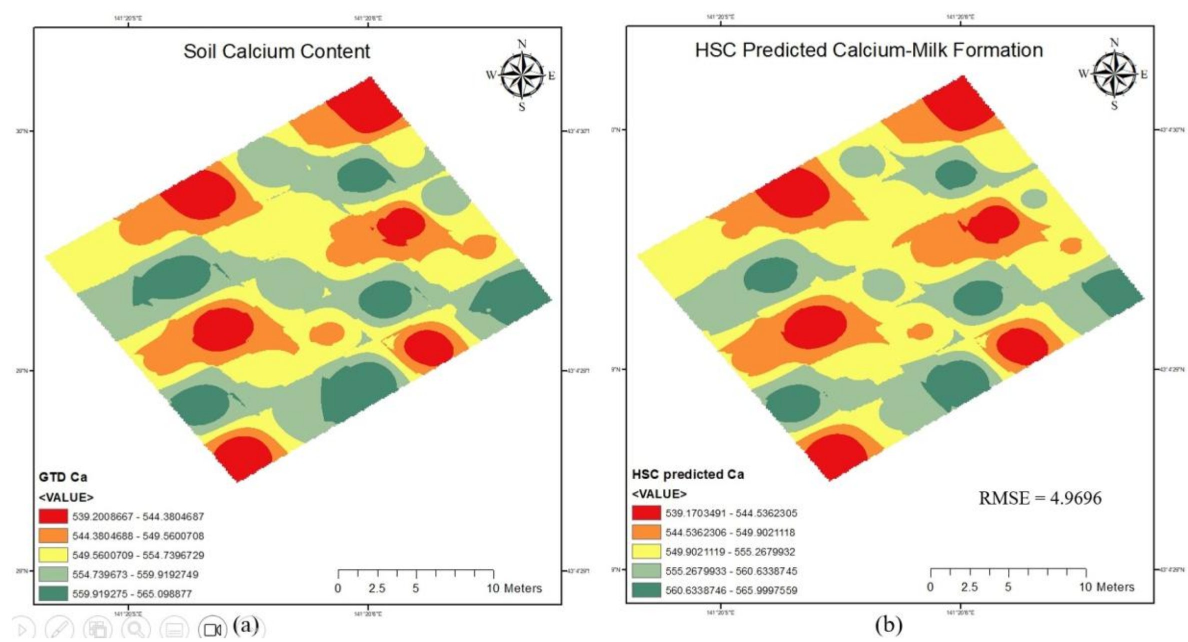

Figure 6.6: Soil calcium content management map (a) GTD map, (b) HSC-based map

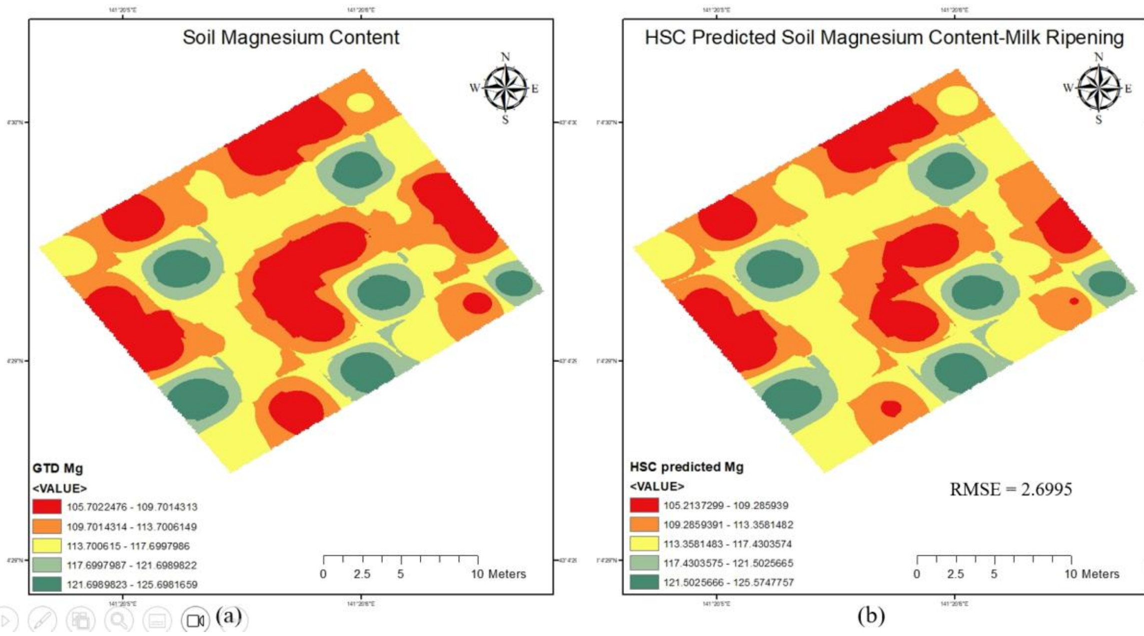

Figure 6.7: Soil magnesium content management map (a) GTD map, (b) HSC-based map

Figures 6.5–6.7 present spatial nutrient maps generated from two distinct datasets: (a) GTD-based and (b) HSC-based approaches. Figure 6.5 illustrates P distribution, where the HSC-based map in Figure 6.5 (b) demonstrates strong potential for rapid P estimation, achieving an RMSE of 0.3544 mg/100g. This low error margin indicates that RS-derived P levels align closely with ground truth measurements, supporting the viability of hyperspectral methods for precise, large-scale phosphorus monitoring (Chlouveraki et al., 2025; Raju and Subramoniam, 2024).

Figure 6.6 displays Ca distribution, with the HSC-based map in Figure 6.6 (b) yielding an RMSE of 4.9696 mg/100g. While this error is higher than that of P, it remains within acceptable limits for field-scale nutrient management, particularly given the natural variability of Ca in agricultural soils. Figure 6.7 focuses on Mg, where the HSC-based map in Figure 6.7 (b) achieves an RMSE of 2.6995 mg/100g, reflecting moderate predictive accuracy suitable for identifying broad Mg availability trends (Chlouveraki et al., 2025; Peng et al., 2021)

6.3.3. Remote sensing-based SC detection

Field crop growth patterns reveal valuable information about environmental conditions, particularly soil properties (Xue and Su, 2017; Zhang et al., 2019). Plant responses can manifest as severe deficiencies visible to the naked eye (RGB spectrum) or as subtle differences detectable only in specific non-visible wavelengths. In this study, wheat field assessment was conducted through vegetation appearance analysis and crop density quantification using FVC.

Table 6.2 presents the subplot treatment average FVC values across five critical growth stages. The growth stages are displayed in the first row, while SC treatments are listed in the first column. A distinct temporal pattern emerges across all SC treatments: FVC increases from the Tillering stage through Pinnacle stage, reaching maximum values at the Heading/Beginning of flowering stage. This pattern then shifts as FVC decreases by 6-9% during the Milk formation stage, followed by a modest 1-4% increase during the final Milk ripening stage. This phenological pattern reflects normal wheat development dynamics, where vegetative growth peaks at Heading before resources are redirected toward grain development (White and Edwards, 2007).

At the Tillering stage, FVC patterns across SC treatments indicated an inverse relationship between SC and vegetation cover. The Control treatment exhibited the highest FVC, showing approximately a 5% difference compared to BD1 (the most compacted) and a 1% difference relative to both BD2 and BD3 treatments. Notably, BD4 and Control treatments displayed nearly equivalent FVC values during Tillering, implying that HSC monitoring effectively detected SC-induced differences in early crop development under the experimental conditions. Visual evidence supporting these Tillering stage results can be found in Figure 6.8. The images illustrate progressively increasing crop cover from BD1 (sparsest) shown in Figure 6.8 (a), through BD2 in Figure 6.8 (b), and BD3 in Figure 6.8 (c), with BD4 in Figure 6.8 (d) and Control in Figure 6.8 (e) exhibiting the most extensive vegetation cover.

Table 6.2: Remote sensing-based wheat development monitoring using FVC

Bulk density	**Tillering**	**Pinnacle**	**Heading/ Beginning of flowering**	**Milk formation**	**Milk ripening**
BD1	0.8051 ± 0.04	0.9061 ± 0.05	0.9751 ± 0.02	0.9164 ± 0.02	0.9263 ± 0.00
BD2	0.8410 ± 0.08	0.9302 ± 0.04	0.9772 ± 0.02	0.9186 ± 0.03	0.9561 ± 0.01
BD3	0.8498 ± 0.03	0.9593 ± 0.02	0.9839 ± 0.01	0.9267 ± 0.03	0.9335 ± 0.03
BD4	0.8526 ± 0.04	0.9610 ± 0.02	0.9887 ± 0.00	0.9226 ± 0.02	0.9276 ± 0.02
Control	0.8531 ± 0.5	0.9356 ± 0.03	0.9690 ± 0.02	0.8794 ± 0.05	0.9158 ± 0.02

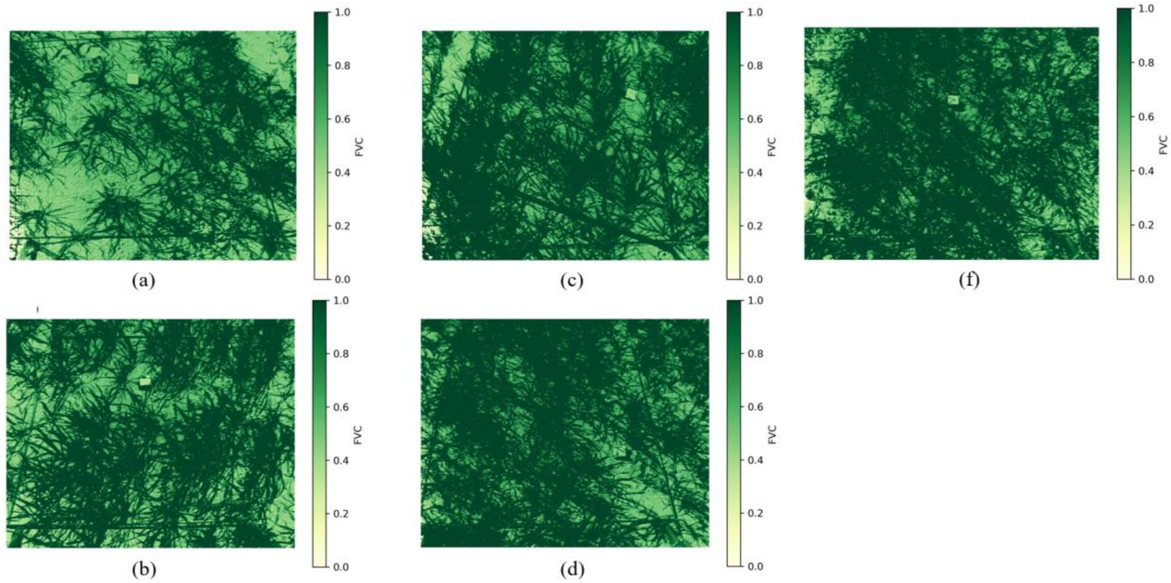

Figure 6.8: Tillering growth stage FVC indicating SC impact on wheat development (a) BD1, (b) BD2, (c) BD3, (d) BD4, (e) Control

During the Pinnacle stage, FVC patterns shifted significantly, with moderate SC levels (BD3 and BD4) displaying the highest values. These treatments exceeded Control by 2-3% and the two most compacted subplots (BD1 and BD2) by 2-6%. This pattern suggests enhanced root system development at this stage in moderately compacted soils, potentially benefiting from improved soil-root contact that optimizes nutrient and moisture transport pathways (Correa et al., 2019; Lipiec and Hatano, 2003). This advantage of moderate compaction continued through the Heading/Beginning of flowering stage, though percentage differences between BD3/BD4 and other treatments decreased to approximately 1%, as shown in Table 6.2.

Similar patterns persisted during Milk formation, but with the Control subplot lagging approximately 5% behind BD3 and BD4, and 4% behind the two most compacted subplots. This unexpected pattern likely results from differential resource allocation; Control subplots plants were channeling resources predominantly into grain formation (as evidenced in Table 5.5), while highly compacted treatments continued vegetative growth to compensate for developmental limitations imposed by SC stress (Asseng et al., 2011; Sadras et al., 2005). By the Milk ripening stage, no discernible pattern remained, as senescence had initiated and wheat plants had begun withering across all treatments (Barraclough et al., 2010).

These findings indicate that the Tillering stage provides the most accurate window for monitoring sequential SC impacts on wheat using FVC. While Pinnacle and Heading stages show potential for SC differentiation, results during these periods tend to favor areas with SC levels approaching optimum conditions for root-soil interactions rather than directly reflecting compaction stress. This temporal specificity in RS-based SC assessment has significant implications for PA timing and intervention strategies.

6.3.4. HSC-based SC assessment: Field applications and future directions

The framework for HSC-based SC detection extends beyond FVC analysis by incorporating soil physical properties, chemical properties, and crop growth data that demonstrate significant response to SC. This comprehensive approach builds upon the analysis presented in Chapter 5, where Kruskal-Wallis ANOVA and H-statistic analyses were employed to evaluate the dependency relationships of all measured and monitored properties across five critical wheat growth stages.

Table 6.3 presents detailed results of property selection using PLSR feature selection methodology, which was informed by the dependency test outcomes. The table is structured with data groups in the first column: 'All' representing the complete set of combined properties; 'Chemical' encompassing soil chemical properties exclusively; 'Physical' designating soil physical properties only; and 'Crop growth data' containing plant development parameters. These explanatory variable groupings are evaluated against the five sequential growth stages presented in the first row. For each combination, the selected features are accompanied by coefficient of determination (R^2) values and Root Mean Square Error (RMSE) metrics, quantifying the accuracy with which the selected properties explain variance in SC as measured by BD.

This methodological approach enables identification of the most relevant parameters for SC assessment at each developmental stage, providing a foundation for temporally-specific RS protocols in PA applications.

Table 6.3: GTD-based feature selection for bulk density prediction using PLSR

Selection of properties	Model score	Tillering	Pinnacle	Heading/ Beginning of flowering	Milk formation	Milk ripening
All		P, Mg, RGR_Crop, VMC, RGR_Root, Height, Crop_MC, SPAD, CEC	MCW, Temp	Mg_w	Ca	K
	R^2/ RMSE	0.702/ 0.034	0.45/ 0.05	0.54/ 0.04	0.33/ 0.05	0.33/ 0.05

Selection of properties	Model score	Tillering	Pinnacle	Heading/ Beginning of flowering	Milk formation	Milk ripening
Chemical		P, Mg	P, Mg	P, Mg	K	Ca
	R^2/ RMSE	0.50/ 0.04	0.50/ 0.04	0.52/ 0.04	0.41/0.05	0.39/0.05
Physical		MCW, VMC	MCD, Temp	VCM, Temp	MCW, Temp, VMC	MCD
	R^2/ RMSE	0.72/ 0.03	0.20/ 0.06	-0.01/ 0.06	-0.14/ 0.07	0.13/ 0.06
Crop growth data		Crop_MC	SPAD, Height	RGR_Crop, Crop_MC, RGR_Root, Height	Crop_MC, RGR_Root, SPAD	RGR_Root
	R^2/ RMSE	-0.004/ 0.06	-0.12/ 0.066	0.26/ 0.05	0.17/ 0.06	-0.03/ 0.07

At the Tillering stage, soil physical properties demonstrated the strongest predictive capacity for SC, achieving an R^2 value of 0.72 with a corresponding RMSE of 0.03 Mg/m³. This was closely followed by the comprehensive "All" category, which yielded an R^2 of 0.70 and RMSE of 0.034 Mg/m³. Despite the "All" category incorporating nine combined physical-chemical-crop parameters, the superior performance of just two parameters under the "Physical" category justified their selection for modeling purposes. This finding aligns with established research by Hu et al. (2020) and Hosseini et al. (2016) that confirms soil moisture content, which was the selected feature under "Physical" in Table 6.3, significantly influences soil BD levels through its effects on soil particle cohesion and aggregation.

By the Pinnacle stage, a notable shift in predictive parameters occurred. Soil chemical properties, specifically P and Mg, emerged as the only selected features achieving an R^2 of 0.50. All other property groups showed diminished predictive capacity, with selected crop growth data (SPAD chlorophyll readings and plant height) recording negative R^2 values. The influence of soil physical properties declined dramatically during this developmental stage, suggesting a transition in how SC manifests in the plant-soil system as wheat development progresses.

At the Heading/Beginning of flowering stage, cumulative soil chemical properties level demonstrated stronger predictive power, with the same P and Mg features selected, yielding an R^2 of 0.52 and RMSE of 0.04 Mg/m³. All other property groups exhibited R^2 values below 0.5 at this growth stage. This pattern continued through the later growth stages, with cumulative soil chemical properties level consistently selected as the best predictors. At the Milk formation stage, K emerged as the strongest predictor ($R^2 = 0.41$, RMSE = 0.05 Mg/m^3), followed by Ca ($R^2 = 0.33$, RMSE = 0.05 Mg/m^3). During the final Milk ripening stage, Ca ($R^2 = 0.39$, RMSE = 0.05 Mg/m^3) and K ($R^2 = 0.35$, RMSE = 0.05 Mg/m^3) remained the dominant predictive elements.

This temporal shift from physical to chemical soil properties as predictors of compaction effects aligns with research by Lipiec and Hatano (2003) and Colombi et al. (2018), who demonstrated that SC initially affects soil physical properties before manifesting in nutrient availability and uptake patterns. As plant roots encounter mechanical impedance in compacted soils, nutrient acquisition pathways, particularly those involving relatively immobile nutrients like P and cations such as K, Ca, and Mg, become increasingly compromised (Nawaz et al., 2013; Tracy et al., 2011).

This feature selection analysis, conducted using GTD-based parameters and PLSR, provides valuable insight into which properties might effectively support HSC-based SC modeling as presented in Table 6.4. The sequential transition from moisture-dominant to nutrient-dominant predictors throughout the growing season suggests that temporal specificity must be considered when developing RS protocols for SC assessment in wheat production systems.

The HSC-based SC models presented in Table 6.4 represent the best-performing models at each crop growth stage, informed by the GTD-based feature selection in Table 6.3. Additional models generated from alternative feature combinations are documented in Tables D7-D11, Appendix D.

At the Tillering stage, the HSC-based equivalent of the strong GTD-based model ($R^2 = 0.72$) performed poorly with an R^2 of -0.0065 as shown in Table 6.4. This substantial performance gap can be attributed to the limited ability of HSC to accurately predict soil moisture content during early growth, a critical factor for SC assessment. As documented in Table D6 (Appendix D), HSC-based soil moisture prediction at the Tillering stage was notably weak (R^2 = -0.01 to 0.06), with optimal moisture prediction occurring during the Milk ripening stage ($R^2 = 0.81$). Despite soil physical properties (particularly soil moisture content) being identified as the most important explanatory variables for SC, HSC's capacity to measure these parameters accurately during early growth was limited. This limitation likely stems from sparse vegetation cover at the Tillering stage, providing insufficient spectral information for reliable soil moisture estimation through vegetation appearance (Sadeghi et al., 2017). Nevertheless, the potential exists to supplement HSC data with in-situ soil moisture sensors as described in Chapter 3 to achieve accuracy comparable to GTD-based models (Babaeian et al., 2019).

The Pinnacle stage models, detailed in Table D8 (Appendix D), showed improvement with the best-performing parameter combination, MCD from physical properties and P from chemical properties, achieving an R^2 of 0.24 and RMSE of 0.054 Mg/m³. While representing significant improvement from the Tillering stage, this performance remains suboptimal. The moderate performance can be attributed to the developmental shift where wheat growth begins to favor moderate SC levels rather than displaying a simple inverse relationship between compaction and development. Thus, despite enhanced HSC sensing capability due to increased vegetation cover, the biological tendency toward optimal SC defeats straightforward model development.

The Heading/Beginning of flowering stage produced the most effective HSC-based SC model, despite being influenced by optimal SC effects. Enhanced HSC sensing capabilities resulting from combined vegetation development and peak SPAD chlorophyll levels (as shown in Figure 5.3, Chapter 5) contributed to this success. The optimal model at this stage incorporated magnesium absorption (Mg_w) in crop biomass measured on a wet basis, achieving an R^2 of 0.45 and RMSE of 0.045 Mg/m³, as presented in Table 6.4.

Models for the final two growth stages featured Ca and K as key parameters. The Milk formation stage model achieved an R^2 of 0.38 with RMSE of 0.051 Mg/m³, while the Milk ripening stage produced comparable results with R^2 of 0.37 and RMSE of 0.052 Mg/m³.

Table 6.4: HSC-based BD predictions using LR/MLR

Growth Stage	**Combination**	**MLR/LR-HSC**	
		R^2	RMSE
Tillering	MCW+VMC→BD	-0.0065	0.0629
Pinnacle	MCD+P →BD	0.2365	0.0543
Heading/Beginning of flowering	Mg_w →BD	0.4518	0.0451
Milk formation	Ca + K →BD	0.3832	0.0510
Milk Ripening	Ca + K →BD	0.3714	0.0515

This comprehensive HSC-based analysis reveals that while soil physical properties are strong indicators of SC at the Tillering stage, sparse vegetation establishment limits spectral information acquisition, preventing development of robust RS models (Kong et al., 2018). The optimal growth stage for HSC-based SC assessment occurs during Heading/Beginning of flowering, confirming the SPAD measurement patterns observed in this experiment.

6.3.4.1. Implementation guidelines

For the practical implementation of these recommendations in the field, various approaches are advised:

1. *Growth stage selection*:

   i. For new fields with spares or less vegetation, complement HSC data with in-situ soil moisture sensors,

   ii. For fields at the Heading/Beginning of flowering stage, HSC-based assessment is recommended by utilizing magnesium absorption indicators, and

   iii. For late-season assessment in wheatfields, focus on calcium and potassium spectral signatures.

2. *Hybrid sensing strategy*:

   i. Install soil moisture sensors at field edges or representative sampling locations,

   ii. Combine the sensor data with an overhead HSC image data taken at optimal growth stages, and

   iii. Integrate data streams using the models provided in Table 6.4.

3. *Field condition considerations*:

   i. For fields with varied initial SC, account for the "optimal SC phenomenon" when explaining results,

   ii. For fields with uniform initial SC, models can be used directly without modification, and

   iii. Consider soil type differences when adapting models to new locations (Keller et al., 2019)

4. *Temporal implementation*:

   i. Schedule primary SC assessment during the Heading/Beginning of flowering growth stage,

   ii. Use early-season assessments as initial indicators only, and

   iii. Conduct late-season assessment to inform next-season management decisions,

These implementation guidelines provide a practical framework for adopting HSC-based SC assessment within PA methods while acknowledging the merit and demerits identified through this research.

6.4.Conclusions

This chapter mainly consists of creating a framework for managing SC specifically for wheat. It uses field experimental data to find the best SC level to help farmers understand how SC affects wheat growth at different stages. This framework gives helpful recommendations for managing SC better and helps farmers avoid problems like soil getting too compacted while boosting wheat yields.

One important part of this study is how it predicts soil bulk density (BD) using HSC data alongside other soil and crop information. This method shows that RS can give reliable SC estimates, making it a quicker and easier option than regular field tests. By including these HSC models in the soil management framework, farmers can monitor soil compaction and make timely decisions about tillage.

The research also studied how crops and soil nutrients interact, resulting in the development of residual nutrient maps that show how nutrients and compaction vary across the field. These maps could help in implementing targeted fertilizer application, which could save resources and reduce environmental impact. By combining advanced RS with regular soil testing, assessing soil condition becomes simpler and cheaper.

Using vegetative indices like fractional vegetation cover (FVC) to monitor SC highlights how useful it is to mix crop and soil data for managing fields. This method cuts down on the need for multiple sampling and allows for real-time monitoring during the growing season.

In the future, more research should validate this framework and the SC models with different wheat types, soil kinds, and weather conditions to make them more effective. Also, integrating this framework into existing farm management systems could help farmers make informed decisions based on changing conditions. Overall, this research is a good step towards improving wheat farming sustainably with smart and data-driven soil management practices that boost yields while keeping the soil healthy for the future.

CHAPTER 7. CONCLUSIONS AND RECOMMENDATIONS

7.1.Synthesis of key findings

This thesis examines how the use of hyperspectral camera (HSC) technology with PA can help address SC issues in wheat farming. The research followed a two-phase testing approach that demonstrates the possibility of assessing SC without needing to collect samples in the traditional manner, and shows that this information can be valuable for planning PT.

In the first part of the experiment, it was found that RS using HSCs can effectively measure soil properties important for evaluating compaction levels. The study highlighted moisture levels and organic matter content (OMC) as key factors that can be measured accurately through spectral data, facilitating the creation of predictive models for SC without invasive sampling methods. The optimized model based on the GTD had an overall error below 5%, while the optimized model based on HSC data had an overall error of about 10%.

In the second part, field trials with spring wheat identified a new ideal SC level at a BD of 1.24 Mg/m^3. This level led to a 12% increase in wheat yields compared to fields that were plowed uniformly (Control subplot). These results challenge the common belief that less compaction is always better, showing that there are specific compaction levels that can help maximize yield for different crops.

Based on these findings, a decision framework was created specifically for wheat production. This framework takes hyperspectral data and turns it into actionable tillage plans aimed at attaining the optimal compaction levels needed for different areas of a field. Instead of using the same tillage method everywhere, this approach focuses on targeted interventions that suit the unique needs of the soil and crop.

Overall, the research suggests that using data from hyperspectral sensors for PT could improve wheat production while possibly lowering the negative environmental effects that come with traditional tillage practices. The methodology offers a solid base for combining advanced sensing technology with practical farming strategies.

7.2.Practical implications for precision tillage implementation

The research demonstrates effective methods for utilizing PT in farming activities. The new HSC-based approach would allow farmers to monitor SC in their fields without disrupting the soil ecosystem or causing the usual delays associated with traditional laboratory testing. This represents a significant improvement over conventional sampling, which is time-consuming and provides limited information.

Identifying the best compaction level for wheat (BD = 1.24 Mg/m^3) gives farmers a clear target for their tillage. Instead of trying to keep compaction to a minimum everywhere, they can do variable-depth tillage to reach this target in different parts of the field. This site-specific approach can reduce extra tillage work in regions of the field that are already good, which can save on fuel, reduce wear and tear on equipment, and lower costs.

To put this into practice, farmers would attach calibrated HSCs to drones or other farm machinery to check soil SC condition in real time. Then, they can adjust tillage depth automatically based on the data they get. Plus, the ability to measure moisture and organic matter adds more benefits for managing soil beyond just compaction. For this wheat-specific PT method to work well in the field, it needs some specific software, like ArcGIS, to turn complex data into easy-to-understand tillage suggestions. These suggestions are made to help farmers at all technological levels and are a key part of the decision support system for PT.

7.3.Economic feasibility assessment

The cost-effectiveness of adopting the HSC-based PT system comes down to key factors. The main difficulty is the upfront costs of the hyperspectral imaging device and the software needed to process the data. Nonetheless, it is important to weigh those costs against the possible benefits, which include:

1. Yield boosts of around 12% are seen in trials, making a real difference to farm profits.
2. Less need for tillage in areas where soil conditions are already good, leading to savings on fuel and less wear on equipment.
3. A potential better use of nutrients thanks to improved soil conditions, which could lower the amount of fertilizer needed.
4. A potential longer lifespan for equipment because it will be used less and will not wear out as fast.

A solid cost-benefit analysis should consider farm size, since bigger farms can spread out that initial investment over more land. For smaller farms, teaming up with others to share costs or using service providers might be a good way to access the technology without bearing the high initial cost.

Looking at the potential for yield increases, medium to larger wheat producers could see their investment pay off within 2-3 growing seasons, especially in areas where soil conditions are a big problem for yields.

7.4.Future research directions

Here are some possible research directions from this study:

1. *Crop-specific optimization*: Since different crops might require different compaction levels, it would be helpful to apply this research to major crops like corn, soybeans, and rice. This could create a useful database of ideal compaction targets for each staple crop.
2. *Temporal dynamics*: It would be interesting to look into how the best compaction levels (when undisturbed) could change over several growing seasons and with different weather. This would likely require long-term field tests.
3. *Technology integration*: Mixing hyperspectral data with other technologies, like ground-penetrating radar, could give a clearer picture of soil profiles, especially at depths greater than 0.30 m.
4. *Better camera technology*: Improvements in HSC technology, like quicker image capture and better resolution, could help fix the slow image capture issue (7.7 seconds per image). This would make field assessments quicker and support timely tillage advice.
5. *Handling light changes*: Researching ways to calibrate systems for varying light (sun radiation) conditions without manual calibration would improve how these methods work in the field.
6. *Assessing deeper soil*: Figuring out how to assess soil properties deeper than 0.30 m would make soil management more effective, especially for crops with deeper roots

7.5.Technology transfer pathways

Getting technology from research to real-life use takes some careful planning. Here are a few ideas:

1. *Demonstration farms*: Setting up local farms where people can see the technology being used. This would help farmers trust the new approach and see its real benefits.
2. *Collaboration with manufacturers*: Partnering with agriculture equipment makers to add new sensing technology to their existing equipment. This way, farmers can buy it through familiar channels.
3. *Simple tools*: Creating easy-to-use software that turns complex data into clear tillage suggestions. This means farmers don't need to be technology experts to benefit.
4. *Training programs*: Developing educational resources and training through extension services. This could help farmers and their advisors feel confident using the technology.
5. *Financial incentives*: Working with policymakers to create rewards for farmers who adopt PA practices, such as PT, that are better for the environment.

6. *Data sharing*: Starting a data collation and sharing platform, where farmers can share access to information about the technology. This would build a useful database that keeps improving recommendations.
7. *Different options for implementation*: Offering a range of packages, from basic assessments to full real-time systems. This way, farms of all sizes can find a fit for them.

These strategies can help turn research into practical applications, leading to more sustainable and productive farming systems.

Reference

References

Abayomi, Y. A., and Wright, D. (1999). Effects of water stress on growth and yield of spring wheat (Triticum aestivum L.) cultivars. *Tropical Agriculture*, *76*(2), 120–125. https://www.mendeley.com/catalogue/22353c24-3743-3c61-b897-209372b62e96/

Abdalla, M., Osborne, B., Lanigan, G., Forristal, D., Williams, M., Smith, P., and Jones, M. B. (2013). Conservation tillage systems: a review of its consequences for greenhouse gas emissions. *Soil Use and Management*, *29*(2), 199–209. https://doi.org/10.1111/sum.12030

Acuña, C. A., Martínez, E. J., Zilli, A. L., Brugnoli, E. A., Espinoza, F., Marcón, F., Urbani, M. H., and Quarin, C. L. (2019). Reproductive Systems in Paspalum: Relevance for Germplasm Collection and Conservation, Breeding Techniques, and Adoption of Released Cultivars. In *Frontiers in Plant Science* (Vol. 10). Frontiers Media S.A. https://doi.org/10.3389/fpls.2019.01377

Adamchuk, V. I., Hummel, J. W., Morgan, M. T., and Upadhyaya, S. K. (2004). On-the-go soil sensors for precision agriculture. *Computers and Electronics in Agriculture*, *44*(1), 71–91. https://doi.org/10.1016/j.compag.2004.03.002

Adamchuk, V. I., Ji, W., Rossel, R. V., Gebbers, R., and Tremblay, N. (2018). *Proximal Soil and Plant Sensing* (pp. 119–140). https://doi.org/10.2134/precisionagbasics.2016.0093

Agriculture Victoria Connect. (2024, December 25). *A brief guide to estimating crop yields*. Department of Energy, Environment and Climate Action. Andersen, M. N., Munkholm, L. J., and Nielsen, A. L. (2013). Soil compaction limits root development, radiation-use efficiency, and yield of three winter wheat (Triticum aestivum L.) cultivars. *Acta Agriculturae Scandinavica Section B: Soil and Plant Science*, *63*(5), 409–419. https://doi.org/10.1080/09064710.2013.789125

Arvidsson, J. (1999). Nutrient uptake and growth of barley as affected by soil compaction. *Plant and Soil*, *208*, 9–19. https://link.springer.com/article/10.1023/A:1004484518652#:~:text=Differences%20in%20plant%20nutrient%20concentrations,as%20the%20fertilizer%20are%20placed.

Arvidsson, J., and Håkansson, I. (2014). Response of different crops to soil compaction-Short-term effects in Swedish field experiments. *Soil and Tillage Research*, *138*, 56–63. https://doi.org/10.1016/j.still.2013.12.006

Askari, M., Abbaspour-Gilandeh, Y., Taghinezhad, E., El Shal, A. M., Hegazy, R., and Okasha, M. (2021). Applying the response surface methodology (Rsm) approach to predict the tractive performance of an agricultural tractor during semi-deep tillage. *Agriculture (Switzerland)*, *11*(11). https://doi.org/10.3390/agriculture11111043

Asseng, S., Foster, I., and Turner, N. C. (2011). The impact of temperature variability on wheat yields. *Global Change Biology*, *17*(2), 997–1012. https://doi.org/10.1111/j.1365-2486.2010.02262.x

Atwell, B. J. (1990). The effect of soil compaction on wheat during early tillering. *New Phytologist*, *115*(1), 29–35. https://doi.org/10.1111/j.1469-8137.1990.tb00918.x

Reference

Auernhammer, H. (2001). Precision farming-the environmental challenge. In *Computers and Electronics in Agriculture* (Vol. 30). www.elsevier.com/locate/compag

Babaeian, E., Sidike, P., Newcomb, M. S., Maimaitijiang, M., White, S. A., Demieville, J., Ward, R. W., Sadeghi, M., LeBauer, D. S., Jones, S. B., Sagan, V., and Tuller, M. (2019). A New Optical Remote Sensing Technique for High-Resolution Mapping of Soil Moisture. *Frontiers in Big Data*, *2*. https://doi.org/10.3389/fdata.2019.00037

Baghdadi, N., Cresson, R., El Hajj, M., Ludwig, R., and La Jeunesse, I. (2012). Estimation of soil parameters over bare agriculture areas from C-band polarimetric SAR data using neural networks. *Hydrology and Earth System Sciences*, *16*(6), 1607–1621. https://doi.org/10.5194/hess-16-1607-2012

Barber, S. A. (1995). *Soil Nutrient Bioavailability: A Mechanistic Approach* (2nd ed.). John Wiley.

Barnes, E. M., Clarke, T. R., Richards, S. E., Colaizzi, P. D., Haberland, J., Kostrzewski, M., Waller, P., Choi, C., Riley, E., Thompson, T., Lascano, R. J., Li, H., and Moran, M. S. (2000). *Coincident detection of crop water stress, nitrogen status and canopy density using ground-based multispectral data*. https://www.tucson.ars.ag.gov/unit/publications/PDFfiles/1356.pdf

Barraclough, P. B., Howarth, J. R., Jones, J., Lopez-Bellido, R., Parmar, S., Shepherd, C. E., and Hawkesford, M. J. (2010). Nitrogen efficiency of wheat: Genotypic and environmental variation and prospects for improvement. *European Journal of Agronomy*, *33*(1), 1–11. https://doi.org/10.1016/j.eja.2010.01.005

Bartholomeus, H. M., Schaepman, M. E., Kooistra, L., Stevens, A., Hoogmoed, W. B., and Spaargaren, O. S. P. (2008). Spectral reflectance based indices for soil organic carbon quantification. *Geoderma*, *145*(1–2), 28–36. https://doi.org/10.1016/j.geoderma.2008.01.010

Basso, B., Shuai, G., Zhang, J., and Robertson, G. P. (2019). Yield stability analysis reveals sources of large-scale nitrogen loss from the US Midwest. *Scientific Reports*, *9*(1). https://doi.org/10.1038/s41598-019-42271-1

Batey, T. (2009). Soil compaction and soil management - A review. In *Soil Use and Management* (Vol. 25, Issue 4, pp. 335–345). https://doi.org/10.1111/j.1475-2743.2009.00236.x

Bayer Group. (2024). *Corn Nutrition*. Crop Science United States. https://www.cropscience.bayer.us/articles/bayer/corn-nutrition-101

Becker, L. (2024). *The Tools of the First Farmers: Exploring Agricultural Innovation in Antiquity*. Ancient History Guide. https://ancienthistoryguide.com/the-tools-of-the-first-farmers-agricultural-innovation-in-antiquity/

Ben-Dor, E., Chabrillat, S., Demattê, J. A. M., Taylor, G. R., Hill, J., Whiting, M. L., and Sommer, S. (2009). Using Imaging Spectroscopy to study soil properties. *Remote Sensing of Environment*, *113*(SUPPL. 1). https://doi.org/10.1016/j.rse.2008.09.019

Reference

Bengough, A. G., McKenzie, B. M., Hallett, P. D., and Valentine, T. A. (2011). Root elongation, water stress, and mechanical impedance: A review of limiting stresses and beneficial root tip traits. In *Journal of Experimental Botany* (Vol. 62, Issue 1, pp. 59–68). https://doi.org/10.1093/jxb/erq350

Bengough, A. G., Mullins, C. E., and Wilson, G. (1997). Estimating soil frictional resistance to metal probes and its relevance to the penetration of soil by roots. *European Journal of Soil Science*, *48*(4), 603–612. https://doi.org/10.1111/j.1365-2389.1997.tb00560.x

Bengough, A. G., Mullins, C. E., Wilson, G., and Wallace, J. (1991). The Design, Construction and Use of a Rotating-tip Penetrometer. *J. Agric. Engng Res*, *48*, 223–227. https://doi.org/10.1016/0021-8634(91)80017-9

Benmoshe, N. (2025). A Simple Solution for the Inverse Distance Weighting Interpolation (IDW) Clustering Problem. *Sci*, *7*(1), 30. https://doi.org/10.3390/sci7010030

Beylich, A., Oberholzer, H. R., Schrader, S., Höper, H., and Wilke, B. M. (2010). Evaluation of soil compaction effects on soil biota and soil biological processes in soils. *Soil and Tillage Research*, *109*(2), 133–143. https://doi.org/10.1016/j.still.2010.05.010

Bhayal, L., Kewat, M. L., Aakash, Jha, A. K., Bhayal, D. and Badkul, A. J. (2022). Effect of Sowing Time and Nutrient Management on Physiological Parameters of Wheat. *International Journal of Economic Plants*, *9*(Nov 4), 271–275. https://doi.org/10.23910/2/2022.ijep0484

Biering, D. (2025). *History of Agriculture Equipment: Important Developments and Examples*. TriStar Plastics Corp. https://www.tstar.com/blog/history-of-agriculture-equipment-important-developments-and-examples

Big Tractor Power. (2001). *Massey Ferguson 4wd Tractor History*. Big Tractor Power. http://bigtractorpower.com/masseyferguson4wdhistory.htm

Bonfil, D. J., Karnieli, A., Raz, M., Mufradi, I., Asido, S., Egozi, H., Hoffman, A., and Schmilovitch, Z. (2004). Decision support system for improving wheat grain quality in the Mediterranean area of Israel. *Field Crops Research*, *89*(1), 153–163. https://doi.org/10.1016/j.fcr.2004.01.017

Bongiovanni, R., and Lowenberg-Deboer, J. (2004). Precision Agriculture and Sustainability. *Precision Agriculture*, *5*, 359–387. https://link.springer.com/article/10.1023/B:PRAG.0000040806.39604.aa

Bouwman, L., Goldewijk, K. K., Van Der Hoek, K. W., Beusen, A. H. W., Van Vuuren, D. P., Willems, J., Rufino, M. C., and Stehfest, E. (2013). Exploring global changes in nitrogen and phosphorus cycles in agriculture induced by livestock production over the 1900-2050 period. *Proceedings of the National Academy of Sciences of the United States of America*, *110*(52), 20882–20887. https://doi.org/10.1073/pnas.1012878108

Bradley, R. S., Kindred, D., Blake, J., and Berry, P. (2008). *The wheat growth guide* (C. Edwards and G. Dodgson, Eds.; 2nd ed.). Agriculture and Horticulture Development Board. https://farmpep.net/sites/default/files/2022-12/Wheat%20Growth%20Guide_2008_UK%20%281%29.pdf

Reference

Breiman, L. (2001). *Random Forests* (Vol. 45). https://doi.org/https://doi.org/10.1023/A:1010933404324

British Columbia Ministry of Agriculture. (2015). *Soil Compaction A Review of its Origin and Characteristics: Factsheet 613.100-1*. https://www2.gov.bc.ca/assets/gov/farming-natural-resources-and-industry/agriculture-and-seafood/agricultural-land-and-environment/soil-nutrients/613100-1_soil_compaction.pdf

Bronick, C. J., and Lal, R. (2005). Soil structure and management: A review. In *Geoderma* (Vol. 124, Issues 1–2, pp. 3–22). https://doi.org/10.1016/j.geoderma.2004.03.005

Bronson, K. F., Booker, J. D., Officer, S. J., Lascano, R. J., Maas, S. J., Searcy, S. W., and Booker, J. (2005). Apparent Electrical Conductivity, Soil Properties and Spatial Covariance in the U.S. Southern High Plains. *Precision Agriculture*, *6*(3), 297–311. https://doi.org/10.1007/s11119-005-1388-6

Brouwer, R. (1983). Functional equilibrium: sense or nonsense? *Netherlands Journal of Agricultural Science*, *31*(4), 335–348. https://doi.org/10.18174/njas.v31i4.16938

Cakmak, I., and Yazici, A. (2010). *Magnesium: A forgotten element in crop production*. https://www.researchgate.net/publication/291869977

Cambardella, C. A., Moorman, T. B., Novak, J. M., Parkin, T. B., Karlen, D. L., Turco, R. F., and Konopka, A. E. (1994). Field-Scale Variability of Soil Properties in Central Iowa Soils. *Soil Science Society of America Journal*, *58*(5), 1501–1511. https://doi.org/10.2136/sssaj1994.03615995005800050033x

Cambi, M., Certini, G., Neri, F., and Marchi, E. (2015). The impact of heavy traffic on forest soils: A review. In *Forest Ecology and Management* (Vol. 338, pp. 124–138). Elsevier. https://doi.org/10.1016/j.foreco.2014.11.022

Campbell, B. M. S., and Bartley, K. (2007). *The Agricultural History Review Volume 55 Part I 2007*. https://www.bahs.org.uk/AGHR/VOLUMES/AGHR55.pdf

Carlson, T. N., and Ripley, D. A. (1997). On the relation between NDVI, fractional vegetation cover, and leaf area index. *Remote Sensing of Environment*, *62*(3), 241–252. https://doi.org/10.1016/S0034-4257(97)00104-1

Cassel, D. K. (1983). Spatial and Temporal Variability of Soil Physical Properties Following Tillage of Norfolk Loamy Sand. *Soil Science Society of America Journal*, *47*(2), 196–201. https://doi.org/10.2136/sssaj1983.03615995004700020004x

Castaldi, F., Castrignanò, A., and Casa, R. (2016). A data fusion and spatial data analysis approach for the estimation of wheat grain nitrogen uptake from satellite data. *International Journal of Remote Sensing*, *37*(18), 4317–4336. https://doi.org/10.1080/01431161.2016.1212423

Castaldi, F., Chabrillat, S., Don, A., and van Wesemael, B. (2019). Soil organic carbon mapping using LUCAS topsoil database and Sentinel-2 data: An approach to reduce soil moisture and crop residue effects. *Remote Sensing*, *11*(18). https://doi.org/10.3390/rs11182121

Reference

Chai, T., and Draxler, R. R. (2014). Root mean square error (RMSE) or mean absolute error (MAE)? – Arguments against avoiding RMSE in the literature. *Geoscientific Model Development*, *7*(3), 1247–1250. https://doi.org/10.5194/gmd-7-1247-2014

Chamen, W. C. T., Moxey, A. P., Towers, W., Balana, B., and Hallett, P. D. (2015). Mitigating arable soil compaction: A review and analysis of available cost and benefit data. *Soil and Tillage Research*, *146*(PA), 10–25. https://doi.org/10.1016/j.still.2014.09.011

Chan, K. Y. (2001). An overview of some tillage impacts on earthworm population abundance and diversity Ð implications for functioning in soils. *Soil and Tillage Research*, *57*, 179–191. https://doi.org/10.1016/S0167-1987(00)00173-2

Chen, X., Cui, Z., Fan, M., Vitousek, P., Zhao, M., Ma, W., Wang, Z., Zhang, W., Yan, X., Yang, J., Deng, X., Gao, Q., Zhang, Q., Guo, S., Ren, J., Li, S., Ye, Y., Wang, Z., Huang, J., … Zhang, F. (2014). Producing more grain with lower environmental costs. *Nature*, *514*(7253), 486–489. https://doi.org/10.1038/nature13609

Chlouveraki, E., Katsenios, N., Efthimiadou, A., Lazarou, E., Kounani, K., Papakonstantinou, E., Vlachakis, D., Kasimati, A., Zafeiriou, I., Espejo-Garcia, B., and Fountas, S. (2025). Estimation of soil properties using Hyperspectral imaging and Machine learning. *Smart Agricultural Technology*, *10*, 100790. https://doi.org/10.1016/j.atech.2025.100790

Chowdhury, D. (2025). *The Evolution of Tractors and Their Impact on Modern Agriculture*. https://www.researchgate.net/publication/387862246

Claassen, R., Duquette, E. N., and Smith, D. J. (2018). Additionality in U.S. Agricultural Conservation Programs. *Land Economics*, *94*(1), 19–35. https://doi.org/10.3368/le.94.1.19

Colombi, T., Braun, S., Keller, T., and Walter, A. (2017). Artificial macropores attract crop roots and enhance plant productivity on compacted soils. *Science of the Total Environment*, *574*, 1283–1293. https://doi.org/10.1016/j.scitotenv.2016.07.194

Colombi, T., & Keller, T. (2019). Developing strategies to recover crop productivity after soil compaction—A plant eco-physiological perspective. *Soil and Tillage Research*, *191*, 156–161. https://doi.org/10.1016/j.still.2019.04.008

Colombi, T., Torres, L. C., Walter, A., and Keller, T. (2018). Feedbacks between soil penetration resistance, root architecture and water uptake limit water accessibility and crop growth – A vicious circle. *Science of The Total Environment*, *626*, 1026–1035. https://doi.org/10.1016/j.scitotenv.2018.01.129

Correa, J., Postma, J. A., Watt, M., & Wojciechowski, T. (2019). Soil compaction and the architectural plasticity of root systems. *Journal of Experimental Botany*, *70*(21), 6019–6034. https://doi.org/10.1093/jxb/erz383

Cortes, C., & Vapnik, V. (1995). Support-vector networks. *Machine Learning*, *20*(3), 273–297. https://doi.org/10.1007/BF00994018

Corwin, D. L., and Lesch, S. M. (2005). Apparent soil electrical conductivity measurements in agriculture. *Computers and Electronics in Agriculture*, *46*(1–3), 11–43. https://doi.org/10.1016/j.compag.2004.10.005

Reference

Cresswell, H., and Kirkegaard, J. (1995). Subsoil amelioration by plant-roots - the process and the evidence. *Soil Research*, *33*(2), 221. https://doi.org/10.1071/SR9950221

Crittenden, S. J., Eswaramurthy, T., de Goede, R. G. M., Brussaard, L., and Pulleman, M. M. (2014). Effect of tillage on earthworms over short- and medium-term in conventional and organic farming. *Applied Soil Ecology*, *83*, 140–148. https://doi.org/10.1016/j.apsoil.2014.03.001

Crossett, R. N., and Campbell, D. J. (1975). The effects of ethylene in the root environment upon the development of barley. *Plant and Soil*, *42*(2), 453–464. https://doi.org/10.1007/BF00010020

Curran, P. J. (1989). Remote sensing of foliar chemistry. *Remote Sensing of Environment*, *30*(3), 271–278. https://doi.org/10.1016/0034-4257(89)90069-2

Daba, N. A., Li, D., Huang, J., Han, T., Zhang, L., Ali, S., Khan, M. N., Du, J., Liu, S., Legesse, T. G., Liu, L., Xu, Y., Zhang, H., and Wang, B. (2021). Long-term fertilization and lime-induced soil ph changes affect nitrogen use efficiency and grain yields in acidic soil under wheat-maize rotation. *Agronomy*, *11*(10). https://doi.org/10.3390/agronomy11102069

Davis, J. G., Whiting, D., Oleszak, H., Hammond, E., and Murgel, J. (2024). *Soil-Amendments-7.235*. https://extension.colostate.edu/topic-areas/yard-garden/choosing-a-soil-amendment/#:~:text=A%20soil%20amendment%20is%20any,a%20better%20environment%20for%20roots.

De Corato, U. (2023). Governance of soil amendment to enhance suppression to soil-borne plant pathogens from a long-term perspective. In *Applied Soil Ecology* (Vol. 182). Elsevier B.V. https://doi.org/10.1016/j.apsoil.2022.104721

De Sousa Mendes, W., Demattê, J. A. M., E Barros, A. S., Salazar, D. F. U., and Amorim, M. T. A. (2020). Geostatistics or machine learning for mapping soil attributes and agricultural practices. *Revista Ceres*, *67*(4), 330–336. https://doi.org/10.1590/0034-737X202067040010

Demetriades-Shah, T. H., Steven, M. D., and Clark, J. A. (1990). High resolution derivative spectra in remote sensing. *Remote Sensing of Environment*, *33*(1), 55–64. https://doi.org/10.1016/0034-4257(90)90055-Q

Derpsch, R., Friedrich, T., Kassam, A., and Hongwen, L. (2010). Current status of adoption of no-till farming in the world and some of its main benefits. *International Journal of Agricultural and Biological Engineering*, *3*(1), 1–25. https://doi.org/10.3965/j.issn.1934-6344.2010.01.001-025

Destain, M.-F., Roisin, C., Dalcq, A.-S., and Mercatoris, B. C. N. (2016). Effect of wheel traffic on the physical properties of a Luvisol. *Geoderma*, *262*, 276–284. https://doi.org/10.1016/j.geoderma.2015.08.028

Dexter, A. R. (1987). Mechanics of root growth. *Plant and Soil*, *98*, 303. https://link.springer.com/article/10.1007/BF02378351

Reference

Dexter, A. R. (2003). *Soil physical quality Part I. Theory, effects of soil texture, density, and organic matter, and effects on root growth*. https://doi.org/10.1016/j.geodermaa.2003.09.005

Diao, X., Silver, J., and Takeshima, H. (2016). *Agricultural Mechanization and Agricultural Transformation*. www.acetforafrica.org

Dierauer, H. (2017). *Rolling of grains to prevent winter kill damage Problem*. https://orgprints.org/id/eprint/31034/19/PA_030_Roll_winter_grains_final_QR.pdf

Dörner, J., Bravo, S., Stoorvogel, M., Dec, D., Valle, S., Clunes, J., Horn, R., Uteau, D., Wendroth, O., Lagos, L., and Zúñiga, F. (2022). Short-term effects of compaction on soil mechanical properties and pore functions of an Andisol. *Soil and Tillage Research*, *221*. https://doi.org/10.1016/j.still.2022.105396

Douaik, A., Van Meirvenne, M., and Tóth, T. (2006). Temporal Stability of Spatial Patterns of Soil Salinity Determined from Laboratory and Field Electrolytic Conductivity. *Arid Land Research and Management*, *20*(1), 1–13. https://doi.org/10.1080/15324980500369392

Drew, M. C. (1975). COMPARISON OF THE EFFECTS OF A LOCALISED SUPPLY OF PHOSPHATE, NITRATE, AMMONIUM AND POTASSIUM ON THE GROWTH OF THE SEMINAL ROOT SYSTEM, AND THE SHOOT, IN BARLEY. *New Phytologist*, *75*(3), 479–490. https://doi.org/10.1111/j.1469-8137.1975.tb01409.x

Duiker, S. W. (2005). *Effects of Soil Compaction 2 Effects of soil compaction*. https://extension.psu.edu/effects-of-soil-compaction

Dunbabin, V. M., Diggle, A. J., Rengel, Z., and Van Hugten, R. (2002). Modelling the interactions between water and nutrient uptake and root growth. In *Plant and Soil* (Vol. 239). http://www.clima.uwa.edu.au/research.

E-Ashid, S., and Sheikh, K. H. (1977). Response of Wheat to Different Levels of Soil Compaction. In *Phyton (Austria)* (Vol. 18). www.biologiezentrum.at

Eavis, B. W., Ratliff, L. F., and Taylor, H. M. (1969). Use of a Dead-Load Technique to Determine Axial Root Growth Pressure [1]. *Agronomy Journal*, *61*(4), 640–643. https://doi.org/10.2134/agronj1969.00021962006100040048x

Fadat, Y. (2024). *The History of Farming Equipments: From Ancient Tools to Modern Innovations*. Evolution of the Progress. https://evolutionoftheprogress.com/history-of-farming-equipment/?utm_source=chatgpt.com

FAO. (2020). Emissions due to agriculture Global, regional, and country trends. *FAOSTAT Analytical Brief Series* , *18*. https://www.fao.org/3/cb3808en/cb3808en.pdf

FAO. (2022). The State of Food and Agriculture 2022. Leveraging automation in agriculture for transforming agrifood systems. In *The State of Food and Agriculture 2022*. FAO. https://doi.org/10.4060/cb9479en

FAO. (2023a). *Standard operating procedure for soil bulk density, cylinder method*. https://doi.org/10.4060/cc7568en

FAO. (2023b). The State of Food and Agriculture 2023 – Revealing the true cost of food to transform agrifood systems. In *The State of Food and Agriculture 2023*. FAO. https://doi.org/10.4060/cc7724en

Feng, C. H., Arai, H., and Rodríguez-Pulido, F. J. (2023). Hyperspectral Imaging Combined with Chemometrics Analysis for Monitoring the Textural Properties of Modified Casing Sausages with Differentiated Additions of Orange Extracts. *Foods*, *12*(5). https://doi.org/10.3390/foods12051069

Feng, X., Huai, Y., Kang, S., Yang, L., Li, Y., Feng, J., Zhang, Z., Maw, M. J. W., Cui, Z., and Ning, P. (2024). Reproductive resilience of growth and nitrogen uptake underpins yield improvement in winter wheat with forced delay of sowing. *Science of the Total Environment*, *949*. https://doi.org/10.1016/j.scitotenv.2024.175108

Field Science Center for Northern Biosphere. (2025). *Experimental farm outline*. https://www.fsc.hokudai.ac.jp/farm/en/outline/#:~:text=Our%20Experiment%20Farm%2C%20The%20Hokkaido%20University%20Farm%2C%20is,and%20Yoichi%20Orchard%20%286ha%29%20in%20Yamadacho%2C%20Yoichi%20Town.

Fitter, A. H. (1987). An architectural approach to the comparative ecology of plant root systems. *New Phytologist*, *106*(s1), 61–77. https://doi.org/10.1111/j.1469-8137.1987.tb04683.x

Fitzgerald, G. J., Rodriguez, D., Christensen, L. K., Belford, R., Sadras, V. O., and Clarke, T. R. (2006). Spectral and thermal sensing for nitrogen and water status in rainfed and irrigated wheat environments. *Precision Agriculture*, *7*(4), 233–248. https://doi.org/10.1007/s11119-006-9011-z

Fountas, S., Carli, G., Sørensen, C. G., Tsiropoulos, Z., Cavalaris, C., Vatsanidou, A., Liakos, B., Canavari, M., Wiebensohn, J., and Tisserye, B. (2015). Farm management information systems: Current situation and future perspectives. *Computers and Electronics in Agriculture*, *115*, 40–50. https://doi.org/10.1016/j.compag.2015.05.011

Frene, J. P., Pandey, B. K., and Castrillo, G. (2024). Under pressure: elucidating soil compaction and its effect on soil functions. In *Plant and Soil*. Springer Science and Business Media Deutschland GmbH. https://doi.org/10.1007/s11104-024-06573-2

Friedman, J. H. (2001). Greedy Function Approximation: A Gradient Boosting Machine. In *Source: The Annals of Statistics* (Vol. 29, Issue 5). https://doi.org/https://www.jstor.org/stable/2699986

Fuglie, K. O., Morgan, S., and Jelliffe, J. (2024). *World Agricultural Production, Resource Use, and Productivity, 1961-2020*. www.ers.usda.gov

Fulton, J. P., Darr, M. J., Taylor, R., and Shearer, S. (2010). *Proper Implementation of Precision Agricultural Technologies for Conducting On-Farm Research*. http://lib.dr.iastate.edu/abe_eng_conf/299

Gao, X. (2000). Optical–Biophysical Relationships of Vegetation Spectra without Background Contamination. *Remote Sensing of Environment*, *74*(3), 609–620. https://doi.org/10.1016/S0034-4257(00)00150-4

Reference

Gartell, J. E. et. al. (1992). *Creek Connections Groundwater Module-Porosity and Permeability*. https://sitesmedia.s3.amazonaws.com/creekconnections/files/2014/03/PorosityPermeability-activity.pdf

Ge, Y., Morgan, C. L. S., Grunwald, S., Brown, D. J., and Sarkhot, D. V. (2011). Comparison of soil reflectance spectra and calibration models obtained using multiple spectrometers. *Geoderma*, *161*(3–4), 202–211. https://doi.org/10.1016/j.geoderma.2010.12.020

Ge, Y., Thomasson, J. A., Morgan, C. L., and Searcy, S. W. (2007). VNIR Diffuse Reflectance Spectroscopy for Agricultural Soil Property Determination Based on Regression-Kriging. *Transactions of the ASABE*, *50*(3), 1081–1092. https://doi.org/10.13031/2013.23122

Gelderman, R., and Lee, S. (2019). *Chapter 11: Nitrogen Management for Wheat Production Wheat Grow*. https://extension.sdstate.edu/sites/default/files/2020-03/S-0005-11-Wheat.pdf

Getahun, S., Kefale, H., and Gelaye, Y. (2024). Application of Precision Agriculture Technologies for Sustainable Crop Production and Environmental Sustainability: A Systematic Review. In *The Scientific World Journal* (Vol. 2024, p. 2126734). https://doi.org/10.1155/2024/2126734

Godwin, R. J. (2007). A review of the effect of implement geometry on soil failure and implement forces. In *Soil and Tillage Research* (Vol. 97, Issue 2, pp. 331–340). https://doi.org/10.1016/j.still.2006.06.010

Godwin, R. J., and Miller, P. C. H. (2003). A review of the technologies for mapping within-field variability. In *Biosystems Engineering* (Vol. 84, Issue 4, pp. 393–407). Academic Press. https://doi.org/10.1016/S1537-5110(02)00283-0

Gomez, C., Gholizadeh, A., Borůvka, L., and Lagacherie, P. (2016). Using legacy data for correction of soil surface clay content predicted from VNIR/SWIR hyperspectral airborne images. *Geoderma*, *276*, 84–92. https://doi.org/10.1016/j.geoderma.2016.04.019

Gomez, C., Viscarra Rossel, R. A., and McBratney, A. B. (2008). Soil organic carbon prediction by hyperspectral remote sensing and field vis-NIR spectroscopy: An Australian case study. *Geoderma*, *146*(3–4), 403–411. https://doi.org/10.1016/j.geoderma.2008.06.011

Goovaerts, P. (1997). *Geostatistics for Natural Resources Evaluation*. Oxford University PressNew York, NY. https://doi.org/10.1093/oso/9780195115383.001.0001

Government of City of Sapporo. (2025). *Overview of Sapporo City*. City of Sapporo. https://www.city.sapporo.jp/city/aramashi/

Greacen, E. L., and Oh, J. S. (1972). Physics of Root Growth. *Nature New Biology*, *235*(53), 24–25. https://www.nature.com/articles/newbio235024a0#citeas

Greene, A. Norton. (2023). *Overview: Animal Power*. Yale University. https://energyhistory.yale.edu/animal-power/.

Reference

Grossman, R. B., and Reinsch, T. G. (2002). Bulk Density and Linear Extensibility: Core Method. In J. H. Dane and G. C. Topp (Eds.), *Methods of Soil Analysis* (pp. 201–228). Madison. https://doi.org/10.2136/sssabookser5.4.c9

Grzesiak, S., Grzesiak, M. T., Hura, T., Marcińska, I., and Rzepka, A. (2013). Changes in root system structure, leaf water potential and gas exchange of maize and triticale seedlings affected by soil compaction. *Environmental and Experimental Botany*, *88*, 2–10. https://doi.org/10.1016/j.envexpbot.2012.01.010

Gürsoy, S. (2021). Soil Compaction Due to Increased Machinery Intensity in Agricultural Production: Its Main Causes, Effects and Management. . In F. Ahmad and M. Sultan (Eds.), *Technology in Agriculture* (pp. 95–111).

Hadir, S., Döring, T. F., Justes, E., Demie, D. T., Paul, M., Legner, N., Kemper, R., Gaiser, T., Weedon, O., Ewert, F., and Seidel, S. J. (2024). Root growth and belowground interactions in spring wheat /faba bean intercrops. *Plant and Soil*. https://doi.org/10.1007/s11104-024-06742-3

Håkansson, I., and Reeder, R. C. (1994). Subsoil compaction by vehicles with high axle load—extent, persistence, and crop response. *Soil and Tillage Research*, *29*(2–3), 277–304. https://doi.org/10.1016/0167-1987(94)90065-5

Hallett, P. D., Marin, M., Bending, G. D., George, T. S., Collins, C. D., and Otten, W. (2022). Building soil sustainability from root–soil interface traits. In *Trends in Plant Science* (Vol. 27, Issue 7, pp. 688–698). Elsevier Ltd. https://doi.org/10.1016/j.tplants.2022.01.010

Hamza, M. A., and Anderson, W. K. (2005). Soil compaction in cropping systems: A review of the nature, causes and possible solutions. In *Soil and Tillage Research* (Vol. 82, Issue 2, pp. 121–145). Elsevier. https://doi.org/10.1016/j.still.2004.08.009

Harris, I., Osborn, T. J., Jones, P., and Lister, D. (2020). Version 4 of the CRU TS monthly high-resolution gridded multivariate climate dataset. *Scientific Data*, *7*(1), 109. https://doi.org/10.1038/s41597-020-0453-3

Hasan, M. K., Tanaka, T. S. T., Alam, M. M., Ali, M. R., and Saha, C. K. (2020). Impact of modern rice harvesting practices over traditional ones. In *Reviews in Agricultural Science* (Vol. 8, pp. 89–108). Gifu University - United Graduate School of Agricultural Science. https://doi.org/10.7831/ras.8.0_89

Hastie, T., Tibshirani, R., and Friedman, J. (2009). *Basis Expansions and Regularization* (pp. 139–189). https://doi.org/10.1007/978-0-387-84858-7_5

Hedley, C. (2015). The role of precision agriculture for improved nutrient management on farms. In *Journal of the Science of Food and Agriculture* (Vol. 95, Issue 1, pp. 12–19). John Wiley and Sons Ltd. https://doi.org/10.1002/jsfa.6734

Hodge, A. (2004). The plastic plant: Root responses to heterogeneous supplies of nutrients. In *New Phytologist* (Vol. 162, Issue 1, pp. 9–24). https://doi.org/10.1111/j.1469-8137.2004.01015.x

Reference

Hoerl, A. E., and Kennard, R. W. (1970). Ridge Regression: Biased Estimation for Nonorthogonal Problems. *Technometrics*, *12*(1), 55. https://doi.org/10.2307/1267351

Holland, J. M. (2004). The environmental consequences of adopting conservation tillage in Europe: Reviewing the evidence. In *Agriculture, Ecosystems and Environment* (Vol. 103, Issue 1, pp. 1–25). https://doi.org/10.1016/j.agee.2003.12.018

Hoque, A., and Padhiary, M. (2024). Automation and AI in Precision Agriculture: Innovations for Enhanced Crop Management and Sustainability. *Asian Journal of Research in Computer Science*, *17*(10), 95–109. https://doi.org/10.9734/ajrcos/2024/v17i10512

Horn, R., Domżżał, H., Słowińska-Jurkiewicz, A., and van Ouwerkerk, C. (1995). Soil compaction processes and their effects on the structure of arable soils and the environment. *Soil and Tillage Research*, *35*(1–2), 23–36. https://doi.org/10.1016/0167-1987(95)00479-C

Horn, R., Way, T., and Rostek, J. (2003). Effect of repeated tractor wheeling on stress/strain properties and consequences on physical properties in structured arable soils. *Soil and Tillage Research*, *73*(1–2), 101–106. https://doi.org/10.1016/S0167-1987(03)00103-X

Hosseini, M., Movahedi Naeini, S. A., Dehghani, A. A., and Khaledian, Y. (2016). Estimation of soil mechanical resistance parameter by using particle swarm optimization, genetic algorithm, and multiple regression methods. *Soil and Tillage Research*, *157*, 32–42. https://doi.org/10.1016/j.still.2015.11.004

Huisman, J. A., Snepvangers, J. J. J. C., Bouten, W., and Heuvelink, G. B. M. (2003). Monitoring Temporal Development of Spatial Soil Water Content Variation: Comparison of Ground Penetrating Radar and Time Domain Reflectometry. *Vadose Zone Journal*, *2*(4), 519–529. https://doi.org/10.2136/vzj2003.5190

Hunter, J. D. (2007). Matplotlib: A 2D Graphics Environment. *Computing in Science and Engineering*, *9*(3), 90–95. https://doi.org/10.1109/MCSE.2007.55

Ihsan, M. Z., El-Nakhlawy, F. S., Ismail, S. M., Fahad, S., and Daur, I. (2016). Wheat phenological development and growth studies as affected by drought and late season high temperature stress under arid environment. *Frontiers in Plant Science*, *7*(June2016). https://doi.org/10.3389/fpls.2016.00795

Ishaq, M., Ibrahim, M., and Lal, R. (2001). Tillage effect on nutrient uptake by wheat and cotton as in¯uenced by fertilizer rate. *Soil and Tillage*, *62*(1), 41–53. https://doi.org/10.1016/S0167-1987(01)00211-2

Ishimwe, R., Abutaleb, K., and Ahmed, F. (2014). Applications of Thermal Imaging in Agriculture—A Review. *Advances in Remote Sensing*, *03*(03), 128–140. https://doi.org/10.4236/ars.2014.33011

Islam, A. F. M. T., Islam, A. K. M. S., Islam, G. M. T., Bala, S. K., Salehin, M., Choudhury, A. K., Dey, N. C., and Hossain, A. (2022). Adaptation strategies to increase water productivity of wheat under changing climate. *Agricultural Water Management*, *264*. https://doi.org/10.1016/j.agwat.2022.107499

Reference

Islam, M., Shaikh, M., Siddique, A., and Sumon, M. (2014). Yield and nutrient uptake by wheat as influenced by integrated use of manures and fertilizers. *Journal of the Bangladesh Agricultural University*, *12*(1), 73–78. https://doi.org/10.3329/jbau.v12i1.21242

Jackson, J., Canadell, R., Ehleringer Mooney, J. H., Sala-ED Schulze, O., Jackson, R., Canadell Mooney, J. H., Ehleringer, J., Sala, O., and Schulze, E. (1996). A global analysis of root distributions for terrestrial biomes. *Oecologia*, *108*, 389–411. http://www.jstor.org/stable/4221432

Jamali, H., Nachimuthu, G., Palmer, B., Hodgson, D., Hundt, A., Nunn, C., and Braunack, M. (2021). Soil compaction in a new light: Know the cost of doing nothing – A cotton case study. *Soil and Tillage Research*, *213*. https://doi.org/10.1016/j.still.2021.105158

James, G., Witten, D., Hastie, T., and Tibshirani, R. (2021). *An Introduction to Statistical Learning*. Springer US. https://doi.org/10.1007/978-1-0716-1418-1

Japan Meteorological Agency. (2024). *SAPPORO WMO Station ID:47412 Lat 43o03.6'N Lon 141o19.7'E*. https://www.data.jma.go.jp/stats/etrn/view/monthly_s3_en.php?block_no=47412andview=2

Jeschke, M., and Lutt, N. (2019). Soil Compaction in Agricultural Production. In *CROP INSIGHTS* (Vol. 28, Issue 10). https://www.pioneer.com/us/agronomy/soil-compaction-ag-production.html

Jin, K., White, P. J., Whalley, W. R., Shen, J., and Shi, L. (2017). Shaping an Optimal Soil by Root–Soil Interaction. In *Trends in Plant Science* (Vol. 22, Issue 10, pp. 823–829). Elsevier Ltd. https://doi.org/10.1016/j.tplants.2017.07.008

Jones, C. (2015). *Nutrient Uptake Timing by Crops to assist with fertilizing decisions*. https://landresources.montana.edu/soilfertility/documents/PDF/pub/NutUpTimeEB0191.pdf

Jones, H. G., Serraj, R., Loveys, B. R., Xiong, L., Wheaton, A., and Price, A. H. (2009). Thermal infrared imaging of crop canopies for the remote diagnosis and quantification of plant responses to water stress in the field. *Functional Plant Biology*, *36*(11), 978–989. https://doi.org/10.1071/FP09123

Jovanović, D., and Govedarica, M. (2014). *Remote sensing as a trend in agriculture*. https://www.researchgate.net/publication/280037536

Juhos, K., Szabo, S., and Ladanyi, M. (2015). Influence of soil properties on crop yield: A multivariate statistical approach. *International Agrophysics*, *29*(4), 433–440. https://doi.org/10.1515/intag-2015-0049

JXCT. (2020). *RS485 Modbus JXBS-3001-NPK-RS Soil NPK Sensor User Manual JXBS-3001-NPK-RS Soil NPK Sensor User Manual RS485 Modbus* (Issue 2.0). https://cdck-file-uploads-europe1.s3.dualstack.eu-west-1.amazonaws.com/arduino/original/4X/c/a/b/cab723f9cbaa1e67db97821226b2560156b368fc.pdf

Reference

Kamilaris, A., Kartakoullis, A., and Prenafeta-Boldú, F. X. (2017). A review on the practice of big data analysis in agriculture. In *Computers and Electronics in Agriculture* (Vol. 143, pp. 23–37). Elsevier B.V. https://doi.org/10.1016/j.compag.2017.09.037

Karimli, N., and Selbesoğlu, M. O. (2023). Remote Sensing-Based Yield Estimation of Winter Wheat Using Vegetation and Soil Indices in Jalilabad, Azerbaijan. *ISPRS International Journal of Geo-Information*, *12*(3). https://doi.org/10.3390/ijgi12030124

Karmakar, P., Teng, S. W., Murshed, M., Pang, S., Li, Y., and Lin, H. (2024). Crop monitoring by multimodal remote sensing: A review. In *Remote Sensing Applications: Society and Environment* (Vol. 33). Elsevier B.V. https://doi.org/10.1016/j.rsase.2023.101093

Kaufmann, M., Tobias, S., and Schulin, R. (2010). Comparison of critical limits for crop plant growth based on different indicators for the state of soil compaction. *Journal of Plant Nutrition and Soil Science*, *173*(4), 573–583. https://doi.org/10.1002/jpln.200900129

Kaur, B., Mansi, Dimri, S., Singh, J., Mishra, S., Chauhan, N., Kukreti, T., Sharma, B., Singh, S. P., Arora, S., Uniyal, D., Agrawal, Y., Akhtar, S., Rather, M. A., Naik, B., Kumar, V., Gupta, A. K., Rustagi, S., and Preet, M. S. (2023). Insights into the harvesting tools and equipment's for horticultural crops: From then to now. *Journal of Agriculture and Food Research*, *14*. https://doi.org/10.1016/j.jafr.2023.100814

Kavoosi, Z., Raoufat, M. H., Dehghani, M., Abdolabbas, J., Kazemeini, S. A., and Nazemossadat, M. J. (2020). Feasibility of satellite and drone images for monitoring soil residue cover. *Journal of the Saudi Society of Agricultural Sciences*, *19*(1), 56–64. https://doi.org/10.1016/j.jssas.2018.06.001

Kazuto, I. (2009). *Agriculture in Hokkaido* (2nd ed., Vol. 2). Laboratory of Crops Science, Research Faculty of Agriculture, Hokkaido University. https://ocw.hokudai.ac.jp/wp-content/uploads/2016/01/AgricultureInHokkaido-2009-Text-All.pdf

Keller, T., Défossez, P., Weisskopf, P., Arvidsson, J., and Richard, G. (2007). SoilFlex: A model for prediction of soil stresses and soil compaction due to agricultural field traffic including a synthesis of analytical approaches. *Soil and Tillage Research*, *93*(2), 391–411. https://doi.org/10.1016/j.still.2006.05.012

Keller, T., Sandin, M., Colombi, T., Horn, R., and Or, D. (2019). Historical increase in agricultural machinery weights enhanced soil stress levels and adversely affected soil functioning. *Soil and Tillage Research*, *194*, 104293. https://doi.org/10.1016/j.still.2019.104293

Kerry, R., and Oliver, M. A. (2007). Determining the effect of asymmetric data on the variogram. I. Underlying asymmetry. *Computers and Geosciences*, *33*(10), 1212–1232. https://doi.org/10.1016/j.cageo.2007.05.008

Khanal, S., Kushal, K. C., Fulton, J. P., Shearer, S., and Ozkan, E. (2020). Remote sensing in agriculture—accomplishments, limitations, and opportunities. In *Remote Sensing* (Vol. 12, Issue 22, pp. 1–29). MDPI AG. https://doi.org/10.3390/rs12223783

Khater, A., Fouda, O., El-Termezy, G., Abdel hamid, S., El-Tantawy, M., El-Beba, A., Sabry, H., and Okasha, M. (2023). Modification of the rice combine harvester for cutting and binding wheat crop. *Journal of Agriculture and Food Research*, *14*. https://doi.org/10.1016/j.jafr.2023.100738

Khosla, R., Inman, D., Westfall, D. G., Reich, R. M., Frasier, M., Mzuku, M., Koch, B., and Hornung, A. (2008). A synthesis of multi-disciplinary research in precision agriculture: Site-specific management zones in the semi-arid western Great Plains of the USA. *Precision Agriculture*, *9*(1–2), 85–100. https://doi.org/10.1007/s11119-008-9057-1

Kirby, E. J. M. (1985). *Botany of the wheat plant* . https://www.fao.org/4/y4011e/y4011e05.htm#:~:text=The%20wheat%20plant%20has%20two,top%2030%20cm%20of%20soil.

Knorr, W., Williams, M., Thum, T., Kaminski, T., Voßbeck, M., Scholze, M., Quaife, T., Smallman, T. L., Steele-Dunne, S. C., Vreugdenhil, M., Green, T., Zaehle, S., Aurela, M., Bouvet, A., Bueechi, E., Dorigo, W., El-Madany, T. S., Migliavacca, M., Honkanen, M., … Drusch, M. (2025). A comprehensive land-surface vegetation model for multi-stream data assimilation, B v1.0. *Geoscientific Model Development*, *18*(7), 2137–2159. https://doi.org/10.5194/gmd-18-2137-2025

Knotters, M., Brus, D. J., and Oude Voshaar, J. H. (1995). A comparison of kriging, co-kriging and kriging combined with regression for spatial interpolation of horizon depth with censored observations. *Geoderma*, *67*(3–4), 227–246. https://doi.org/10.1016/0016-7061(95)00011-C

Kock, N., and Lynn, G. (2012). Lateral Collinearity and Misleading Results in Variance-Based SEM: An Illustration and Recommendations. *Journal of the Association for Information Systems*, *13*(7), 546–580. https://doi.org/10.17705/1jais.00302

Kodaira, M., and Shibusawa, S. (2020). Mobile proximal sensing with visible and near infrared spectroscopy for digital soil mapping. *Soil Systems*, *4*(3), 1–22. https://doi.org/10.3390/soilsystems4030040

Kong, J., Yang, J., Zhen, P., Li, J., and Yang, L. (2018). A Coupling Model for Soil Moisture Retrieval in Sparse Vegetation Covered Areas Based on Microwave and Optical Remote Sensing Data. *IEEE Transactions on Geoscience and Remote Sensing*, *56*(12), 7162–7173. https://doi.org/10.1109/TGRS.2018.2849009

Kopittke, P. M., Menzies, N. W., Wang, P., McKenna, B. A., and Lombi, E. (2019). Soil and the intensification of agriculture for global food security. In *Environment International* (Vol. 132). Elsevier Ltd. https://doi.org/10.1016/j.envint.2019.105078

Kuang, B., Mahmood, H. S., Quraishi, M. Z., Hoogmoed, W. B., Mouazen, A. M., and van Henten, E. J. (2012). *Sensing Soil Properties in the Laboratory, In Situ, and On-Line* (pp. 155–223). https://doi.org/10.1016/B978-0-12-394275-3.00003-1

Kuhn, M., and Johnson, K. (2013). *Applied Predictive Modeling*. Springer New York. https://doi.org/10.1007/978-1-4614-6849-3

Kumar, S., and Moore, K. B. (2002). The Evolution of Global Positioning System (GPS) Technology. *Journal of Science Education and Technology*, *11*(1), 59–80. https://doi.org/10.1023/A:1013999415003

Reference

Kushwaha, M., Singh, S., Singh, V., and Dwivedi, S. (2024). Precision Farming: A Review of Methods, Technologies, and Future Prospects. *International Journal of Environment, Agriculture and Biotechnology*, *9*(2). https://doi.org/10.22161/ijeab

Lal, R. (2004). *Soil Carbon Sequestration Impacts on Global Climate Change and Food Security*. https://www.science.org/doi/pdf/10.1126/science.1097396

Lal, R. (2015). Restoring soil quality to mitigate soil degradation. *Sustainability (Switzerland)*, *7*(5), 5875–5895. https://doi.org/10.3390/su7055875

Lark, R. M. (2011). Spatially nested sampling schemes for spatial variance components: Scope for their optimization. *Computers and Geosciences*, *37*(10), 1633–1641. https://doi.org/10.1016/j.cageo.2010.12.010

Lipiec, J., and Hatano, R. (2003). Quantification of compaction effects on soil physical properties and crop growth. *Geoderma*, *116*(1–2), 107–136. https://doi.org/10.1016/S0016-7061(03)00097-1

Lipiec, J., and Stcpniewski, W. (1995). Effects of soil compaction and tillage systems on uptake and losses of nutrients. In *Soil and Tillage Research* (Vol. 35).

Liu, H., Colombi, T., Jäck, O., Keller, T., and Weih, M. (2022). Effects of soil compaction on grain yield of wheat depend on weather conditions. *Science of the Total Environment*, *807*. https://doi.org/10.1016/j.scitotenv.2021.150763

Lobell, D. B., and Asner, G. P. (2002). Moisture Effects on Soil Reflectance. *Soil Science Society of America Journal*, *66*(3), 722–727. https://doi.org/10.2136/sssaj2002.7220

Long, Z., Wang, Y., Sun, B., Tang, X., and Jin, K. (2024). Impact of mechanical compaction on crop growth and sustainable agriculture. In *Frontiers of Agricultural Science and Engineering* (Vol. 11, Issue 2, pp. 243–252). Higher Education Press Limited Company. https://doi.org/10.15302/J-FASE-2024566

Longepierre, M., Feola Conz, R., Barthel, M., Bru, D., Philippot, L., Six, J., and Hartmann, M. (2022). Mixed Effects of Soil Compaction on the Nitrogen Cycle Under Pea and Wheat. *Frontiers in Microbiology*, *12*. https://doi.org/10.3389/fmicb.2021.822487

Lowenberg-DeBoer, J., Huang, I. Y., Grigoriadis, V., and Blackmore, S. (2020). Economics of robots and automation in field crop production. *Precision Agriculture*, *21*(2), 278–299. https://doi.org/10.1007/s11119-019-09667-5

Lukaszewski, A. J., Alberti, A., Sharpe, A., Kilian, A., Stanca, A. M., Keller, B., Clavijo, B. J., Friebe, B., Gill, B., Wulff, B., Chapman, B., Steuernagel, B., Feuillet, C., Viseux, C., Pozniak, C., Rokhsar, D. S., Klassen, D., Edwards, D., Akhunov, E., … Dubská, Z. (2014). A chromosome-based draft sequence of the hexaploid bread wheat (*Triticum aestivum*) genome. *Science*, *345*(6194). https://doi.org/10.1126/science.1251788

Luo, Z., Wang, E., and Sun, O. J. (2010). Can no-tillage stimulate carbon sequestration in agricultural soils? A meta-analysis of paired experiments. *Agriculture, Ecosystems and Environment*, *139*(1–2), 224–231. https://doi.org/10.1016/j.agee.2010.08.006

Lynch, J. P. (2007). Roots of the Second Green Revolution. *Australian Journal of Botany*, *55*(5), 493. https://doi.org/10.1071/BT0611 8

Reference

Lynch, J. P. (2019). Root phenotypes for improved nutrient capture: an underexploited opportunity for global agriculture. In *New Phytologist* (Vol. 223, Issue 2, pp. 548–564). Blackwell Publishing Ltd. https://doi.org/10.1111/nph.15738

Ma, J., Tang, X., Sun, B., Wei, J., Ma, L., Yuan, M., Zhang, D., Shao, Y., Li, C., Chen, K. M., and Jiang, L. (2022). A NAC transcription factor, TaNAC5D-2, acts as a positive regulator of drought tolerance through regulating water loss in wheat (Triticum aestivum L.). *Environmental and Experimental Botany*, *196*. https://doi.org/10.1016/j.envexpbot.2022.104805

Ma, W., Renwick, A., and Grafton, Q. (2018). Farm machinery use, off-farm employment, and farm performance in China. *Australian Journal of Agricultural and Resource Economics*, *62*(2), 279–298. https://doi.org/10.1111/1467-8489.12249

Machine Finder. (2025). *John Deere Engine History: A Production Timeline*. MachineFinder Blog. https://blog.machinefinder.com/28582/john-deere-engine-history-a-production-timeline

Maldonado, S. (2025). *Breaking Soil Compaction One Root at a Time*. https://wcngg.com/2025/02/11/breaking-soil-compaction-one-root-at-a-time/

Marçal de Queiroz, D., Valente, D. S. M., and Coelho, A. L. de F. (2022). Control and Automation Systems in Agricultural Machinery. In *Digital Agriculture* (pp. 143–156). Springer International Publishing. https://doi.org/10.1007/978-3-031-14533-9_9

Marchant, B. P., and Lark, R. M. (2007). Robust estimation of the variogram by residual maximum likelihood. *Geoderma*, *140*(1–2), 62–72. https://doi.org/10.1016/j.geoderma.2007.03.005

Martin, K., Shroyer, J., Shoup, D., Olson, B., and Duncan, S. (2011). *Estimating Wheat Yield*. https://bookstore.ksre.ksu.edu/pubs/estimating-wheat-yield_MF3044.pdf

Masud Cheema, M. J., Iqbal, T., Daccache, A., Hussain, S., and Awais, M. (2023). Precision agriculture technologies. In *Precision Agriculture* (pp. 231–250). Elsevier. https://doi.org/10.1016/B978-0-443-18953-1.00011-8

McBratney, A. B., Mendonça Santos, M. L., and Minasny, B. (2003). On digital soil mapping. *Geoderma*, *117*(1–2), 3–52. https://doi.org/10.1016/S0016-7061(03)00223-4

McBratney, A., Whelan, B., Ancev, T., and Bouma, J. (2005). *Future Directions of Precision Agriculture w*. https://doi.org/10.1007/s11119-005-0681-8

Mceldowney, J. (2020). *EU agricultural policy and climate change*. https://www.europarl.europa.eu/RegData/etudes/BRIE/2020/651922/EPRS_BRI(2020)651922_EN.pdf

McKinney, W. (2010). Data Structures for Statistical Computing in Python. *PROC. OF THE 9th PYTHON IN SCIENCE CONF*, 56–61. https://doi.org/10.25080/Majora-92bf1922-00a

McWilliams, F. A. (2019). *Equine Machines: Horses and Tractors on British Farms c*. https://kclpure.kcl.ac.uk/ws/portalfiles/portal/130771714/2020_McWilliams_Felicity_Ann_1568785_ethesis.pdf

Reference

Mehmood, T., Liland, K. H., Snipen, L., and Sæbø, S. (2012). A review of variable selection methods in Partial Least Squares Regression. In *Chemometrics and Intelligent Laboratory Systems* (Vol. 118, pp. 62–69). https://doi.org/10.1016/j.chemolab.2012.07.010

Mehra, P., Baker, J., Sojka, R. E., Bolan, N., Desbiolles, J., Kirkham, M. B., Ross, C., and Gupta, R. (2018). *A Review of Tillage Practices and Their Potential to Impact the Soil Carbon Dynamics* (pp. 185–230). https://doi.org/10.1016/bs.agron.2018.03.002

Meng, Q., Yue, S., Chen, X., Cui, Z., Ye, Y., Ma, W., Tong, Y., and Zhang, F. (2013). Understanding Dry Matter and Nitrogen Accumulation with Time-Course for High-Yielding Wheat Production in China. *PLoS ONE*, *8*(7). https://doi.org/10.1371/journal.pone.0068783

Mevik, B. H., and Wehrens, R. (2007). The **pls** Package: Principal Component and Partial Least Squares Regression in *R*. *Journal of Statistical Software*, *18*(2). https://doi.org/10.18637/jss.v018.i02

Mgendi, G. (2024). Unlocking the potential of precision agriculture for sustainable farming. *Discover Agriculture*, *2*(1), 87. https://doi.org/10.1007/s44279-024-00078-3

Miller, T. D. (1996). *Growth Stages of Wheat: Identification and Understanding Improve Crop Management*. https://lubbock.tamu.edu/files/2011/10/wheatgrowthstages_26.pdf

Milne, A. E., and Lark, R. M. (2009). Wavelet Transforms Applied to Irregularly Sampled Soil Data. *Mathematical Geosciences*, *41*(6), 661–678. https://doi.org/10.1007/s11004-009-9234-4

Mohanty, A., Zhang, M., Dutt, A., Ramelow, S., Nussenzveig, P., and Lipson, M. (2017). Quantum interference between transverse spatial waveguide modes. *Nature Communications*, *8*. https://doi.org/10.1038/ncomms14010

Mohite, J., Sawant, S., Pandit, A., and Pappula, S. (2023). Estimation of Soil Organic Carbon and Bulk Density for Carbon Stock Assessment in Croplands Using the Sentinel-1 and 2 Observations. *IGARSS 2023 - 2023 IEEE International Geoscience and Remote Sensing Symposium*, *2023-July*, 3494–3497. https://doi.org/10.1109/IGARSS52108.2023.10282350

Moitzi, G., Wagentristl, H., Refenner, K., Weingartmann, H., Piringer, G., Boxberger, J., Gronauer, A., and Gronauer, A. 2014. (2014). *Effects of working depth and wheel slip on fuel consumption of selected tillage implements* (Vol. 16, Issue 1). http://www.cigrjournal.org

Mondal, S., and Chakraborty, D. (2023). Root growth and physiological responses in wheat to topsoil and subsoil compaction with or without artificial vertical macropores. *Heliyon*, *9*(8), e18834. https://doi.org/10.1016/j.heliyon.2023.e18834

Montero, G., Escobar, J. M., Rodríguez, E., and Montenegro, R. (2009). Solar radiation and shadow modelling with adaptive triangular meshes. *Solar Energy*, *83*(7), 998–1012. https://doi.org/10.1016/j.solener.2009.01.004

Reference

Montgomery, D. R. and Matson, P. A. (2007). *Soil erosion and agricultural sustainability*. https://www.pnas.org/doi/pdf/10.1073/pnas.0611508104

Mooney, S. J., Pridmore, T. P., Helliwell, J., and Bennett, M. J. (2012). Developing X-ray computed tomography to non-invasively image 3-D root systems architecture in soil. In *Plant and Soil* (Vol. 352, Issues 1–2, pp. 1–22). https://doi.org/10.1007/s11104-011-1039-9

Motsara, M. R., Roy, R. N., and Food and Agriculture Organization of the United Nations. (2008). *Guide to laboratory establishment for plant nutrient analysis*. Food and Agriculture Organization of the United Nations.

Mouazen, A. M., and Kuang, B. (2016). On-line visible and near infrared spectroscopy for in-field phosphorous management. *Soil and Tillage Research*, *155*, 471–477. https://doi.org/10.1016/j.still.2015.04.003

Mouazen, A. M., and Ramon, H. (2006). Development of on-line measurement system of bulk density based on on-line measured draught, depth, and soil moisture content. *Soil and Tillage Research*, *86*(2), 218–229. https://doi.org/10.1016/j.still.2005.02.026

Mousazadeh, H., Keyhani, A., Javadi, A., Mobli, H., Abrinia, K., and Sharifi, A. (2011). Design, construction and evaluation of a sun-tracking system on a mobile structure. *Journal of Solar Energy Engineering, Transactions of the ASME*, *133*(1). https://doi.org/10.1115/1.4003296

Mu, T., Liu, G., Yang, X., and Yu, Y. (2023). Soil-Moisture Estimation Based on Multiple-Source Remote-Sensing Images. *Remote Sensing*, *15*(1). https://doi.org/10.3390/rs15010139

Mueller, T. G., Pierce, F. J., Schabenberger, O., and Warncke, D. D. (2001). Map Quality for Site-Specific Fertility Management. *Soil Science Society of America Journal*, *65*(5), 1547–1558. https://doi.org/10.2136/sssaj2001.6551547x

Mulder, V. L., de Bruin, S., Schaepman, M. E., and Mayr, T. R. (2011). The use of remote sensing in soil and terrain mapping — A review. *Geoderma*, *162*(1–2), 1–19. https://doi.org/10.1016/j.geoderma.2010.12.018

Mulla, D. J. (2013). Twenty five years of remote sensing in precision agriculture: Key advances and remaining knowledge gaps. In *Biosystems Engineering* (Vol. 114, Issue 4, pp. 358–371). Academic Press. https://doi.org/10.1016/j.biosystemseng.2012.08.009

Naderi-Boldaji, M., Sharifi, A., Alimardani, R., Hemmat, A., Keyhani, A., Loonstra, E. H., Weisskopf, P., Stettler, M., and Keller, T. (2013). Use of a triple-sensor fusion system for on-the-go measurement of soil compaction. *Soil and Tillage Research*, *128*, 44–53. https://doi.org/10.1016/j.still.2012.10.002

Naderi-Boldaji, M., Weisskopf, P., Stettler, M., and Keller, T. (2016). Predicting the relative density from on-the-go horizontal penetrometer measurements at some arable topsoils in Northern Switzerland. *Soil and Tillage Research*, *159*, 23–32. https://doi.org/10.1016/j.still.2015.12.002

Reference

Najdenko, E., Lorenz, F., Dittert, K., and Olfs, H. W. (2024). Rapid in-field soil analysis of plant-available nutrients and pH for precision agriculture—a review. In *Precision Agriculture*. Springer. https://doi.org/10.1007/s11119-024-10181-6

NARO. (2017). *Hokkaido Agricultural Research Center, NARO（HARC/NARO）*. https://www.naro.go.jp/publicity_report/publication/files/2017NARO_english_1.pdf

Nawar, S., Buddenbaum, H., Hill, J., Kozak, J., and Mouazen, A. M. (2016). Estimating the soil clay content and organic matter by means of different calibration methods of vis-NIR diffuse reflectance spectroscopy. *Soil and Tillage Research*, *155*, 510–522. https://doi.org/10.1016/j.still.2015.07.021

Nawaz, M. F., Bourrié, G., and Trolard, F. (2013). Soil compaction impact and modelling. A review. *Agronomy for Sustainable Development*, *33*(2), 291–309. https://doi.org/10.1007/s13593-011-0071-8

NCSU. (2025). *Agricultural Machinery and Traffic Induced Compaction*. https://content.ces.ncsu.edu/managing-agricultural-machinery-to-limit-soil-compaction-in-north-carolina#

Nkebiwe, P. M., Weinmann, M., Bar-Tal, A., and Müller, T. (2016). Fertilizer placement to improve crop nutrient acquisition and yield: A review and meta-analysis. In *Field Crops Research* (Vol. 196, pp. 389–401). Elsevier B.V. https://doi.org/10.1016/j.fcr.2016.07.018

Nosalewicz, A., and Lipiec, J. (2014). The effect of compacted soil layers on vertical root distribution and water uptake by wheat. *Plant and Soil*, *375*(1–2), 229–240. https://doi.org/10.1007/s11104-013-1961-0

Notarnicola, B., Tassielli, G., Renzulli, P. A., Castellani, V., and Sala, S. (2017). Environmental impacts of food consumption in Europe. *Journal of Cleaner Production*, *140*, 753–765. https://doi.org/10.1016/j.jclepro.2016.06.080

Nye, P. H. (1966). The effect of the nutrient intensity and buffering power of a soil, and the absorbing power, size, and root hairs of a root, on nutrient absorption by diffusion. *Plant and Soil*, *25*(1), 81–105. https://doi.org/10.1007/BF01347964

Obour, P. B., Schjønning, P., Peng, Y., and Munkholm, L. J. (2017). Subsoil compaction assessed by visual evaluation and laboratory methods. *Soil and Tillage Research*, *173*, 4–14. https://doi.org/10.1016/j.still.2016.08.015

O'brien, R. M. (2007). A caution regarding rules of thumb for variance inflation factors. *Quality and Quantity*, *41*(5), 673–690. https://doi.org/10.1007/s11135-006-9018-6

Odeh, I. O. A., McBratney, A. B., and Chittleborough, D. J. (1995). Further results on prediction of soil properties from terrain attributes: heterotopic cokriging and regression-kriging. *Geoderma*, *67*(3–4), 215–226. https://doi.org/10.1016/0016-7061(95)00007-B

O'Neill, R. V., DeAnglis, D. L., Waide, J. B., and Allen, T. F. H. (2021). *A Hierarchical Concept of Ecosystems. (MPB-23), Volume 23*. Princeton University Press. https://doi.org/10.2307/j.ctv1sfsf8d

Reference

Orangi, A., Narsilio, G. A., and Ryu, D. (2019). A laboratory study on non-invasive soil water content estimation using capacitive based sensors. *Sensors (Switzerland)*, *19*(3). https://doi.org/10.3390/s19030651

Özdemir, N., Demir, Z., and Bülbül, E. (2022). Relationships between some soil properties and bulk density under different land use. *Soil Studies*, *11*(2), 43–50. https://doi.org/10.21657/soilst.1218353

Padarian, J., Minasny, B., and McBratney, A. B. (2019). Transfer learning to localise a continental soil vis-NIR calibration model. *Geoderma*, *340*, 279–288. https://doi.org/10.1016/j.geoderma.2019.01.009

Page-Dumroese, D. S., Busse, M. D., Jurgensen, M. F., and Jokela, E. J. (2021). Sustaining forest soil quality and productivity. In *Soils and Landscape Restoration* (pp. 63–93). Elsevier. https://doi.org/10.1016/B978-0-12-813193-0.00003-5

Panda, R. K., Behera, S. K., and Kashyap, P. S. (2003). Effective management of irrigation water for wheat under stressed conditions. *Agricultural Water Management*, *63*, 37–56. https://doi.org/10.1016/S0378-3774(03)00099-4

Pandey, M., Shrestha, J., Subedi, S., and Shah, K. K. (2020). ROLE OF NUTRIENTS IN WHEAT: A REVIEW. *Tropical Agrobiodiversity*, *1*(1), 18–23. https://doi.org/10.26480/trab.01.2020.18.23

Parras-Burgos, D., Molina Martínez, M., and García-Mateos, G. (2018). *Agriculture 4.0-the Future of Farming Technology*. https://www.bollettinoadapt.it/wp-content/uploads/2019/12/OliverWyman-Report_English-LOW.pdf

Paulsen, G. M., Whitney, D. A. Peterson, D. E., Leroy, H., and Rogers, D. H. (1997). *Contents Growth and Development Nutrient Management Weed Management Insect Management Irrigation Management Storage Management Profit Prospects*. https://bookstore.ksre.ksu.edu/pubs/wheat-production-handbook_C529.pdf

Pedregosa, F., Michel, V., Grisel, O., Blondel, M., Prettenhofer, P., Weiss, R., Vanderplas, J., Cournapeau, D., Pedregosa, F., Varoquaux, G., Gramfort, A., Thirion, B., Grisel, O., Dubourg, V., Passos, A., Brucher, M., Perrot É. M., Duchesnay, É., and Duchesnay, F. (2011). Scikit-learn: Machine Learning in Python Gaël Varoquaux Bertrand Thirion Vincent Dubourg Alexandre Passos PEDREGOSA, VAROQUAUX, GRAMFORT ET AL. Matthieu Perrot. In *Journal of Machine Learning Research* (Vol. 12). http://scikit-learn.sourceforge.net.

Peng, J., Zhao, Z., and Liu, D. (2022). Impact of Agricultural Mechanization on Agricultural Production, Income, and Mechanism: Evidence From Hubei Province, China. *Frontiers in Environmental Science*, *10*. https://doi.org/10.3389/fenvs.2022.838686

Peng, Y., Wang, L., Zhao, L., Liu, Z., Lin, C., Hu, Y., and Liu, L. (2021). Estimation of soil nutrient content using hyperspectral data. *Agriculture (Switzerland)*, *11*(11). https://doi.org/10.3390/agriculture11111129

Peralta Ogorek, L. L., Gao, Y., Farrar, E., and Pandey, B. K. (2024). Soil compaction sensing mechanisms and root responses. In *Trends in Plant Science*. Elsevier Ltd. https://doi.org/10.1016/j.tplants.2024.10.014

Reference

Petrović, B., Bumbálek, R., Zoubek, T., Kuneš, R., Smutný, L., and Bartoš, P. (2024). Application of precision agriculture technologies in Central Europe-review. In *Journal of Agriculture and Food Research* (Vol. 15). Elsevier B.V. https://doi.org/10.1016/j.jafr.2024.101048

Pierce, F. J., and Nowak, P. (1999). *Aspects of Precision Agriculture* (pp. 1–85). https://doi.org/10.1016/S0065-2113(08)60513-1

Pivoto, D., Waquil, P. D., Talamini, E., Finocchio, C. P. S., Dalla Corte, V. F., and de Vargas Mores, G. (2018). Scientific development of smart farming technologies and their application in Brazil. *Information Processing in Agriculture*, *5*(1), 21–32. https://doi.org/10.1016/j.inpa.2017.12.002

Poppiel, R. R., Paiva, A. F. da S., and Demattê, J. A. M. (2022). Bridging the gap between soil spectroscopy and traditional laboratory: Insights for routine implementation. *Geoderma*, *425*. https://doi.org/10.1016/j.geoderma.2022.116029

Quraishi, M. Z., and Mouazen, A. M. (2013). A prototype sensor for the assessment of soil bulk density. *Soil and Tillage Research*, *134*, 97–110. https://doi.org/10.1016/j.still.2013.07.011

Raid, I., Kusnezowa, T., and Seewig, J. (2013). Application of ordinary kriging for interpolation of micro-structured technical surfaces. *Measurement Science and Technology*, *24*(9), 095201. https://doi.org/10.1088/0957-0233/24/9/095201

Raju, A., and Subramoniam, R. (2024). Assessing soil nutrient content and mapping in tropical Tamil Nadu, India, through precursors Iperspettrale della missione applicativa hyperspectral spectroscopy. *Applied Sciences (Switzerland)*, *14*(1). https://doi.org/10.3390/app14010186

Ram, B. G., Oduor, P., Igathinathane, C., Howatt, K., and Sun, X. (2024). A systematic review of hyperspectral imaging in precision agriculture: Analysis of its current state and future prospects. In *Computers and Electronics in Agriculture* (Vol. 222). Elsevier B.V. https://doi.org/10.1016/j.compag.2024.109037

Rankel, K. (2024). *Understanding Common Wheat Height*. https://greg.app/common-wheat-size/#:~:text=Mature%20Height%20and%20Spreadandtext=Common%20wheat%20typically%20reaches%20a,genetic%20traits%20influence%20growth%20patterns.

Raper, R. L. (2005). Agricultural traffic impacts on soil. *Journal of Terramechanics*, *42*(3–4), 259–280. https://doi.org/10.1016/j.jterra.2004.10.010

Read, J. M., and Torrado, M. (2009). Remote Sensing. In *International Encyclopedia of Human Geography* (pp. 335–346). Elsevier. https://doi.org/10.1016/B978-008044910-4.00508-3

Reetz, H. F. (2016). *Fertilizers and their Efficient Use*. https://www.fertilizer.org/wp-content/uploads/2023/01/2016_ifa_reetz.pdf

Reintam, E., TrüKmann, K., Kuht, J., Nugis, E., Edesi, L., Astover, A., Noormets, M., Kauer, K., Krebstein, K., and Rannik, K. (2009). Soil compaction effects on soil bulk density and penetration resistance and growth of spring barley (Hordeum vulgare L.). *Acta*

Agriculturae Scandinavica Section B: Soil and Plant Science, *59*(3), 265–272. https://doi.org/10.1080/09064710802030070

Renger, M. (1970). On the influence of drainage on the structure and the water permeability of cohesive soils. *Mitteilgn. Dtsch. Bodenkundl. Gesellsch* 11 (1970): 23-28.

Reynolds, M. P., and Braun, H. J. (2022). Wheat Improvement: Food Security in a Changing Climate. In *Wheat Improvement: Food Security in a Changing Climate*. Springer International Publishing. https://doi.org/10.1007/978-3-030-90673-3

Richard, G., Cousin, I., Sillon, J. F., Bruand, A., and Guérif, J. (2001). Effect of compaction on the porosity of a silty soil: influence on unsaturated hydraulic properties. *European Journal of Soil Science*, *52*(1), 49–58. https://doi.org/10.1046/j.1365-2389.2001.00357.x

Rogge, D., Bauer, A., Zeidler, J., Mueller, A., Esch, T., and Heiden, U. (2018). Building an exposed soil composite processor (SCMaP) for mapping spatial and temporal characteristics of soils with Landsat imagery (1984–2014). *Remote Sensing of Environment*, *205*, 1–17. https://doi.org/10.1016/j.rse.2017.11.004

Romero-Ruiz, A., Linde, N., Baron, L., Breitenstein, D., Keller, T., and Or, D. (2022). Lasting Effects of Soil Compaction on Soil Water Regime Confirmed by Geoelectrical Monitoring. *Water Resources Research*, *58*(2). https://doi.org/10.1029/2021WR030696

Ruane, J. (2019). *Proceedings of the International Symposium on Agricultual Innovation for Family Farmers : unlocking the potential of agricultural innovation to achieve the sustainable development goals*. Food and Agriculture Organization of the United Nations. https://openknowledge.fao.org/server/api/core/bitstreams/4fcc4da9-c22b-45bb-812e-deab1759cbce/content

Saco, P. M., McDonough, K. R., Rodriguez, J. F., Rivera-Zayas, J., and Sandi, S. G. (2021). The role of soils in the regulation of hazards and extreme events. *Philosophical Transactions of the Royal Society B: Biological Sciences*, *376*(1834). https://doi.org/10.1098/rstb.2020.0178

Sadeghi, M., Babaeian, E., Tuller, M., and Jones, S. B. (2017). The optical trapezoid model: A novel approach to remote sensing of soil moisture applied to Sentinel-2 and Landsat-8 observations. *Remote Sensing of Environment*, *198*, 52–68. https://doi.org/10.1016/j.rse.2017.05.04 1

Sadras, V. O., O'Leary, G. J., and Roget, D. K. (2005). Crop responses to compacted soil: capture and efficiency in the use of water and radiation. *Field Crops Research*, *91*(2–3), 131–148. https://doi.org/10.1016/j.fcr.2004.06.011

Sandhya, K., Gayathri, B., Papireddy, M., Praveenkumar, R., Vishwanath, Swathi, B., and Naveen, D. V. (2023). Assessing the Nutrient Status and Soil Fertility Using Nutrient Indexed of Farmer's Fields in Chikkaballapura District, Karnataka. *International Journal of Plant and Soil Science*, *35*(23), 639–649. https://doi.org/10.9734/ijpss/2023/v35i234283

Reference

Šarauskis, E., Kriaučiūnienė, Z., Romaneckas, K., and Buragienė, S. (2018). *Impact of Tillage Methods on Environment, Energy and Economy* (pp. 53–97). https://doi.org/10.1007/978-3-319-99076-7_2

Šarauskis, E., Sokas, S., and Rukaitė, J. (2024). Variable Depth Tillage: Importance, Applicability, and Impact—An Overview. In *AgriEngineering* (Vol. 6, Issue 2, pp. 1870–1885). Multidisciplinary Digital Publishing Institute (MDPI). https://doi.org/10.3390/agriengineering6020109

Schaepman-Strub, G., Schaepman, M. E., Painter, T. H., Dangel, S., and Martonchik, J. V. (2006). Reflectance quantities in optical remote sensing—definitions and case studies. *Remote Sensing of Environment*, *103*(1), 27–42. https://doi.org/10.1016/j.rse.2006.03.002

Schjønning, P., van den Akker, J. J. H., Keller, T., Greve, M. H., Lamandé, M., Simojoki, A., Stettler, M., Arvidsson, J., and Breuning-Madsen, H. (2015). *Driver-Pressure-State-Impact-Response (DPSIR) Analysis and Risk Assessment for Soil Compaction—A European Perspective* (pp. 183–237). https://doi.org/10.1016/bs.agron.2015.06.001

Scott, E. E., and Haggard, B. E. (2021). Natural characteristics and human activity influence turbidity and ion concentrations in streams. *Journal of Contemporary Water Research and Education*, *172*(1), 34–49. https://doi.org/10.1111/j.1936-704x.2021.3353.x

Seeling, B., and Zasoski, R. J. (1993). Microbial effects in maintaining organic and inorganic solution phosphorus concentrations in a grassland topsoil. *Plant and Soil*, *148*(2), 277–284. https://doi.org/10.1007/BF00012865

Sela, G. (2024). *From seed to grain: how to grow wheat for optimal yields*. Cropaia. https://cropaia.com/blog/from-seed-to-grain-how-to-grow-wheat-for-optimal-yields/#:~:text=stress%20tolerance%20mechanisms.-,IRRIGATION,including%20both%20precipitation%20and%20irrigation.andtext=To%20calculate%20water%20requirements%20for,estimate%20crop%20evapotranspiration%20(ETc).

Selolo, K. R., Mzezewa, J., and Odhiambo, J. J. (2023). Short-term effects of tillage and leaf mulch on soil properties and sunflower yield under semi-arid conditions. *Plant, Soil and Environment*, *69*(2), 55–61. https://doi.org/10.17221/160/2022-PSE

Shaheb, M. R., Venkatesh, R., and Shearer, S. A. (2021). A Review on the Effect of Soil Compaction and its Management for Sustainable Crop Production. In *Journal of Biosystems Engineering* (Vol. 46, Issue 4, pp. 417–439). Springer Science and Business Media Deutschland GmbH. https://doi.org/10.1007/s42853-021-00117-7

Shahin, G., Viggiani, G., and Buscarnera, G. (2020). Simulating spatial heterogeneity through a CT-FE mapping scheme discloses boundary effects on emerging compaction bands. *International Journal of Solids and Structures*, *206*, 247–261. https://doi.org/10.1016/j.ijsolstr.2020.08.016

Shamal, S. A. M., Alhwaimel, S. A., and Mouazen, A. M. (2016). Application of an on-line sensor to map soil packing density for site specific cultivation. *Soil and Tillage Research*, *162*, 78–86. https://doi.org/10.1016/j.still.2016.04.016

Shamshiri, R. R., Kalantari, F., Ting, K. C., Thorp, K. R., Hameed, I. A., Weltzien, C., Ahmad, D., and Shad, Z. (2018). Advances in greenhouse automation and controlled environment agriculture: A transition to plant factories and urban agriculture. *International Journal of Agricultural and Biological Engineering*, *11*(1), 1–22. https://doi.org/10.25165/j.ijabe.20181101.3210

Shunlin, L. (2003). Quantitative remote sensing of land surfaces. In *Quantitative Remote Sensing of Land Surfaces* (pp. 1–24). Wiley. https://doi.org/10.1002/047172372X.ch1

Singh, D., Mishra, A. K., Patra, S., Dwivedi, A. K., Ojha, C. S. P., Singh, V. P., Mariappan, S., Babu, S., Singh, N., Yadav, D., Ojasvi, P. R., Kumar, G., Madhu, M. G., Sena, D. R., Chand, L., and Kumar, S. (2023). Effect of long-term tillage practices on runoff and soil erosion in sloping croplands of Himalaya, India. *Sustainability (Switzerland)*, *15*(10). https://doi.org/10.3390/su15108285

Singh, N. K., Sanghvi, G., Yadav, M., Padhiyar, H., Christian, J., and Singh, V. (2023). Fate of pesticides in agricultural runoff treatment systems: Occurrence, impacts and technological progress. *Environmental Research*, *237*, 117100. https://doi.org/10.1016/j.envres.2023.117100

Six, J., Elliott, E. T., and Paustian, K. (2000). Soil macroaggregate turnover and microaggregate formation: a mechanism for C sequestration under no-tillage agriculture. *Soil Biology and Biochemistry*, *32*, 2099–2103. https://doi.org/10.1016/S0038-0717(00)00179-6

Soil Survey Staff. (2014). *Soil Survey Field and Laboratory Methods Manual; Soil Survey Investigations Report No. 51; Version 2 (2014)*. https://www.nrcs.usda.gov/sites/default/files/2023-01/SSIR51.pdf

Somers, B., Asner, G. P., Tits, L., and Coppin, P. (2011). Endmember variability in Spectral Mixture Analysis: A review. *Remote Sensing of Environment*, *115*(7), 1603–1616. https://doi.org/10.1016/j.rse.2011.03.003

Stafford, J. V. (2000). Implementing precision agriculture in the 21st century. *Journal of Agricultural and Engineering Research*, *76*(3), 267–275. https://doi.org/10.1006/jaer.2000.0577

Starr, G. C. (2005). Assessing temporal stability and spatial variability of soil water patterns with implications for precision water management. *Agricultural Water Management*, *72*(3), 223–243. https://doi.org/10.1016/j.agwat.2004.09.020

Steensland, A. (2022). *2022 Global Agricultural Productivity Report: Troublesome trends and system shocks* (T. Thompson and J. Agnew, Eds.). https://globalagriculturalproductivity.org/wp-content/uploads/2024/12/GAP-Initiative-Prospectus.pdf

Stenberg, B., Viscarra Rossel, R. A., Mouazen, A. M., and Wetterlind, J. (2010). Visible and Near Infrared Spectroscopy in Soil Science. *Advances in Agronomy*, *107*, 163–215. https://doi.org/10.1016/S0065-2113(10)07005-7

Sudduth, K. (2025). *Soil Compaction: Where, How Bad, What to Do?* https://www.ars.usda.gov/ARSUserFiles/5478/Sudduth_Compaction_CMC07.pdf

Reference

Sun, W., Shi, F., Chen, H., Zhang, Y., Guo, Y., and Mao, R. (2021). Relationship between relative growth rate and C:N:P stoichiometry for the marsh herbaceous plants under water-level stress conditions. *Global Ecology and Conservation*, *25*. https://doi.org/10.1016/j.gecco.2020.e01416

Sun, Z., Yang, R., Wang, J., Zhou, P., Gong, Y., Gao, F., and Wang, C. (2024). Effects of Nutrient Deficiency on Crop Yield and Soil Nutrients Under Winter Wheat–Summer Maize Rotation System in the North China Plain. *Agronomy*, *14*(11). https://doi.org/10.3390/agronomy14112690

Tamirat, T. W., Pedersen, S. M., Farquharson, R. J., de Bruin, S., Forristal, P. D., Sørensen, C. G., Nuyttens, D., Pedersen, H. H., and Thomsen, M. N. (2022). Controlled traffic farming and field traffic management: Perceptions of farmers groups from Northern and Western European countries. *Soil and Tillage Research*, *217*. https://doi.org/10.1016/j.still.2021.105288

Tan, R. T. (2014). Specularity, Specular Reflectance. In K. Ikeuchi (Ed.), *Computer Vision* (pp. 750–752). Springer US. https://doi.org/10.1007/978-0-387-31439-6_538

Tan, Y., Cheng, E., Feng, X., Zhao, B., Chen, J., Xie, Q., Peng, H., Li, C., Lu, C., Li, Y., Zhang, B., and Peng, D. (2024). Application of APSIM model in winter wheat growth monitoring. *Frontiers in Plant Science*, *15*. https://doi.org/10.3389/fpls.2024.1500103

Tekin, Y., Kul, B., and Okursoy, R. (2008). Sensing and 3D mapping of soil compaction. *Sensors*, *8*(5), 3447–3459. https://doi.org/10.3390/s8053447

Thenkabail, P. S., Smith, R. B., and De Pauw, E. (2000). Hyperspectral Vegetation Indices and Their Relationships with Agricultural Crop Characteristics. *Remote Sensing of Environment*, *71*(2), 158–182. https://doi.org/10.1016/S0034-4257(99)00067-X

Thompson, P. B. (2009). Marcel Mazoyer and Lawrence Roudart, A history of world agriculture from the neolithic age to the current crisis, James H. Membrez, Tr. *Journal of Agricultural and Environmental Ethics*, *22*(1), 101–104. https://doi.org/10.1007/s10806-008-9123-8

Tibshirani, R. (1996). Regression shrinkage and selection via the Lasso. *Journal of the Royal Statistical Society Series B: Statistical Methodology*, *58*(1), 267–288. https://doi.org/10.1111/j.2517-6161.1996.tb02080.x

Tinker, P. B., and Nye, P. (2000). *Solute movement in the rhizosphere*. Oxford University Press. https://doi.org/10.1093/oso/9780195124927.001.0001

Tissier, A.-S., Brankart, J.-M., Testut, C.-E., Ruggiero, G., Cosme, E., and Brasseur, P. (2019). A multiscale ocean data assimilation approach combining spatial and spectral localisation. *Ocean Science*, *15*(2), 443–457. https://doi.org/10.5194/os-15-443-2019

Tracy, S. R., Black, C. R., Roberts, J. A., and Mooney, S. J. (2011). Soil compaction: A review of past and present techniques for investigating effects on root growth. *Journal of the Science of Food and Agriculture*, *91*(9), 1528–1537. https://doi.org/10.1002/jsfa.4424

Tracy, S. R., Black, C. R., Roberts, J. A., and Mooney, S. J. (2013). Exploring the interacting effect of soil texture and bulk density on root system development in tomato (Solanum lycopersicum L.). *Environmental and Experimental Botany*, *91*, 38–47. https://doi.org/10.1016/j.envexpbot.2013.03.003

Tsakiridis, N. L., Theocharis, J. B., Ben-Dor, E., and Zalidis, G. C. (2019). Using interpretable fuzzy rule-based models for the estimation of soil organic carbon from VNIR/SWIR spectra and soil texture. *Chemometrics and Intelligent Laboratory Systems*, *189*, 39–55. https://doi.org/10.1016/j.chemolab.2019.03.011

Tsukagoshi, S., and Shinohara, Y. (2020). Nutrition and nutrient uptake in soilless culture systems. In *Plant Factory* (pp. 221–229). Elsevier. https://doi.org/10.1016/B978-0-12-816691-8.00014-5

Tullberg, J., Antille, D. L., Bluett, C., Eberhard, J., and Scheer, C. (2018). Controlled traffic farming effects on soil emissions of nitrous oxide and methane. *Soil and Tillage Research*, *176*, 18–25. https://doi.org/10.1016/j.still.2017.09.014

Turay, S. P., Jalloh, M. T., Bandabla, T., Kassoh, F. S., and S. Yillah, D. (2022). The Role of Animal Traction Technology in enhancing Production for Small Scale Farmers in Sierra Leone. *International Journal of Environment, Agriculture and Biotechnology*, *7*(6), 043–051. https://doi.org/10.22161/ijeab.76.5

Twum, E. K. A., and Nii-Annang, S. (2015). Impact of Soil Compaction on Bulk Density and Root Biomass of Quercus petraea L. at Reclaimed Post-Lignite Mining Site in Lusatia, Germany. *Applied and Environmental Soil Science*, *2015*. https://doi.org/10.1155/2015/504603

United Nations. (2013). *World economic and social survey 2013*. UN. https://doi.org/10.18356/d30cb118-en

US Department of forest service. (2022). *Identifying Soils Trafficability: Soils Operability Conditions for Machine Traffic*. https://www.fs.usda.gov/rm/pubs_journals/2022/rmrs_2022_nash_m001.pdf

Usowicz, B., and Lipiec, J. (2017). Spatial variability of soil properties and cereal yield in a cultivated field on sandy soil. *Soil and Tillage Research*, *174*, 241–250. https://doi.org/10.1016/j.still.2017.07.015

Vachaud, G., Passerat De Silans, A., Balabanis, P., and Vauclin, M. (1985). Temporal Stability of Spatially Measured Soil Water Probability Density Function. *Soil Science Society of America Journal*, *49*(4), 822–828. https://doi.org/10.2136/sssaj1985.03615995004900040006x

Van Der Leeuw, E., Van Leeuwen, W. J. D., Marsh, S. E., and Archer, S. R. (2024). Using fine resolution remotely sensed data-derived land cover to inform dryland state and transition models. *Rangeland Ecology and Management*, *96*, 128–142. https://doi.org/10.1016/j.rama.2024.06.003

Veronesi, F., Corstanje, R., and Mayr, T. (2012). Mapping soil compaction in 3D with depth functions. *Soil and Tillage Research*, *124*, 111–118. https://doi.org/10.1016/j.still.2012.05.009

Verrelst, J., Romijn, E., and Kooistra, L. (2012). Mapping vegetation density in a heterogeneous river floodplain ecosystem using pointable CHRIS/PROBA data. *Remote Sensing*, *4*(9), 2866–2889. https://doi.org/10.3390/rs4092866

Virtanen, P., Gommers, R., Oliphant, T. E., Haberland, M., Reddy, T., Cournapeau, D., Burovski, E., Peterson, P., Weckesser, W., Bright, J., van der Walt, S. J., Brett, M., Wilson, J., Millman, K. J., Mayorov, N., Nelson, A. R. J., Jones, E., Kern, R., Larson, E., … Vázquez-Baeza, Y. (2020). SciPy 1.0: fundamental algorithms for scientific computing in Python. *Nature Methods*, *17*(3), 261–272. https://doi.org/10.1038/s41592-019-0686-2

Viscarra Rossel, R. A., Cattle, S. R., Ortega, A., and Fouad, Y. (2009). In situ measurements of soil colour, mineral composition and clay content by vis-NIR spectroscopy. *Geoderma*, *150*(3–4), 253–266. https://doi.org/10.1016/j.geoderma.2009.01.025

Viscarra Rossel, R. A., Walvoort, D. J. J., McBratney, A. B., Janik, L. J., and Skjemstad, J. O. (2006). Visible, near infrared, mid infrared or combined diffuse reflectance spectroscopy for simultaneous assessment of various soil properties. *Geoderma*, *131*(1–2), 59–75. https://doi.org/10.1016/j.geoderma.2005.03.007

Walter, A., Finger, R., Huber, R., and Buchmann, N. (2017). Smart farming is key to developing sustainable agriculture. In *Proceedings of the National Academy of Sciences of the United States of America* (Vol. 114, Issue 24, pp. 6148–6150). National Academy of Sciences. https://doi.org/10.1073/pnas.1707462114

Walters, R. (2021). *Soil particle and bulk density technical note 2*. https://agrosphere-international.net/Documents/DHC/Particle%20and%20Bulk%20Density.pdf

Wang, F., Cui, X., Sun, Y., and Dong, C. H. (2013). Ethylene signaling and regulation in plant growth and stress responses. In *Plant Cell Reports* (Vol. 32, Issue 7, pp. 1099–1109). https://doi.org/10.1007/s00299-013-1421-6

Warner, J. M., Mann, M. L., Chamberlin, J., and Tizale, C. Y. (2023). Estimating acid soil effects on selected cereal crop productivities in Ethiopia: Comparing economic cost-effectiveness of lime and fertilizer applications. *PLoS ONE*, *18*(1 January). https://doi.org/10.1371/journal.pone.0280230

Waskom, M. (2021). Seaborn: statistical data visualization. *Journal of Open Source Software*, *6*(60), 3021. https://doi.org/10.21105/joss.03021

Webster, R. (2000). Is soil variation random? *Geoderma*, *97*(3–4), 149–163. https://doi.org/10.1016/S0016-7061(00)00036-7

Webster, R., Welham, S. J., Potts, J. M., and Oliver, M. A. (2006). Estimating the spatial scales of regionalized variables by nested sampling, hierarchical analysis of variance and residual maximum likelihood. *Computers and Geosciences*, *32*(9), 1320–1333. https://doi.org/10.1016/j.cageo.2005.12.002

Whalley, W. R., Watts, C. W., Gregory, A. S., Mooney, S. J., Clark, L. J., and Whitmore, A. P. (2008). The effect of soil strength on the yield of wheat. *Plant and Soil*, *306*(1–2), 237–247. https://doi.org/10.1007/s11104-008-9577-5

WHH. (2023). *Policy brief sustainable food security through climate resilience*. June. https://reliefweb.int/report/world/sustainable-food-security-through-climate-resilience

White, J., and Edwards, J. (2007). *Wheat growth and development*. https://www.dpi.nsw.gov.au/__data/assets/pdf_file/0006/449367/Procrop-wheat-growth-and-development.pdf

White, R. G., and Kirkegaard, J. A. (2010). The distribution and abundance of wheat roots in a dense, structured subsoil - Implications for water uptake. *Plant, Cell and Environment*, *33*(2), 133–148. https://doi.org/10.1111/j.1365-3040.2009.02059.x

Wise, K., Shaner, G., and Mansfield, C. (2024). *Managing wheat by growth stage*. https://www.extension.purdue.edu/extmedia/id/id-422.pdfm.

Wold, S., Sjostrom, M., Eriksson, L., and Sweden˚˚, S. (2001). PLS-regression: a basic tool of chemometrics. In *Chemometrics and Intelligent Laboratory Systems* (Vol. 58). https://doi.org/10.1016/S0169-7439(01)00155-1

Wolfert, S., Ge, L., Verdouw, C., and Bogaardt, M. J. (2017). Big Data in Smart Farming – A review. In *Agricultural Systems* (Vol. 153, pp. 69–80). Elsevier Ltd. https://doi.org/10.1016/j.agsy.2017.01.023

World Bank. (2024). *Agriculture and Food*. World Bank Group. https://www.worldbank.org/en/topic/agriculture/overview

Wu, Q., Yang, L., Liang, H., Liu, M., Chen, Y., Chen, D., and Shen, P. (2024). Impacts of soil compaction and phosphorus levels on the dynamics of phosphate-solubilizing and nitrogen-fixing bacteria in the peanut rhizosphere. *Agronomy*, *14*(9), 1971. https://doi.org/10.3390/agronomy14091971

Xie, S., Ding, F., Chen, S., Wang, X., Li, Y., and Ma, K. (2022). Prediction of soil organic matter content based on characteristic band selection method. *Spectrochimica Acta - Part A: Molecular and Biomolecular Spectroscopy*, *273*. https://doi.org/10.1016/j.saa.2022.120949

Xue, J., and Su, B. (2017). Significant Remote Sensing Vegetation Indices: A Review of Developments and Applications. *Journal of Sensors*, *2017*, 1–17. https://doi.org/10.1155/2017/1353691

Xue, W., Feng, L., Yang, J., Xu, Y., Ho, H. C., Luo, R., Menenti, M., and Wong, M. S. (2025). Retrieval of Vegetation Indices and Vegetation Fraction in Highly Compact Urban Areas: A 3D Radiative Transfer Approach. Remote Sensing, 17(1), 143. https://doi.org/10.3390/rs17010143

Yamasaki, Y., Morie, M., and Noguchi, N. (2022). Development of a high-accuracy autonomous sensing system for a field scouting robot. *Computers and Electronics in Agriculture*, *193*. https://doi.org/10.1016/j.compag.2021.106630

Yang, C., Hou, J., and Wang, Y. (2021). Extraction of land covers from remote sensing images based on a deep learning model of NDVI-RSU-Net. *Arabian Journal of Geosciences*, *14*(20), 2073. https://doi.org/10.1007/s12517-021-08420-5

Reference

Yin, Q., Zhang, Y., Li, W., Wang, J., Wang, W., Ahmad, I., Zhou, G., and Huo, Z. (2023). Estimation of Winter Wheat SPAD Values Based on UAV Multispectral Remote Sensing. *Remote Sensing*, *15*(14). https://doi.org/10.3390/rs15143595

Yin, Z., Lei, T., Yan, Q., Chen, Z., and Dong, Y. (2013). A near-infrared reflectance sensor for soil surface moisture measurement. *Computers and Electronics in Agriculture*, *99*, 101–107. https://doi.org/10.1016/j.compag.2013.08.029

Yu, C., Mawodza, T., Atkinson, B. S., Atkinson, J. A., Sturrock, C. J., Whalley, R., Hawkesford, M. J., Cooper, H., Zhang, X., Zhou, H., and Mooney, S. J. (2024). The effects of soil compaction on wheat seedling root growth are specific to soil texture and soil moisture status. *Rhizosphere*, *29*. https://doi.org/10.1016/j.rhisph.2023.100838

Zhang, B., Jia, Y., Fan, H., Guo, C., Fu, J., Li, S., Li, M., Liu, B., and Ma, R. (2024). Soil compaction due to agricultural machinery impact: A systematic review. In *Land Degradation and Development* (Vol. 35, Issue 10, pp. 3256–3273). John Wiley and Sons Ltd. https://doi.org/10.1002/ldr.5144

Zhang, N., Wang, M., and Wang, N. (2002). Precision agriculture - a worldwide overview. *Computers and Electronics in Agriculture*, *36*, 113–132. www.elsevier.com/locate/compag

Zhang, Y., Luo, C., Zhang, Y., Gao, L., Wang, Y., Wu, Z., Zhang, W., and Liu, H. (2024). Integration of bare soil and crop growth remote sensing data to improve the accuracy of soil organic matter mapping in black soil areas. *Soil and Tillage Research*, *244*, 106269. https://doi.org/10.1016/j.still.2024.106269

Zhang, Z., Yuan, Y., Liu, Q., and Yin, H. (2019). Plant nitrogen acquisition from inorganic and organic sources via root and mycelia pathways in ectomycorrhizal alpine forests. *Soil Biology and Biochemistry*, *136*. https://doi.org/10.1016/j.soilbio.2019.06.013

Zhao, Y., Chen, X. P., Cui, Z. L., and Lobell, D. B. (2015). Using satellite remote sensing to understand maize yield gaps in the North China Plain. *Field Crops Research*, *183*, 31–42. https://doi.org/10.1016/j.fcr.2015.07.004

Zheng, K., Cheng, J., Xia, J., Liu, G., and Xu, L. (2021). Effects of soil bulk density and moisture content on the physico-mechanical properties of paddy soil in plough layer. *Water (Switzerland)*, *13*(16). https://doi.org/10.3390/w13162290

Zhou, J., Zhang, Z., Xin, Y., Chen, G., Wu, Q., Liang, X., and Zhai, Y. (2022). Effects of planting density on root spatial and temporal distribution and yield of winter wheat. *Agronomy*, *12*(12). https://doi.org/10.3390/agronomy12123014

Zörb, C., Ludewig, U., and Hawkesford, M. J. (2018). Perspective on wheat yield and quality with reduced nitrogen supply. In *Trends in Plant Science* (Vol. 23, Issue 11, pp. 1029–1037). Elsevier Ltd. https://doi.org/10.1016/j.tplants.2018.08.012

Zou, H., and Hastie, T. (2005). Regularization and variable selection via the elastic net. *Journal of the Royal Statistical Society Series B: Statistical Methodology*, *67*(2), 301–320. https://doi.org/10.1111/j.1467-9868.2005.00503.x

Appendix

Appendix A- Packing density and properties maps from the first experiment

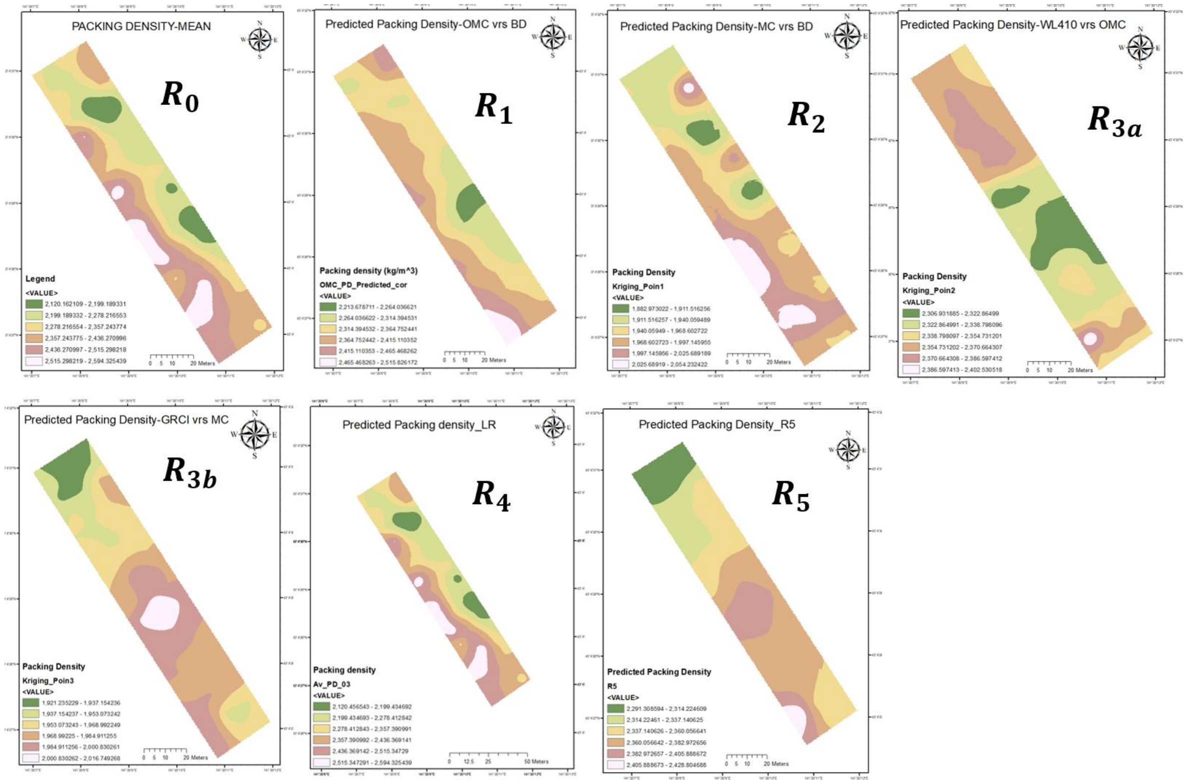

Figure A1: PD maps from the different models

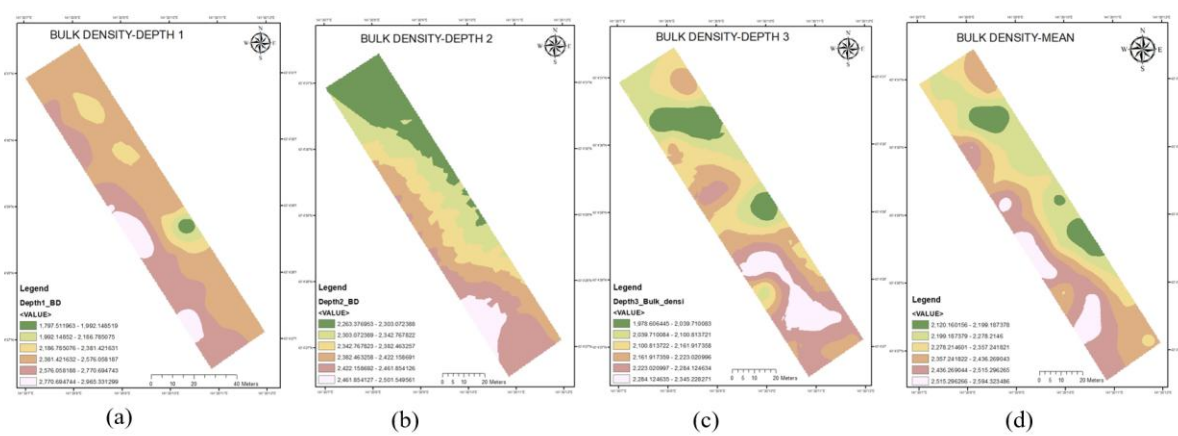

Figure A2: BD spatial maps (a) 0.2-0.3 m (b) 0.1-0.2 m (c) 0-0.1 m (d) 0-0.3 m

Appendix

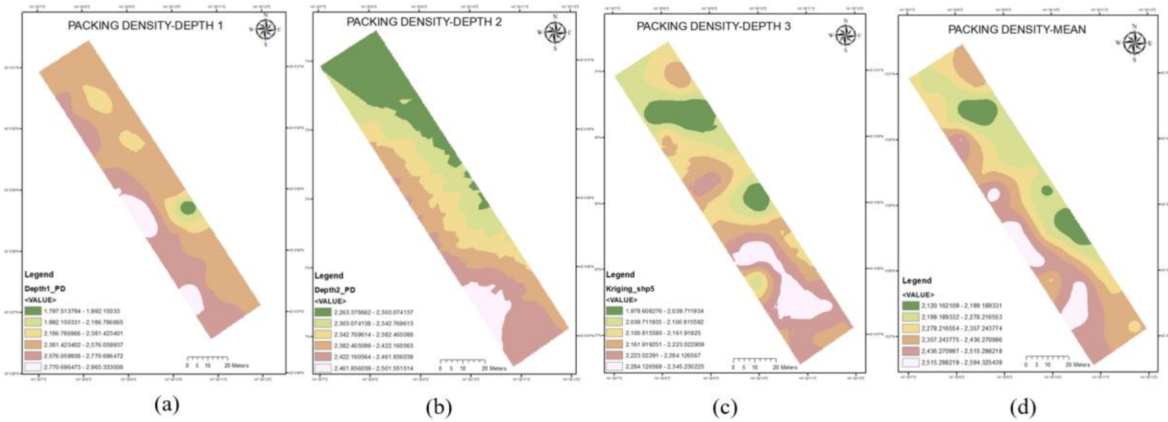

Figure A3: PD spatial maps (a) 0.2-0.3 m (b) 0.1-0.2 m (c) 0-0.1 m (d) 0-0.3 m

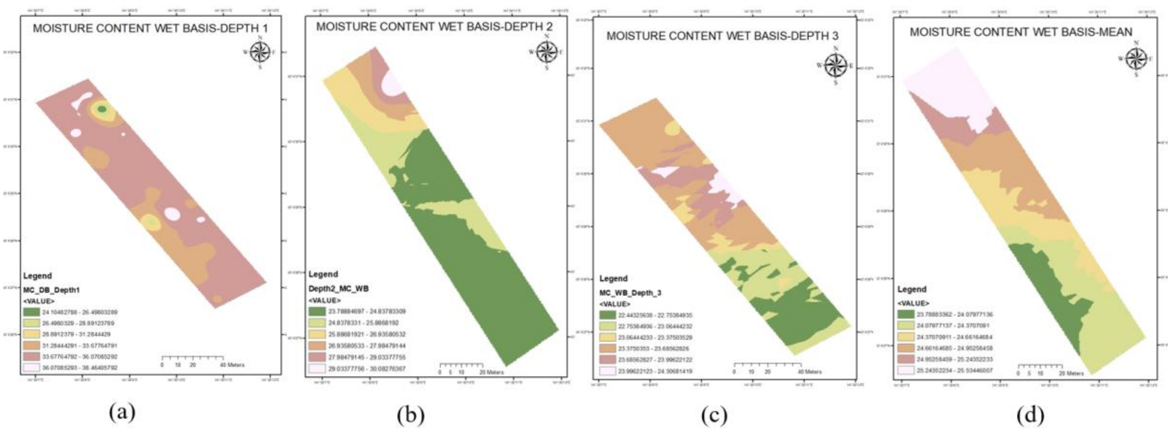

Figure A4: MCW spatial maps (a) 0.2-0.3 m (b) 0.1-0.2 m (c) 0-0.1 m (d) 0-0.3 m

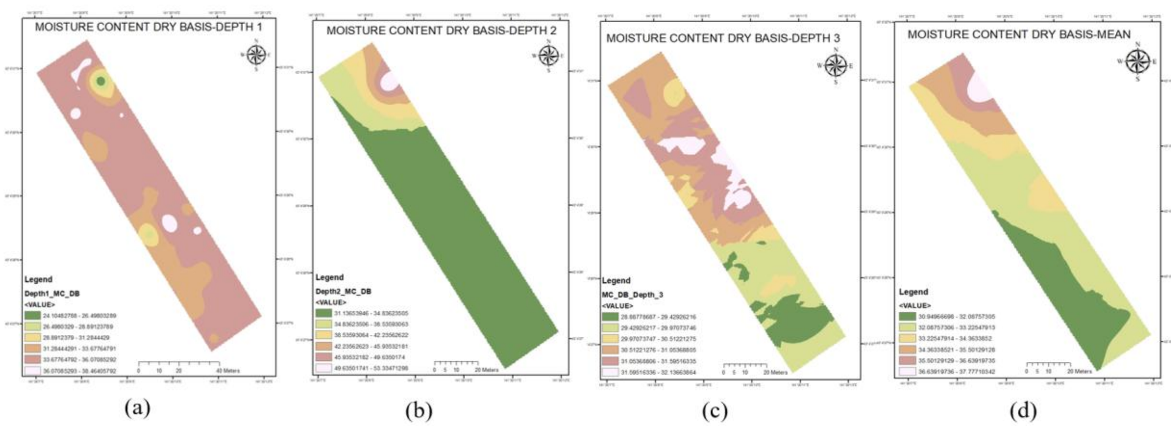

Figure A5: MCD spatial maps (a) 0.2-0.3 m (b) 0.1-0.2 m (c) 0-0.1 m (d) 0-0.3 m

Appendix

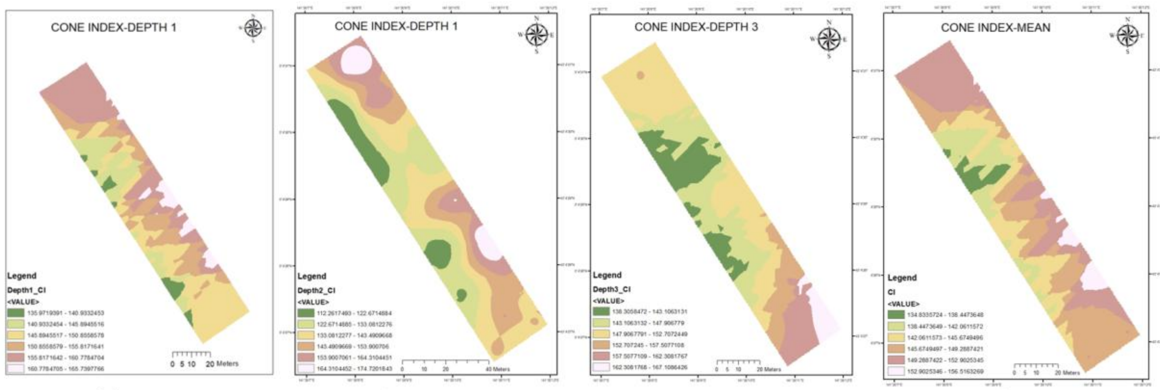

(a) (b) (c) (d)

Figure A6: CI spatial maps (a) 0.2-0.3 m (b) 0.1-0.2 m (c) 0-0.1 m (d) 0-0.3 m

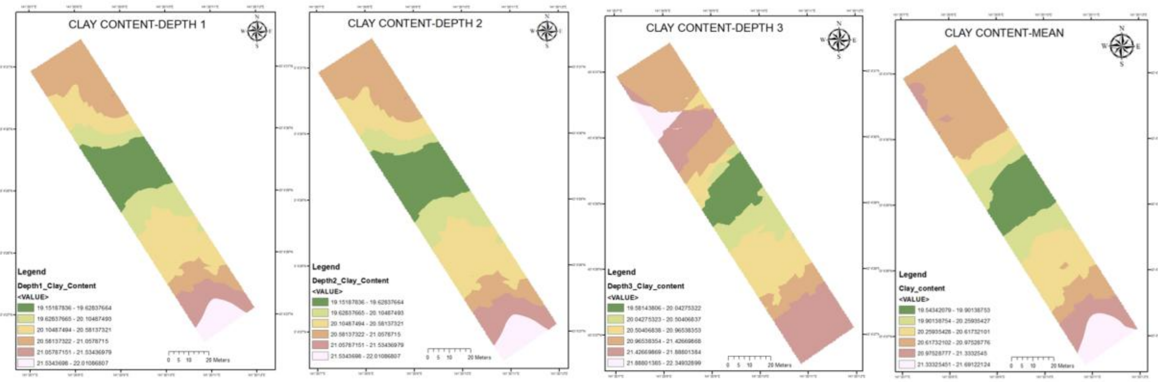

(a) (b) (c) (d)

Figure A7: CC spatial maps (a) 0.2-0.3 m (b) 0.1-0.2 m (c) 0-0.1 m (d) 0-0.3 m

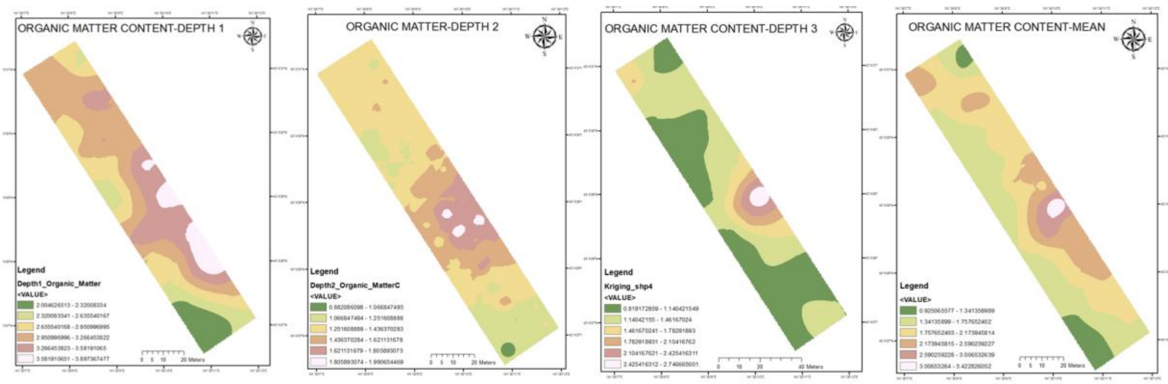

(a) (b) (c) (d)

Figure A8: OMC spatial maps (a) 0.2-0.3 m (b) 0.1-0.2 m (c) 0-0.1 m (d) 0-0.3 m

Appendix

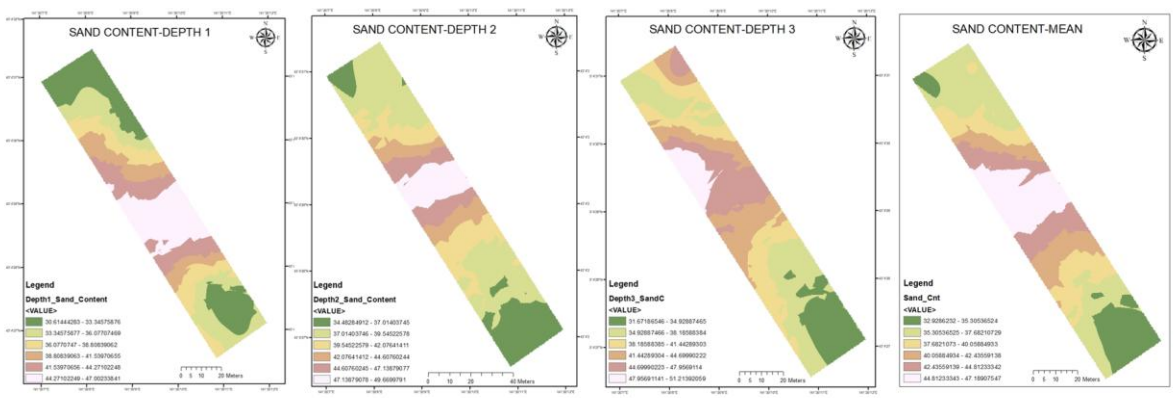

(a) (b) (c) (d)

Figure A9: SC spatial maps (a) 0.2-0.3 m (b) 0.1-0.2 m (c) 0-0.1 m (d) 0-0.3 m

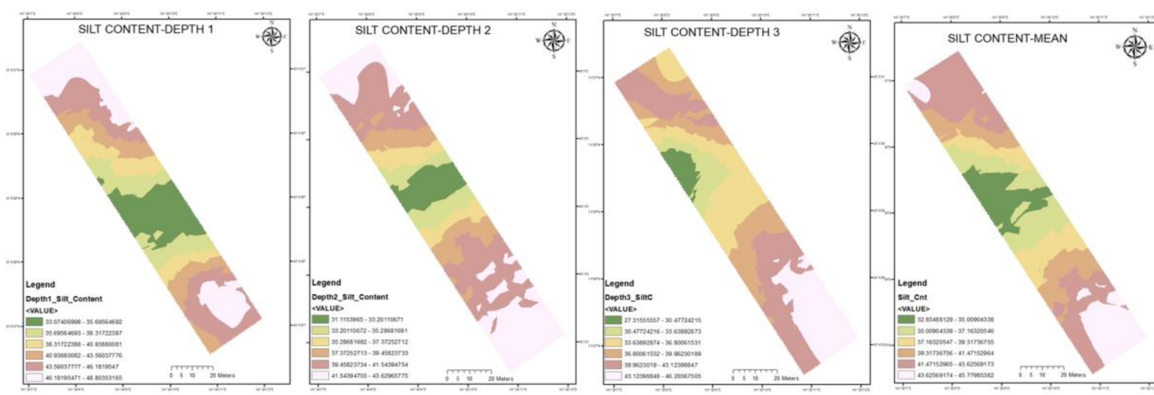

(a) (b) (c) (d)

Figure A10: STC spatial maps (a) 0.2-0.3 m (b) 0.1-0.2 m (c) 0-0.1 m (d) 0-0.3 m

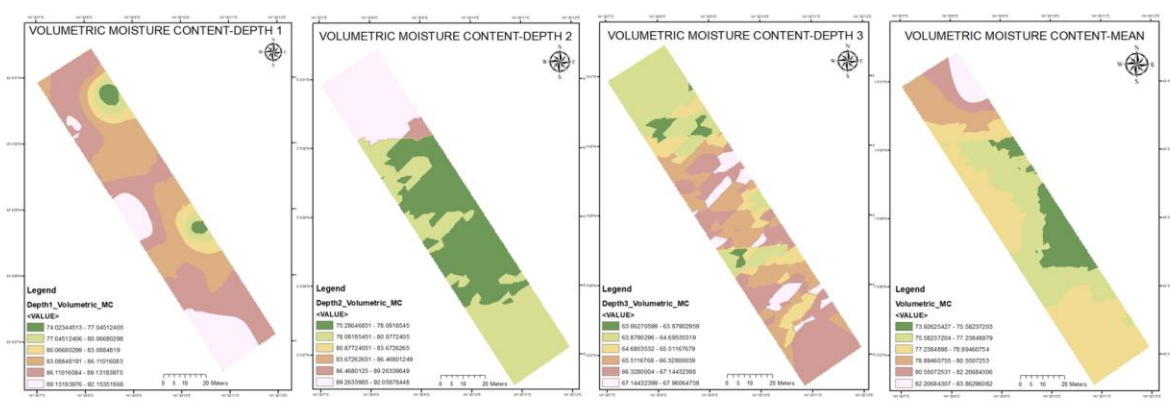

(a) (b) (c) (d)

Figure A11: VMC spatial maps (a) 0.2-0.3 m (b) 0.1-0.2 m (c) 0-0.1 m (d) 0-0.3 m

Appendix

Appendix B: GTD-based yield prediction models

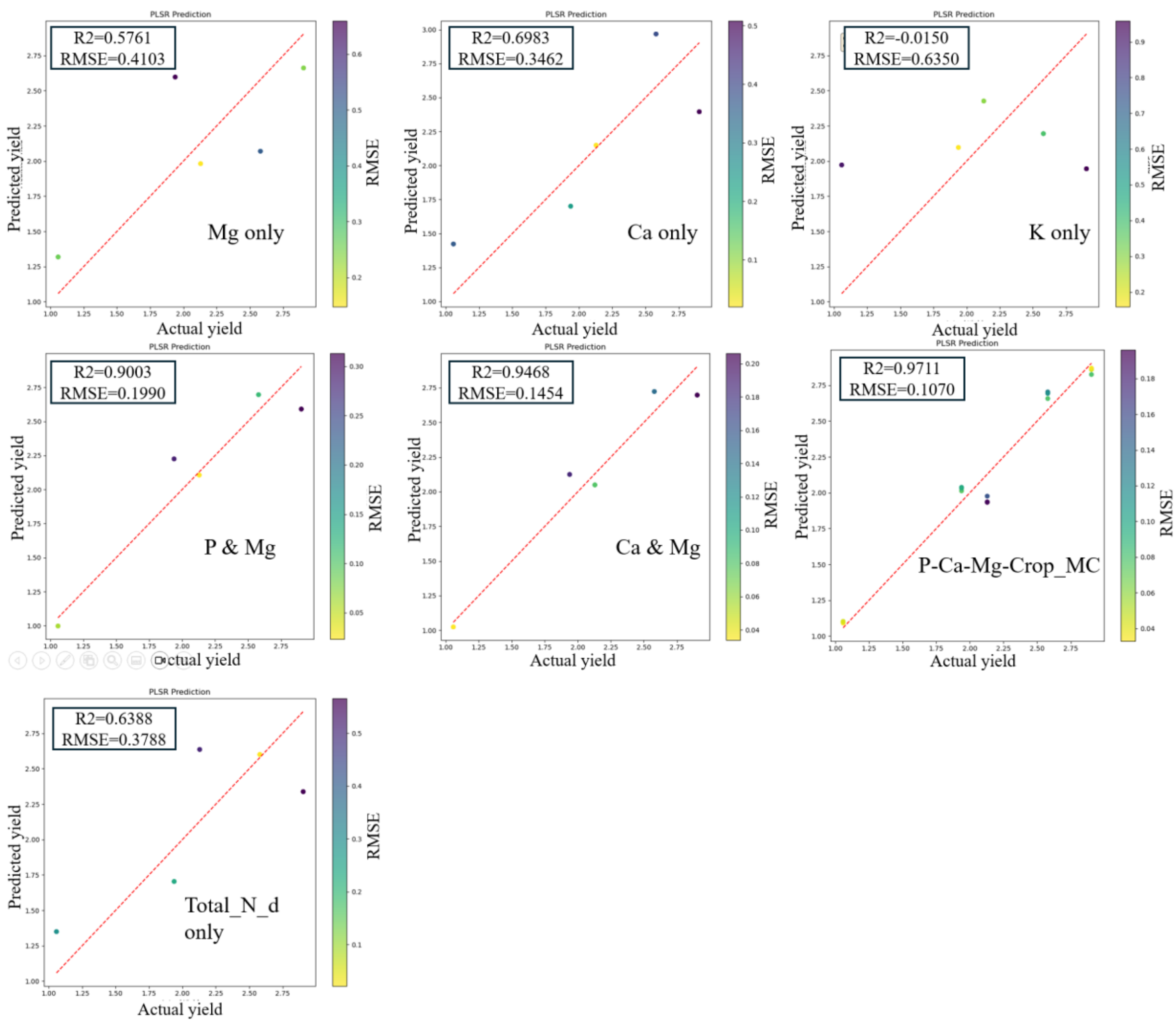

Figure B1: Extra GTD-based yield prediction models

Appendix

Appendix C: HSC-based properties and yield prediction models

Table C1: HSC estimation of highly influential properties

PROPERTY	R^2	RMSE	Data
P	0.5583	0.5107	Original reflectance
	0.5629	0.5080	Original + Savitzky-Golay
	0.6796	0.4349	Savitzky-Golay
	0.7509	0.3835	1^{st} derivative
	0.6741	0.4387	All combine
	0.7873	0.3544	1^{st} derivative + VI
Ca	**0.3339**	**7.3788**	**Original reflectance**
	0.3968	7.0221	Original + Savitzky-Golay
	0.4880	6.4690	Savitzky-Golay
	0.6979	4.9696	1^{st} derivative + VI
	0.6239	5.5445	All combine
Mg	**0.6375**	**4.2963**	**Original reflectance**
	0.5298	4.8930	Original + Savitzky-Golay
	0.6441	4.2573	Savitzky-Golay
	0.8364	2.8866	All combine
	0.8569	2.6995	1^{st} derivative + VI
Total N_d	**0.4651**	**0.0623**	**Original reflectance**
	0.4939	0.0606	Original + Savitzky-Golay
	0.5205	0.0590	Savitzky-Golay
	0.4567	0.0628	All combine
	0.72	0.05	1^{st} derivative + VI

Appendix

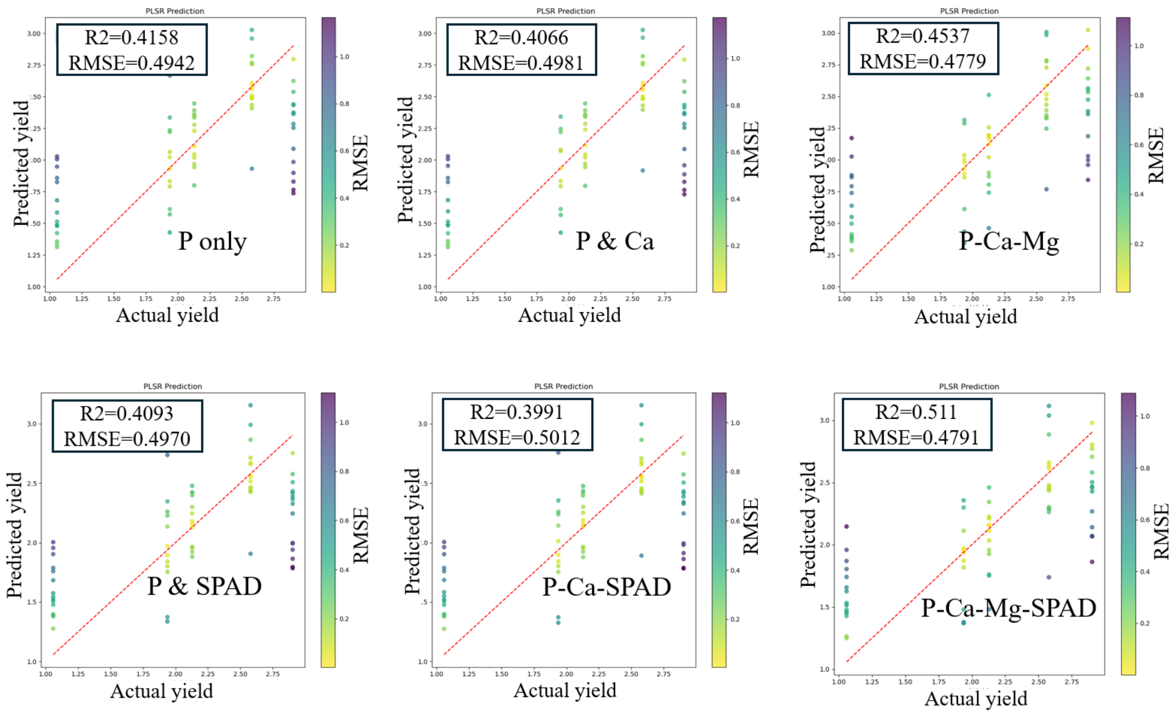

Figure C1: HSC yield prediction at the Tillering stage

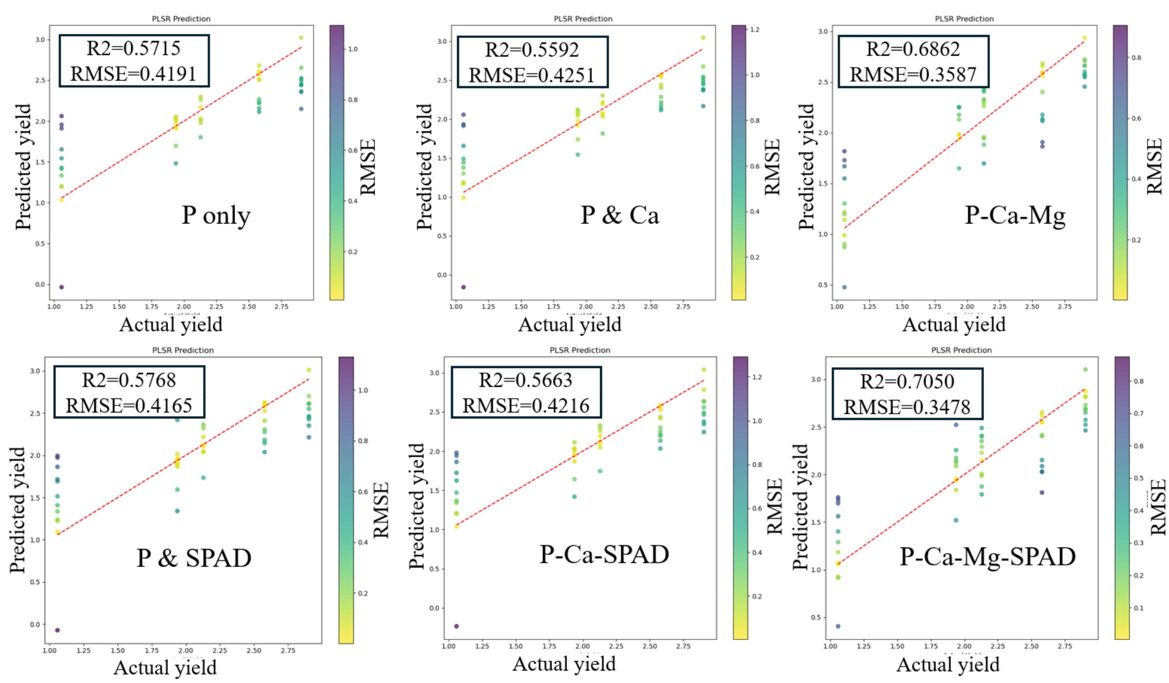

Figure C2: HSC yield prediction at the Pinnacle stage

Appendix

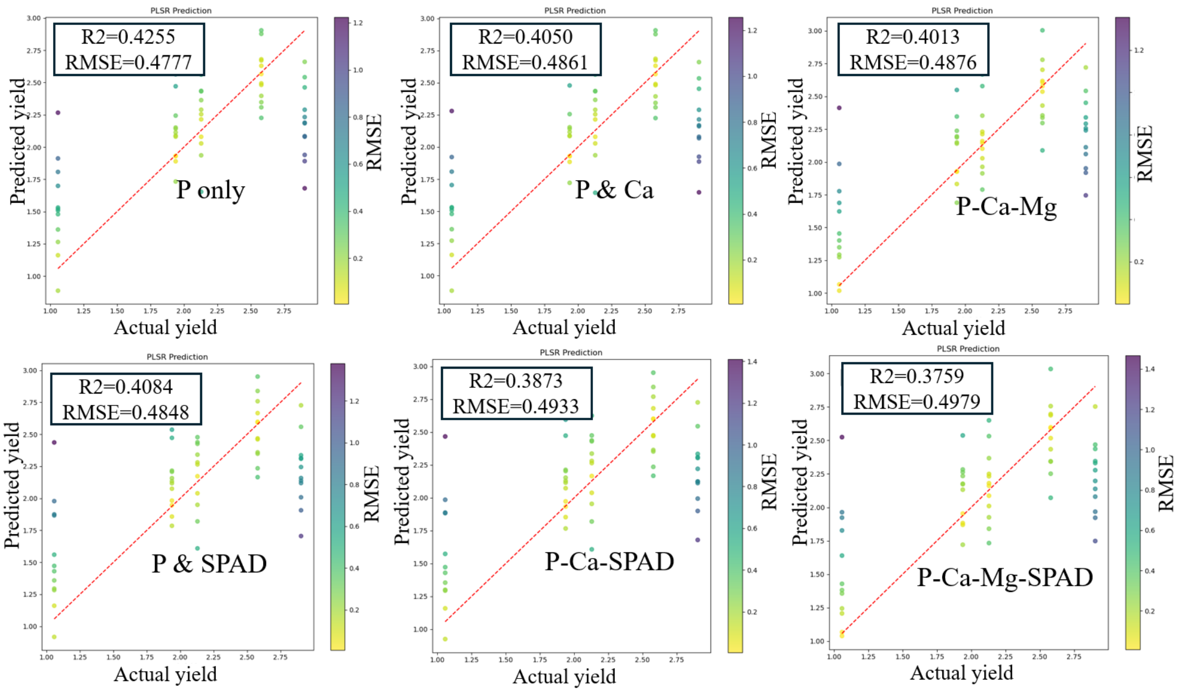

Figure C3: HSC yield prediction at the Heading/Beginning of flowering stage

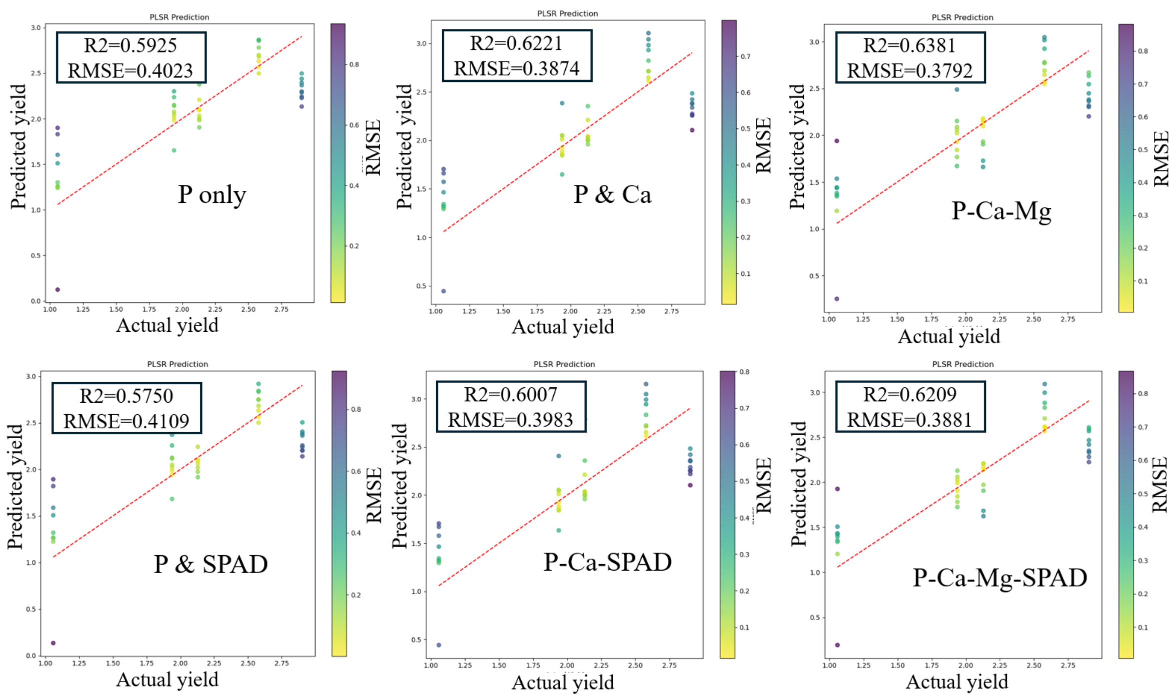

Figure C4: HSC yield prediction at the Milk formation stage

Appendix D: HSC predicted and GTD properties map

Table D1: Features for HSC predicted properties- Tillering

PROPERTIES	FEATURES	R^2	RMSE
Mg	CARI, GRVI, NGRDI, SAVI, NDVI, GNDVI, FVC, PR14, PSRI, ARI, WI, HNDVI	0.1535	6.6267
P	wl820der, wl905der, wl940der, wl465der, wl775der, wl600der, wl945der,wl590der, wl545der, wl795der, wl815der, wl910der, wl800der, wl790der, wl870der, wl760der, wl805der	0.481	0.5683
MCW	wl690, wl985, wl640, wl925, wl700, wl950, wl890, wl760, wl770, wl800, wl980, wl940, wl910, wl990, wl960	0.0483	1.5593
VMC	wl800der, wl935der, wl580der, wl545der, wl540der, wl585der	-0.0105	2.857
Crop_MC	GNDVI, wl415der, wl975, wl775der, wl585der, wl980, PSRI, ARI, wl545der, wl775der, wl570der, NGRDI, wl680der, wl575der, wl925der, wl480der, wl800der, wl580der, wl765der	0.6098	2.6203
RGR_Crop	wl720, wl465der, wl865, wl600, wl650, wl925, wl840, wl895, wl480der, wl400sg, wl510, wl740, wl885, wl970	0.6126	0.0041
RGR_Root	wl570der, NGRDI, SAVI, wl915der, wl575der, wl690der, PR14, wl675der, wl910der, wl560der, wl835der, wl490der, wl595der, wl590der, wl940der, wl780der, wl945der, ARI, wl580der, wl790der	0.5881	0.0065
CEC	wl775, wl985, wl935, wl855, wl900, wl965, wl600, wl910, wl740, wl400sg, wl970	0.3992	0.4641

Table D2: Features for HSC predicted properties- Pinnacle

PROPERTIES	FEATURES	R^2	RMSE
Mg	wl580der, wl590der, wl745der, wl565der, wl555der, wl910der, wl560der, wl750der, wl865der, wl860der, wl755der, wl760der, wl595der, wl550der, wl770der	0.7573	3.5702

PROPERTIES	FEATURES	R^2	RMSE
P	ARI, PSRI, wl545der, SAVI, WI, GNDVI, PR14, FVC, CARI	0.487	0.56
MCW	wl510sg, wl575sg, wl900sg, wl570sg, wl490sg, wl940sg, wl750sg, wl1000sg wl980sg, wl975sg, wl460der, wl935sg, wl465, wl485der	0.5496	1.2794
MCD	wl510sg, wl575sg, wl900sg, wl570sg, wl490sg, wl940sg, wl750sg, wl1000sg, wl980sg, wl975sg, wl460der, wl935sg, wl465der, wl485der	0.5496	3.5758

Table D3: Features for HSC predicted properties- Heading/Beginning of flowering

PROPERTIES	FEATURES	R^2	RMSE
Mg	wl685sg, wl475der, wl900sg, wl500der, wl850sg, wl925sg, wl830sg, wl970sg, wl945sg, wl465der, wl855sg, wl660sg, wl825sg, wl820sg, wl480der	0.3901	5.5728
P	wl830sg, wl875sg, wl500der, wl475der, wl785sg, wl795sg, wl825sg, wl820sg, wl970sg, wl965sg, wl790sg, wl480der	0.4172	0.5866
Mg_w	wl705sg, wl875, wl705, wl690sg, wl690, wl695sg, wl700sg, wl695, wl700	0.6904	0.0032
Crop_MC	HNDVI, wl660der, wl935der, wl820der, wl700der, wl885der, wl750der, wl795der, wl705der, wl860der, wl865der, wl715der, wl755der, wl760der, wl800der, PSRI, wl550der, PR14, ARI	0.6455	4.3271
RGR_Crop	wl810der, wl815der, CARI, wl770der, wl595der, HNDVI, wl820der, GNDVI, ARI	0.5693	0.0168
RGR_Root	Wl810der, RECI, wl785der, wl600der, wl595der, wl550der, ARI	0.7693	0.0211
Height	Canopy height model (CHM) = digital surface model (DSM) – digital terrain model (DTM)]/sin(camera angle)	1	0.00

Table D4: Features for HSC predicted properties- Milk formation

PROPERTIES	FEATURES	R^2	RMSE
Ca	wl755, wl660, wl725, wl735, wl685, wl765, wl990, wl470, wl950, wl905, wl835, wl980, wl840, wl700, wl935, wl870, wl730	0.857	3.4192
K	Wl830der, Wl910der, wl775der, wl755der, wl770der, Wl930der, Wl840de, rwl765der, wl880der, Wl810der, wl485der, wl580der, wl555der, wl560der	0.6691	0.3489
Crop_MC	wl740der, Wl940der, wl755der, wl565der, wl545der, wl560der, wl620der, Wl945der, Wl810der, wl890der, wl895der, wl790der, wl850der, wl785der, wl580der, ‘wl780der, Wl815der, Wl845der	0.6924	1.154
RGR_Root	wl685der, Wl910der, Wl945der, wl605der, wl575der, wl755der, NGRDI, Wl915der, PR14, wl875der, Wl815der, PVI, NDVI, Wl810der, wl555der, wl560der, wl880der, wl770der	0.7705	0.0234

Table D5: Features for HSC predicted properties- Milk Ripening

Properties	Features	R^2	RMSE
Ca	NDVI, wl495der, wl740der, PR14, wl845der, CARI, wl785der, HNDVI, wl600der, wl770der, wl850der, wl830der, wl775der, GNDVI, wl680der, wl800der, wl875der, wl780der, wl815der, PSRI	0.653	5.3259
K	wl625sg, wl655sg, wl490sg, wl970sg, wl805sg, wl455der, wl855sg, wl765sg, wl620sg, wl800sg, wl860sg, wl460der, wl480der	0.6276	0.3702
MCD	wl795sg, wl625sg, wl970sg, wl620sg, wl855sg, wl850sg, wl845sg, wl800sg, wl655sg, wl465der, wl455der, wl460der, wl480der	0.8522	2.2013

Table D6: Measured soil and crop growth properties with R^2 and RSME for HSC prediction model

Appendix

Property	Tillering		Pinnacle		Heading/Beginning of flowering		Milk formation		Milk ripening	
	R^2	RMSE	R^2	RMSE	R^2	RMSE	R^2	RMSE	R^2	RMSE
Physical properties										
MCD	-0.01	2.40	0.33	4.36	0.33	2.56	0.71	2.66	0.81	2.50
MCW	0.06	1.55	0.33	1.56	0.33	0.92	0.71	0.95	0.81	0.89
VMC	-0.01	2.85	0.33	1.62	0.33	0.95	0.71	0.99	0.81	0.93
Chemical properties										
PH	0.24	0.34	0.23	0.31	0.66	0.16	0.64	0.12	0.86	0.06
CEC	0.47	0.43	0.29	0.49	0.42	0.44	0.76	0.28	0.77	0.28
Mg	0.19	6.47	0.75	3.63	0.38	5.61	0.46	5.23	0.84	2.86
P	0.47	0.57	0.50	0.55	0.42	0.59	0.73	0.40	0.75	0.38
K	0.63	0.37	0.46	0.45	0.65	0.36	0.65	0.36	0.55	0.41
Ca	0.55	6.14	0.49	6.50	0.50	6.39	0.86	3.44	0.65	5.35
Crop data										
Height_CHM	1	0.00	1	0.00	1	0.00	1	0.00	1	0.00
Height_Ref	0.46	1.30	0.75	0.99	0.64	1.58	0.83	1.13	0.85	0.62
SPAD	0.58	1.49	0.64	1.12	0.45	1.24	0.90	1.00	0.93	0.73
Crop MC	0.63	2.56	0.45	1.88	0.64	4.39	0.71	1.12	0.63	1.99
RGR Crop	0.64	0.00	0.38	0.02	0.57	0.02	0.63	0.01	0.86	0.01
RGR Root	0.60	0.01	0.57	0.03	0.77	0.02	0.76	0.02	0.76	0.02
Number of Pod per m^2	0.32	22.72	0.60	17.35	0.46	19.72	0.60	17.04	0.81	11.79
Number of Grains per pod	0.42	3.18	0.60	2.62	0.46	19.72	0.60	2.56	0.72	2.16
100 Grains weight	0.43	0.19	0.53	0.17	0.39	0.19	0.69	0.14	0.74	0.13
Yield ha/ton	0.39	0.51	0.55	0.43	0.49	0.45	0.52	0.43	0.74	0.32

Table D7: Tillering SC models

FUNCTION	MIN ERROR	MAX ERROR	0-4.9%	5-9.9%	10-14.9%	15-20%
T1: BD_{GTD}=-1.3307+0.0529P-0.0004Mg+2.3362RGR_Crop+0.0006VMC-1.4412RGR_Root+0.0022Crop_MC+0.0398CEC	0.0080	12.67	81.7%	15.5%	2.8%	0
T2: BD_{GTD}= 0.1171+0.0696P-0.0033Mg	0.0173	12.58	80.3%	16.9%	2.8%	0
T3: BD_{GTD}= 1.5132-0.0727MCW+0.0379VMC	0.0130	12.96	90.1%	8.5	1.4%	0
T4:BD_{HSC}=-0.6908+0.0696P-0.0046Mg+1.7151RGR_Crop+0.0013VMC-0.7659RGR_Root+0.0031Crop_MC+0.0197CEC	0.1297	16.25	80.3%	12.7%	4.2%	2.8%
T5: BD_{HSC}= 0.3329+0.0650P-0.0043Mg	0.1693	14.58	80.3%	14.1%	5.6%	0
T6: BD_{HSC}= 1.7439-0.0101MCW-0.0123VMC	0.0578	18.79	74.6%	19.7%	2.8%	2.8%

Table D8: Pinnacle SC models

FUNCTION	MIN ERROR	MAX ERROR	0-4.9%	5-9.9%	10-14.9%	15-20%
P1: BD_{GTD}=1.3460-0.0162MCW	0.1922	14.485	67.9%	26.8%	5.4%	0
P2: BD_{GTD}=0.0949+0.0695P-0.0031Mg	0.1009	12.3065	80.4%	17.9%	1.8%	0
P3: BD_{GTD}=1.3444-0.0058MCD	0.1922	14.4848	67.9%	26.8%	5.4%	0
P4: BD_{GTD}=0.4092-0.0039MCD+0.0419P	0.0536	12.1083	82.1%	16.1%	1.8%	0
P5:BD_{HSC}= 1.3314-0.0141MCW	0.0386	15.3959	64.3%	32.1%	1.8%	0
P6: BD_{HSC}= 0.3273+0.0520P-0.0019Mg	0.0895	16.4132	83.9%	8.9%	5.4%	1.8%

FUNCTION	MIN ERROR	MAX ERROR	0-4.9%	5-9.9%	10-14.9%	15-20%
P7: $\boldsymbol{BD_{HSC}}$= 1.3300-0.0050MCD	0.0386	15.3959	64.3%	32.1%	1.8%	1.8%
P8: $\boldsymbol{BD_{HSC}}$= 0.5564-0.0040MCD+0.0350P	0.0249	14.7654	76.8%	17.9%	5.4%	0

Table D9: Heading/ Beginning of flowering Sc models

FUNCTION	MIN ERROR	MAX ERROR	0-4.9%	5-9.9%	10-14.9%	15-20%
H1: $\boldsymbol{BD_{GTD}}$=0.4687+7.8472Mg_w	0.045	14.0153	85%	11.7%	3.3%	0
H2: $\boldsymbol{BD_{GTD}}$=0.1247+0.0689P-0.0033Mg	0.0137	12.6534	80%	16.7%	3.3%	0
H3: $\boldsymbol{BD_{GTD}}$= 1.1418 +0.0021Crop_MC-0.5316RGR_Crop + 0.6164RGR_Root - 0.0004Height	0.14	18.872	70%	25%	3.3%	1.7%
H4:$\boldsymbol{BD_{HSC}}$= 0.4648+7.8957Mg_w	0.0034	18.0913	86.7%	11.7%	0	1.7%
H5: $\boldsymbol{BD_{HSC}}$= 0.2794+0.0510P-0.0012Mg	0.1795	18.4746	85%	11.7%	1.7%	1.7%
H6: $\boldsymbol{BD_{HSC}}$= 1.0907 +0.0016Crop_MC-0.0833RGR_Crop + 0.4609RGR_Root - 0.0006$\mathbf{Height_{HSC-CHm}}$	0.1568	21.3133	70%	26.7%	0	1.7%

Table D10: Milk formation SC models

FUNCTION	MIN ERROR	MAX ERROR	0-4.9%	5-9.9%	10-14.9%	15-20%
MF1: $\boldsymbol{BD_{GTD}}$=-1.0663+0.0042Ca	0.0025	13.0054	71.1%	22.2%	6.7%	0

Appendix

FUNCTION	MIN ERROR	MAX ERROR	0-4.9%	5-9.9%	10-14.9%	15-20%
MF2: $\boldsymbol{BD_{GTD}}$=3.8450-0.0668K	0.0919	16.7795	84.4%	8.9%	4.4%	2.2%
MF3: $\boldsymbol{BD_{GTD}}$= 1.0285 + 0.0032Crop_MC - 0.4030RGR_Root	0.1382	16.6626	62.2%	26.7%	8.9%	2.2%
MF4: $\boldsymbol{BD_{GTD}}$=1.6280 - 0.0494K + 0.0028Ca	0.0549	13.6261	82.2%	15.6%	2.2%	0
MF5:$\boldsymbol{BD_{HSC}}$= -1.0078+0.0041Ca	0.0753	15.2314	75.6%	20%	2.2%	2.2%
MF6: $\boldsymbol{BD_{HSC}}$= 3.7390-0.0640K	0.2721	14.7157	71.1%	24.4%	4.4%	0
MF7: $\boldsymbol{BD_{HSC}}$= 1.1828 + 0.0007Crop_MC - 0.3516RGR_Root	0.2687	17.7146	66.7%	26.7%	4.4%	2.2%
MF8:$\boldsymbol{BD_{HSC}}$= 1.3309+0.0032Ca – 0.0477K	0.0037	12.8819	77.8%	20%	2.2%	0

Table D11: Milk ripening SC models

FUNCTION	MIN ERROR	MAX ERROR	0-4.9%	5-9.9%	10-14.9%	15-20%
MR1: $\boldsymbol{BD_{GTD}}$= 3.8450 – 0.0668K	0.0919	16.7795	86.7%	8.9%	2.2%	2.2%
MR2: $\boldsymbol{BD_{GTD}}$=-1.0663 - 0.0042Ca	0.0025	13.0054	71.1%	22.2	6.7%	0
MR3: $\boldsymbol{BD_{GTD}}$= 1.3296 - 0.0052MCD	0.1429	14.7274	66.7%	26.7%	6.7%	0
MR4: $\boldsymbol{BD_{GTD}}$=1.6342 - 0.0495K + 0.0028Ca	0.0549	13.6261	82.2%	15.6%	2.2%	0
MR5:$\boldsymbol{BD_{HSC}}$= 3.8339 – 0.0665K	0.0740	13.6814	73.3%	24.4%	2.2%	0

Appendix

FUNCTION	MIN ERROR	MAX ERROR	0-4.9%	5-9.9%	10-14.9%	15-20%
MR6: $\boldsymbol{BD_{HSC}}$= -0.9950 + 0.0040Ca	0.1647	13.6814	73.3%	24.4%	2.2%	0
MR7: $\boldsymbol{BD_{HSC}}$= 1.3260 - 0.0050MCD	0.2086	15.6126	64.4%	31.1%	2.2%	2.2%
MR8:$\boldsymbol{BD_{HSC}}$= 1.4380 - 0.0430K - 0.0430Ca	0.0211	15.1289	77.8%	20%	0	2.2%

Table D12: Optimum SC validation test data (n=7)

	BULK DENSITY (MG/M^3)		
DEPT (M)	**MEAN**	**MIN**	**MAX**
0-0.10	1.122 ± 0.038	1.0703	1.1873
0.10-0.20	1.198 ± 0.122	1.051	1.4001
0.20-0.30	1.426 ± 0.045	1.3582	1.487
Average	1.2486 ± 0.129	1.1598	1.3581

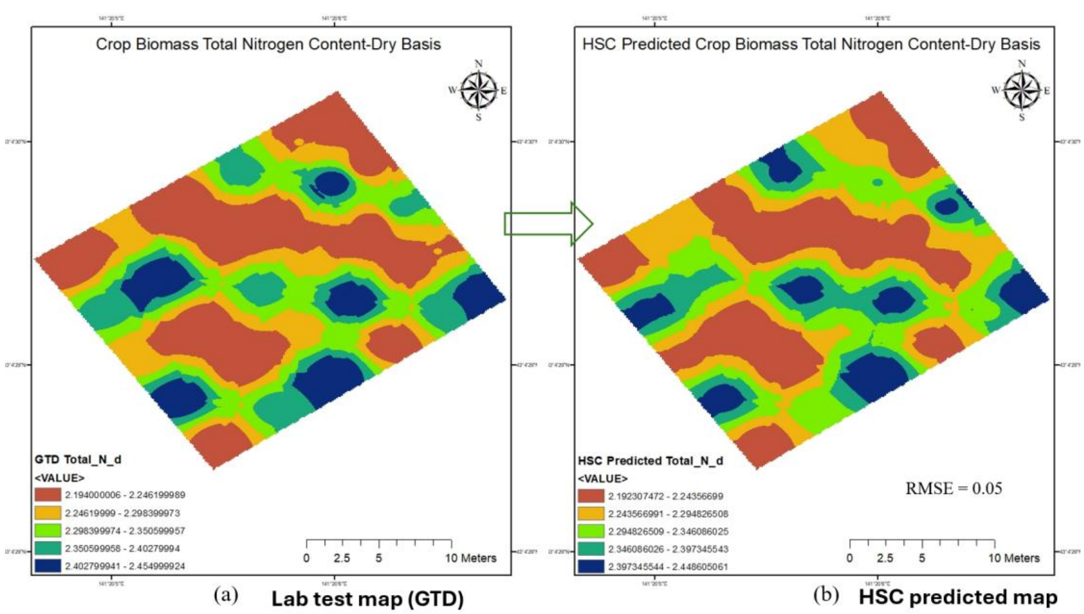

Figure D1: Crop biomass total Nitrogen content spatial map

Appendix

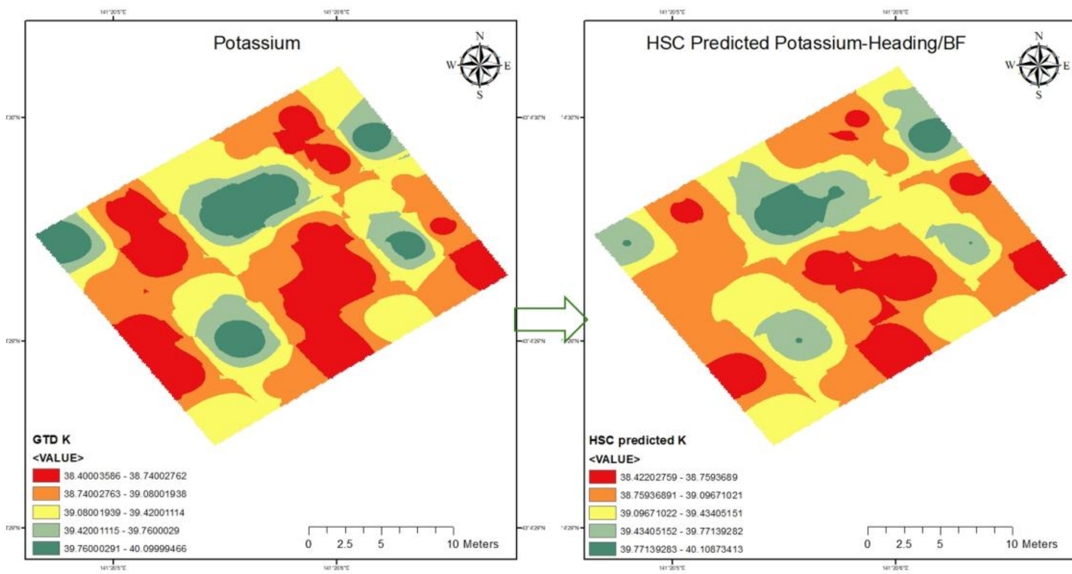

(a) **GTD data map** (b) **HSC prediction map**

Figure D2: K spatial map

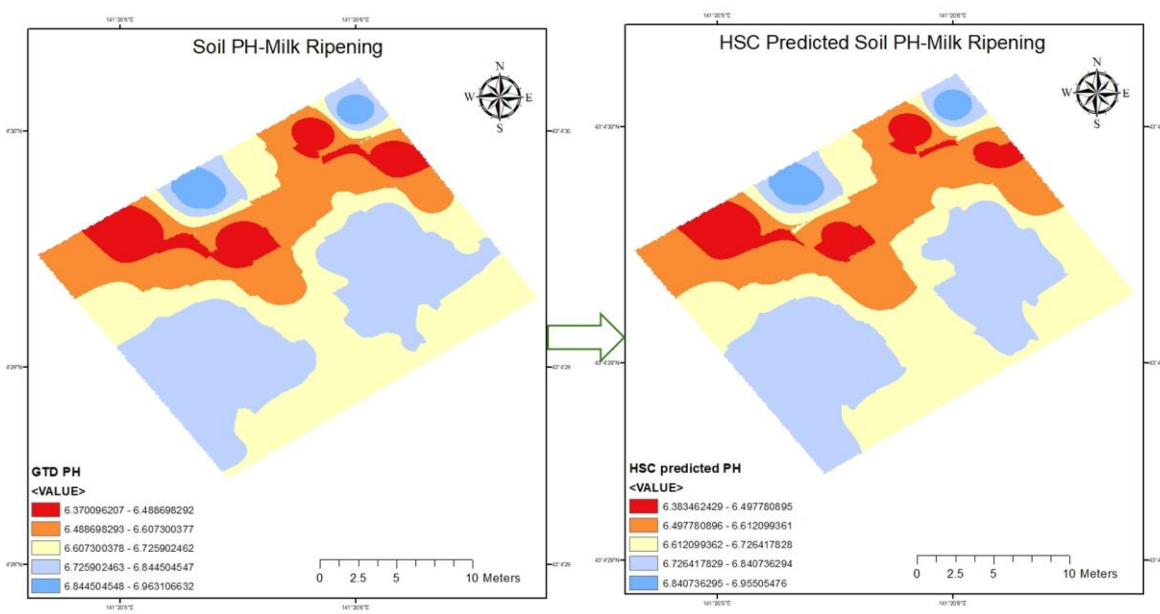

(a) **GTD data map** (b) **HSC prediction map**

Figure D3: pH spatial map

Appendix

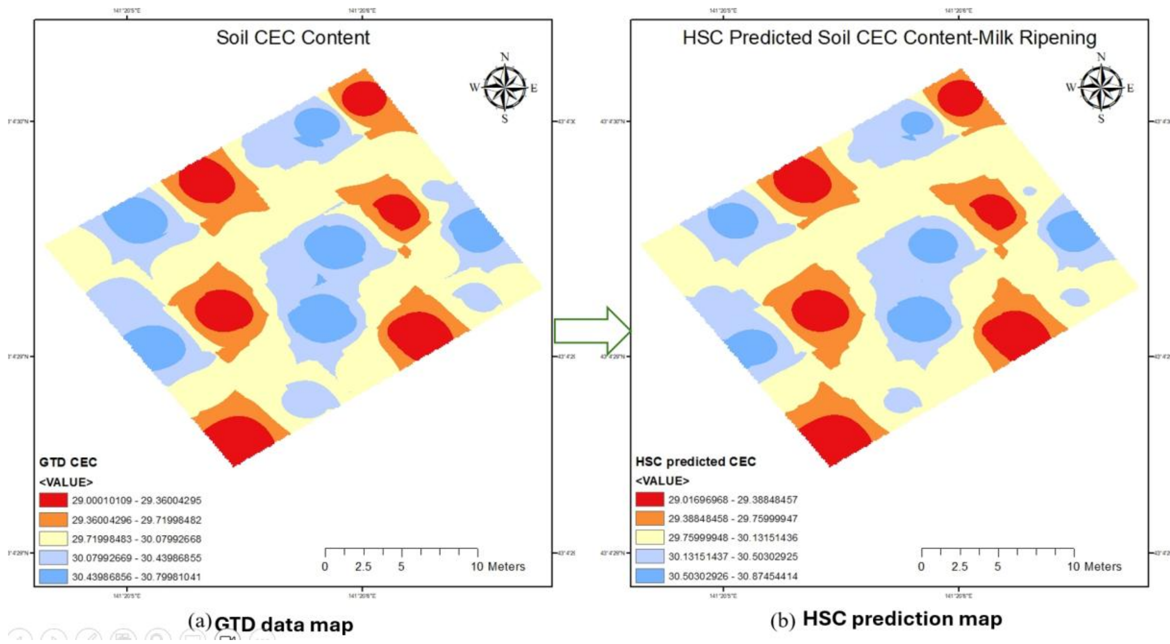

Figure D4: CEC spatial map

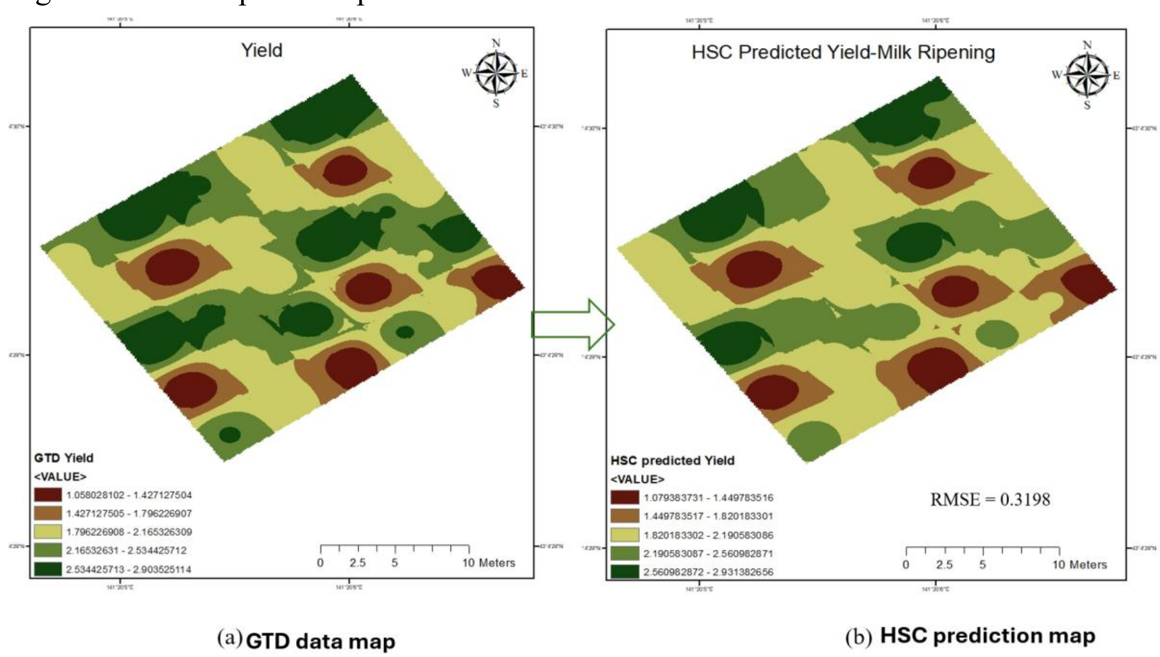

Figure D5: Wheat yields spatial map